A TRAPPED ION QUANTUM SIMULATOR FOR TWO-DIMENSIONAL SPIN SYSTEMS

Marissa Danielle D'Onofrio

Submitted to the faculty of the University Graduate School
in partial fulfillment of the requirements
for the degree
Doctor of Philosophy
in the Department of Physics
Indiana University

December 2022

Accepted by the Graduate Faculty, Indiana University, in partial fulfillment of the requirements for the degree of Doctor of Philosophy.

Doctoral Committee:

Phil Richerme, Ph.D.
Department of Physics
Indiana University

Gerardo Ortiz, Ph.D.
Department of Physics
Indiana University

Herb Fertig, Ph.D.
Department of Physics
Indiana University

Mike Snow, Ph.D.
Department of Physics
Indiana University

08/08/2022

To my family.

ACKNOWLEDGMENTS

Physics does happen in a vacuum (at least ours does), but no man is an island. None of the work presented in this thesis would have been possible without the hard work and support of a huge number of people.

First, I would like to thank Phil Richerme, who has been an incredible advisor and possibly the most patient human being I've ever met. Beyond being generally brilliant, Phil was always available and willing to help, and he was almost unbelievably supportive and optimist. I couldn't have asked to be trained by a better scientist.

I want to thank all of my labmates for creating a warm environment in a temperature-controlled basement. Yuanheng, we shared the unique experience of being senior graduate students as first years and everything that entails. We built the lab together and share its legacy, and I wish you all the best in your own impending graduation and life after. A.J., I've always been in awe of your work ethic and your physical intuition. I can always expect you to have 'crazy ideas' for lab solutions and new experiments, and you also have a great sense of humor and are a fun person to work with. Noah, Paula, and Evangeline, you were great friends and labmates, and I've missed having you around these most recent years. Jiafeng and Antonis, we had limited time together, but your guidance as postdocs was invaluable. It would have been really nice if you were around from the beginning! Finally, best of luck to Frank and Ilyoung; the lab's future rests in your hands... no pressure!

I'd like to thank my high school physics teacher, Edward Lawrence, who dramatically altered my life trajectory. Having a hugely supportive physics teacher with a philosophy background, whose nanotechnology research had an active positive impact on the world, turned me from "not really a math person" into "well, maybe I'll major in engineering".

I'd like to thank my Berry professors - Dr. Hilbert (Hilly-B), Dr. Lane, Dr. T, and Dr. Ron- as well as my Berry research group, Mitchell Crum, Alex Skinner, and William Newman. It was the positive atmosphere and incredible community of the Berry physics department that fully converted me to physics, and it was your encouragement and support that motivated me to pursue a graduate degree.

Many thanks to my committee members Gerardo Ortiz, Herb Fertig, and Mike Snow for their guidance and support throughout my graduate career, and for accommodating my somewhat stringent defense timeline.

I also want to thank Rajibul Islam and Crystal Senko for the work they put into their incredible graduate theses. If I had physical copies, they would be well-worn. I hope mine can be even partially as helpful for incoming students as yours were for me.

I want to extend enormous appreciation to all those who were there for me during some really great times and also really rough times throughout the process. There are fortunately too many to name, and I love you all, but I specifically want to thank John Bollenbacher, Ko Dokmai, Sam Hollis-White, Sara Melcher, Jackie Ducros, and Kaitlyn Sancé. Y'all have been rocks.

Finally, this thesis is dedicated to my parents and grandparents- Jana and Dan D'Onofrio, and Jerry and Lauree Johnson- who raised me to be everything I am and supported me through it all.

Marissa Danielle D'Onofrio

A TRAPPED ION QUANTUM SIMULATOR FOR TWO-DIMENSIONAL SPIN SYSTEMS

Universal, fault-tolerant quantum computing would require millions of physical qubits to practically implement most proposed algorithms, a target currently out of reach of experimental capability. In the near term, noisy systems on the order of tens of qubits can employ quantum simulation of particular Hamiltonians to surpass classical computational abilities and solve interesting problems. In particular, one-dimensional (1D) ion chains in radiofrequency (RF) traps have seen remarkable success in simulating 1D quantum spin systems. A comparable ability to manipulate two-dimensional (2D) ion crystals in RF traps would significantly expand the class of systems accessible to quantum simulation. Notably, 2D ion arrays are conducive to studies of many-body systems such as geometrically frustrated lattices, topological materials, and spin-liquid states.

In this thesis, I present advances toward the goal of creating programmable, "radial-2D" arrays of trapped $^{171}\mathrm{Yb}^+$ ions for quantum simulation. Qubits are embedded within two hyperfine electronic energy levels, cooled to their motional ground state, and measured via spin-dependent fluorescence. A precisely controlled entangling mechanism allows for the creation of a wide variety of spin models, including Ising or Heisenberg interactions. We present an experimental study which establishes radial-2D crystals of $^{171}\mathrm{Yb}^+$ ions as a robust platform for quantum simulation, through characterization of ion positions, structural phases, normal mode frequencies, and effects from RF heating. We also design and experimentally demonstrate a new open-endcap, blade-style RF trap which can confine and resolve large numbers of ions in the radial-2D crystal phase. Finally, we examine other challenges faced by trapped ion systems: optimally cooling to the motional ground state, accurately determining ion temperature, and measuring susceptibility to the presence of ionizing radiation.

TABLE OF CONTENTS

Acknowledgments iv

List of Tables xiv

List of Figures xv

Chapter 1: Introduction 1

1.1 Quantum Mechanics 1

1.2 Quantum Computation and Simulation 2

1.3 Ion Trap Quantum Simulation 3

1.3.1 Two-Dimensional Ion Crystals 4

1.4 Thesis Outline 5

Chapter 2: Theoretical Background 7

2.1 Section overview 7

2.2 The Paul Trap 7

2.2.1 Trapping Potential and Secular Frequencies 8

2.2.2 Structural Phases of Ion Crystals 10

2.2.3 Normal Modes of Motion 11

2.3 The $^{171}\mathrm{Yb}^+$ Qubit 13

2.3.0.1 Ionization Process 14

2.3.1 The Versatile 369 nm Transition 14

2.3.1.1 Doppler Cooling 15

2.3.1.2 State Initialization 18

2.3.1.3 Detection 19

2.3.2 Coherent Operations 20

2.3.2.1 Qubit Rotations 23

2.3.2.2 Entanglement Creation 28

Chapter 3: Experimental Implementation 35

3.1 Section Overview 35

3.2 The Paul Trap 35

3.2.1 The Rod Trap 36

3.2.2 The Blade Trap 38

3.2.3 Trap Voltages 40

3.2.3.1 Applied RF Voltage 40

3.2.3.2 Applied DC Voltages 41

3.3 Laser Systems 42

3.3.1 CW Diode Lasers: 399 nm and 935 nm 42

3.3.2 369 nm Frequency-Doubled Ti:Saph 43

3.3.3 355 nm COHERENT Paladin 44

3.3.4 HeNe Frequency Reference 44

3.4 Experimental $^{171}\mathrm{Yb}^{+}$ Qubit Realization 45

3.4.1 Near-Resonance Lasers . . . 45

3.4.2 Loading Process . . . 49

3.4.3 Imaging System . . . 50

3.4.3.1 Installation Procedure . . . 51

3.4.4 Coherent Operations . . . 51

3.4.4.1 Beatnote Lock . . . 54

3.4.4.2 Raman Beam Alignment . . . 54

Chapter 4: Experimental Sequencing . . . 57

4.1 Section Overview . . . 57

4.2 Experiment Control . . . 57

4.2.1 Sinara Hardware . . . 58

4.3 ARTIQ Software . . . 60

4.4 Trapping an Ion for the First Time . . . 61

4.4.1 Doppler-Free Spectroscopy . . . 62

4.4.2 Imaging Neutral Yb . . . 66

4.4.3 ^{174}Yb for Troubleshooting . . . 67

4.4.4 Troubleshooting Summary . . . 68

4.5 System Calibration for Quantum Simulation . . . 69

4.5.1 Optimizations with One Ion . . . 69

4.5.1.1 Trapping $^{171}\text{Yb}^+$ and Minimizing Micromotion . . . 69

4.5.1.2 Doppler Cooling, Detection, and Optical Pumping . . . 70

4.5.1.3 Rabi Oscillations, Sideband Scans, and Thermometry . . . 71

4.5.1.4 Ramsey Experiments 75

4.5.2 Optimization with Two Ions 75

Chapter 5: Optimized Pulsed Sideband Cooling and Enhanced Thermometry of Trapped Ions 78

5.1 Section Overview 78

5.2 Resolved Sideband Cooling Theory 79

5.3 Optimized Pulsed SBC Protocols 82

5.3.1 Graph-Theoretic Description of Pulsed Sideband Cooling 82

5.3.2 Fixed protocol 84

5.3.3 Optimal Protocol 85

5.3.4 Multiorder Optimization 86

5.4 Thermometry of Sideband Cooled Distributions 89

5.4.1 Existing Methods 90

5.4.2 Modeling Post-SBC Distributions 91

5.4.3 Time-averaged Thermometry 93

5.5 Experimental Results 94

5.5.1 Thermal Distribution 95

5.5.2 Sideband Cooled Distribution 97

5.6 Conclusion 101

Chapter 6: Susceptibility of Trapped-Ion Qubits to Low-Dose Radiation Sources . . . 103

6.1 Section Overview 103

6.2 Experimental Apparatus and Radiation Sources 104

6.3 Results 106

6.3.1 Lifetime Measurements 106

6.3.2 Coherence time and Single-Qubit Gate Fidelity Measurements 107

6.3.3 Heating Rate Measurements 109

6.4 Conclusion 111

Chapter 7: Characterization of Radial-2D Crystals in a Linear Paul Trap 112

7.1 Section Overview 112

7.2 Coulomb Crystals 112

7.3 Two-Dimensional Ion Crystals 113

7.3.1 Lateral-2D Crystals 113

7.3.2 Radial-2D Crystals 114

7.4 Experimental Setup 114

7.4.1 Raman Spectrosocpy 114

7.4.2 Secular Frequency Determination 116

7.4.3 Note on Micromotion Amplitude 116

7.5 Phase Boundaries and Transverse Mode Spectrum 116

7.5.1 Structural Phase Boundaries 116

7.5.2 Axial Mode Spectrum 120

7.6 Micromotion-Induced Heating 120

7.6.1 Crystal Lifetime Measurements 121

7.6.2 Voigt Fluorescence Profiles 121

7.6.3 Axial Heating Rate 123

7.7 Conclusion 125

Chapter 8: An open-endcap blade trap for radial-2D ion crystals 127

8.1 Section Overview 127

8.2 Open-Endcap Trap Design 127

8.2.1 Linear Paul Traps 127

8.2.2 Design Considerations 129

8.2.3 Finite-Element Simulations 130

8.3 Trap Fabrication 134

8.3.1 Material Selection 134

8.3.2 Blade Fabrication and Assembly 134

8.4 Electronics and Voltage Control 137

8.4.1 Helical Resonator 137

8.4.2 rf Locking and Stability 138

8.4.3 DC Control 139

8.5 Experimental Demonstration 141

8.5.1 Laser Access and Internal States 141

8.5.2 Confinement and Imaging of Radial-2D Crystals 141

8.5.3 Ion Trajectory Analysis 144

8.6 Conclusion 145

Chapter 9: Conclusion and Outlook 146

Appendices 148

Appendix A: Floquet-Lyapunov Solution of Ion Motion 148

  A.1 Dynamic Solution of Ion Motion 148

Appendix B: Voigt Distibution 152

Appendix C: Thermometry 153

  C.1 Ratio Thermometry 153

  C.2 SVD Thermometry 153

References 155

Curriculum Vita . . . .

LIST OF TABLES

3.1 Intensities and frequency shifts of relevant beams 49

3.2 Separation between imaging system optical components 51

4.1 Calibrated ^{174}Yb+ transition frequencies for trapping and cooling 67

4.2 Calibrated ^{171}Yb^{+} transition frequencies for trapping and cooling 69

6.1 Integrated, low-dose α, β, and γ radiation sources 106

LIST OF FIGURES

2.1 Secular motion and micromotion of an ion in a linear Paul trap 9

2.2 Structural phase transitions of an ion crystal 11

2.3 Relevant levels of a $^{171}\mathrm{Yb}^{+}$ atom 13

2.4 2-photon ionization process of neutral $^{171}\mathrm{Yb}$ 15

2.5 An illustration of the Doppler cooling mechanism 17

2.6 Stimulated transitions for optical pumping and detection 18

2.7 Photon count distribution curve for ion detection 20

2.8 The Bloch sphere 21

2.9 A stimulated Raman transition between qubit states 22

2.10 Carrier, red sideband, and blue sideband transitions 26

2.11 Mølmer-Sørensen interaction 29

3.1 Front and back view of the trap chamber 37

3.2 Solidworks model of the rod-style Paul trap 38

3.3 Assembled blade-style Paul trap mounted in its vacuum chamber 40

3.4 Optical pathways of near-resonant lasers 46

3.5 Guppy images of beam intensity profiles 47

3.6 Ray diagram of imaging system optical components 50

3.7 355 nm beam path diagram and photograph of COHERENT laser head 53

3.8 Raman beatnote lock 55

4.1 Modular hardware for experimental control system (Sinara chassis) 58

4.2 GUI for experiment control (Artiq dashboard) 61

4.3 Doppler-free spectroscopy experimental setup 62

4.4 Doppler-free absorption spectrums for $S \rightarrow P$ transitions of neutral and ionized Yb 64

4.5 Doppler-free absorption spectrum for the 935 nm transition in $^{174}\mathrm{Yb}^{+}$ 65

4.6 399 nm neutral fluorescence 66

4.7 $^{174}\mathrm{Yb}^{+}$ energy level diagram 68

4.8 Optical pumping calibration data 71

4.9 Rabi oscillation calibration data 72

4.10 Axial sideband spectrum data 73

4.11 Time-averaged heating rate measurement 74

4.12 Mølmer-Sørensen interaction curve 77

5.1 Graph representation of first-order SBC theory 83

5.2 Weight matrix elements 84

5.3 Comparison of classical, fixed, optimal, and multiorder SBC protocols 87

5.4 Thermometry comparisons of thermally-distributed ion motional states 96

5.5 Ratio method comparison to simulation 98

5.6 Thermometry comparisons of a sideband cooled ion. 100

6.1 Experimental apparatus for radiation susceptibility study 104

6.2 Single-qubit X-gate fidelities with various low-dose radiation sources introduced . . 107

6.3 Heating rate measurements with various low-dose radiation sources introduced . . 110

7.1 Experimental setup for Raman sideband spectroscopy and secular frequency measurements 115

7.2 Predicted and measured ion positions for each structural phase of a Coulomb crystal in a linear Paul trap 117

7.3 Phase diagram and axial mode spectrum 119

7.4 Radial heating rate for seven ions 122

7.5 Axial heating rate for one ion and seven ions 124

8.1 Assembled blade trap mounted in its vacuum chamber 131

8.2 Finite-element simulation of trapping potential and ion positions 133

8.3 Profilometry of a blade electrode after wire-EDM machining and polishing 135

8.4 Two-coil resonator design 138

8.5 Active stabilization of RF amplitude 139

8.6 DC circuit diagram of blade trap 140

8.7 Concept drawing of the trap and laser beam configurations 142

8.8 CCD images of radial-2D ion crystals 143

CHAPTER 1

INTRODUCTION

1.1 Quantum Mechanics

In a classical world, motion is governed by Newton's second law

$$F = m\frac{d^2\vec{r}}{dt^2} = -\nabla V(\vec{r}), \tag{1.1}$$

where complete knowledge of a system allows for its full, deterministic characterization over all time. That is to say, given an instantaneous position $\vec{r}$ and momentum $m(d\vec{r}/dt)$ of a particle with mass m, along with a potential function V, we can solve for any other dynamical variable.

Quantum mechanics, on the other hand, does not provide a deterministic description but rather defines the world in terms of probability amplitudes. Analogous to how position is governed by Newton's 2^{nd} law, quantum mechanical dynamics are governed by the Schrodinger equation

$$i\hbar\frac{\partial}{\partial t}\Psi(\vec{r},t) = \mathcal{H}\Psi(\vec{r},t), \tag{1.2}$$

where the wavefunction $\Psi(\vec{r},t)$ is a complex probability amplitude containing all available information about the system, and $\mathcal{H}$ is the system's Hamiltonian.

An interesting property of quantum mechanics is that the state vector $|\Psi\rangle$ of a physical system can be in a superposition of several possible states at the same time. For example, the wavefunction for an N-particle, two-level system is

$$|\Psi\rangle = \sum_{s_i=\uparrow,\downarrow} a_{s_i \ldots s_n} \left| s_i \ldots s_n \right\rangle, \tag{1.3}$$

which has 2^n probability amplitudes. Quantum mechanics also gives rise to genuinely non-classical properties such as entanglement and non-local correlations, resulting in phenomenon such as the Einstein-Podolsky-Rosen (EPR) paradox [1].

1.2 Quantum Computation and Simulation

Classical computational bits work within the binary $\{0, 1\}$, and so the number of classical bits required to simulate a quantum system such as Equation 1.3 scales exponentially with particle number. Simulating a system of only 300 two-level quantum particles would require 2^{300} classical bits, which is greater than the number of atoms in the known universe. That would be hard to build! In Richard Feynman's famous 1982 lecture [2], 'Simulating Physics with Computers,' he proposed an alternative to a classical probability simulator: using a computer that is itself probabilistic.

In such a computer, each experiment does not yield the same result as nature. Rather, after repeating an experiment enough times, it is the frequency of final states proportional to the number of repetitions that should match nature. Feynman also proposed a universal quantum simulator, or so-called quantum computer, with which any local quantum mechanical system can be simulated efficiently. This postulate was shown to be correct by Seth Lloyd in 1996 [3], who proved that evolving in small time steps would allow polynomial rather than exponential growth in the overall time required to simulate any many-body quantum Hamiltonian containing few particle interactions.

Around this time, the field of quantum computing took off. In 1989, David Deutsch discovered a problem which can be solved faster with a quantum computer than a classical one [4]. Soon after, in 1994, Peter Shor showed that the prime factorization of an integer could be solved efficiently on a quantum computer. The DiVincenzo criteria, or the necessary criteria for a universal quantum simulator, were explicitly specified in 2000 [5]. They include a scalable physical system with a well-characterized qubit, a method of state initialization, a method for universal gate implementation, long coherence times, and a method for measurement and state readout. Unfortunately, this set of criteria results in a catch-22: the system must be well-isolated in order to retain its quantum properties, but it also must be accessible to the world in order for us to perform computation and read results.

The long-term solution to the DiVincenzo criteria's catch-22 will most likely require quantum error correction (QEC) protocol. The objective of QEC is fault-tolerant quantum computing, where errors are corrected faster than they're created. However, for the presently available quantum devices on the order of 100 qubits, the required overhead for fault-tolerance is out of range of experimental capability [6]. Returning to Feynman's original proposal, we can design non-universal quantum simulation devices as a way to harness as much computational power as possible from the systems currently available to us.

Non-universal quantum simulators are special purpose devices, programmed to provide insight about specific physical systems. These simulators can be 'digital' simulators, where the desired Hamiltonian is constructed through a Trotterization [7]

$$e^{-iHt} \approx \left(e^{-iH_1 t/n} e^{-H_2 t/n} ... e^{-iH_n t/n}\right)^n \tag{1.4}$$

of n steps, or they can be 'analog' simulators, which continuously follow a Hamiltonian that maps mathematically to a desired physical system [8]. Quantum simulators have been realized in many physical systems, including trapped ions [9], optical lattices [10], nuclear magnetic resonance systems [11], and superconducting circuits [12].

1.3 Ion Trap Quantum Simulation

Trapped ions were identified by Cirac and Zoller in 1995 as the first realistic system with which to implement a quantum computer [13]. Later that year, the first controlled bit flip on two qubits embedded in a single ion was demonstrated by David Wineland's group at NIST [14], representing the birth of experimental quantum computing. The first universal gate set on a 2-ion string was performed by Schmidt-Kaler in 2003 [15]. Since then, trapped ions have remained a frontrunner in the push for fault-tolerant quantum computation [16, 17, 18] and have seen remarkable success in simulating quantum spin systems [9, 19, 20], .

A major benefit of trapped ions is the provision of identical qubits. This thesis discusses a trapped ion platform using $^{171}\mathrm{Yb}^{+}$, which along with the general benefits of trapped ions also has specific advantages. The qubit states of $^{171}\mathrm{Yb}^{+}$ are hyperfine ground states with effectively infinite lifetimes. Under ultra-high vacuum (UHV), the longest measured coherence time of a $^{171}\mathrm{Yb}^{+}$ qubit state is one hour at room temperature [21]. Readily available laser-cooling techniques allow for ions to be cooled to mK temperatures within milliseconds, and additionally cooled to near the motional ground state. The absence of thermal motion, combined with the $5-10$ μm separation between ions due to the Coulomb interaction, allows for qubit state detection with near-perfect efficiency [22]. State initialization through optical pumping also yields typical fidelities $> 99\%$, and effective spin interactions can be varied over a wide range- making ions especially well-suited for simulating long-range spin models [9].

1.3.1 Two-Dimensional Ion Crystals

The majority of quantum simulation experiments have been performed on one-dimensional (1D) chains of ions, but many applications of quantum information processing experiments are not well-matched to the capabilities of this linear geometry. In particular, quantum simulation of interesting many-body systems such as geometrically frustrated lattices, topological materials, and spin-liquid states would benefit from native two-dimensional (2D) geometries [23, 24, 25, 26, 27]. In addition, 2D arrays can hold larger numbers of qubits more efficiently than 1D strings, with a higher error threshold for fault-tolerance [28, 29], and may simplify preparations of 2D cluster states for one-way quantum computing [30, 31].

A number of efforts are underway to control and probe 2D ion crystals. Penning traps in particular have been quite successful in simulating and studying quantum spin models [19, 32], though the fast crystal rotation in such traps poses a significant challenge to individual ion addressing. Other 2D efforts include microfabricated ion arrays [33] with ions trapped in individual harmonic wells, dynamical engineering of effective 2D lattices using 1D chains [34], and quantum charge coupled device (QCCD) architecture where ions are rearranged and transported between trapping regions and gate regions [16]. In order to keep traditional ion trap strengths such as individual addressing, site resolved measurements and readout, and fast coupling rates, we have elected to build a radiofrequency (RF) Paul trap, with parameters chosen carefully such that ions self-assemble into a 2D Coulomb crystal. This thesis presents the experimental implementation of such a system, and the chapter outline is included below.

1.4 Thesis Outline

Chapter 2 provides a theoretical background for quantum simulation with $^{171}\text{Yb}^{+}$. First we look at the Paul trap, describing the resultant trapping potential and how to use this potential to create two-dimensional Coulomb crystals. We define a qubit within the electronic energy levels of $^{171}\text{Yb}^{+}$, outlining methods to cool the ion as well as detect and initialize the qubit state. Finally, we describe coherent qubit rotations and entanglement operations via stimulated Raman transitions.

Chapter 3 describes the experimental implementation of all the methods presented in Chapter 2. It gives an overview of the home-built Paul traps used in experiments and integral hardware such as the vacuum chamber, voltage control, optical pathways, and imaging system. All the experimental setup and calibrations that must be performed before an ion can be trapped are described in this chapter- for example, aligning the imaging system and optical pathways, and locking laser frequencies.

Chapter 4 describes experimental sequencing, beginning with implementation of the Artiq control system and associated Sinara hardware. This chapter includes all the troubleshooting procedures that can be applied when first trapping $^{171}\text{Yb}^{+}$ as well as the optimization procedures that follow. A daily protocol is outlined which results in the realization of an entangling gate.

Chapters 5 and 6 discuss single-ion studies performed in a rod-style linear Paul trap. The former improves on standard atomic physics techniques for cooling and thermometry, and the latter contributes to our understanding of radiation effects in trapped ion systems. Chapter 5 demonstrates methods for optimized pulsed sideband cooling (SBC) and enhanced thermometry of trapped ions as presented in [35]. It reviews the standard theory of pulsed resolved SBC and recasts the problem into a matrix formalism that allows for efficient optimization of SBC pulse sequences. After extensive cooling, we find that the ion motional distribution is distinctly nonthermal and thus not amenable to standard thermometry techniques. We therefore develop and experimentally validate an improved method to measure ion temperatures after sideband cooling.

Chapter 6 discusses the real-time susceptibility of trapped-ion systems to small doses of ionizing radiation, as presented in [36]. We expose an ion-trap apparatus to a variety of α, β, and γ sources and measure the resulting changes in trapped-ion qubit lifetimes, coherence times, gate fidelities, and motional heating rates. No quantifiable degradation of ion trap performance is found in the presence of low-dose radiation sources for any of the measurements performed, an encouraging finding for the long-term prospects of using ion-based quantum information system in extreme environments.

Chapter 7 details an experimental study which establishes radial-2D crystals as a robust experimental platform for quantum simulation [37]. This chapter demonstrates, using arrays of up to 19 $^{171}\mathrm{Yb}^{+}$ ions, that the structural phase boundaries of radial-2D crystals are well-described by the pseudopotential approximation despite the presence of micromotion. Heating rate measurements verify that the transverse motional modes, used in quatum simulation schemes, are well-predictable numerically and can remain decoupled from the radial modes.

Chapter 8 presents the design and experimental demonstration of an open-endcap radio frequency trap for radial-2D crystals [38]. The central axis of the trap is kept free of obstructions to allow for site-resolved imaging in the 2D crystal plane, and confining potentials are provided by four segmented blade electrodes. We discuss design challenges, fabrication techniques, and voltage requirements, and we validate the trap operation by confining up to 29 ions in a radial-2D triangular lattice.

Chapter 9 gives an overview of current lab efforts and outlook for future directions.

CHAPTER 2

THEORETICAL BACKGROUND

2.1 Section overview

Section 2.2 will describe the Paul trap. First I will show how an oscillating RF voltage and a static DC voltage can be combined to trap charged particles. Then I will describe how the resulting potential can be approximated as a harmonic oscillator where ions off the trap center experience driven micromotion. This section will also summarize how trap voltages can be defined to result in a two-dimensional triangular lattice configuration favorable for quantum simulation experiments.

In Section 2.3, we will take a look at the electronic energy levels of $^{171}\mathrm{Yb}^{+}$ and I will describe how it can be ionized and cooled. We will see how the $^{171}\mathrm{Yb}^{+}$ ion is realized as an effective spin-1/2 system for quantum simulation experiments by defining two qubit states which can be initialized and detected using cyclic transitions. Finally we will describe how stimulated Raman transitions can be used to perform coherent operations for qubit manipulation in quantum simulation as well as to sideband cool the ion to near-zero temperatures.

2.2 The Paul Trap

The linear Paul trap is a type of ion trap that relies on dynamic and static electric fields in order to bypass Earnshaw's theorem, which states that in free space it is not possible to create a 3D potential minimum out of static charges. This is a consequence of the fact that any potential $\Phi(\vec{r})$ satisfying Laplace's equation

$$\nabla^2\Phi = 0 \tag{2.1}$$

can have no maxima or minima. The Laplace condition imposes that, for an electric quadrupole potential of the form

$$\Phi(x, y, z) = \alpha x^2 + \beta y^2 + \gamma z^2, \tag{2.2}$$

the constants α, β, and γ must satisfy the condition $\alpha+\beta+\gamma=0$. One way to satisfy this condition is by setting $\alpha=\beta, \gamma=-2\alpha$, which results in the static 3D field

$$\Phi(x,y,z)=\alpha(2z^2-x^2-y^2). \tag{2.3}$$

In a linear Paul trap [39], an oscillating RF voltage V_0 is applied jointly with the static DC voltage U_0, to create a rotating potential saddle. Near the center of the trap, the potential then has the form

$$\begin{aligned}\Phi(\vec{r},t)&=\Phi_{RF}(\vec{r},t)+\Phi_{DC}(\vec{r})\\&=\frac{V_0\cos(\Omega_t t)}{2r_0^2}(x^2-y^2)+\frac{\kappa U_0}{2z_0^2}(2z^2-x^2-y^2)\end{aligned} \tag{2.4}$$

where r_0 and z_0 are the radial (x,y) and axial (z) trap dimensions, Ω_t is the trap drive frequency, and κ is a geometric factor of order 1. This trapping potential gives rise to secular motion, which can be approximated as a harmonic pseudopotential, as well as micromotion- small, fast oscillation at the RF drive frequency which affects ions off the RF null.

2.2.1 Trapping Potential and Secular Frequencies

The equation of motion for a particle of mass m and charge Q in an electric field is

$$\vec{F}=Q\nabla\Phi(\vec{r})=m\frac{d^2}{dt^2}(\vec{r}). \tag{2.5}$$

Substituting our ion trap potential (Equation 2.4) into Equation 2.5 results in the Mathieu equations

$$\frac{d^2r_i}{d\zeta^2}+[a_i+2q_i\cos(2\zeta)]r_i=0 \tag{2.6}$$

for directions $i\in\{x,y,z\}$, dimensionless time $\zeta=\frac{\Omega_t t}{2}$, and Mathieu parameters

$$a_{x,y}=\frac{4Q\kappa U_0}{mz_0^2\Omega_t^2}\,, q_x=-q_y=\frac{2QV_0}{mr_0^2\Omega_t^2}. \tag{2.7}$$

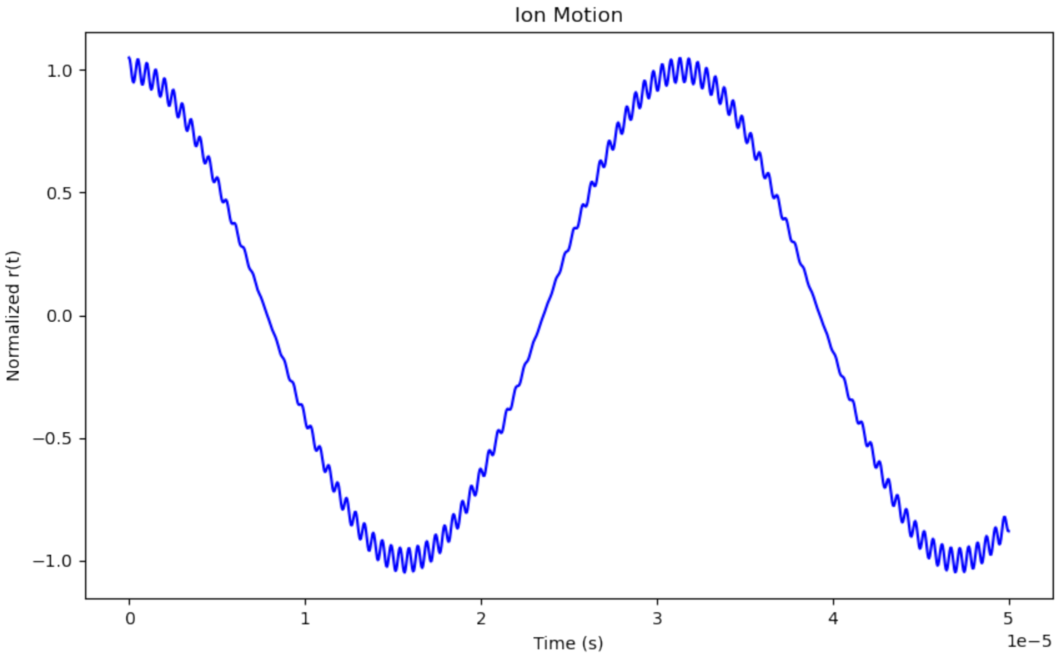

Figure 2.1: The motion of an ion in a Paul trap as described by Equation 2.8, where I have set Ω_t = 27 MHz, $\omega_i = 0.2$ MHz, and $q_i = 0.1$. The large amplitude motion is the trap secular frequency, and the overlaid small, fast oscillations are known as micromotion.

for ion mass m and charge Q, and κ is a geometric factor of order unity.

For $a_i < q_i^2 \ll 1$, the solution (to first order in a and second order in q) is given by

$$\begin{aligned} r_i(t) = A_i \Bigg(& \cos(\omega_i t) \left[1 + \frac{q_i}{2} \cos(\Omega_t t) + \frac{q_i^2}{32} \cos(2\Omega_t t) \right] \\ & + \beta_i \frac{q_i}{2} \sin(\omega_i t) \sin(\Omega_t t) \Bigg) \end{aligned} \tag{2.8}$$

for $\beta_i \approx (a_i + q_i^2/2)^{1/2}$ and A_i dependent on initial conditions. Particle motion in the trap is stable when $0 \leq \beta_i \leq 1$ in all three directions, and so in order to design a stable trap, parameters such as voltage and frequency (on which the a and q values depend) must be carefully chosen.

The large amplitude motion at ω_i is the secular motion, with resonant frequencies $\omega_i = \beta_i \Omega_t / 2$, while the fast, small oscillation at Ω_t is known as micromotion. The motion described by Equation 2.8 above is shown in Figure 2.1.

At mK temperatures, the secular motion of an ion near the center of a near radially-symmetric trap potential is well-described by the 3D harmonic pseudopotential

$$Q\Phi(x,y,z) = \frac{1}{2}m\left(\omega_x^2x^2 + \omega_y^2y^2 + \omega_z^2z^2\right). \tag{2.9}$$

Under this pseudopotential approximation, the trap secular frequencies can be written

$$\omega_x \approx \omega_y = \sqrt{\frac{Q}{m}\left(\frac{qV_0}{4r_0^2} - \frac{\kappa U_0}{z_0^2}\right)}, \omega_z = \sqrt{\frac{Q}{m}\frac{2\kappa U_0}{z_0^2}}. \tag{2.10}$$

Following Equation 2.8 above, micromotion drives the ions' radial coordinates about their equilibrium positions as

$$\vec{r}(t) = \vec{r}_0 + \vec{r}_1\cos(\Omega_t) + \vec{r}_2\cos(2\Omega_t) + ... \tag{2.11}$$

with coefficients $|\vec{r}_1| = \frac{q}{2}r_0$ and $|\vec{r}_2| = \frac{q^2}{32}r_0$. For a stable trap, $q \ll 1$; in this regime the micromotion amplitude is generally well approximated by $|\vec{r}_1|$.

2.2.2 Structural Phases of Ion Crystals

If the trap axial frequency w_z is increased relative to the radial frequency ω_r, a crystal of N ions will pass through a series of structural phase transitions as shown in Figure 2.2. Beginning in a 1D chain configuration, ions will pass through 2D zig-zag and 3D spheroidal configurations before breaking into a 2D crystal in the radial plane. Under the pseudopotential approximation, this radial-2D phase is achieved when the trap aspect ratio $\omega_z/\omega_r > (2.264N)^{1/4}$ [40].

For the higher-α phases, ions that lie away from the trap's central axis are subject to rf-driven micromotion as defined in Equation 2.11. The radial-2D phase has been the primary interest of theoretical studies of 2D ion crystals, though there is also a body of working using 'lateral' 2D crystals- an extension of the zig-zag phase with highly non-degenerate radial frequencies. Further discussion and characterization of radial-2D crystals for quantum simulation is provided in Chapter

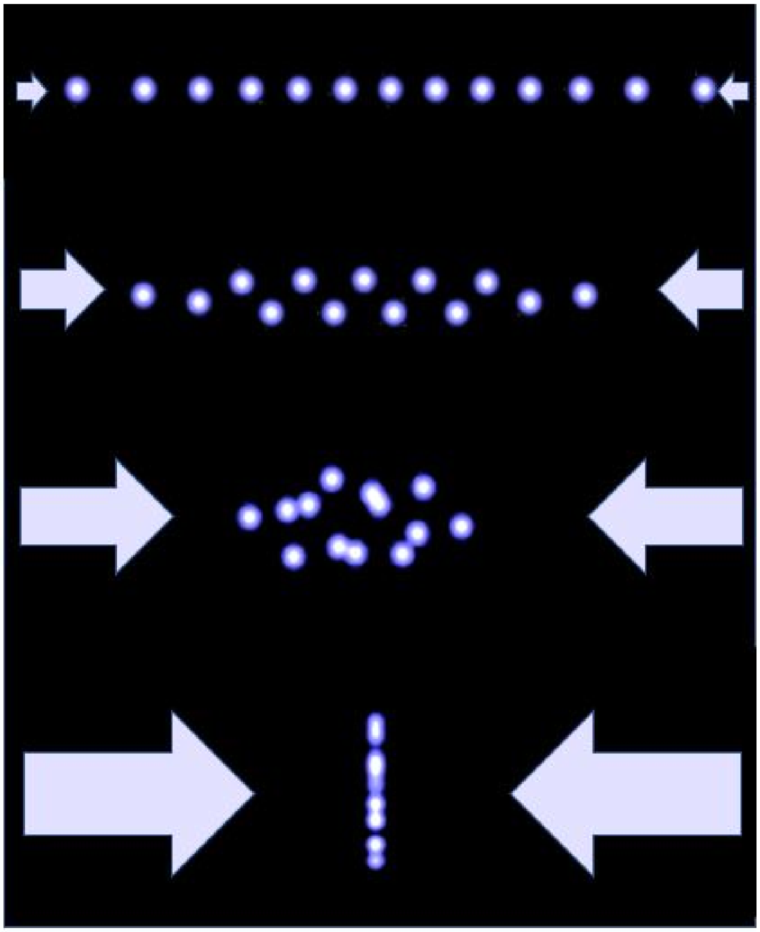

Figure 2.2: For low axial confinement (top), ions spread out in a chain along the RF null. As axial confinement is increased relative to radial confinement, they will go through a series of phase transitions involving a 2D zig-zag configuration (second from top) and 3D spheroidal phases (second from bottom), before aligning into a triangular lattice in the radial plane (bottom, shown from side).

7.

2.2.3 Normal Modes of Motion

The potential

$$V(x,y) = \sum_i (\frac{1}{2}m\omega_x^2 x_i^2 + \frac{1}{2}m\omega_y^2 y_i^2) + \sum_{i<j} \frac{Q^2}{4\pi\epsilon_0 r_{ij}} \tag{2.12}$$

experienced by i ions in the radial-2D lattice is a combination of the confining potential of the Paul trap and repulsive Coulomb potential between ions. Here,

$r_{ij} = \sqrt{(x_i - x_j)^2 + (y_i - y_j)^2}$, and the equilibrium ion positions are the set of coordinates $\{x_i, y_i\}$ which minimize the energy. For small numbers of ions, this can be done with direct numerical minimization, and finding the equilibrium position for large numbers of ions is generally achieved with a molecular dynamics simulation with added dissipation [26].

Any small perturbation of an N-ion lattice from equilibrium creates an oscillation about equilibrium, with motional components along the three trap principal axes. Ions remain coupled by the Coulomb potential, and complex oscillatory motion can be decomposed into $3N$ normal modes of vibration. Axial (transverse) motional modes are used for the quantum simulation protocol described in Section 2.3.2. To calculate these vibrational modes, the Coulomb potential is expanded to second order about the equilibrium positions and diagonalized in order to find the eigenvectors b_i^k and eigenvalues ω_k. The axial trapping potential for i ions to second order is given by

$$V(z) = \sum_i \frac{1}{2} m \omega_z^2 z_i^2 + \frac{Q^2}{4\pi\epsilon_0} \sum_{i \neq j} \frac{1}{r_{ij}^3} (z_i z_j - z_i^2). \tag{2.13}$$

In a radial-2D crystal, the highest frequency motional mode is the center-of-mass (COM) mode, in which all ions move back and forth with uniform motion. The eigenvector of the COM mode is always $(1/N)[1, 1, 1, ...1]^T$, and the eigenfrequency is the axial trap secular frequency ω_z. The lowest frequency mode is the zig-zag mode, in which alternating ions oscillate in opposite directions. The trapping potential determines the spacing between these modes and the ‘forest’ of modes between them, and each mode makes a contribution to the interaction Hamiltonian described in Section 2.3.2.

This description of normal modes has ignored micromotion, which adds time-dependence to the equilibrium positions of the ions. Our results in Chapter 7 suggest that this is valid, though a time-dependent method for motional mode analysis has been included in Appendix A.

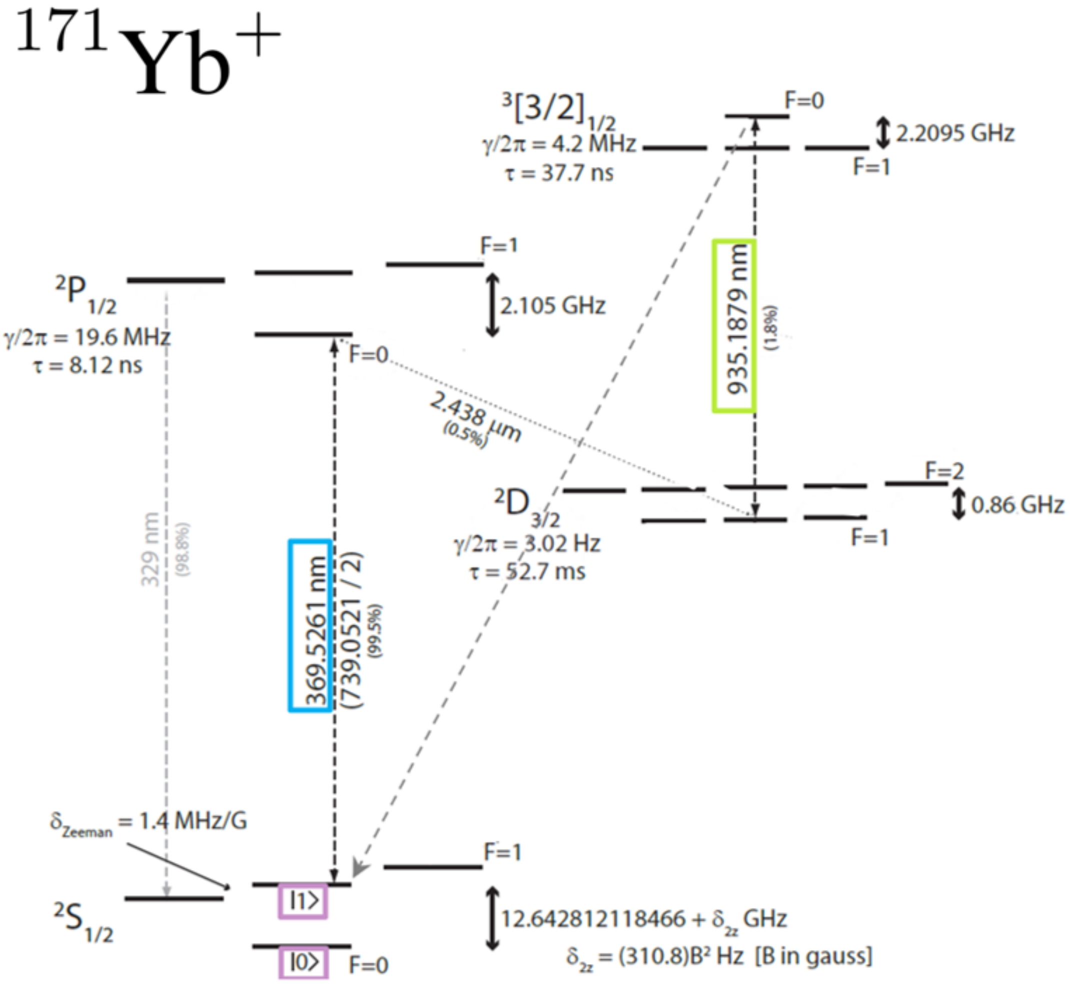

Figure 2.3: Relevant levels of a ^{171}Yb$^+$ atom are shown. The spin qubit states $|0\rangle$ and $|1\rangle$, highlighted in purple, are embedded in the two $m = 0$ ground states of the $^2S_{1/2}$ manifold. Most relevant operations are performed along the 369 nm $^2S_{1/2} \rightarrow ^2 P_{1/2}$ transition line, highlighted in blue. A 935 nm repump, highlighted in green, is required to close the cycle on this transition, as there is a small chance of decaying from $^2P_{1/2}$ to the long-lived $^2D_{3/2}$ state.

2.3 The ^{171}Yb$^+$ Qubit

Our effective spin-1/2 state, or qubit, is embedded in two hyperfine ground states of a ^{171}Yb$^+$ ion, for which the relevant electronic energy levels are shown in Figure 2.3. Ytterbium is similar to an alkaline earth metal; after a single ionization, it is left with one valence electron and a hydrogenlike electronic energy structure. Hyperfine sublevels arise from its spin-$\frac{1}{2}$ nucleus, resulting in four ground states (the $^2S_{\frac{1}{2}}$ manifold) which correspond to the singlet state $|f = 0, m = 0\rangle$ and triplet state $\{|f = 1, m = -1\rangle$, $|f = 1, m = 0\rangle$, $|f = 1, m = -1\rangle\}$, for hyperfine manifolds $f = \{0, 1\}$ and magnetic quantum number $m = \{-1, 0, 1\}$.

Hyperfine ground states are advantageous as qubits due to their effectively infinite lifetimes, and the $m = 0$ states are first-order insensitive to any external electric or magnetic field perturbations. We choose the qubit states $|0\rangle \equiv |f = 0, m = 0\rangle$ and $|1\rangle \equiv |f = 1, m = 0\rangle$, to form an effective spin-1/2 system. These states, highlighted purple in Figure 2.3, may be referred to respectively as the 'dark' and 'bright' states or 'spin-up' and 'spin-down' states, and they are separated by $w_{HF} = 12642812118.5$ Hz + $310.8B^2$ (Hz/G). Applying an external magnetic field B induces a Zeeman splitting of $\delta_{Zeeman} = 1.4$ MHz/G, which allows us to decrease coupling to the non-qubit ground states ($f = 1$; $m = -1, +1$) and avoid coherent population trapping [41] by shifting the Zeeman levels away from the ω_{HF} transition.

2.3.0 Ionization Process

^{171}Yb$^+$ is created through a two-photon ionization process of neutral ^{171}Yb, as shown in Figure 2.4. Light at 398.9 nm excites the $^1S_0 \leftrightarrow {}^1P_1$ transition, and then any wavelength below 394.5 nm can send the electron into the continuum, resulting in ionization [42]. The two laser frequencies we use to excite from the $^1P_1$ state to the continuum are 355 nm and 369 nm, as these frequencies serve other primary purposes in our lab and are therefore easily accessible.

2.3.1 The Versatile 369 nm Transition

The 369 nm $^2S_{\frac{1}{2}} \rightarrow^2 P_{\frac{1}{2}}$ transition serves many purposes, providing the first stage of laser cooling, state initialization, and state detection/discrimination.

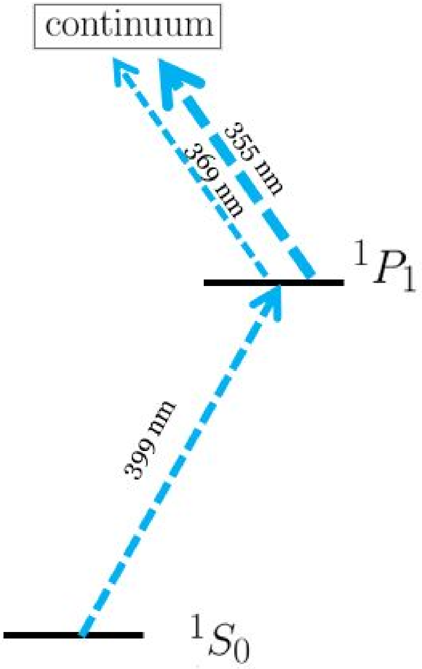

Figure 2.4: Neutral ^{171}Yb is ionized through a two-photon process. Light at 398.9 nm excites the $^1S_0 \leftrightarrow {}^1P_1$ transition, and then any wavelength < 394.5 nm can send the electron into the continuum, resulting in ionization. The frequencies used in our lab to excite from the $^1P_1$ state to the continuum are 355 nm and 369 nm.

2.3.1 Doppler Cooling

Following ionization of a ^{171}Yb atom, we use Doppler cooling to bring it closer to its ground state. Doppler cooling is a mechanism that utilizes light slightly red-detuned below an electronic transition, such that counter-propagating ions are more likely to absorb photons [43]. When a near-resonant photon is absorbed, the energy $\hbar\omega$ of the light raises the internal energy of the ion and alters the internal angular momentum by $l = \pm 1$, whereas the linear momentum $\vec{p} = \hbar\vec{k}$ changes the motion of the atoms in the lab frame. In the case of well-directed light from a laser beam, the momentum exchange between the light and atoms results in the force

$$\vec{F} = \frac{d\vec{p}}{dt} = \hbar\vec{k}\Gamma \tag{2.14}$$

where Γ is the excitation (scattering) rate of the ions. Since $\vec{k}$ is counter to the ion's initial velocity, the ion slows. For a low enough light intensity, ions are likely to return to the ground state via spontaneous emission. The emitted photon then carries off momentum $\hbar k$ in a random direction such that the momentum exchange due to emission averages to zero. Thus the net force on the ion is equivalent to that from absorption, illustrated in Figure 2.5.

The scattering rate is given by the Lorentzian

$$\Gamma = \frac{\frac{I}{I_{sat}}\frac{\gamma}{2}}{1 + \frac{I}{I_{sat}} + \frac{4\Delta^2}{(\gamma)^2}} \tag{2.15}$$

where $\gamma/2\pi$ is the natural linewidth (19.6 MHz for ^{171}Yb^{+}), Δ is the laser detuning from resonance, I is the laser intensity, and the saturation intensity

$$I_{sat} = \frac{\pi h c \gamma}{3\lambda^3 R_{br}} \tag{2.16}$$

is the intensity necessary to create equal populations in the ground and excited state of the ion. Here R_{br} is the branching ratio, and λ is the transition wavelength.

Solving the energy rate equation as outlined in [44] shows that the Doppler cooling limit can be found by setting $\Delta = -\gamma/2$, with $I/I_{sat} \ll 1$. Assuming a Maxwell-Boltzmann velocity distribution, this gives the temperature relation

$$k_B T = \frac{\hbar\gamma}{2} \tag{2.17}$$

which we can then equate to the energy of a harmonic oscillator level $E_{HO} = \hbar\omega(n + 1/2)$ for secular trap frequency ω. Doing so gives an minimum average occupation value

$$\bar{n}_{min} \approx \frac{\gamma}{2\omega}. \tag{2.18}$$

In the case of the $^2S_{1/2} \rightarrow^2 P_{1/2}$ transition in ^{171}Yb^{+} and a trap frequency $\omega = 2\pi \times 1$ MHz, we find a Doppler cooling limit of .5 mK or $\bar{n} \approx 10$. Note that the above derivation is one-dimensional; Doppler cooling must be performed along all three trap axes, and the cooling rate may be different for each.

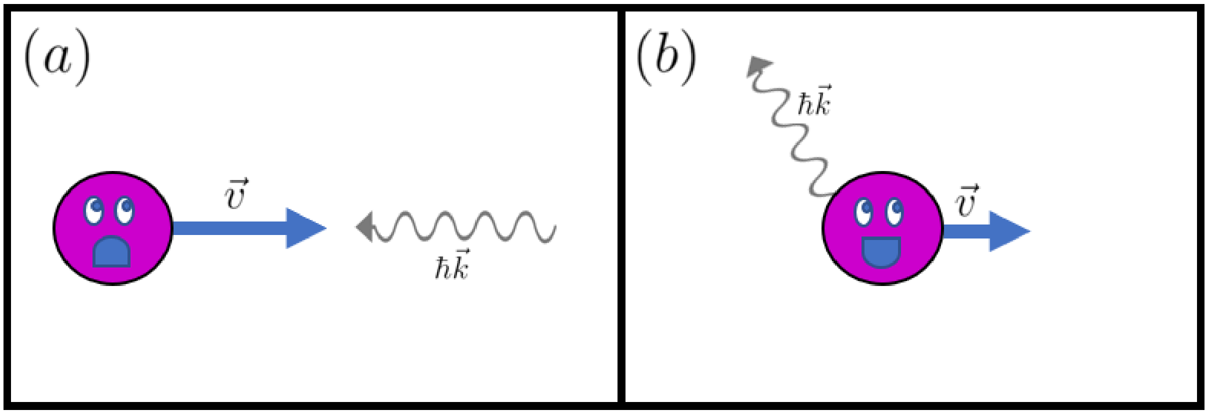

Figure 2.5: An illustration of the Doppler cooling mechanism. (a) A photon traveling left with momentum $\hbar\vec{k}$ is absorbed by an ion traveling to the right with velocity $\vec{v}$. (b) The ion's velocity slows due to momentum exchange, and the photon is re-emitted in a random direction. This mechanism is repeated many times such that the momentum exchange due to emission averages to zero and the net force on the ion is opposite its initial direction of motion. Cold ions are happy ions!

In a radial-2D configuration, the ion crystal experiences micromotion along the radial direction but not axial. The existence of micromotion in an ion array makes Doppler cooling qualitatively different (and more complex) in the radial directions than cooling a single ion or linear chain. As ions travel back and forth during a period of micromotion, they see a time-dependent Doppler shift of the cooling laser frequency. This leads to a single-ion cooling profile that is no longer Lorentzian, as well as an uneven fluorescence profile over the crystal. The cooling rate for an ion experiencing micromotion can be found using the optical Bloch equations, or approximated by including micromotion Doppler shifts in the laser damping term of pseudopotential theories [45].

Laser cooling rates under micromotion are sensitive to the frequency modulation index

$$\beta = \vec{k} \cdot q\vec{r_s}/2 \tag{2.19}$$

where $\vec{k}$ is the wavevector of the cooling laser, q is the Matheiu q parameter, and r_s is the ion displacement due to micromotion. Depending on array size and ion position in the array, this modulation can change the sign of the damping rate so that heating occurs where cooling is expected, or it may mean that the cooling laser is no longer near resonance. A partial solution to this is multi-tone laser cooling, which demonstrably allows the trapping and cooling of larger radial-2D crystals than with a single tone Doppler beam [46].

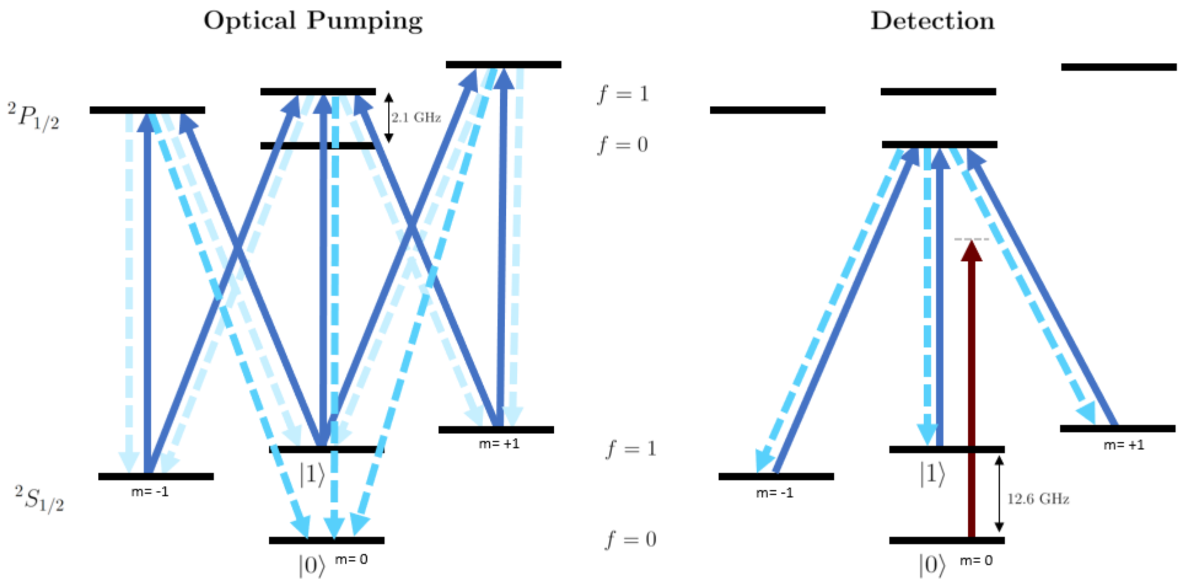

Figure 2.6: **Optical Pumping (left)**: Stimulated transitions (solid, purple) bridge the $^2S_{1/2}$ and $^2P_{1/2}$, $f = 1$ manifolds, and the ion decays with a $1/3$ probability of initializing to $|0\rangle$. All allowed decays from the $^2P_{1/2}$ manifold are depicted as dashed blue lines, with the applicable transitions to $|0\rangle$ highlighted. Repeating this cycle many times ensures state initialization with high fidelity. **Detection (right)**: Stimulated transitions (solid, purple) excite ions from $^2S_{1/2}$, $f = 1$ to $^2P_{1/2}$, $f = 0$, which then decay (dashed, blue) back to the $^2S_{1/2}$, $f = 1$ manifold, creating a closed cycle. By continuously stimulating this cycle, an ion in state $|1\rangle$ will result in the emission of many photons, whereas the the 12.6 GHz detuning between $|0\rangle$ and $|1\rangle$ prevents fluorescence from $|0\rangle$ (as indicated by the red arrow). This provides a detection method which discriminates between the two qubit states. [Not pictured: Decay from $^2P_{1/2}$ to $^2D_{3/2}$ and 935 nm repump]

2.3.1 State Initialization

Prior to performing a quantum simulation, we initialize all ions to the $|0\rangle$ state via optical pumping, as shown in Figure 2.6. Stimulated transitions bridge the $^2S_{1/2}$ and $^2P_{1/2}$, $f = 1$ manifolds, and the ion decays to $|0\rangle$ with $1/3$ probability. The $|0\rangle$ state is detuned by 12.6 GHz from the optical pumping beam, and so any population which decays to $|0\rangle$ becomes trapped. Repeating many optical pumping cycles ensures state initialization with high fidelity.

2.3.1 Detection

To detect the spin state of an ion, we create a closed cyclic transition between the $|1\rangle$ state and the first excited state using resonant 369 nm light. Stimulated transitions resonantly excite ions from ${}^2S_{1/2}$, $f = 1$ to ${}^2P_{1/2}$, $f = 0$, which then spontaneously decay back to the ${}^2S_{1/2}$, $f = 1$ manifold after about 8 ns. Since a decay from ${}^2P_{1/2}$, $f = 0$ to $|0\rangle$ is forbidden, continuous stimulation of this cycle will result in the emission of many photons from an ion beginning in state $|1\rangle$. The 12.6 GHz detuning between $|0\rangle$ and $|1\rangle$ ensures that very few photons are scattered from $|0\rangle$, providing a detection method which discriminates between the two qubit states as shown in Figure 2.6.

The ${}^2P_{1/2}$ state will decay to ${}^2D_{3/2} \sim .5\%$ of the time. The ${}^2D_{3/2}$ state has a lifetime of 52.7 ms and can trap the ion for the duration of the detection cycle, which is typically < 1 ms. In order to close the detection transition, we use a 935 nm repump beam, highlighted green in Figure 2.3, to excite the ion to the ${}^3[3/2]_{1/2}$ bracket state which decays back to the ${}^2S_{1/2}$ manifold in 37.7 ns. For a perfectly closed cyclic transition, the probability of detecting n photons during a detection cycle would be

$$P_{bright}(n) = \frac{e^{-\lambda_0}\lambda_0^n}{n!}, \tag{2.20}$$

with a mean number of detected photons λ_0 dependent on the scattering rate.

However, off-resonant coupling to the ${}^2P_{1/2}$, $f = 1$ manifold, which may decay to either spin state, can result in detection error. The 2.1 GHz separation between the ${}^2P_{1/2}$ hyperfine manifolds results in about a 10^{-5} probability of off-resonant coupling [47]. The presence of off-resonant coupling shifts the Poissonian bright distribution and adds an exponentially decaying probability of photon detection from a dark ion [48]. An example of the photon detection distribution curve for one ion is shown in Figure 2.7; the area where the dark and bright curves overlap represents detection infidelity. A balance between collecting more photons via longer detection times and

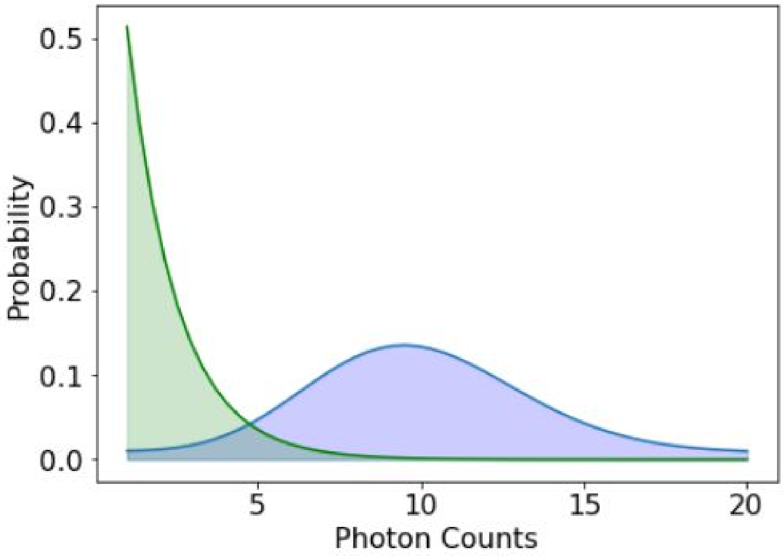

Figure 2.7: The photon count distribution curve for ion detection consists of a Poissonian bright distribution, as well as an exponentially decaying dark distribution which occurs due to off-resonant coupling. The overlap between the bright and dark distributions represents detection infidelity.

avoiding off-resonant coupling via shorter detection times is experimentally calibrated to maximize fidelity.

Finally, an ion will occasionally "go dark", meaning it won't respond to any 369 nm light. When this happens, the ion can often be brought back using 355 nm light. A plausible explanation for this, related to higher-level bracket states, is given in Section 2.2.2 of [49]. If 355 nm light does not work to bring back dark ions, they are most likely doubly ionized (if they go dark during an experiment) or a different isotope (if they load dark).

2.3.2 Coherent Operations

To visualize the state of an ion, we use the Bloch Sphere representation shown in Figure 2.8. The north and south poles of the sphere, along the $\pm z$ direction, correspond to states $|0\rangle$ and $|1\rangle$, and all points on the sphere can be represented by

$$|\Psi\rangle = \cos(\frac{\theta}{2})\,|0\rangle + e^{i\phi}\sin(\frac{\theta}{2})\,|1\rangle\,. \tag{2.21}$$

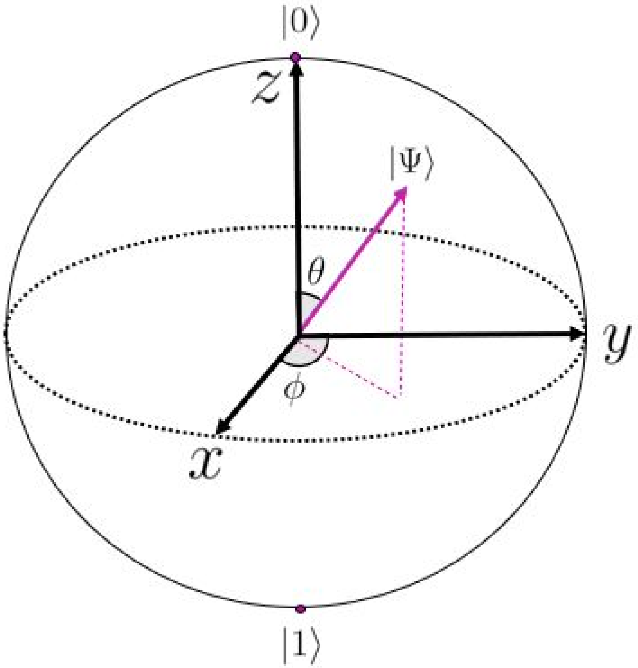

Figure 2.8: A qubit state $|\Psi\rangle$ can be represented as a vector on the Bloch sphere, where $|0\rangle$ is along the $+z$ direction and $|1\rangle$ is along the $-z$ direction. Two angles, θ and ϕ, completely specify the general state $|\Psi\rangle = \cos\frac{\theta}{2}|0\rangle + e^{i\phi}\sin\frac{\theta}{2}|1\rangle$.

The time evolution of the ionic state varies with spherical coordinates ϕ and θ, and a unitary operator $U(t)$ can be defined in terms of the rotation operator

$$R(\theta,\phi) = e^{i\frac{\theta}{2}\sigma_\phi} = \cos\frac{\theta}{2}I + i\sin\frac{\theta}{2}\sigma_\phi \tag{2.22}$$

where

$$\sigma_\phi = \cos\phi\sigma_x + \sin\phi\sigma_y \tag{2.23}$$

for Pauli operators σ_x and σ_y.

We have two ways of physically controlling an ion's state vector. The first is via microwave transitions resonant with the 12.6 GHz hyperfine splitting, which couple the magnetic dipole moments. The second is via two-photon stimulated Raman transitions induced by optical fields. Coupling to both internal and external degrees of freedom is required for communication between qubits, which makes optical radiation the preferred method. An ion's motional state changes with photon absorption or emission due to recoil energy $E_r = (\hbar k)^2/2m$, whereas microwave entangling operations require an external magnetic field gradient. Faster interactions are also achieved optically as $\lambda_{laser} \ll \lambda_{rf}$.

In our lab, microwave radiation is typically used for troubleshooting and beam alignment purposes, while most coherent operations stem from stimulated Raman transitions using high intensity 355 nm light. A three-level system undergoing stimulated Raman transitions is shown in Figure 2.9. A forbidden transition between states $|0\rangle$ and $|1\rangle$ is achieved by off-resonantly coupling both states to an excited state $|e\rangle$ via laser fields at frequencies ω_{L0} and ω_{L1}. A large detuning Δ from $|e\rangle$ allows for the adiabatic elimination of the excited state.

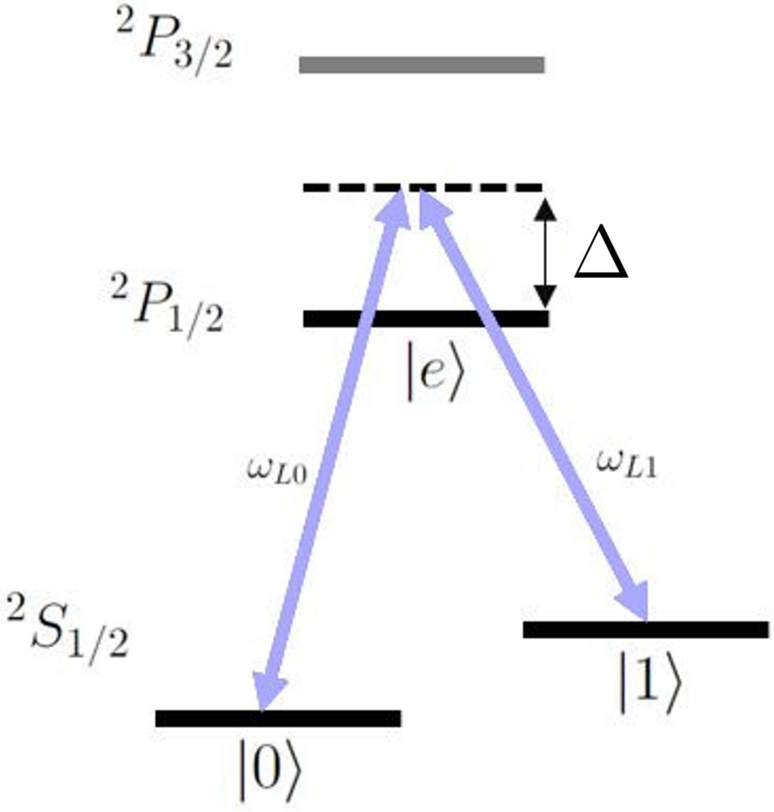

Figure 2.9: A stimulated Raman transition drives rotations between qubit states $|0\rangle$ and $|1\rangle$. The states are off-resonantly coupled (with detuning Δ) to the $^2P_{1/2}$ state ($|e\rangle$) by the 'beatnote' between two laser fields at frequencies ω_{L0} and ω_{L1}.

The next two sections present a theoretical overview of the coherent operations used experimentally on a day-to-day basis[1]. A mathematically rigorous treatment of the more cursory derivations can be found in [47], [50], and [49].

2.3.2 Qubit Rotations

In this section, we write down the Hamiltonian for rotations in a monochromatic microwave or laser field, as well as an analogous Hamiltonian for stimulated Raman transitions. Focusing on a few special laser frequencies and pulse durations, we see how these Hamiltonians allow us to control the qubit state and couple qubit states to motional states.

The relevant Hamiltonian consists of an interaction between a spin-1/2 system, a harmonic oscillator potential, and a radiation field:

$$\begin{aligned} H &= H_0 + H_I \\ &= (H_{spin} + H_{HO}) + H_{field} \\ &= \hbar\omega_{hf}\hat{\sigma_z} + \hbar\omega_{tr}(a^\dagger a + \frac{1}{2}) - \vec{\mu_E} \cdot \vec{E}. \end{aligned}$$

Here, ω_{hf} is the hyperfine splitting, $\hat{\sigma}_z$ is the Pauli-Z operator, ω_{tr} is the trap secular frequency, a and $a^\dagger$ are the harmonic oscillator raising and lower operators, and $\vec{\mu_E}$ is the electric dipole operator. We can assume a laser field $\vec{E} = E_0\hat{x}\cos(kz - \omega_L t + \phi)$ that is $\hat{x}$-polarized and propagating in $\hat{z}$. This field has amplitude E_0, wavevector $k = 2\pi/\lambda$, frequency ω_L, and phase ϕ. From now on, we set $\hbar = 1$.

For a microwave field, we can write an analogous interaction term $H_I = -\mu_x B_0 \cos(kz - w_{rf}t + \phi)$, where μ_x is the x-component of the magnetic moment, ω_{rf} is the radiation frequency, B_0 is the amplitude of radiation, and ϕ is a phase. Following [50], the time evolution of a resonant

---

[1] If anything in this section reads too similarly to the Mølmer-Sørensen Wikipedia page, it's because I'm using this document to write that page.

microwave field (i.e., any microwave operation described in this text) is given by

$$\Psi(t) = \begin{bmatrix} \cos\frac{\Omega_R}{2}t & -ie^{i\phi}\sin\frac{\Omega_R}{2}t \\ -ie^{-i\phi}\sin\frac{\Omega_R}{2}t & \cos\frac{\Omega_R}{2}t \end{bmatrix} \Psi(0) \tag{2.24}$$

with Rabi frequency $\Omega_R \equiv -\mu_B B/4$.

Rotations about the Bloch sphere are denoted by $R(\theta, \phi)$ where $\theta = \Omega_R t$ is the rotation angle and rotation axis is determined by ϕ. For the first rotation, this axis can be chosen arbitrarily so long as it is kept track of, and we can assume $\phi = 0$ which happens to correspond to the $R_{-x}(t)$ rotation operator. Notable times in the evolution are the π-time, which completes a full population transfer between $|0\rangle$ and $|1\rangle$, and the $\pi/2$-time, which creates an equal superposition between $|0\rangle$ and $|1\rangle$. For example, an ion initialized to $|0\rangle$ rotating about the y-axis will evolve as

$$R_y(\pi)\,|0\rangle = |1\rangle \;\; ; \;\; R_y(\pi/2)\,|0\rangle = \frac{1}{\sqrt{2}}(|0\rangle + |1\rangle). \tag{2.25}$$

For two-photon stimulated Raman transitions as in Figure 2.9, the interaction term of the Hamiltonian becomes $-\sum_i \vec{\mu}_{E,i} \cdot \vec{E_i}$, for $i = \{1,2\}$ and $\vec{E_i} = E_i \hat{\epsilon_i} \cos(\vec{k_i} \cdot \vec{r} - \omega_{L_i} t + \phi_i)$. Following [47] and [50], the excited state $|e\rangle$ can be adiabatically eliminated and a rotating wave approximation performed to obtain an interaction Hamiltonian analogous to a two-level system

$$H_I = -\frac{|g|^2}{2\Delta} I - \frac{\Omega_{eff}}{2}(\sigma_- + \sigma_+)(e^{i(\Delta k \cdot \vec{r} - (\omega_{L0} - \omega_{L1})t + \Delta\phi)} + h.c.). \tag{2.26}$$

Here, we have defined the Raman beam wavevector difference $\Delta k = \vec{k_{L0}} - \vec{k_{L1}}$, frequency difference $\omega_{L0} - \omega_{L1}$, phase difference $\Delta\phi = \phi_{L0} - \phi_{L1}$, and we have introduced Pauli operators $\sigma_\pm = \sigma_x \pm i\sigma_y$. The $-\frac{|g|^2}{2\Delta}$ term is the two-photon A.C. Stark shift, which is eliminated experimentally by tuning the Raman beatnote to compensate for the shift. The single photon Rabi frequencies for each beam ($g_0 = g_1 \equiv g$) are proportional to beam intensity and define the effective two photon Rabi frequency $\Omega \equiv \Omega_{eff} e^{i\Delta\phi} = |g|^2/2\Delta$.

Now we detune the the frequency difference $\omega_{L0} - \omega_{L1}$ between lasers by δ from the qubit frequency ω_{hf}, and absorb $\Delta\phi$ into the effective Rabi frequency $\Omega_{eff} \equiv \Omega_{eff}e^{i\Delta\phi}$. In our experiments, Δk is aligned along the z axis of the trap, so as to only couple to the axial modes of motion, and Raman beam polarizations are aligned parallel to a quantization axis defined by a vertical magnetic field. Finally, it is useful to transform to the interaction picture, where $H \rightarrow U^{\dagger}H_I U$ for $U = e^{-iH_0 t/\hbar}$. Then

$$H_I = \frac{\Omega_{eff}}{2}e^{-i[\eta(ae^{-iw_{tr}t}+a^{\dagger}e^{iw_{tr}t})-\delta t+\Delta\phi]}\sigma_- - \frac{\Omega_{eff}}{2}e^{i[\eta(ae^{-iw_{tr}t}+a^{\dagger}e^{iw_{tr}t})-\delta t+\Delta\phi]}\sigma_+, \tag{2.27}$$

where we have used $\Delta k z = \eta(ae^{-i\omega_{tr}t} + a^{\dagger}e^{i\omega_{tr}t})$ at trap frequency ω_{tr}. The spread of the wavefunction in the $\hat{z}$-direction is $z = z_0(ae^{-i\omega_{tr}t} + a^{\dagger}e^{i\omega_{tr}t})$, and the Lamb-Dicke parameter $\eta = \Delta k z_0$ parameterizes the size of the motional ground state wavepacket of the ion $z_0 = (\hbar/2M\omega_{tr})^{1/2}$ compared to radiation wavelength λ. We will often mention being in the 'Lamb-Dicke regime', for which $\eta(2n+1) \ll 1$ and z_0 is confined to a region much smaller than the laser wavelength.

Within the Lamb-Dicke regime, we can make the approximation $e^{-i\eta(e^{i\omega_{tr}t}a^{\dagger}+e^{-i\omega_{tr}t}a)} \approx 1 - i\eta(e^{i\omega_{tr}t}a^{\dagger} + e^{-i\omega_{tr}t}a)$. Doing so splits our Hamiltonian into three parts which correspond to the carrier, red sideband (RSB), and blue sideband (BSB) transitions:

$$H_{eff} = \frac{\Omega}{2}\sigma_-(e^{i\delta t} - i\eta e^{i(\delta+\omega_{tr})t}a^{\dagger} - i\eta e^{i(\delta-\omega_{tr})t}a) + h.c. \tag{2.28}$$

Now we examine each piece, relying again on the rotating wave approximation to neglect fast-oscillating terms. Illustrations of the carrier, RSB, and BSB transitions are shown in Figure 2.10.

- **Carrier Transition**: $\delta = 0$

  Here, $|\omega_{tr}| \gg \delta$, so we keep only the first term of Equation 2.28. Then

  $$H_{carrier} = \frac{\Omega}{2}(\sigma_- + \sigma_+). \tag{2.29}$$

  The carrier transition alters the spin state of the ion without affecting the motional state, and

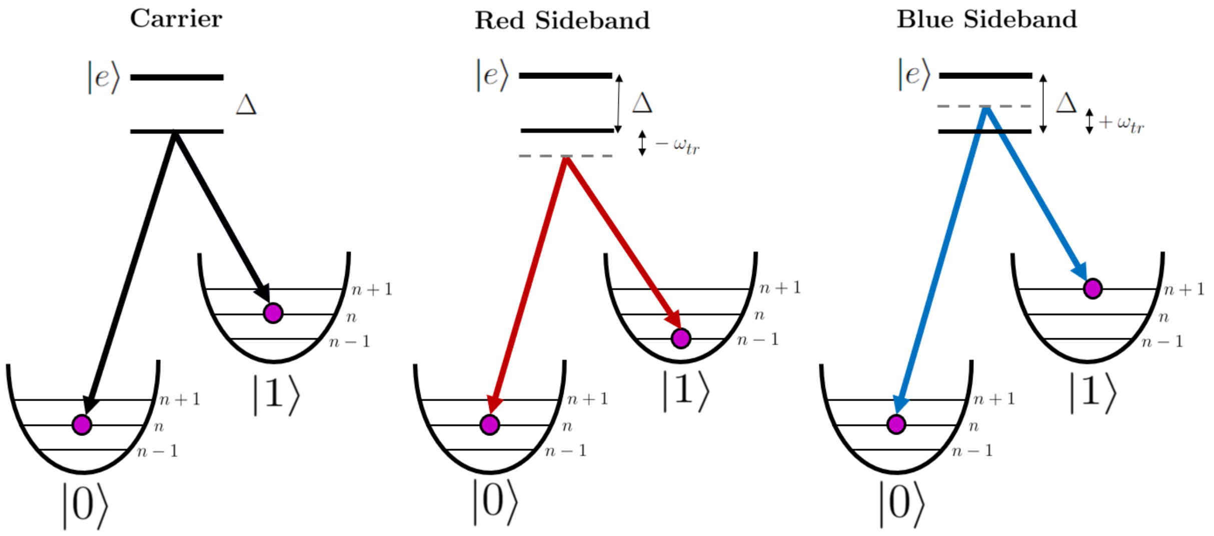

Figure 2.10: Stimulated Raman transitions at three critical laser detunings are shown, with spin states $|0\rangle$ and $|1\rangle$ depicted as harmonic oscillators with levels $n-1$, n, and $n+1$. **Left:** The resonant carrier transition ($\delta = 0$) facilitates $|0,n\rangle \rightarrow |1,n\rangle$. **Center:** The red-detuned ‘red sideband‘ transition ($\delta = -\omega_{tr}$) facilitates $|0,n\rangle \rightarrow |1,n-1\rangle$. **Right:** The blue-detuned ‘blue sideband’ transition ($\delta = +\omega_{tr}$) facilitates $|0,n\rangle \rightarrow |1,n+1\rangle$

.

can be written

$$H_{carrier} = \frac{\Omega}{2}\sigma_{\phi}, \tag{2.30}$$

where $\sigma_{\phi} = \cos{(\Delta\phi)}\sigma_x + \sin{(\Delta\phi)}\sigma_y$. Then the time evolution operator is given by

$$U(t) = e^{-iHt} = e^{-i\theta\sigma_{\phi}}, \tag{2.31}$$

which is a Bloch sphere rotation for $\theta = \Omega t/2$ and rotation axis set by ϕ. During a carrier transition, an ion initialized in $|0\rangle$ evolves as

$$U(t)\,|0\rangle = \cos\theta\,|0\rangle + ie^{i(\Delta\phi)}\sin\theta\,|1\rangle\,. \tag{2.32}$$

- **Red Sideband Transition**: $\delta = -\omega_{tr}$

  For Rabi oscillations near the red sideband, $|\delta + \omega_{tr}| \ll |\delta|, |\delta - \omega_{tr}|$ so we keep only the second term of Equation 2.28.

$$H_{RSB} = -i\eta\frac{\Omega}{2}(a^\dagger\sigma_-)e^{i(\delta+\omega_{tr})t} + h.c. \tag{2.33}$$

  The RSB transition can be thought of as an 'exchange' of motion for spin. For an ion with phonon occupation number n, an RSB π-pulse will take $|0, n\rangle \to |1, n-1\rangle$ with oscillation frequency $\Omega_{RSB} = \eta\Omega\sqrt{n}$. The red sideband transition is used in conjunction with optical pumping to cool the ion to near the ground state, by performing a red sideband π-pulse $|0, n\rangle \to |1, n-1\rangle$, optically pumping back to $|0\rangle$, and repeating for many iterations. An in-depth description of the sideband cooling (SBC) process is given in Chapter 5; we generally cool using the 'fixed pulsed' SBC method with both 1^{st} and 2^{nd} order cooling sequences.

- **Blue Sideband Transition**: $\delta = +\omega_{tr}$

  For Rabi oscillations near the blue sideband, $|\delta - \omega_{tr}| \ll |\delta|, |\delta + \omega_{tr}|$ so we keep only the third term of Equation 2.28.

$$H_{BSB} = -i\eta\frac{\Omega}{2}(a\sigma_-)e^{i(\delta-\omega_{tr})t} + h.c. \tag{2.34}$$

  The BSB transition is also a spin-motion exchange. For an ion with phonon occupation number n, a BSB π-pulse will take $|0, n\rangle \to |1, n+1\rangle$ with oscillation frequency $\Omega_{BSB} = \eta\Omega\sqrt{n+1}$.

2.3.2 Entanglement Creation

When Cirac and Zoller identified trapped ions as a quantum computing platform, they proposed a procedure for implementing a CNOT gate by coupling ions through their collective motion [13]. However, this scheme requires the trapped ion system to be restricted to its joint motional ground state, which is difficult to achieve experimentally. Today, a more widely used entanglement gate in ion traps is the Mølmer-Sørensen (MS) gate [51, 52, 53] which produces an Ising-like interaction Hamiltonian using a bichromatic laser field. Mølmer and Sørensen identified two regimes in which this is possible:

1. The weak-field (slow gate) regime, in which single-photon absorption is suppressed and two-photon processes destructively interfere in a way that makes internal state dynamics insensitive to phonon number
2. The strong-field (fast gate) regime, in which individual ions are coherently excited such that motion and spin are highly entangled during the gate and deterministically removed toward the end of the interaction

In both regimes, a red sideband and blue sideband interaction are applied simultaneously to each ion, with the red and blue tones symmetrically detuned by δ' from the relevant motional mode. Then the laser detunings are then $\delta_{r,b} = \pm(\omega_{tr} + \delta')$, resulting in Raman beatnote frequencies

$$\omega_R = \omega_{hf} - \omega_{tr} - \delta' \tag{2.35}$$

$$\omega_B = \omega_{hf} + \omega_{tr} + \delta'. \tag{2.36}$$

In this thesis, only slow gates were attempted experimentally, and so we focus on the weak-field regime, for which $\eta\Omega \ll |\omega_{tr} - \delta'|$.

If we consider two ions, each illuminated by lasers with the above detunings, the only energy conserving transitions are between $|00\rangle \leftrightarrow |11\rangle$ and $|01\rangle \leftrightarrow |10\rangle$. An intuitive way to think about the Mølmer-Sørensen gate in the weak-field regime is to consider the allowed transition pathways between $|00\rangle$ and $|11\rangle$, as shown in Figure 2.11 for two ions. In this regime, we set δ' large enough that intermediate states with phonon number $n \pm 1$ are negligibly populated and enter the scheme only virtually. Here we also assume that the laser detuning is near center-of-mass (COM) mode (ω_{tr}), thus excluding other modes from the analysis. A different mode may be used so long as each ion participates in the mode with equal amplitude.

Then there are four possible transition pathways to consider:

$$|00,n\rangle \leftrightarrow |01,n+1\rangle\,, |01,n+1\rangle \leftrightarrow |11,n\rangle$$

$$|00,n\rangle \leftrightarrow |10,n+1\rangle\,, |10,n+1\rangle \leftrightarrow |11,n\rangle$$

$$|00,n\rangle \leftrightarrow |01,n-1\rangle\,, |01,n-1\rangle \leftrightarrow |11,n\rangle$$

$$|00,n\rangle \leftrightarrow |10,n-1\rangle\,, |10,n-1\rangle \leftrightarrow |11,n\rangle$$

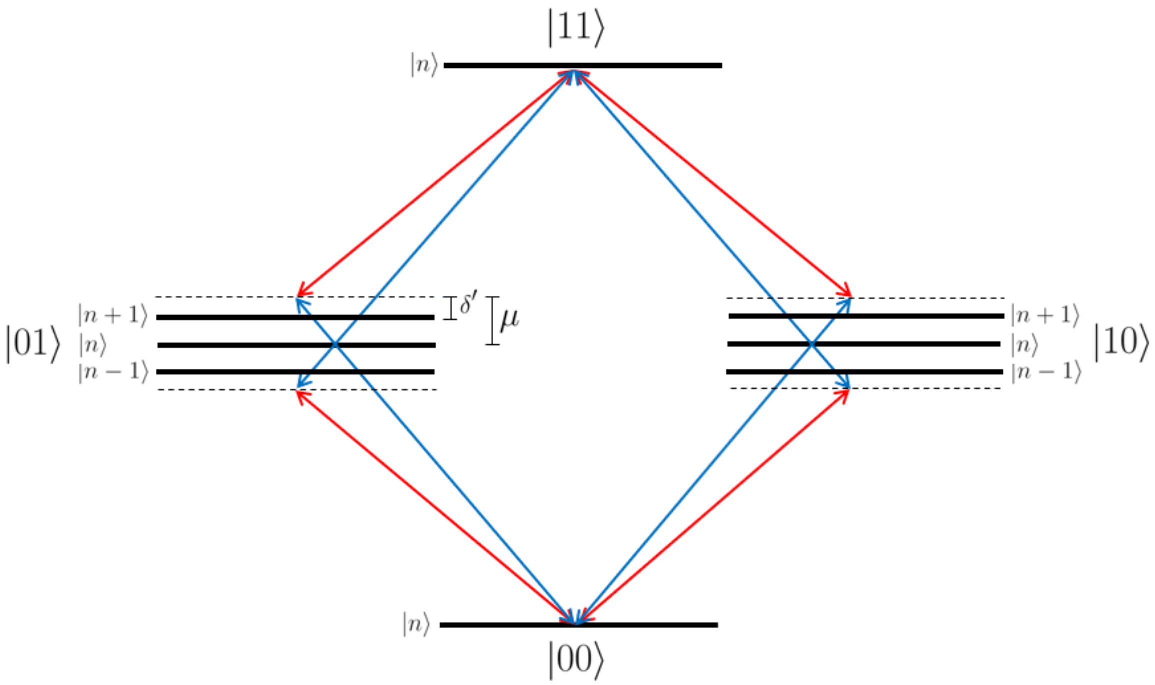

Figure 2.11: The level diagram for a 2-ion MS interaction is shown. Red and blue sidebands detuned from the COM motional mode create four possible pathways that couple $|00,n\rangle$ and $|11,n\rangle$. The four pathways experience partial destructive interference such that any n-dependence cancels.

Following [51], second order perturbation theory can be used to determine the effective Rabi frequency $\tilde{\Omega}$ for the $|00, n\rangle \leftrightarrow |11, n\rangle$ transition via intermediate states m:

$$\tilde{\Omega} = 2\sum_{m} \frac{\langle 11, n| H_{int} |m\rangle \langle m| H_{int} |00, n\rangle}{E_{00,n} + \hbar\omega_{R,B} - E_m}. \tag{2.37}$$

The pathways involving intermediate states with $n+1$ quanta yield $(n+1)\Omega^2\eta^2/4(\delta - \omega_{tr})$, while the pathways involving intermediate states with $n-1$ quanta yield $-n\Omega^2\eta^2/4(\delta - \omega_{tr})$. Summing terms, the effective Rabi frequency

$$\tilde{\Omega} = \frac{(\Omega\eta)^2}{\delta'}, \tag{2.38}$$

is found to be independent of phonon number, due to destructive interference between pathways. Four similar pathways can be identified between $|01, n\rangle$ and $|10, n\rangle$, resulting in the overall state evolution

$$\begin{aligned}
|00\rangle &\rightarrow \cos(\frac{\tilde{\Omega}t}{2}) |00\rangle + i\sin(\frac{\tilde{\Omega}t}{2}) |11\rangle \\
|11\rangle &\rightarrow \cos(\frac{\tilde{\Omega}t}{2}) |11\rangle + i\sin(\frac{\tilde{\Omega}t}{2}) |00\rangle \\
|01\rangle &\rightarrow \cos(\frac{\tilde{\Omega}t}{2}) |01\rangle - i\sin(\frac{\tilde{\Omega}t}{2}) |10\rangle \\
|10\rangle &\rightarrow \cos(\frac{\tilde{\Omega}t}{2}) |10\rangle - i\sin(\frac{\tilde{\Omega}t}{2}) |01\rangle
\end{aligned}$$

Thus, the MS interaction creates a sinusoidal oscillation between $|00\rangle \leftrightarrow |11\rangle$ or $|01\rangle \leftrightarrow |10\rangle$, with maximally entangled states created at time $t = \pi/(2|\tilde{\Omega}|)$. This is the same evolution as the Ising Hamiltonian

$$H_{Ising} = J_{1,2}\sigma_x^1\sigma_x^2 \tag{2.39}$$

with effective Ising coupling $J_{1,2} = (\eta\Omega)^2/\delta'$ between ions 1 and 2. To reconcile this section with the following section, it is good to note that inclusion of off-resonant coupling between the two sidebands modifies the Ising coupling

$$J_{1,2} \rightarrow \frac{(\eta\Omega)^2\omega}{\mu^2 - \omega^2} \tag{2.40}$$

for $\mu \equiv \delta_B = -\delta_R$.

Another way of thinking about the MS gate is by writing down a general Hamiltonian and evolution operator using Equation 2.33 and Equation 2.34. The red and blue tones will have the effective Rabi frequencies $\Omega_R = \Omega e^{i\phi_R}$ and $\Omega_B = \Omega e^{i\phi_B}$, respectively, and so we can write the applied red and blue sideband Hamiltonians as

$$H_R = i\eta\frac{\Omega_R}{2}\sigma_- a^\dagger e^{i\delta_R t} + h.c. \tag{2.41}$$

$$H_B = i\eta\frac{\Omega_B}{2}\sigma_- a e^{i\delta_B t} + h.c. \tag{2.42}$$

Now we will sum over j ions, and also consider all k motional modes with eigenvectors b^k and eigenfrequencies ω_k as described in Section 2.2.3. Writing the detuning from each motional mode as $\mu_k \equiv \mu - \omega_k$, we arrive at the MS interaction Hamiltonian

$$H_{int} = i\sum_{j,k}\eta_{j,k}\frac{\Omega_j}{2}\sigma_{-,j}[a_k e^{-i(\mu_k t - \phi_R)} + a_k^\dagger e^{i(\mu_k t + \phi_B)}] + h.c. \tag{2.43}$$

where $\eta_{j,k} = \Delta k\sqrt{\hbar/(2M\omega_k)}b_j^k$.

Now we define spin and motional phases

$$\phi_s \equiv \frac{\phi_B + \phi_R}{2} \ , \ \phi_m \equiv \frac{\phi_B - \phi_R}{2}. \tag{2.44}$$

such that the Hamiltonian can be separated into its spin and motion components:

$$\begin{aligned}
H_{int} &= i\sum_{j,k}\eta_{j,k}\frac{\Omega_j}{2}[e^{i(\mu_k t+\phi_B)}\sigma_{-,j}a_k - e^{-(\mu_k t+\phi_B)}\sigma_{+,j}a_k^\dagger + e^{-i(\mu_k t+\phi_R)}\sigma_{-,j}a_k^\dagger - e^{i(\mu_k t-\phi_R)}\sigma_{+,j}a_k] \\
&= i\sum_{j,k}\eta_{j,k}\frac{\Omega_j}{2}[(\sigma_{-,j}e^{i\phi_s} - \sigma_{+,j}e^{-i\phi_s})(a_k e^{i\mu_k t}e^{i\phi_m} + a_k^\dagger e^{-i\mu_k t}e^{-i\phi_m})] \\
&\equiv i\sum_{j,k}\eta_{j,k}\frac{\Omega_j}{2}[\hat{\sigma}_j \otimes \hat{A}_k(t)]
\end{aligned}$$

where we have now defined the spin operator $\hat{\sigma}$ and displacement operator $\hat{A}(t)$.

The time evolution operator $U(t)$ is then obtained through the Magnus expansion

$$U(t) = e^{\sum_{l=1}^{\infty} M_l(t)} \tag{2.45}$$

where the first two $M_l(t)$ are

$$\begin{aligned}
M_1(t) &= -\frac{i}{\hbar}\int_0^t H_{int}(t_1)dt_1 \\
M_2(t) &= \frac{1}{2}(-\frac{i}{\hbar})^2\int_0^t\int_0^{t_1}[H_{int}(t_1), H_{int}(t_2)]dt_2 dt_1
\end{aligned}$$

and higher order terms vanish for the MS Hamiltonian since $[M_2(t_1), H_{int}(t_2)] = 0$.

The first order term is

$$M_1(t) = \sum_{j,k}\hat{\sigma}_j[\alpha_{j,k}(t)a_k + \alpha^*_{j,k}(t)a_k^\dagger], \tag{2.46}$$

where

$$\alpha_{j,k}(t) = \eta_{j,k}(\Omega_j/2\mu_k)e^{i\mu_k t/2}\sin(\mu_k t/2)e^{i\phi_m} \tag{2.47}$$

describes the displacement of the k^{th} motional mode through phase space. In the weak field regime, where $\eta\Omega \ll \mu$, this term can be neglected, as the phase space trajectory consists of very small, fast loops about the origin. In the strong-field regime, care must be taken to end the gate at a time when all motional modes have returned to the origin in phase space ($\alpha = 0 \longrightarrow \mu_k t_{gate} = 2\pi$, for each mode k).

The second order term is

$$M_2(t) = i \sum_{\substack{i,j,k \\ i<j}} \hat{\sigma}_i \hat{\sigma}_j \frac{\eta_{i,k}\eta_{j,k}\Omega_i\Omega_j}{2\mu_k}(\mu_k t - \sin(\mu_k t)) \tag{2.48}$$

over ion pairs $\{i, j\}$. In the strong-field regime, where $\mu_k t_{gate} = 2\pi$, this yields the time evolution operator

$$U_{fast}(t_{gate}) = \exp[i\frac{\pi}{2} \sum_{\substack{i,j,k \\ i<j}} \frac{\eta_{i,k}\eta_{j,k}\Omega_i\Omega_j}{\mu_k^2} \hat{\sigma}_i \hat{\sigma}_j], \tag{2.49}$$

and if we set the phases of the lasers such that $\phi_R = 0$ and $\phi_B = \pi$, then $\hat{\sigma} \to -\sigma_x$.

In the weak-field regime, this is not quite the end of the story. We relied on the rotating wave approximation to get the intial red and blue sideband Hamiltonians, which is only a good approximation if the Raman beatnote predominately excites high-frequency modes. When counter-rotating terms are re-introduced, a linear term appears that dominates at long times, and the effective time evolution operator becomes

$$U_{slow}(t) \approx \exp[i \sum_{\substack{i,j,k \\ i<j}} (\hat{\sigma}_i \hat{\sigma}_j) \frac{\eta_{i,k}\eta_{j,k}\Omega_i\Omega_j}{\mu^2 - \omega_k^2} \omega_k t], \tag{2.50}$$

which is equivalent to that of an Ising Hamiltonian

$$H_{eff} \approx \sum_{i<j} J_{ij} \hat{\sigma}_i \hat{\sigma}_j, \tag{2.51}$$

with couplings between spins i and j given by

$$J_{ij} \approx \Omega_i \Omega_j \sum_k \frac{\eta_{i,k}\eta_{j,k}}{\mu^2 - \omega_k^2} \omega_k. \tag{2.52}$$

The J_{ij} coupling follows a power law $J_{ij} \approx \frac{J_0}{|i-j|^\alpha}$, where J_0 is the nearest-neighbor coupling and

$0 < \alpha < 3$. We tune α experimentally by adjusting μ.

CHAPTER 3

EXPERIMENTAL IMPLEMENTATION

3.1 Section Overview

This section will discuss our lab's experimental implementation of the atomic physics techniques detailed in Chapter 2. In Section 3.2, I will discuss the Paul trap itself. This section will give a brief overview of each of the two home-built Paul traps relevant for the experiments detailed in this thesis, as well a description of the vacuum chamber and voltage control systems they share.

In Section 3.3, I will describe the laser systems required to produce the optical frequencies mentioned in Chapter 2. This includes two continuous-wave Moglabs diode lasers at 399 nm (photionization) and 935 nm (repump from $^2D_{3/2}$ state), a frequency-doubled Titanium Sapphire (Ti:Saph) laser at 369 nm ($^2S_{1/2} \rightarrow ^2 P_{1/2}$ cooling, detection, and state initialization), and a 355 nm COHERENT pulsed laser (stimulated Raman transitions), as well as a Helium Neon (HeNe) laser used for frequency calibration of the other lasers.

Section 3.4 describes the experimental realization of the $^{171}\text{Yb}^+$ qubit as described as Chapter 2, giving a discussion of beam pathways, polarization, geometries, power, etc for Doppler cooling, optical pumping, detection, and coherent operations. I will also discuss the creation of the imaging system used for state readout. The experimental setup and calibrations that must be performed before an ion can be trapped and manipulated are described in this section.

3.2 The Paul Trap

An ion trap's "house" is an ultra-high vacuum (UHV) chamber, built with standard ConFlat components. A UHV environment is essential, as collisions with background will heat ions and/or destroy spin states. By baking the chamber and using a scroll pump, turbo pump, and ion pump we can reach pressures below 10^{-11} Torr, where the room temperature Langevin collision rate is approximately 1 collision per ion per 30 minutes. Cleaning, assembling, baking, and pumping down the vacuum chamber is a crucial process, a full description of which can be found in Yuanheng Xie's thesis. We currently have two vacuum chambers available for the main experiment- one in use, and one as backup. In a pinch, we can do the majority of the pump down and baking process for a trap in a separate location, and then move it to the laser apparatus.

A front and back view of the vacuum chamber is shown in Figure 3.1, where feedthroughs for the RF voltage, DC voltage, and oven current are labeled. Also depicted are three magnetic field coils. The top coil, centered directly over the trap to create a field along $\hat{z}$, is the only coil used during quantum simulation experiments. A 5 G field is created by running a 1.1A through the coil, shifting our Zeeman levels by 6 MHz. The front and side coils allow control of the magnetic field along all three axes, which is required for the Ramsey experiments described in Section 3.4.4. There are three viewports for optical access. The front viewport, which aligns with the imaging system, is anti-reflection coated for UV light.

Two home-built Paul traps were used during my time in the Richerme lab: the "rod trap" and the "blade trap". The rod trap was designed as a simple 'test' trap to verify that we could trap ions before implementing the more complex blade-style trap with an optimized design for 2D lattices. However, before it retired, the rod trap was used for a sideband cooling study (Chapter 5), a radiation susceptibility study (Chapter 6), and a characterization of radial-2D crystals (Chapter 7). At the time of writing, the main experiment uses the blade trap, while the rod trap resides in the backup vacuum chamber on a different optics table.

3.2.1 The Rod Trap

The rod trap is pictured in Figure 3.2. It consists of four stainless steel rods with two "needle" endcaps along the $\hat{z}$ (axial) direction. An oscillating RF voltage V_0 is applied to two opposing rods (the other two are grounded), creating a quadrapole potential in the xy (radial) plane, while a static DC voltage U_0 is applied to the two endcaps. Radial and axial trap dimensions are $r_0 = 460\ \mu$m and $z_0 = 335\ \mu$m, respectively, and we drive the RF rods with $\Omega_t = 2\pi \times 21$ MHz. The trap

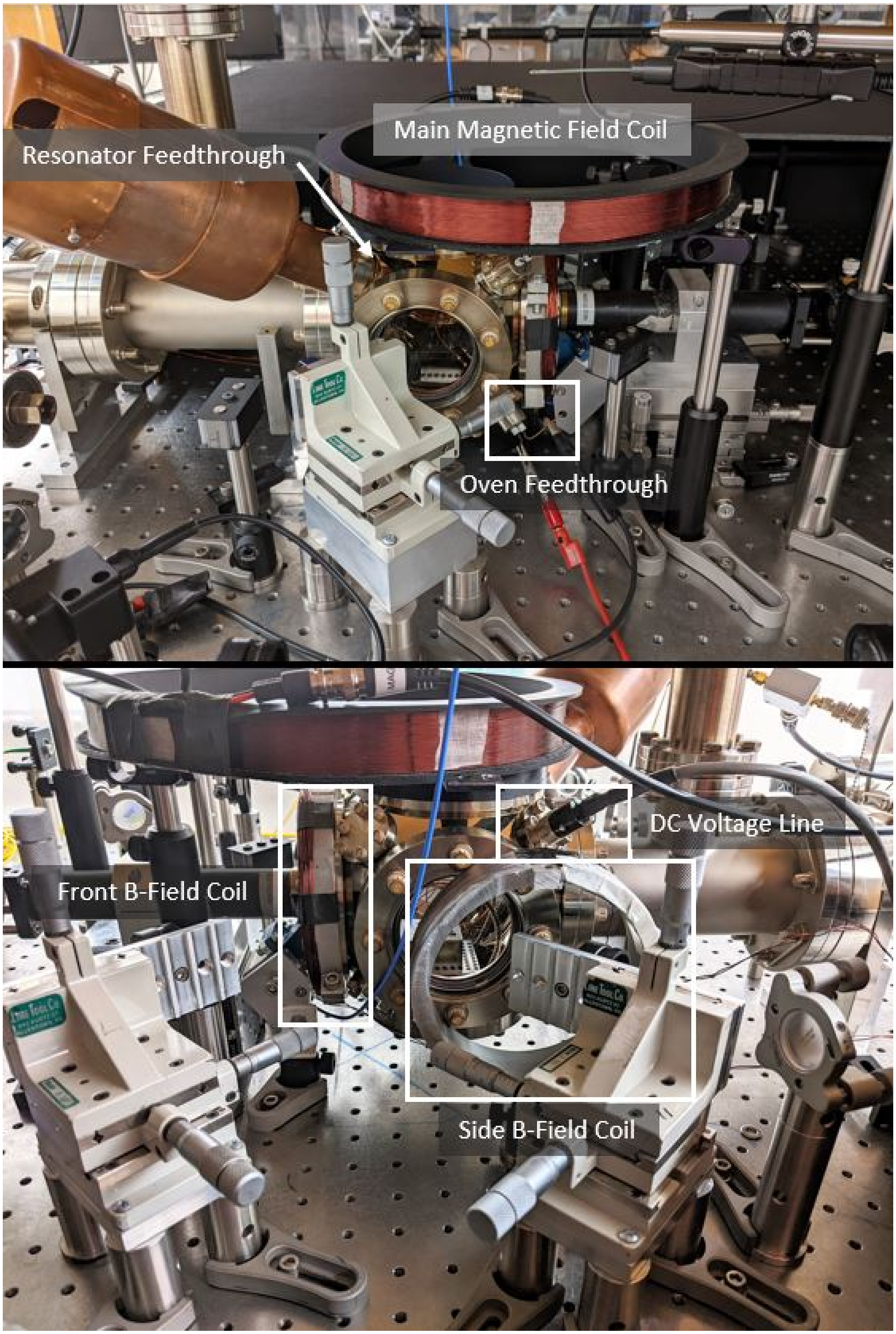

Figure 3.1: Front (top) and back (bottom) view of the trap chamber.

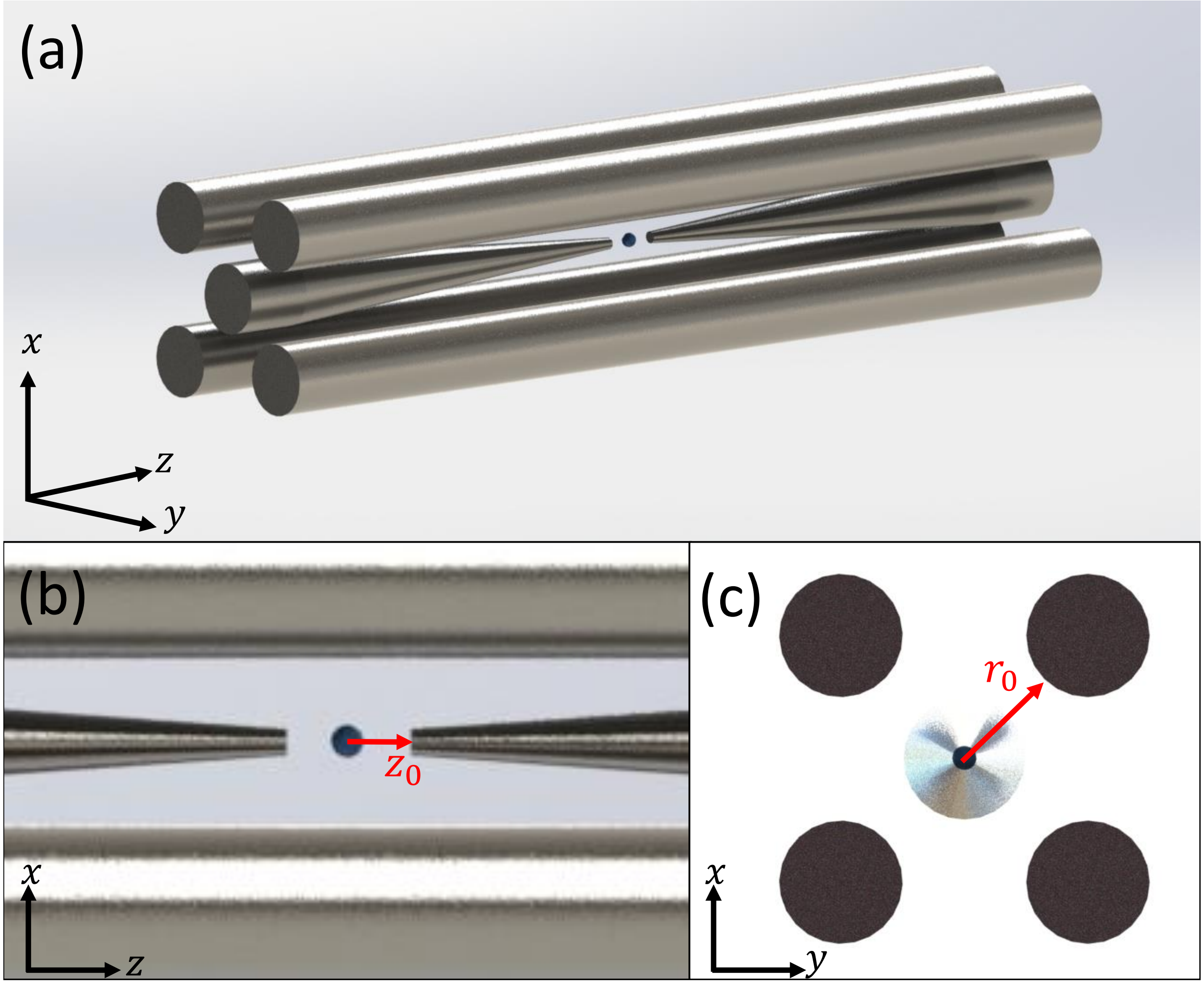

Figure 3.2: Solidworks model of the (a) full view, (b) front view, and (c) side view of the four-rod linear Paul trap, with designated trap coordinate axes (lower left) and dimensional parameters (red).

geometric factor is determined through frequency measurements to be $\kappa \simeq 0.12$. In this trap, the radial plane is perpendicular to the imaging plane, which does not allow for site-resolved imaging of ion lattices. This is the main reason we switched to a blade-style trap.

3.2.2 The Blade Trap

The blade trap was specifically designed to allow appropriate (and experimentally reasonable) trap dimensions, voltages, and frequencies that ensure we can reach the radial-2D regime $\omega_z/\omega_r > (2.264N)^{1/4}$ for large numbers of ions. This is most easily accomplished when ω_z is large, which requires large U_0 and/or small z_0. Both of these conditions have a deconfining effect in the radial direction, and so to counter this effect, V_0 must also be moderately large while keeping r_0 small. A large trap drive frequency Ω_t is desirable to keep the Matheiu q parameter (and thus micromotion amplitude) small as well. A segmented-blade design was chosen for this trap due to three advantageous properties:

1. Open endcaps allow imaging perpendicular to the 2D ion plane.
2. Trap dimensions r_0 and z_0 can be made small to avoid unreasonably high V_0 and U_0.
3. Blades can be designed to avoid compromising the numerical aperture (NA) of the imaging optics.

An image of the blade trap is shown in Figure 3.3. Four tungsten blades are mounted on insulating Macor pieces within a stainless steel frame. Tungsten was chosen for its strength and low resistivity, which limits blade heating and any associated vacuum pressure increases when large RF voltage is applied. Two opposing blades are driven with RF, and the other set of opposing blades are the DC blades, which have three segments: two endcaps and one central electrode. Each DC segment is 300 μm long and separated by a 50 μm gap. The RF blades are continuous and are the same total length as the DC blades (1 mm). All blades (including RF blades) can be biased to allow to translation along all three principle axes. Radial and axial trap dimensions are given by $r_0 = 230\ \mu$m and $z_0 = 100\ \mu$m respectively, and RF blades are driven with $\Omega_t = 2\pi \times 27.51$ MHz. Compensation electrodes are mounted above and below the trap to provide additional voltage adjustment. On-chip capacitors (800 pF) on each DC segment provide filtering of RF pickup. Further description and characterization of the blade trap system is provided in Chapter 8. For the remainder of Chapter 3 and Chapter 4, I will assume the blade trap is in place.

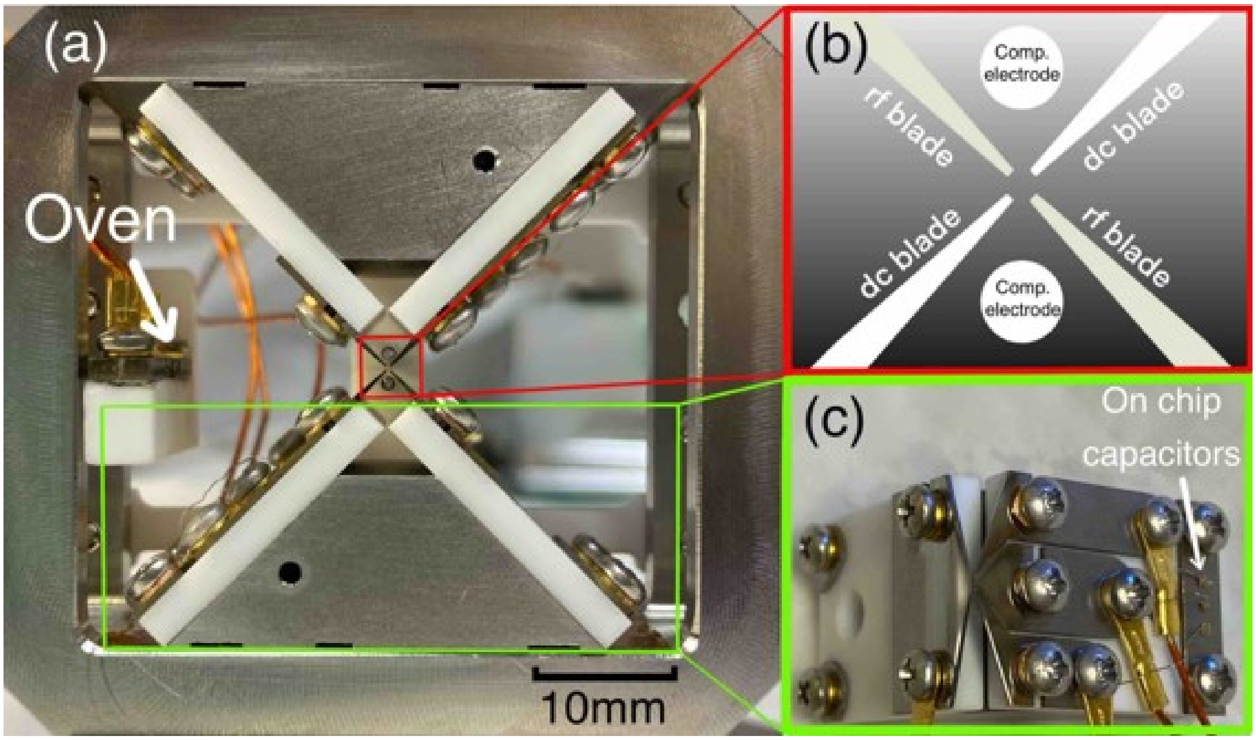

Figure 3.3: (a) A photograph of the blade trap. Four tungsten blades are mounted on insulating Macor pieces within a stainless steel frame. (b) Opposing blades are driven with RF (set 1) and DC (set 2). Compensation electrodes placed above and below the trap offer additional voltage flexibility. (c) DC blades are segmented, each segment being 300 μm long and separated by a 50 μm gap. RF blades are continuous and the same total length as the DC blades. On-chip capacitors (800 pF) on each DC segment provide filtering of RF pickup.

3.2.3 Trap Voltages

3.2.3 Applied RF Voltage

Rf voltage is coupled into the trap via a single-coil helical resonator (rf can), the design of which closely follows [54]. At times, we have used a two-coil resonator (described in Chapter 8), but we found that the 2-coil design facilitates anomalous sidebands in the motional mode spectrum of our ions. The resonator consists of a copper shield and two inner coils which couple inductively. The main coil couples RF to the trap blades via vacuum feedthroughs. The resonator shield is grounded through the vacuum chamber and optics table, which are connected by a copper cable to earth ground. Bias tee ports allow for DC voltage compensation along the the RF blade axis. Rf originates at an HP8648A signal generator, set to the the resonance frequency of the can. The initial

RF signal passes through an amplifier, low pass filter, and a directional coupler which samples the reflection signal of the resonator to be monitored on an oscilloscope.

The peak output voltage of the resonator is

$$V_{out} = (L/C)^{1/4}\sqrt{2P_{in}Q} \tag{3.1}$$

where P_{in} is the input power, Q is the resonator Q-factor, L is the coil inductance, and C is the trap capacitance. For resonance frequency ω_0 and FWHM $\Delta\omega$,

$$Q = \frac{\omega_0}{\Delta\omega}. \tag{3.2}$$

Typically, $Q > 100$ and is best optimized by using a vector network analyzer (VNA) to find the resonance frequency of the can, and adjusting the resonator geometry to decrease reflection. If the resonator is already well-functioning, RF frequency and resonator geometry can be optimized without the VNA by minimizing the reflection signal on an oscilloscope.

3.2.3 Applied DC Voltages

DC voltage is provided to all trap blades (6 DC segments + 2 RF blades), as well as two compensation rods above and below the trap used to mitigate stray fields. With DC voltage control along each trap axis, we have full control over the trapping potential. With a 2-coil resonator, RF blades can be biased individually, but with the single coil resonator, both blades receive the same bias voltage. Matsusada R4G250-.3 high-voltage (HV) power supplies provide DC voltage to the four trap 'endcaps'. HV supply output voltage is controlled using a 0-10V external signal, provided through the Artiq control system described in Chapter 4. The RF blades and middle DC blade segments are directly controlled with Artiq DAC voltages, and compensation voltages on rods below and above the trap are provided by a Rigol DP832 programmable power supply.

An adaptive box takes BNC inputs from all contributed DC voltages and connects them via D-sub connector to an inductor array, which prevents RF pickup on the DC blades from traveling up the DC line. The inductor array connects via C-sub connector to a 9-pin vacuum feedthrough. Six isolated pins provide voltage to the DC blades; the other three connect the power supply grounds to earth via the trap frame and vacuum chamber. The Matsusada and Rigol supplies must be left floating to avoid a ground loop.

3.3 Laser Systems

The critical optical frequencies from Chapter 2 are 399 nm (photionization), 369 nm ($^2S_{1/2} \rightarrow {}^2P_{1/2}$ transition), 935 nm (repump), and 355 nm (coherent operations). Producing each of these frequencies requires a well-maintained laser system.

3.3.1 CW Diode Lasers: 399 nm and 935 nm

Our continuous wave (CW) 398.9 nm ionization beam and 935 nm repump beam are produced by external cavity diode (ECD) lasers from Moglabs. The lasers are machined from solid aluminum blocks and contain semiconductor laser diodes with low reflectivity front facets (internal cavity) and high reflectivity rear facets. The output beam from the front facet is collimated with a high-NA lens and is incident on a diffraction grating, which is angled such that the first order reflection is directed back into the laser diode. The diffraction grating and rear facet make up the external cavity.

Coarse frequency adjustments can be made by adjusting the diffraction grating, temperature, and diode injection current. Small frequency adjustments can be made by controlling the external cavity length with a piezo-electric actuator. The ECD's have diode laser controller (DCL) boxes which control injection current, frequency, and temperature. A PID circuit reads a frequency error signal derived from monitoring the laser on a wavelength meter (WLM) (HighFinesse WS Ultimate 10), and the PID output is sent to the diode laser controller (DLC) which adjusts the piezo-electric actuator in order to lock the frequency. Currently the 935 nm ECD is locked using this method, and the 399 nm laser is free-running as it is only used for short periods during the loading process.

3.3.2 369 nm Frequency-Doubled Ti:Saph

Our 369 nm $^2S_{1/2} \rightarrow {}^2P_{1/2}$ transition is bridged using a frequency-doubled M-Squared Ti:Saph output, with the Ti:Saph pumped by a 532 nm Lighthouse Photonics Sprout. Each component of this system is described below with its location noted in Figure 3.4:

- **Sprout**: The Lighthouse Photonics Sprout is a diode-pumped solid state laser providing a 532 nm CW ouput up to 10 W. This laser is a sealed system with a monolithic laserhead and a power supply containing an integrated thermoelectrically cooled (TEC) chiller.
- **PIK**: The SolsTiS Pump Integration Kit (PIK) is a telescope that routes and steers the pump beam from the pump to the SolsTiS and can be manually aligned.
- **SolsTiS-SRX**: The PIK aligns the Sprout output into the SolsTiS, where it pumps a Ti:Saph crystal and subsequently outputs frequency-locked 740 nm light. Laser oscillation within a Ti:Saph cavity occurs on a number of well-defined, equally spaced cavity frequencies, with the number of cavity modes restricted by optical elements. An optical diode and bow-tie ring cavity configuration within the SolsTis restricts the number of cavity modes by forcing unidirectional light, enabling the SolsTis to oscillate on a single frequency. To tune the output wavelength, a motorized intracavity birefringent filter (BRF) is used, which introduces a wavelength-dependent loss. Finally, for a finer frequency selection, an etalon introduces a sharper spectral loss function than the BRF. Final output frequency is tuned by electronically adjusting the etalon spacing and locking it to the nearest cavity longitudinal mode. The SolsTiS comes with an ICE-Bloc control module, which connects via Ethernet and includes a software UI that allows frequency tuning, locking, and scanning. The SolsTiS must be cooled when pumped with > 5 W; we do this with a Thermotek recirculating chiller running at 20 C.
- **Reference Cavity**: A high stability reference cavity following the SolsTiS provides finer frequency control by locking the SolsTiS output frequency to a reference cavity fringe using

a resonator piezo device. The reference cavity also includes a 740 pickoff which is monitored by the WLM. A frequency error signal is processed by a PID box, the output of which is sent to the ICE-Bloc for frequency locking.

- **Telescope**: A telescope after the reference cavity aligns the SolsTiS output into a frequency-doubling cavity.
- **ECD-X**: An external cavity doubler (ECD-X) resonantly enhances CW input light and frequency doubles 740 nm light using a nonlinear crystal. Control electronics lock the maximum intensity within the cavity, by scanning the cavity length via piezo modulation. With 10 W power at the Sprout, the final output should be 1 W of 369 nm light. The frequency-doubler is also controlled by the ICE-Bloc and the M-Squared software UI. The frequency-doubling cavity is a sealed unit which needs to be opened occasionally for careful alignment, following instructions in the ECD-X manual.

3.3.3 355 nm COHERENT Paladin

Stimulated Raman transitions are performed with a 355 nm COHERENT Paladin high power, mode-locked UV laser with picosecond pulses at a 80.935 MHz repetition rate. The pump module of the system is 1064 nm output from a laser diode, powered by an oscillator current. Two Vanadate crystals pump and amplify IR light, and two more crystal stages generate second and third harmonic frequencies at 532 nm and 355 nm. A saturable Bragg reflector is used for mode locking. The Paladin can provide up to 8 W of light, and is cooled by a Termotek AG chiller. It is an industrial laser that comes in a closed box with no access to the cavity; all laser parameters are controlled through the Paladin Optimization Software GUI.

3.3.4 HeNe Frequency Reference

A stabilized Helium Neon (HeNe) Laser centered at 632.992 nm serves as a frequency reference. The 935 nm, 399 nm, and 740 nm laser frequencies are measured relative to the HeNe and calibrated regularly by the WLM.

3.4 Experimental ^{171}Yb^{+} Qubit Realization

In this section, we discuss experimental implementation of the laser-based atomic physics techniques described in Section 2.3.

3.4.1 Near-Resonance Lasers

An optical pathway diagram for the near-resonant lasers is shown in Figure 3.4. A ~ 10 mW 740 nm pickoff from the Ti:Saph is sent to the wavemeter (WLM) for locking, and the 369 nm ECD output is split into four beams (Doppler, Detection, Protection, and Optical Pumping). Relative beam powers are controlled by half wave plates (HWP) and polarizing beamsplitter (PBS) cubes. Beams are frequency-shifted by varying amounts via electro-optical modulators (EOMs) and/or acousto-optical modulators (AOMs), then coupled to optical fibers. The 369 nm output from the ECD is locked to a frequency 430 MHz below the $^2S_{1/2}\,|f=1,m=0\rangle \leftrightarrow {}^2P_{1/2}\,|f=0,m=0\rangle$ transition.

Each 396 nm pathway contains an AOM (Brimrose CQF-420-100-369) which upshifts the beam to near resonance, powered with RF generated by Artiq and amplified to 2W. AOM efficiency is dependent on beam polarization, which is controlled via a HWP placed before each AOM. Beams are focused into the AOMs with 100 mm telescoping lenses. The Doppler and Optical Pumping boards also include a 14.7 GHz EOM (Qubig EO-WG14.7M2-VIS) and 2.1 GHz EOM (Qubig EO-Yb171+), respectively. The frequency-shifted beams, along with the unshifted 0^{th} order Doppler beam (referred to as Protection+) are coupled via optical fiber to an array of fiberports near the trap, from which the beams are recombined and focused on the ion.

The 935 nm and 399 nm beams are combined and focused on the ion along the same pathway, and the 935 nm optical fiber is coupled through a 3.1 GHz fiber EOM (EOSpace Lithium Niobate). The final lens before the trap is a 150 mm Best Form, which focuses a beam to a minimum waist size

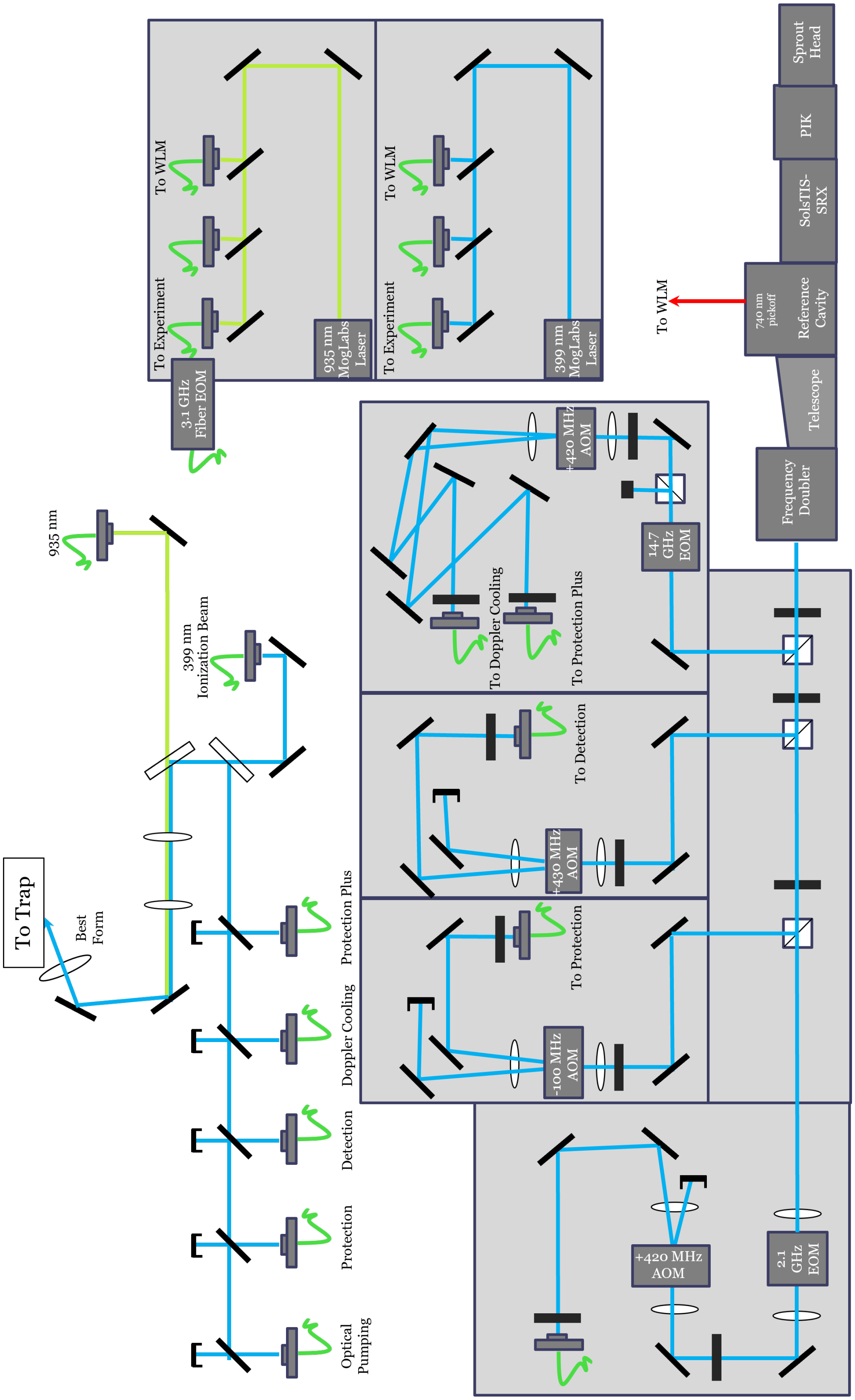

Figure 3.4: Optical pathways of near-resonant lasers

$$\omega_{min} = \frac{4\lambda f}{\pi D} \sim 100\mu m \tag{3.3}$$

at the ion, where D is the diameter of the beam prior to the Best Form, λ is the laser wavelength, and f is the focal length of the Best Form. We image beam profiles using a Guppy PRO F-503B as illustrated in Figure 3.5. Beam waist diameters are measured by fitting the Guppy image intensity profile to a Gaussian beam profile.

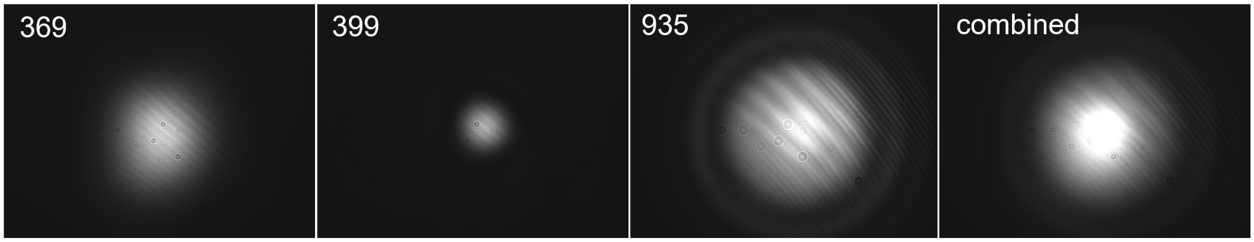

Figure 3.5: Intensity profiles of the 369nm, 399 nm, and 935 nm beams, as well as the combined beam through the trap, are imaged on a Guppy camera.

Each beam pathway is described in more detail below:

- **Doppler**: An amplified HP8671B synthesizer powers an EOM with 0.95 W, creating 14.747811 GHz sidebands which allow both the $f = 0$ and $f = 1$ ground state manifolds to cool along the ${}^2S_{1/2} \leftrightarrow {}^2 P_{1/2}$ transition. An AOM upshifted by +420 MHz leaves us 10 MHz red-detuned from resonance for optimal cooling of one ion. The 0th order (unshifted) beam produced by the AOM is labeled **'Protection+'** and is also sent to the trap, with its on/off status controlled by an optical shutter. This beam helps to trap initially when ions are hot, or to re-cool the crystal after a melting event. The Doppler beam must contain σ^-, σ^+, and π polarized light; final beam polarization is optimized with a HWP before the fiberport. Large polarization fluctuations induced by the EOM are negated by introducing a PBS between the EOM and the AOM HWP.

- **Detection**: An AOM upshifted by 430 MHz leaves the detection beam perfectly resonant with the ${}^2S_{1/2}, f = 1 \leftrightarrow {}^2 P_{1/2}, f = 0$ transition. This beam also must contain all polarization components, and is optimized with a HPW before the fiberport.

- **Protection**: The protection beam is a far detuned cooling beam that helps with recrystallization after collision events and improves cooling for 2D lattices. The Protection AOM is upshifted by 330 MHz (100 MHz detuning) based on [55].

- **Optical Pumping**: An amplified HP8664A RF generator powers the 2.105 GHz EOM. The 2.1 GHz sidebands allow the ${}^2S_{1/2}$, $f = 1$ manifold to couple to the ${}^2P_{1/2}$, $f = 1$ manifold which can decay to $|0\rangle$ for state initialization. The optical pumping AOM is upshifted by 430 MHz so that the beams are on resonance with the ${}^2S_{1/2}, f = 1 \leftrightarrow^2 P_{1/2}, f = 0, 1$ transition.

- **399 and 935**: The 399 nm and 935 nm beam pathways include isolators to prevent back-reflection into the laser cavity. The majority of each beam is sent to the trap, controlled by an optical shutter, and a small percentage of light is sampled by the WLM. Sidebands created by a 3.1 GHz fiber EOM, powered by an HP 8648C RF generator, bridge the ${}^2D_{3/2}$, $f = 1$ and ${}^3[3/2]_{1/2}$ transition for repump.

- **Beam Recombination**: The 369 nm beams are aligned along the same pathway using 50-50 beamsplitters. The 399 nm and 935 nm beams are combined in series using dichroic mirrors, and the beams are re-sized using a (50mm:125mm) telescope before they are focused into the trap by a 150 mm Best Form lens. Alignment through the trap can be roughly verified using a Celestron Portable HD microscope. The final beam enters the trap at a small angle relative to the table to allow Doppler cooling along all three trap axes.

Frequency shifts, as well as beam powers at the final fiberport, are listed in Table 3.1. The 369 nm beam powers listed are optimized for one ion; powers increase as ion number increases and average ion position shifts away from the beam center. Optimal powers are determined experimentally by measuring the ion temperature, characteristic optical pumping time, and detection fidelity as described in Chapter 4.

Beam	Frequency Shift	Power (fiberport)
Detection	+430 MHz	200 μW
Optical Pumping	+430 MHz,+2.1 GHz	350 μW
Doppler	+420 MHz,+14.7 GHz	100 μW
Protection	+330 MHz	400 μW
Protection+	+0 MHz	Max (varies)
935 Repump	3.1 GHz	Max (11 mW)
399 Ionization	N/A	Max (1.5 mW)

Table 3.1: Frequency shifts and power at final fiberport for near-resonance lasers are given, set optimally for one ion.

3.4.2 Loading Process

During ionization, a beam of neutral Yb is produced thermally and sprayed into the trap by resistively heating one of two ovens (a natural abundance Yb oven and a ^{171}Yb oven). In Figure 3.1, the high power feedthrough to the ^{171}Yb oven is visible while the feedthrough to the natural abundance oven is obscured by a lens translation stage. The ovens are needles stuffed with pure Yb and are mounted inside the chamber facing the trap, as shown in Figure 3.3.

Neutral Yb atoms moving at an average velocity $v_{avg} = \sqrt{\frac{8k_BT}{\pi m}}$ are then produced within the trapping potential and met with ionization beams, which enter at a 45 degree angle to the ion trajectory, resulting in frequency shift

$$f_{ion} = [1 - \frac{v_{avg} \cos\frac{\pi}{4}}{c}] f_{beam}. \tag{3.4}$$

Here, 'ionization beams' refer to the 399 nm CW Moglabs diode laser which excites the $^1S_0 \leftrightarrow ^1 P_1$ transition, as well the Doppler, Protection, and 355 nm Raman beams which are each capable of completing the ionization process. Doppler, Protection, and the 935 nm repump are turned on in conjunction with the 399 nm ionization beam, while the 355 nm beam is pulsed quickly and for short durations. The high energy and intensity of the 355 nm beams ionize atoms far more efficiently than Doppler and Protection; without the Raman beams aligned it can take a long time to trap and may require a higher oven current. Loading with low current and 355 nm light is

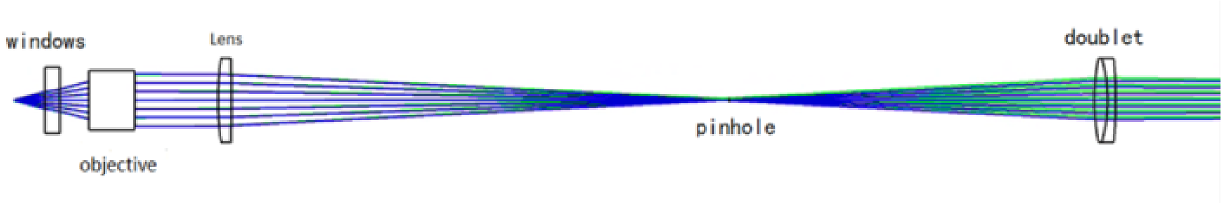

Figure 3.6: A ray diagram of the imaging system optical components is shown. Light is magnified (x5) by a high-NA objective, focused by a Best Form through a 100 mm pinhole, and further magnified (x8) by a doublet lens.

preferred to avoid coating the blades with neutral Yb, which can alter the trapping potential. Once an atom is ionized, the Doppler and Protection beams cool its temperature to near the Doppler limit.

3.4.3 Imaging System

Imaging systems optics, optimized by a Zemax simulation, are shown in Figure 3.6. The total magnification is designed to be x40. Light from an ion point source is collimated by a 0.28 NA from Special Optics, which results in a diffraction limited spot size

$$\frac{1}{2}(\frac{1.22\lambda}{NA}) = 0.8\ \mu\text{m} \tag{3.5}$$

and x5 magnification. This image is focused through a 100 mm pinhole using a Best Form lens, then further magnified and projected onto a detection device using a doublet (x8 magnification). The objective, Best Form, pinhole, and doublet are held by Thorlabs cage plates with kinematic mounts for open access and fine individual alignment.

After the doublet, light passes through two spectral filters and enters a dark box sealed to prevent excess background. Inside the dark box, a flip mirror controlled by a TTL pulse sends light to either a photomultiplier tube located within the box, or an Andor iXon 897 EMCCD camera connected to the box by optically sealed lens tubing. Distance between optical components are listed in Table 3.2.

Optics	Separation
Objective : Best Form	25 mm
Best Form : Pinhole	150 mm
Pinhole : Doublet	110 mm
Doublet : EMCCD/PMT	860 mm

Table 3.2: Separation between imaging system optical components

3.4.3 Installation Procedure

For any future student who may need to switch out the trap, I've included a brief description of objective alignment. To align the objective, illuminate the trap with a flashlight and turn off the room light, adjusting the translation stage such that a centered image of the trap silhouette can be seen on an index card about 150 mm from the trap. When the image is centered, attach the translation stage to the table, making sure that it is reasonably close to the trap window. Attach the rest of the optics, minus the pinhole, and image the four trap blades (or the 2 DC endcaps, for the rod trap) by slighting misaligning the beams to create scattering from the blades. The trap center in the xy plane will be the average value of the measured blade locations. A roughly accurate z-position can be found by moving the objective toward the chamber by half the trap length.

3.4.4 Coherent Operations

Raman beam alignment and occasional coherence measurements require Rabi oscillations via a microwave horn. The horn is located by the front vacuum chamber window and faces the trap at a 45 degree angle. RF is sent to the horn via a HP 8672A frequency synthesizer set to the qubit frequency ω_{hf}, controlled by an RF switch. The horn receives 29 dBm of power when on, with $\sim$ 30 dB isolation. It is important to keep the horn off when doing anything other than alignment or coherence measurements, as even with high isolation, leakage from the horn can create confusing signals.

With the exception of beam alignment and occasional coherence measurements, all coherent operations are performed via stimulated Raman transitions with the 355 nm COHERENT Paladin pulsed laser pictured in Figure 3.7b. This section describes the optical pathway and frequency lock for the Paladin, as well as instructions for aligning the Raman beams. The 355 nm beam path is illustrated in Figure 3.7, and the individual components are described below:

- **First Polarizer and Beamsplitter**: Laser output is sampled by a fast photodiode, which is used in the frequency locking circuit described in Section 3.4.4.
- **Second Polarizer and PBS**: This combination determines how much power is sent to the trap and deflects the rest to a beam dump. With the polarizer set to transmit max power through the PBS, each arm should be sending 1 W to the trap. If 1 W per arm is unmanageable, AOM efficiency may be low, or the laser may need to be re-optimized or moved to a new spot on the crystal.
- **50-50 Beamsplitter**: Sends equal power to each arm.
- **AOMs**: Frequency, phase and amplitude of Raman beams are controlled with 200 MHz AOMs (Brimrose CQF-210-40-355). The inner arm is driven by a single-frequency AOM and is used in the beatnote lock; the outer AOM is driven with multiple frequencies for MS operations.
- **Intermediate Focus**: A telescope inserted after the AOMs has lenses mounted on translation stages to provide finer control over beam alignment at the trap.
- **QWP and HWP**: A quarter wave plate (QWP) and half wave plate (HWP) provide full polarization control. Assuming a vertical magnetic field, the two beam paths must have horizontal polarization, which can be optimized by minimizing coupling to Zeeman levels as described in Chapter 4.
- **Delay Stage**: Since the Paladin is a pulsed laser, pulses need to be in phase at the ion. A delay stage increases the length of the inner arm to make it equivalent to the length of the outer arm.

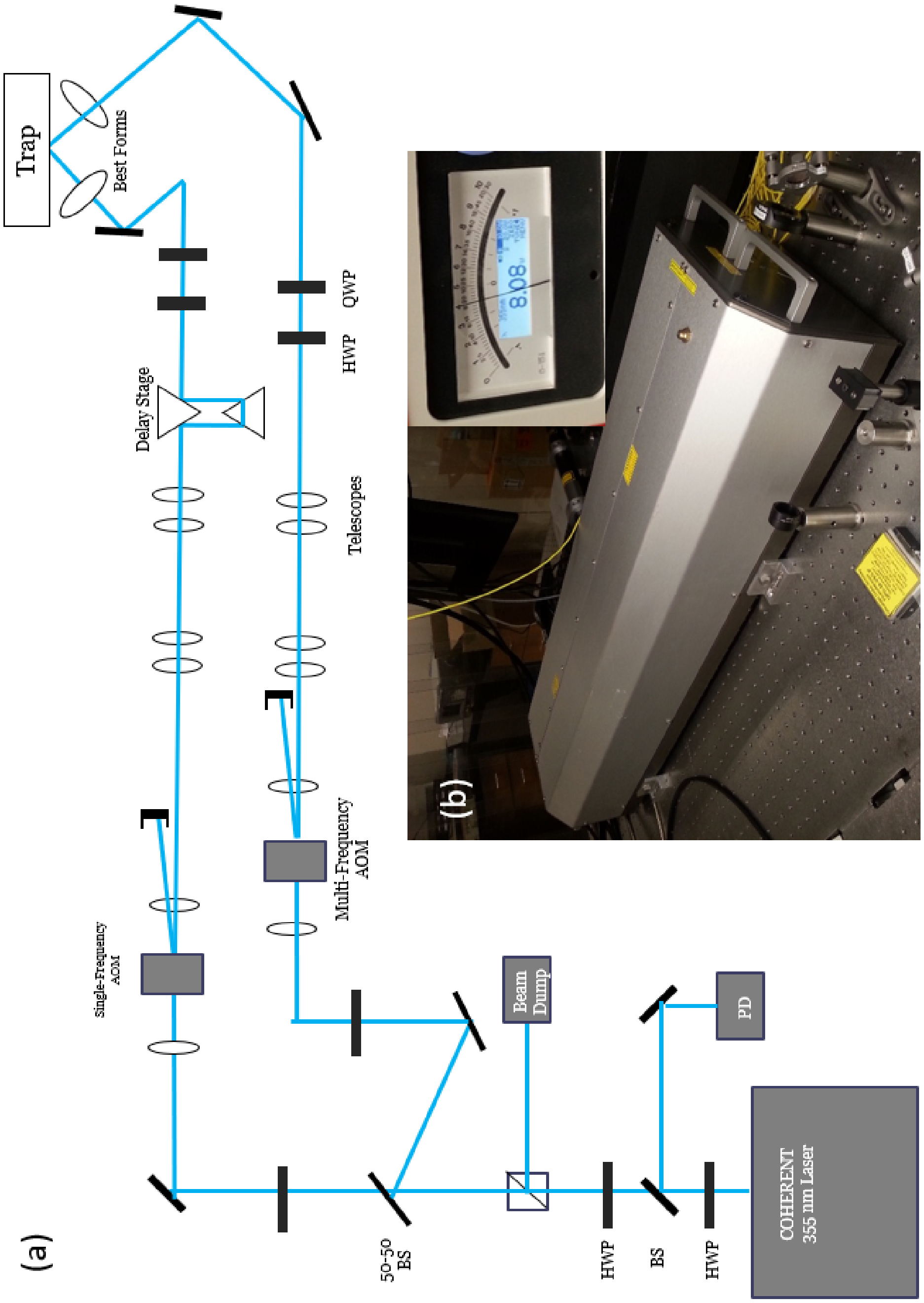

Figure 3.7: (a) 355 beam path (b) Image of Coherent Paladin outputting 8W power

- **Best Forms**: Two 150 mm Best Form lenses focus the beam into the trap, with a final waist diameter $\sim 100\mu$m. The resultant wavevector $\Delta\vec{k} = \vec{k_1} - \vec{k_2}$ is along the axial (transverse) direction relative to the ion lattice.

3.4.4 Beatnote Lock

The frequency difference between the two Raman beams needs to be locked to the qubit frequency ω_{hf}. Each Raman beam generated by the Paladin has an optical frequency comb, with comb teeth spaced evenly by the repetition rate ν_{rep}. We lock our single-frequency AOM to the 158^{th} comb tooth such that the beatnote at ω_{hf} is generated by all comb teeth separated by $158\nu_{rep}$. Then the ion will absorb a photon from the nth comb tooth of beam 1 and emit to the $(n + 158)^{th}$ comb tooth of beam 2, making the transition between $|0\rangle$ and $|1\rangle$.

Schematics for the beatnote lock closely follow [56] and are shown in Figure 3.8. Light is sampled by an Alphalas fast photodetector and passes through an amplifier and $11.7 - 12.8$ GHz bandpass filter to transmit the 158^{th} comb tooth. The signal is then mixed with a ~ 12.4 GHz signal from an HP8672, and the 200 MHz beatnote between the comb tooth and HP8672 is sent to a phase-locked loop (PLL). Within the PLL, an HP8640 is modulated via a PID controller to output a signal phase locked with the beatnote. The output signal is monitored on an oscilloscope.

3.4.4 Raman Beam Alignment

To perform coherent operations with the Paladin, the two Raman beam path lengths must match to less than 2.5 mm and overlap with the ion. First, we measure and adjust the length of both arms to get a rough temporal alignment, and then adjust the final lens stage to center the beam through the trap. Once an ion is trapped, we perform Ramsey experiments using the microwave horn to optimize spatial alignment, and we perform Rabi oscillation experiments to finalize temporal alignment.

- **Ramsey Experiment:** The experimental sequence for a Ramsey alignment experiment is as follows: *Doppler Cool* $\rightarrow$ *Optically Pump* $\rightarrow$ $\pi/2$ *microwave pulse* $\rightarrow$ *Delay* $\rightarrow$ $\pi/2$

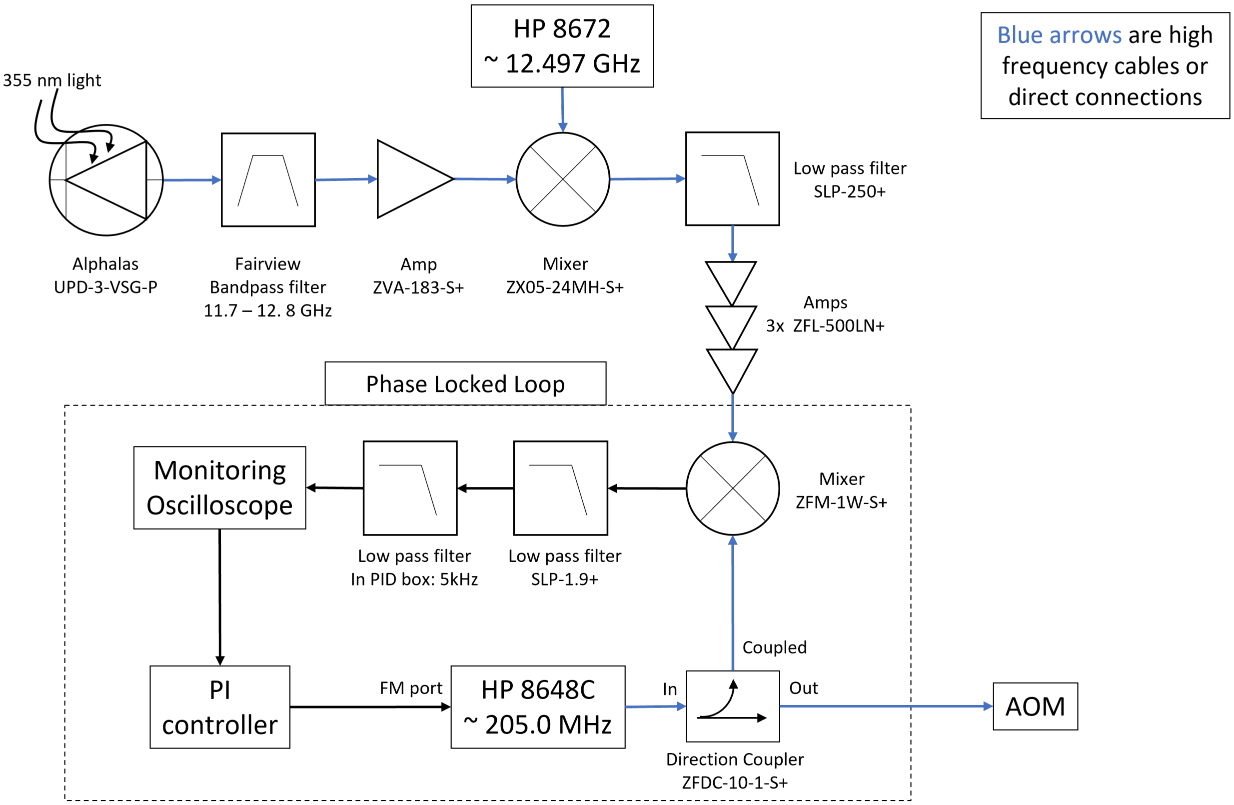

Figure 3.8: We lock our single-frequency AOM to the 158^{th} comb tooth of the optical frequency comb in the inner Raman arm. Light is sampled by an Alphalas fast photodetector and passes through an amplifier and $11.7 - 12.8$ GHz bandpass filter to transmit the 158^{th} comb tooth. The signal is then mixed with a ~ 12.4 GHz signal from an HP8672, and the 200 MHz beatnote between the comb tooth and HP8672 is sent to a phase-locked loop (PLL). Within the PLL, an HP8640 is modulated via a PID controller to output a signal phase locked with the beatnote.The output signal is monitored on an oscilloscope.

microwave pulse $\rightarrow$ Detect $\rightarrow$ Increase Delay Time $\rightarrow$ Repeat.

If the horn frequency is perfectly on resonance with ω_{hf}, every iteration should result in a perfect π-pulse regardless of delay time. If the horn frequency is detuned by δ from the atomic transition, the detected bright state population will oscillate with frequency δ. Turning on a Raman beam during the delay will create a two-photon Stark shift that scales with laser intensity. Higher beam intensities (better alignment) will shift the hyperfine levels by larger amounts, creating larger imperfections in the $\pi/2$ pulses, and therefore the bright state population will oscillate with a higher frequency.

First, an initial Ramsey experiment with no laser light during the delay time is used to measure a control frequency. Then a Ramsey experiment is run with a 355 nm Raman beam pulsed during the delay, and the frequency difference between the two experiment Ramsey oscillations is measured. Raman beam positioning is adjusted to maximize the frequency difference.

- **Rabi Oscillations:** The experimental sequence for a Rabi oscillation is as follows: *Doppler Cool $\rightarrow$ Optically Pump $\rightarrow$ Raman Pulse of Time t $\rightarrow$ Detect $\rightarrow$ Increase Pulse Time $\rightarrow$ Repeat.*

  If the Raman beatnote frequency is locked to the hyperfine transition frequency, and the pulse timing between beams overlaps, then each timestep in the experimental sequence should induce a carrier transition (Equation 2.29). Since the Rabi frequency Ω_R scales linearly with laser intensity ($\Omega_R \propto \sqrt{I_1 I_2}$), we sample the $\pi/2$-time on the first oscillation of the Rabi curve and adjust the delay stage and beam alignment until Ω_R is maximized. Then we remeasure the $\pi/2$-time and repeat until Ω_R can no longer be increased.

CHAPTER 4
EXPERIMENTAL SEQUENCING

4.1 Section Overview

Section 4.2 will give an overview of our experimental control system and how to do experimental sequencing. It includes a description of how lab equipment is connected to and controlled by modular Sinara hardware, and how control sequences are implemented and synchronized by Artiq control software.

Section 4.3 will describe everything that went into trapping an ion for the first time. This includes Doppler-free spectroscopy in order to verify transition lines, as well as troubleshooting techniques such as imaging neutral Yb and using the ^{174}Yb isotope for troubleshooting. Some tips and tricks for what to do if you can't find ions are here.

Section 4.4 discusses system calibration once $^{171}\text{Yb}^+$ is trapped. It describes a daily protocol which results in realizing a Mølmer-Sørensen gate with multiple ions.

4.2 Experiment Control

Our experimental control system uses Advanced Real-Time Infrastructure for Quantum physics (ARTIQ), developed by M-Labs and the NIST Ion Storage Group [57]. ARTIQ is a control software designed to be used with an FPGA-controlled modular ecosystem of devices known as Sinara hardware. A chassis (the 'Kasli crate') containing an arbitrary combination of desired Sinara modules can be assembled and purchased through M-Labs. A central "core device" controls peripheral devices and satellite crates using real-time in/out (RTIO) protocol, which synchronizes clocking and enables nanosecond timing resolution across experimental devices.

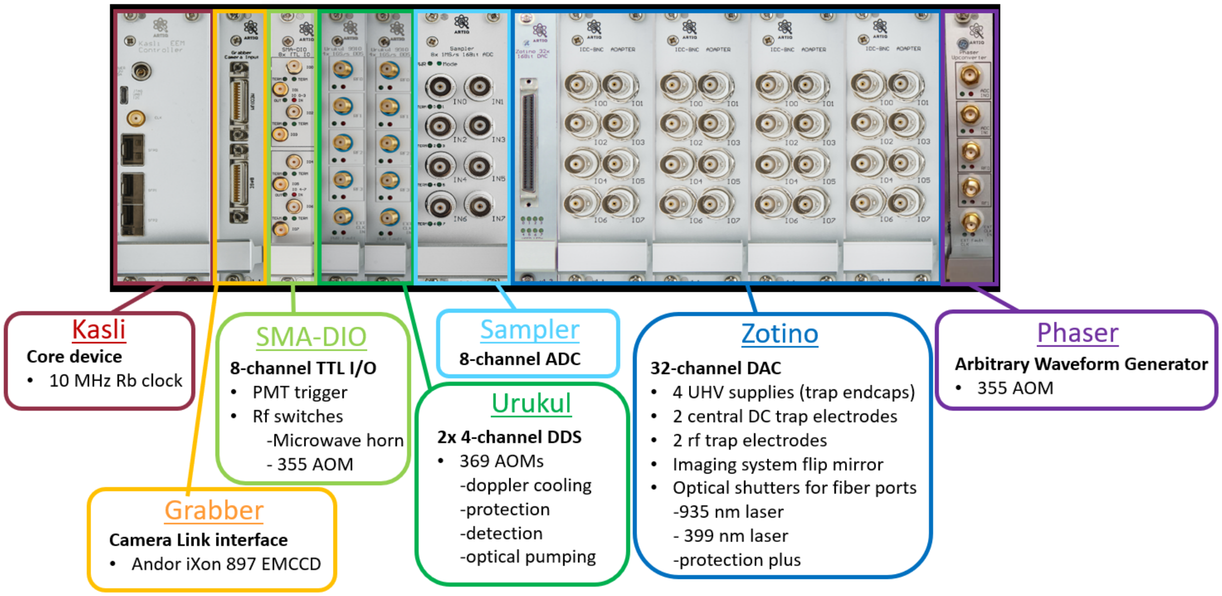

Figure 4.1: A rendering of the Richerme lab Sinara chassis. Individual modules are linked to color-coded boxes containing their name, description, and a list of devices externally connected to that board. The core device (Kasli), controls and synchronizes peripheral devices (Grabber, Sampler, Urukul, Zotino, Phaser, and SMA-DIO) which all contribute to experimental sequencing.

4.2.1 Sinara Hardware

The Richerme lab Kasli crate is rendered in Figure 4.1, and a description of each module is provided below:

- **Kasli**: The core device, Kasli, is capable of controlling up to 12 Eurocard Extension Modules (EEMs), and can act either as a central core device or as a satellite connected to the master via DRTIO. The EEM peripherals are powered by Kasli via ribbon cables, using the EEM Connector interface, and Kasli is connected to the experiment computer via Ethernet. We use an external 10 MHz Rb clock as a frequency reference rather than Kasli's internal 125 MHz clock, connected to Kasli's clock distribution chip via SMA.
- **Grabber**: The camera grabber interfaces with the EMCCD via a CameraLink port, which emits digitized pixel data from specified regions of interest (ROI's) at high speeds. As of now, the camera grabber seems limited in the number of ROI's it can handle within an

experiment timeframe, and we've continued to use Andor SOLIS software for acquisition and image processing.

- **SMA-DIO**: Eight digital IO's divided are into two banks of 4 channels. Each bank can be set to either output or read TTL pulses. We use two output TTL lines from the top bank to control RF switches for the microwave horn and the 200 MHz single-frequency Raman AOM. An input line from the bottom bank reads PMT counts during detection sequences.
- **Urukul**: Urukul is a 4-channel $1 - 400+$ MHz DDS-based RF synthesizer which offers control over frequency, amplitude, and phase of generated RF signals. Our chassis contains two Urukul boards, and 4 channels are used to control our ~ 420 MHz Brimrose AOM's.
- **Sampler**: The Sampler is an 8-channel, 1.5 MS/s data-acquisition device with 16-bit resolution.
- **Zotino**: Zotino is a 32-channel, 16-bit DAC which outputs ± 10 V with an update rate of 1MSPS. We use Zotino to control the output voltage of our HV power supplies, as well as to directly control the voltage on the central DC electrodes and RF trap electrodes. Zotino voltages also control the imaging system flip mirror and optical shutters for the 935 nm, 399nm, and Protection+ beams.
- **Phaser**: The Phaser is an 1.25 GS/s Arbitrary Waveform Generator (AWG) with integrated RF upconversion. A 4-channel, 16-bit DAC drives an I/Q modulator and digital upconverter (DUC). Four oscillators with frequency, amplitude, and phase control can be placed within a 20 MHz window relative to the DUC frequency, which can be shifted [-400, 400] MHz from a [0.3, 4.8] GHz carrier. The Phaser is used to drive multiple tones on a 220 MHz AOM for entanglement protocol.

4.3 ARTIQ Software

ARTIQ experiment sequences are written in Python, and the program flow is split between code that runs on the host computer and code executed on an embedded kernel in the core device FPGA. Artiq language modules and core device modules that run on the kernel are Python extensions which can be used with a strict subset of Python 3 (ARTIQ Python). Lab-specific packages ('Sub_Artiq') contain subroutines for experiments, specialized calculations, analysis, and other utilities.

The Artiq 'core device' can run a piece of code ('kernel'), which has access to specialized timing logic. Anything that requires precise timing must be compiled and executed on the core device rather than being interpreted and executed as regular Python code. 'ARTIQ Master' is the central program in the management system which schedules and executes events. A direct access memory (DMA) engine, which we typically program for sideband cooling, is also included with the core device as a way of scheduling many fast events while avoiding underflow errors. It preschedules events in FPGA memory and plays back the schedule out of the FPGA memory when called by the user.

An Artiq experiment file is split into four sections as defined by the Artiq language environment:

- **Build()**: Imports devices using keys from a device database, and allows you to set arguments to build the frontend of the experiment.

- **Prepare()**: The entry point for pre-computing data. Doing computations in *prepare()* rather than *run()* enables more efficient scheduling across multiple experiments that share hardware. In this section we could, for example, save input data, set datasets, calculate pulse schedules, or estimate the experiment run time.

- **Run()**: Requires an @*kernel* decorator, and is the only section that can interact with hardware. The *Run()* section is the body of the experiment and typically includes many Sub_Artiq routines such as Doppler cooling, detection, and optical pumping.

- **Analyze()**: The entry point for analyzing results where we might, for example, plot or fit experiment data.

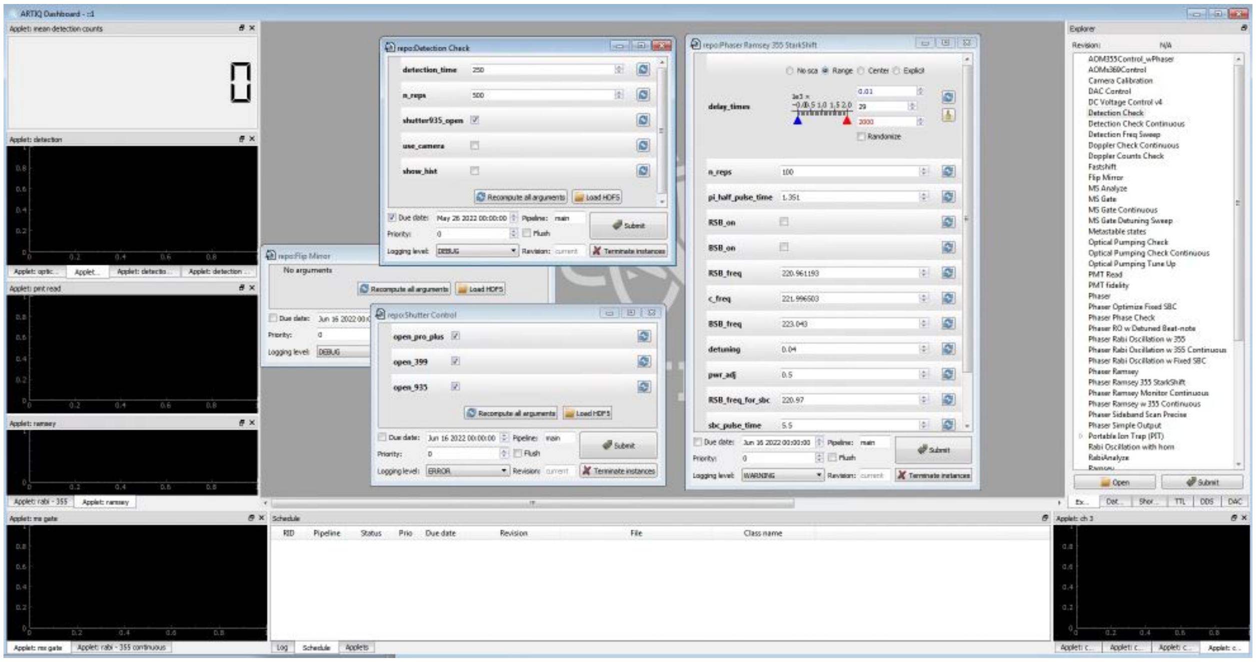

repo:Detection Check
detection_time 250
n_reps 500
shutter935_open ☑
use_camera ☐
show_hist ☐
☑ Due date: May 26 2022 00:00:00 Pipeline: main
Priority: 0 ☐ Flush
Logging level: DEBUG Revision: current

repo:Flip Mirror
No arguments
☐ Due date: Jun 16 2022 00:0
Priority: 0
Logging level: DEBUG

repo:Shutter Control
open_pro_plus ☑
open_399 ☑
open_935 ☑
☐ Due date: Jun 16 2022 00:00:00 Pipeline: main
Priority: 0 ☐ Flush
Logging level: ERROR Revision: current

repo:Phaser Ramsey 355 StarkShift
○ No sca ● Range ○ Center ○ Explicit
delay_times 0.01 29 2000 ☐ Randomize
n_reps 100
pi_half_pulse_time 1.351
RSB_on ☐
BSB_on ☐
RSB_freq 220.961193
c_freq 221.996503
BSB_freq 223.043
detuning 0.04
pwr_adj 0.5
RSB_freq_for_sbc 220.97
sbc_pulse_time 5.5
☐ Due date: Jun 16 2022 00:00:00 Pipeline: main
Priority: 0 ☐ Flush
Logging level: WARNING Revision: current

Explorer
Revision: N/A

Figure 4.2: The Artiq dashboard is a GUI for experiment control. A list of experiments is shown in the Explorer panel on the right, and they are run from the central window. Applets for plotting can broadcast datasets to give rapid feedback during experiments, and a log at the bottom shows experiment scheduling and output.

Experiments are submitted through the ARTIQ dashboard, shown in Figure 4.2. Experiment interfaces are opened in the central window, and a list of available experiments is shown in the 'Explorer' dock. Applets for plotting can broadcast datasets to give rapid feedback during an experiment, and experiment scheduling and output is read from the log at the bottom of the page.

4.4 Trapping an Ion for the First Time

In order to first trap a $^{171}\text{Yb}^{+}$ ion (and know that you trapped it), a lot of things have to go right all at the same time– e.g., laser frequencies and powers, beam alignments, RF and DC voltages, EOM and AOM functionality, and camera alignment. Some of these things can be checked independently.

Transition frequencies can be verified and calibrated via Doppler-free spectroscopy. Fluorescence tests with neutral ^{174}Yb can weed out laser alignment, camera position, and ionization laser frequency as possible issues. The simpler level structure of ^{174}Yb can be exploited to obtain confidence in trap voltages, laser alignment, 369 nm and 935 nm transition frequencies, and camera position. Here we go through each of these methods and give a description of what you should see when troubleshooting with ^{174}Yb/^{174}Yb^{+}.

4.4.1 Doppler-Free Spectroscopy

Physically important spectra are often obscured by Doppler broadening of spectral lines. This broadening comes from the thermal motion of the atoms and has a Maxwellian velocity distribution about $v = 0$. We perform Doppler-free saturated absorption spectroscopy as described in [58] to measure sharp absorption peaks for relevant optical transitions.

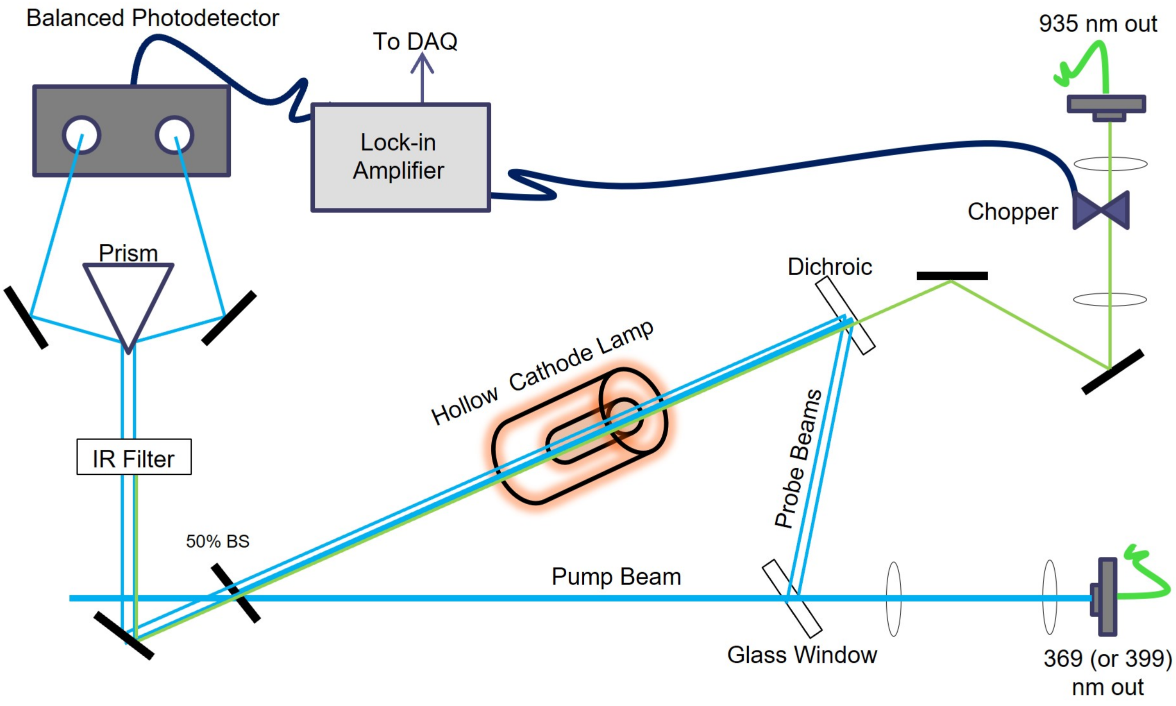

Figure 4.3: The experimental setup for Doppler-free spectroscopy is shown. Two probe beams and a counter-propagating pump beam, which overlaps completely with one of the probe beams, pass through a hollow cathode lamp coated with all Yb isotopes. Probe beam intensities are measured on a balanced photodetector.

Doppler-free saturated absorption spectroscopy as described uses three beams: a strong pump beam, and two weak probe beams which counter-propagate relative to the pump beam such that they only overlap in excitation for atoms with velocity $v = 0$. One probe beam (P1) exactly overlaps with the pump beam, and the other probe beam (P2) comes in parallel to the other two beams but does not overlap. For exactly $v = 0$, the pump beam burns a large hole in the ground state distribution of atoms as seen by P1.

The resulting fluorescence profile measured from P1 is a Doppler-broadened spectrum with a sharp 'Lamb dip' at $v = 0$, characteristic of saturated absorption. This Lamb dip can be orders of magnitude narrower than the Doppler-broadened peak, limited by the natural linewidth of the transition. P2 sees a standard absoprtion profile, and we can subtract the probes beam intensities $I(P2) - I(P1)$ via a balanced photodetector to remove the Doppler-broadened profile and obtain the Lamb dip only.

The experimental setup is shown in Figure 4.3. We use a Photron Hollow Cathode Lamp (HCL) coated with all Yb isotopes in natural abundance, powered at 10 A for measuring 369 nm transitions or 2.5 A for measuring 399 nm transitions. Incoming 369 or 399 nm light is focused by a telescope to fit through the cathode, then it is split by a glass window into two probe beam (4% of total power each) and a pump beam. The probe beams are sent through the cathode to two separate photodiodes of a PDB210A balanced amplified photodetector (PD) to monitor intensity. The pump beam, after passing through the same window, is split by a 50-50 beamsplitter. Half of the light is aligned to overlap with one of the probe beams inside the HCL, and the other half is either blocked or sent to a power meter for intensity normalization if laser intensity fluctuations are expected.

The 935 nm resonance frequency for repump is measured by sending in a 935 nm beam to overlap with the pump/probe 369 nm setup, with the 369 nm laser held at its experimentally measured resonance for a specific isotope. Then the 935 nm laser is scanned. On resonance, ions trapped in the $^2D_{3/2}$ state are returned to the ground state and re-excited by the 369 nm beam. 935 nm light is blocked from the photodetector with an IR filter, and we see a peak in 369 nm fluorescence

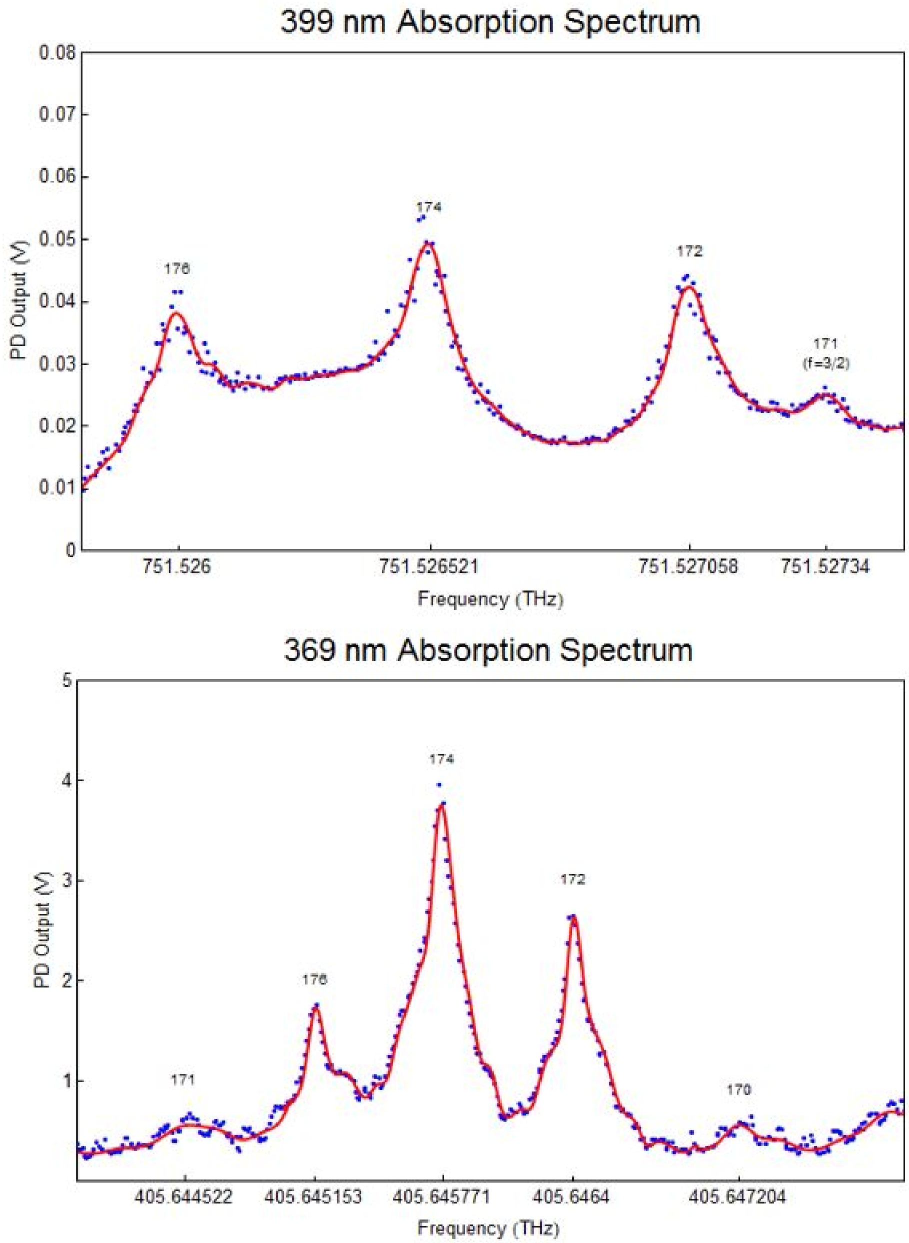

Figure 4.4: The difference in probe beam intensity (measured as PD voltage difference) is plotted vs frequency for 369 nm (top) and 399 nm (bottom) light. The resulting curves are absorption spectrums for the neutral (top) and ionized (bottom) ytterbium S $\rightarrow$ P transitions. The labeled isotopes and corresponding frequencies are determined through comparison to known values; measured peaks are within 25 MHz of expected.

at the 935 nm resonance frequency. The optical chopper and SR510 lock-in amplifier from Stanford Research Systems are placed in the path of the probe beams when scanning 369 or 399 nm frequencies.

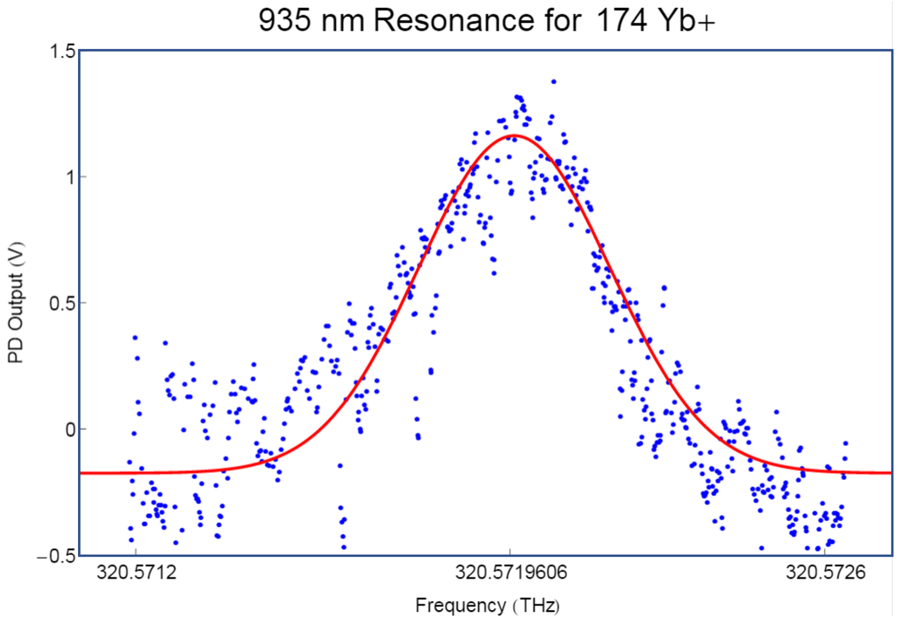

Figure 4.5: The 935 nm transition for ^{174}Yb^{+} is measured with the Doppler-free spectroscopy setup by holding the 369 nm beam at resonance and scanning the frequency of an overlapping 935 nm probe beam.

Absorption profiles are shown in Figure 4.4 and Figure 4.5. For the 369 and 399 nm absorption profiles in Figure 4.4, data has been binned for every 5 MHz, and a smoothing spline interpolation was done on which peak finding was performed. When compared to known values taken from the Monroe lab, all peak values in the 369 and 399 nm spectrum were within 25 MHz of expected. For the 935 nm profile, data was fit to a Gaussian centered 100 MHz above the expected value.

Since the natural abundance of ^{174}Yb is more than twice that of ^{171}Yb, transition frequencies for ^{174}Yb are found more precisely. Fortunately, the frequency differences between the isotopes are known to high accuracy, and calibrated frequencies for ^{171}Yb are easily determined from the spectroscopically determined ^{174}Yb frequencies. The Doppler-free spectroscopy setup can also be used to verify AOM frequency shifts by sending over light from the 369 nm boards of the main experiment.

4.4.2 Imaging Neutral Yb

Oven functionality, laser alignment, camera position, and 399 nm laser frequency can be verified by performing a fluorescence test with neutral Yb. To do this, oven current will need to be higher than when hunting for ions; historically, oven current for fluorescence measurements has been 3.5-4.5 A. It is important to be conservative with the oven current and amount of time the oven is on, as heavily coating the blades with Yb will create electronic shorts that lead to trap dysfunction.

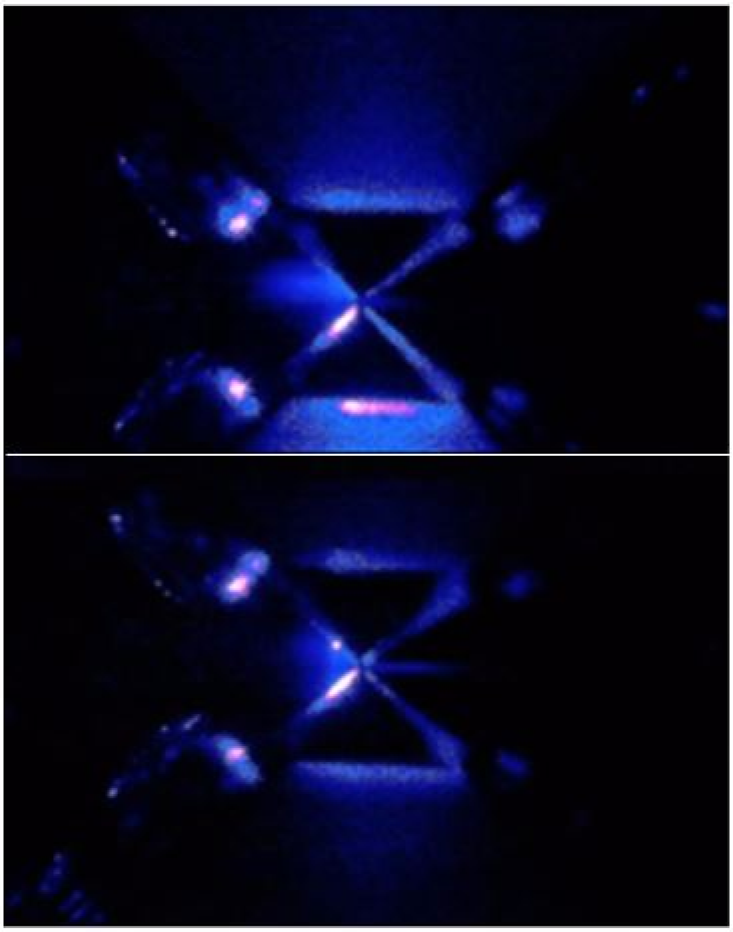

Figure 4.6: A microscope images 399 nm fluorescence from neutral Yb diffusing through the trap center.

Fluorescence tests can be done with the Celestron MicroDirect microscope, as illustrated in Figure 4.6, to verify oven functionality and beam alignment through the trap, or with the EMCCD to get a rough estimate of camera position. To do a fluorescence test with the EMCCD, align the imaging system to the trap following protocol in Chapter 3, and replace the 369 nm spectral filter pair with the 399 nm spectral filter. With the EMCCD aligned to the trap, a cloud of neutral atoms will show on the camera and disappear when the oven is turned off. If the camera isn't well-focused, it can be difficult to see the cloud by eye. In this case, it is better to look at the total counts on the CCD, which should rise after a couple of minutes and drop sharply when the oven is shut off. If the alignment/camera position/frequency combo is good, the count drop will be > 50 at saturation.

It is also possible to check for ion creation by pulsing the 355 nm arms. With both arms at 1 W, you should see a drop of in counts at saturation, as the ionized atoms no longer fluoresce 399 nm light. In our experience, the drop is only about 2-4 counts, so if the imaging system or 355 beams aren't well aligned, there may not be a clear signal.

4.4.3 ^{174}Yb for Troubleshooting

The simpler level structure of $^{174}\text{Yb}^+$ (Figure 4.7) makes it easier to trap and detect and compare to $^{171}\text{Yb}^+$. The absence of hyperfine structure due to its spin-0 nucleus removes dependence on the magnetic field, Doppler beam polarization, and EOM functionality. The lack of hyperfine levels also eliminates coherent population trapping, leading to additional detection counts and decreasing sensitivity to laser scatter, small misalignments, and camera focus. Confidence in trap voltages, laser alignment, transition frequencies, and camera position can be obtained using $^{174}\text{Yb}^+$. All relevant experimental parameters should be optimized for a $^{174}\text{Yb}^+$ ion before attempting to trap $^{171}\text{Yb}^+$. Calibrated $^{174}\text{Yb}^+$ trapping frequencies are shown in Table 4.1.

^{174}Yb+	
Transition	Frequency (THz)
399 nm	751.527300
369 nm (Doppler)	405.645570
935 nm	320.572021

Table 4.1: Calibrated ^{174}Yb+ transition frequencies for trapping and cooling

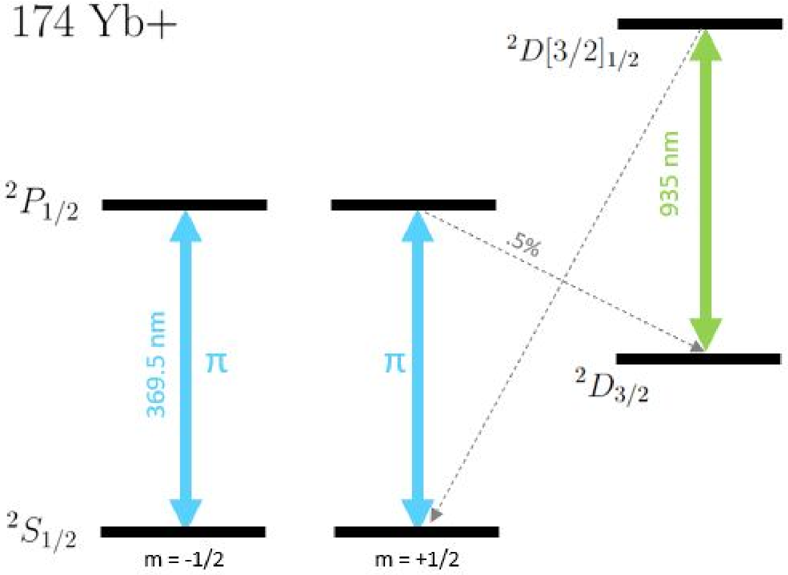

Figure 4.7: The level structure of ^{174}Yb$^+$ is shown. As with ^{171}Yb$^+$, 369 nm light bridges the $^2S_{1/2} \rightarrow ^2 P_{1/2}$ transition, and the 935 nm light repumps ions that are trapped in the $^2D[3/2]_{1/2}$ state. The absence of hyperfine splitting simplifies the trapping process for ^{174}Yb$^+$ compared to ^{171}Yb$^+$.

4.4.4 Troubleshooting Summary

At each step in the trapping/troubleshooting process, I have listed possible issues that may prevent you from seeing ions:

- **Neutral Fluorescence**: Oven functionality, 399 nm frequency or alignment (microscope), and camera position (EMCCD)
- **^{174}Yb+**: Trapping voltages (resonator Q-factor or ω_z/ω_r trap stability), 369/935 nm laser frequencies and alignments, camera focus (more sensitive for ions than neutral Yb), and previous items
- **^{171}Yb$^+$**: EOM frequencies and powers, Doppler beam polarization, magnetic field, and previous items

4.5 System Calibration for Quantum Simulation

This is an instructional section describing the typical daily experiments required to calibrate our system, the final step being implementation of an MS entanglement operation.

4.5.1 Optimizations with One Ion

4.5.1 Trapping $^{171}Yb^{+}$ and Minimizing Micromotion

First, check that the 369 nm and 935 nm laser frequencies are correct and locked to the target frequency to within a MHz. Calibrated target frequencies for ^{171}Yb+ at the time of writing are given in Table 4.2:

$^{171}\mathrm{Yb}^{+}$	
Transition	Frequency (THz)
399 nm	751.528250
369 nm (Doppler)	405.644370
935 nm	320.569295

Table 4.2: Calibrated $^{171}\mathrm{Yb}^{+}$ transition frequencies for trapping and cooling

After trapping an ion via the loading process described in Section 3.4.2, close the optical shutters corresponding to Protection+ and the 399 nm ionization beam. Scan the RF voltage through as wide a range as possible, while monitoring ion position on the EMCCD. If the ion position changes due to increasing or decreasing RF confinement, then the ion is not positioned on the RF null and is therefore experiencing micromotion. This is due to poor overlap of the RF and DC potentials, and can be remedied by adjusting the DC compensation voltages until the ion is centered on the micromotion minimum. A well-compensated ion position will no longer vary with RF power. A mismatch in RF and DC potentials may be caused by misalignments in blade geometry when first trapping, or by a drift in trap potentials over time due to buildup of Yb+ on the trap blades.

4.5.1 Doppler Cooling, Detection, and Optical Pumping

The Doppler cooling, detection, and optical pumping beams should be aligned together and then optimized independently. Align the Doppler cooling beam over the ion as precisely as possible, by maximizing the highest count value per pixel as read on the EMCCD. Check that the rest of the 369 nm beams are overlapped well with the Doppler beam pathway. Then optimize Detection alignment and power, using the following experiment sequences:

Doppler Cool $\rightarrow$ *Detect*

Doppler Cool $\rightarrow$ *Close 935 Shutter* $\rightarrow$ *Detect*

The second experiment sequence provides a measure of dark counts. Without the 935 nm beam, ions will become trapped in the ${}^2D_{3/2}$ state and no longer fluoresce. The Doppler Cooling sequence is usually between 5-10 ms, and an optimal PMT detection time is generally ~ 250 μs with about 1 background count and 7-9 bright counts, found via fidelity measurements as described in Section 2.3.1. The HWP prior to the Doppler and Detection fiberports should be adjusted to optimize counts, and the measured optimal value of laser power out of the Doppler cooling fiber is $90 - 100$ μW. Optimal cooling power can be determined using a variety of thermometry measurements, described in Chapter 5 and Chapter 7.

Now perform an optical pumping experiment:

Doppler Cool $\rightarrow$ *Optically Pump for Time* t $\rightarrow$ *Detect* $\rightarrow$ *Increase* t $\rightarrow$ *Repeat*

For $t = 0$ (no optical pumping), the ion will be detected in the bright state ($|1\rangle$) according to the measured detection fidelity. As t is increased, the probability of finding the ion in $|1\rangle$ will decrease exponentially with a characteristic decay time τ. The results of an optical pumping experiment are shown in Figure 4.8, with a $1/e$ characteristic decay time of about 0.28 μs. If the optical pumping beam is too strong, it may heat the ion within a sideband cooling cycle due to power broadening; however, this has not been a measurable effect in our system. To optically pump one ion, we use a beam power of 0.35 mW, and for larger numbers of ions, we increase optical pumping power as needed to keep the characteristic decay time below 0.5 μs.

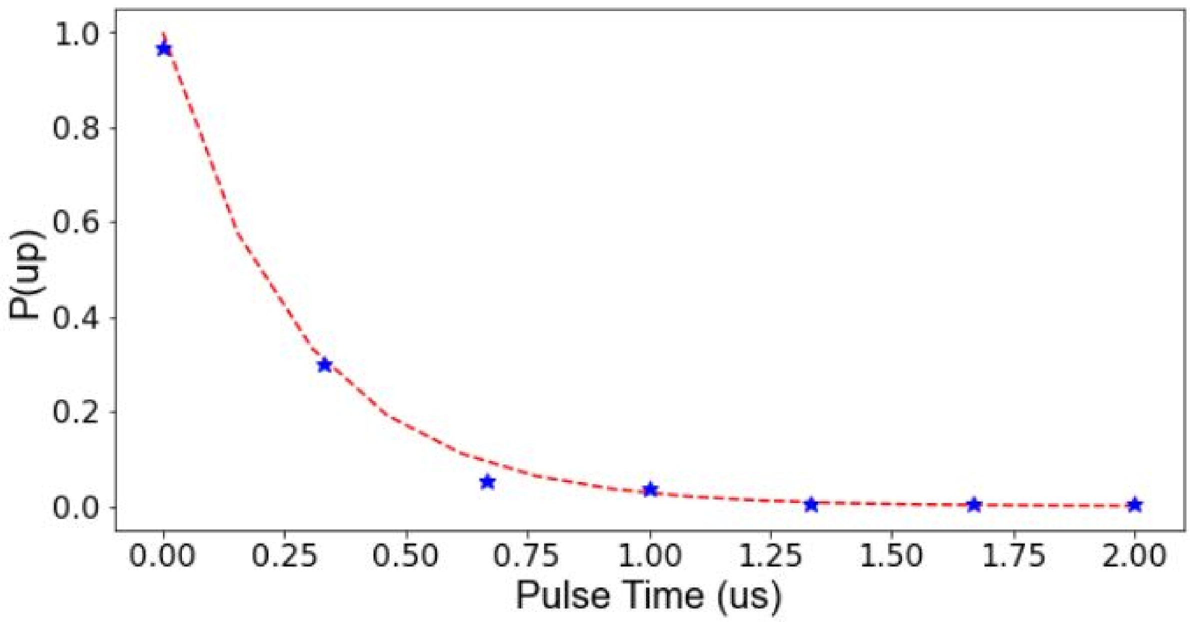

Figure 4.8: The probability of detecting an ion in the $|1\rangle$ (up) state is plotted against optical pumping pulse times and fit to an exponential curve with a characteristic decay time 0.28 μs.

4.5.1 Rabi Oscillations, Sideband Scans, and Thermometry

To begin optimizing coherent operations, check that the 355 nm beatnote lock is on, and set the beatnote frequency to that of the carrier transition (Ω_R). Obtain a carrier π-time (used later for Ramsey experiments) by performing a Rabi oscillation:

Doppler cool $\rightarrow$ *Optically Pump* $\rightarrow$ *Sideband Cool* $\rightarrow$ *Raman pulse of time* t $\rightarrow$ *Detect* $\rightarrow$
Increase t $\rightarrow$ *Repeat*

A Rabi curve fit to $\frac{1}{2}[1-\cos(\Omega_R t+\phi)e^{-t/\tau}]$ is shown in Figure 4.9. For calibration experiments performed with 0.13 W in each Raman arm, our carrier π-time is around 2.5 μs with a characteristic decay $\tau > 300$ μs, which we suspect arise due to decoherence from power fluctuations, beam pointing instability, and ion heating.

If the carrier and red sideband frequencies are completely unknown, a sideband scan (described below) must be performed prior to the Rabi experiment. If sideband cooling is inefficent, a few iterations of the experiments described in this section may need to be completed in order to fully optimize the system, as the π-time of a Rabi oscillation is temperature-dependent, and sideband

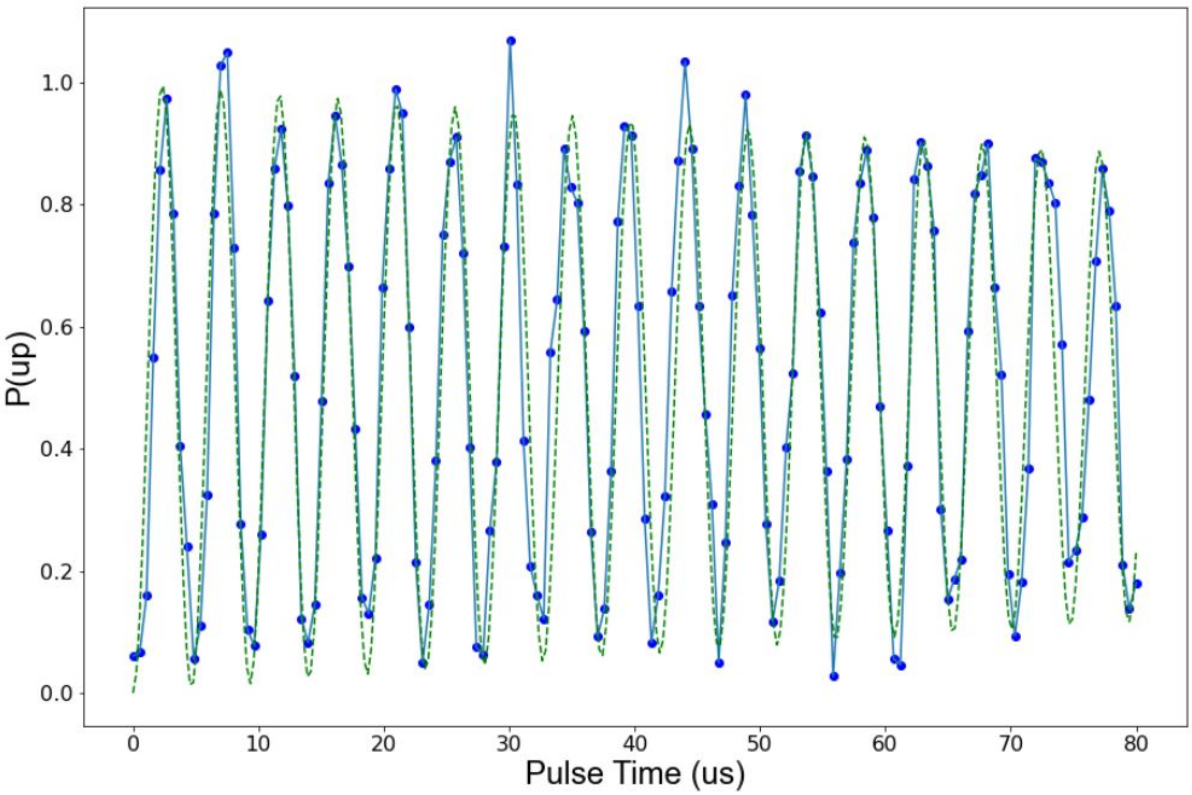

Figure 4.9: The probability of detecting an ion in the $|1\rangle$ (up) state is plotted against Rabi pulse times and fit to a 214 MHz Rabi frequency and 300 μs decay time.

cooling requires an accurate RSB frequency and RSB π-time.

Three types of sideband scans are performed during calibration, with the following experiment sequencing:

Doppler cool $\rightarrow$ *Optically Pump* $\rightarrow$ *Apply* π*-pulse at frequency* f $\rightarrow$ *Detect* $\rightarrow$ *Increase* f $\rightarrow$ *Repeat*

1. **Broad Scan:** A broad, coarse sideband scan is used to check for Zeeman state excitation. The $m = -1, +1$ Zeeman levels couple to the qubit states through σ^+ and σ^- light, which is minimized by adjusting the QWP's and HWP's in the Raman beamline. An example of a broad sideband scan with strong Zeeman coupling at ± 6 MHz is shown in the top panel of Figure 4.10, and an example of the desired spectrum is shown in the bottom panel. The bottom panel includes only the carrier, first order RSB/BSB, and second order RSB/BSB

peaks. The pulse time used in Figure 4.10 is the RSB π-time, which results in an overdriven carrier profile about the 222 MHz carrier AOM frequency.

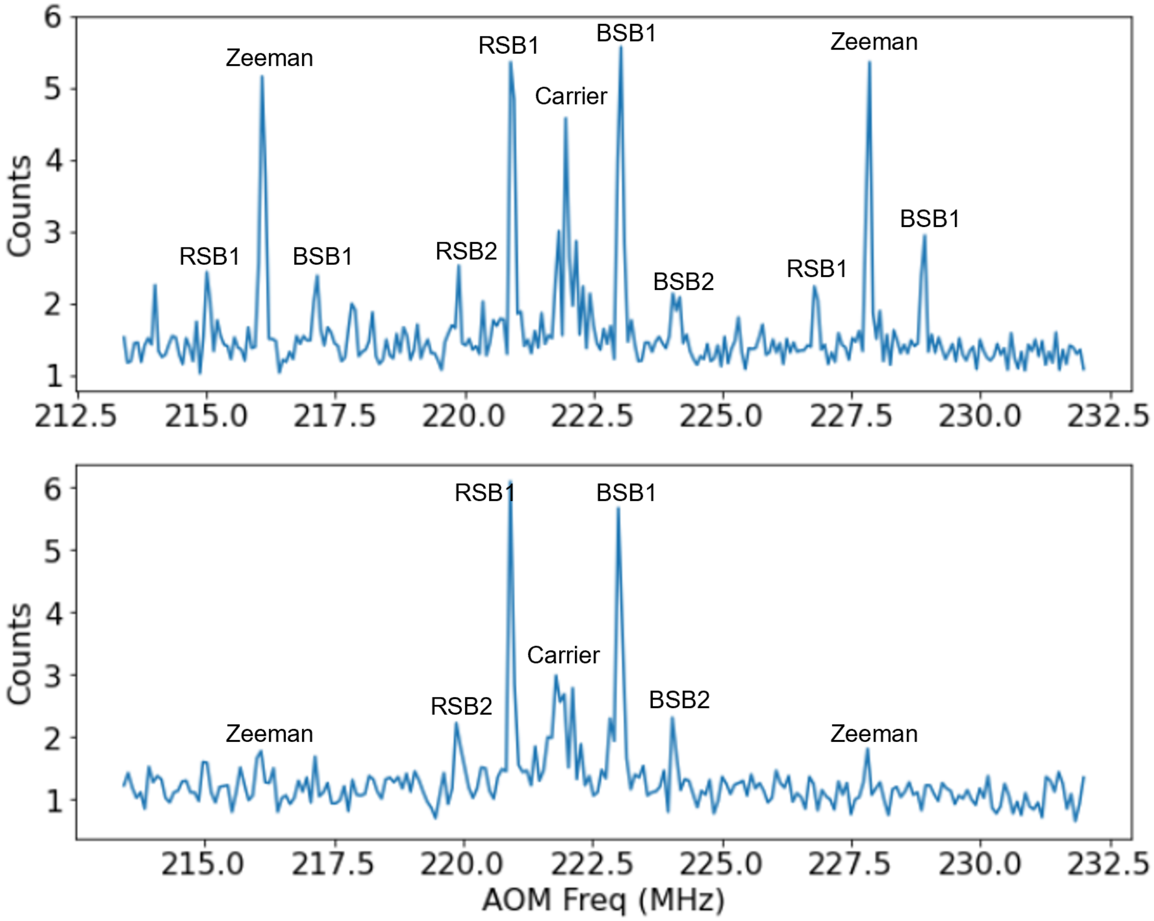

Figure 4.10: Axial sideband spectrum with heavy coupling to Zeeman states (top) and with Zeeman state coupling well-suppressed (bottom). The pulse time for this scan is the RSB π-time, resulting in an overdriven carrier profile.

2. **High Power Scan**: A precise RSB frequency value for sideband cooling is found by doing a narrow, fine frequency scan across the red sideband and fitting the peak to a Gaussian. At high power, the measured RSB frequency includes a two-photon Stark shift (Equation 2.27), as well as a far stronger four-photon Stark shift caused by off-resonant coupling to the carrier.

3. **Low Power Scan**: The sideband frequencies in the limit of zero power do not contain AC Stark shifts. By highly attenuating the Raman beams and using longer pulse times (due to

decreased Rabi frequency), we measure RSB and BSB frequencies far closer to their true values. These are the frequencies that are used for entangling operations.

With an accurately measured RSB frequency, we can perform time-averaged thermometry measurements as described in Chapter 5 to determine the RSB π-time, sideband-cooled ion temperature, and heating rate of the axial motional mode. A thermometry measurement is shown in Figure 4.11 for an ion in the blade trap, with a final sideband-cooled phonon occupation number $\bar{n} = 0.3$ and a linear heating rate of 0.2 quanta/sec. In order to decrease the number of experiments required, our time-averaging calibrations assume a thermal final state distribution and therefore overestimate the ion temperature. This is okay; the purpose of the time-average calibration is simply to minimize the final temperature by varying pulse times and to reveal the existence of any excess heating.

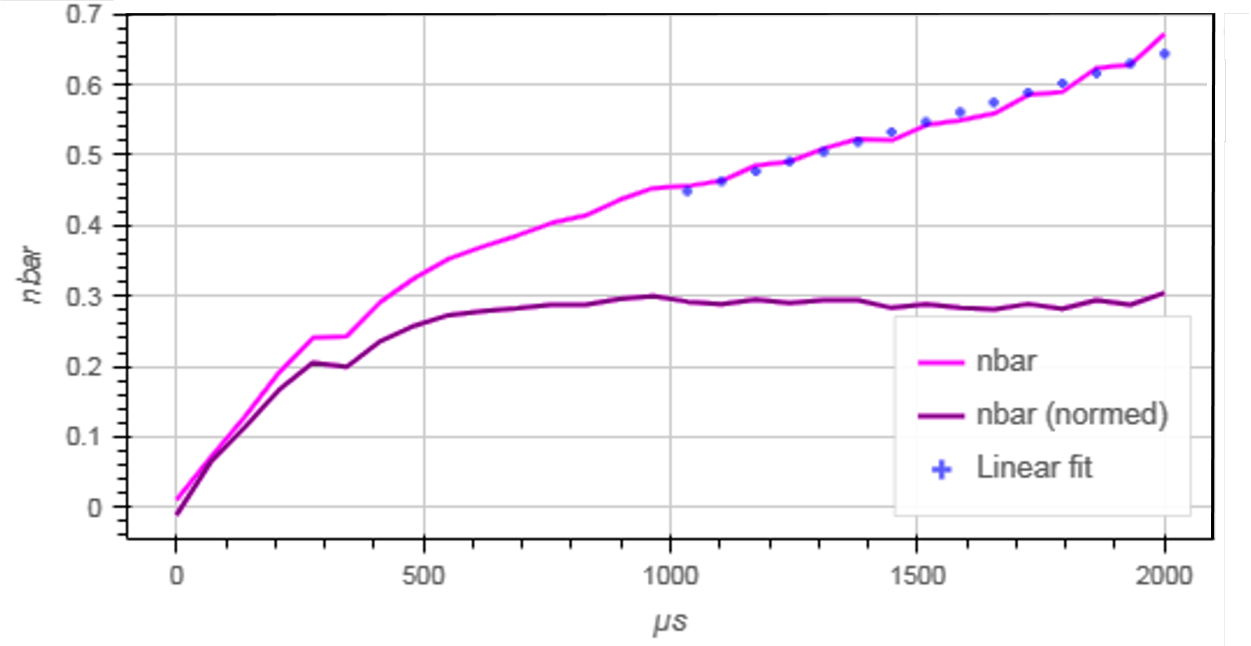

Figure 4.11: A time-averaged heating rate measurement of $\dot{n} = 0.2$ q/s for an ion sideband-cooled to $\bar{n} < 0.3$

4.5.1 Ramsey Experiments

Ramsey experiments are used for beam alignment, coherence measurements, finding an accurate carrier frequency, and for balancing the differential AC Stark shift. Here, the microwave $\pi/2$ pulses used in Section 3.4.4 are replaced with 355 nm Raman pulses:

Doppler Cool → *Optically Pump* → *Sideband Cool* → *Raman* $\pi/2$ *Carrier Pulse* → *Delay*
→ *Raman* $\pi/2$ *Carrier Pulse* → *Detect* → *Increase Delay Time* → *Repeat.*

To measure the Rabi carrier frequency, nothing happens during the delay. We adjust the carrier frequency until the ion is detected as bright for every delay time out to at least 5 ms. To measure coherence time, still nothing happens during the delay, but the beatnote frequency is slightly detuned from the carrier resonance so that an exponential decay due to decoherence can be fit to the Ramsey fringe decay. Beam alignment is measured by turning on individual Raman arms during the delay, as described in Section 3.4.4.

Finally, we balance the power in the Raman arms by submitting simultaneous red and blue tones during the delay, symmetrically-detuned by δ from the red and blue sidebands. We set δ to be $\geq 3(\eta\Omega)$ to avoid populating the phonon modes $n \pm 1$. The symmetrically-detuned red and blue tones contribute Stark shifts that, given equally intense and well-aligned Raman beams, should be equal in magnitude and opposite in sign. If the Stark shifts do not cancel, a Ramsey fringe will appear as the delay time is scanned. We adjust the power in one arm relative to the other until the Ramsey fringe has been eliminated. Power adjustment experiments are often performed with the second Ramsey $\pi/2$ rotation about the x-axis of the Bloch sphere rather than z. This puts the expected counts at half contrast, and we avoid measuring any decay effects on fluorescence.

4.5.2 Optimization with Two Ions

Now that the experiment is calibrated for one ion, we load a second ion and do a similar set of experiments. The micromotion minimum and optimal laser alignments should not have changed, but the Doppler, Detection, and Optical Pumping powers will need to be increased, as the ions will have moved symmetrically away from the micromotion minimum resulting in a lower red-detuned transition frequency. This also means that detection counts will not increase linearly with ion number.

We find that it is helpful (and often necessary) to cool both axial modes of motion, and so a high power sideband scan is required to pinpoint the zig-zag motional mode frequency. We then measure the COM mode heating rate, which is expected to be twice that of one ion. In Chapter 7 this is shown not to be the case for the rod trap, in which we observe heavily uncorrelated heating. My guess regarding the difference in heating mechanisms is that the blade trap is more sensitive to electric field fluctuations due to its smaller dimensions. Independent temperature measurements for each of the two ions, using the Andor software, can be helpful in diagnosing mistakes in micromotion minimization and in Doppler and Raman beam alignment. The power balance of the Raman beams should be re-verified as well, as a difference in AOM deflection of the red and blue tones will have a larger effect on two ions than on one.

Now we can perform the MS oscillation protocol:

Doppler Cool $\rightarrow$ *Optically Pump* $\rightarrow$ *Sideband Cool* $\rightarrow$ *Drive Symmetrically-Detuned RSB and BSB Tones for Pulse Time* t $\rightarrow$ *Detect* $\rightarrow$ *Increase Pulse Time* $\rightarrow$ *Repeat.*

The ions should oscillate between $|00\rangle$ and $|11\rangle$ at a frequency determined by the Ising couplings J_{ij} (Equation 2.52), and reach the maximally-entangled Greenberger-Horne-Zeilinger (GHZ) state $\frac{1}{\sqrt{2}}|00\rangle + |11\rangle$ at the $\pi/2$-time. The symmetry of the detuning δ can be further optimized by scanning the RSB frequency to pinpoint the maximum $|00\rangle \rightarrow |11\rangle$ transition probability. A MS oscillation curve is shown in Figure 4.12, fit to an exponentially decaying $\sin^2$ curve with a characteristic decay time of 610 μs.

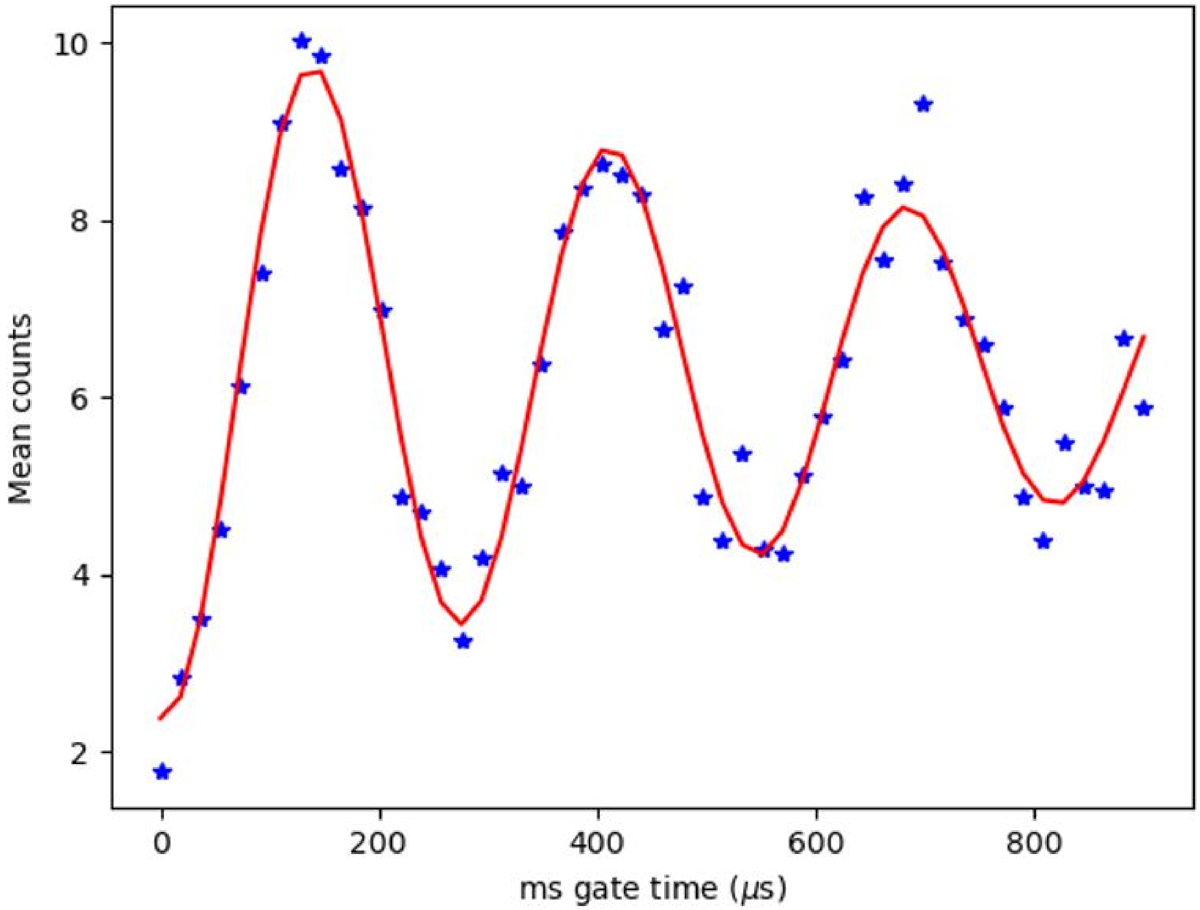

Figure 4.12: A Mølmer-Sørensen interaction curve is shown, fit to an exponentially decaying $\sin^2$ curve with a characteristic decay time of 610 μs.

CHAPTER 5

OPTIMIZED PULSED SIDEBAND COOLING AND ENHANCED THERMOMETRY OF TRAPPED IONS

5.1 Section Overview

For trapped ion experiments, resolved sideband cooling (SBC) is the most popular sub-Doppler cooling technique used to prepare systems near their motional ground state [59, 60, 61, 62]. Its widespread use stems largely from its applicability to most trapped-ion setups, since its effectiveness does not rely on using a specific ion species or trap geometry [50, 63]. In practice, SBC allows trapped ions to be initialized in a nearly-pure state of motion, with a typical average harmonic occupation $\bar{n} \lesssim 0.05$ [59]. However, SBC is often the longest time component in an experimental cycle by a significant factor [64], especially when many motional modes need to be cooled. Although individual addressing can facilitate some speedups in long ion chains [63], this chapter presents the first general method for determining an optimal SBC protocol.

Accurate ion thermometry goes hand-in-hand with near-ground-state cooling techniques such as SBC. Estimating ion temperatures and heating rates are essential characterizations in ion trap experiments [65, 50] since they inform the efficacy of cooling protocols and potential sources of noise. Yet, standard methods for measuring $\bar{n}$ near the ground state implicitly assume the motion is well-described by a thermal distribution of harmonic oscillator levels [59, 61]. When this assumption is violated, as is the case for Fock states, coherent states, or states following significant SBC [66, 67], more sophisticated thermometry methods must be employed to accurately characterize ion motional temperatures.

Here, we present a framework for calculating the optimal sequence of SBC pulses for near-ground-state cooling, and we develop an improved thermometry technique to more accurately measure $\bar{n}$ following SBC. Our optimal cooling strategy is applicable to any trapped ion experiment using pulsed SBC and flexible enough to incorporate decoherence effects or heating models if desired. Likewise, our method to determine ion temperatures requires only the experimental hardware needed for implementing pulsed SBC. We benchmark both our optimized SBC sequences and our new thermometry technique using a trapped $^{171}\mathrm{Yb}^{+}$ ion, finding close experimental agreement with theory predictions as well as significant improvements compared with traditional cooling and thermometry protocols.

This chapter is structured as follows. Section 5.2 reviews the standard theory of pulsed resolved SBC. In Section 5.3 we recast the pulsed SBC problem into a matrix formalism that allows for efficient numerical optimization of SBC pulse sequences. Section 5.4 introduces a new experimental technique to accurately measure ion temperatures following sub-Doppler cooling, followed by experimental validation in Section 5.5. We summarize with concluding remarks in Section 5.6.

5.2 Resolved Sideband Cooling Theory

When a trapped ion of mass m is confined to a 1D harmonic potential of frequency ω, resolved SBC allows for sub-Doppler cooling of the ion temperature. Prior to the onset of SBC, we assume that the ion has been Doppler cooled using a transition of linewidth Γ to the Doppler cooling limit [68, 69]

$$\bar{n}_i \approx \frac{\Gamma}{2\omega}. \tag{5.1}$$

Following Doppler cooling, the probability of finding the ion in the n^{th} harmonic oscillator level is well-described by the thermal distribution

$$p_{\text{th}}(n) = \frac{\bar{n}^n}{(\bar{n}+1)^{n+1}} \tag{5.2}$$

which is solely parameterized by the average harmonic state of the ion $\bar{n}$.

SBC protocols may be implemented for both optical and hyperfine qubits; here we begin by focusing on the latter. Typically, far-detuned Raman transitions of wavelength λ and linewidth $\gamma_{\text{rad}} \ll \omega$ are used to manipulate the electronic and motional states of the ion. When the Raman transition frequency is in resonance with the qubit splitting, it drives a "carrier" transition between qubit levels $|\downarrow\rangle$ and $|\uparrow\rangle$ at Rabi frequency Ω, with no change to the motional state. Detuning the Raman frequency by integer multiples of the trap secular frequency ω excites a "sideband" transition, coupling spin flips to a change in motional state from $|n\rangle$ to $|n'\rangle$, at Rabi rate [70, 50]

$$\Omega_{n,n'} = \Omega e^{-\eta^2/2} \sqrt{\frac{n_<!}{n_>!}} \eta^{|n-n'|} \mathcal{L}_{n_<}^{|n-n'|}(\eta^2), \tag{5.3}$$

where $n_<$ ($n_>$) is the lesser (greater) of n and n',

$$\mathcal{L}_n^{(\alpha)}(X) = \sum_{i=0}^{n} (-1)^i \binom{n+\alpha}{n-i} \frac{X^i}{i!} \tag{5.4}$$

is the generalized Laguerre polynomial, and

$$\eta \equiv \Delta k x_0 = 2\sin(\theta/2) \frac{2\pi}{\lambda} \sqrt{\frac{\hbar}{2m\omega}}. \tag{5.5}$$

is the Lamb-Dicke parameter for counter-propagating Raman beams which intersect at an angle θ. Here, we will refer to an $n - n' = 1$ transition as a first-order red sideband (RSB) transition and an $n - n' = -1$ transition as a first-order blue sideband (BSB) transition.

SBC of hyperfine qubits is typically characterized by a sequence of discrete RSB pulses interleaved with optical pumping. A traditional pulsed SBC protocol (which we will call the "classic" protocol) executes as follows [59, 61]. After Doppler cooling to an average harmonic occupation $\bar{n}_i$, and optical pumping to the qubit state $|\downarrow\rangle$, an initial motional level $n_i \gg \bar{n}_i$ is selected as the entry point for SBC. A first-order RSB π-pulse is then applied for $t = \pi/\Omega_{n_i,n_i-1}$ followed by fast optical pumping, to drive the transition $|\downarrow, n_i\rangle \rightarrow |\downarrow, n_i - 1\rangle$. Then another iteration is performed using $t = \pi/\Omega_{n_i-1,n_i-2}$, and so on, until the sequence concludes with a final $t = \pi/\Omega_{1,0}$ pulse. In principle, this protocol sweeps the fraction of population for which $n \leq n_i$ into the motional ground state.

By starting at larger n_i and iterating for more pulses, the classic SBC protocol can theoretically reach the SBC limit of $\bar{n}_{\text{min}} \approx (\gamma_{\text{rad}}/2\omega)^2 \ll 1$ [50, 71, 70, 72]. In practice, the achievable final $\bar{n}$ may be limited by effects such as imperfect RSB π-pulses, motional heating, and nearly-infinite RSB π-times (Section 5.3.4); this is indeed the case for several trapped-ion experiments [73, 67, 74]. Nevertheless, post-SBC temperatures of $\bar{n} \lesssim 0.05$ are routinely achieved with the classic method [59, 61], particularly when the initial state before SBC is in the "low η-$\bar{n}_i$ regime": $\eta \ll 1$ and $\bar{n}_i \lesssim 10$.

For optical qubits, continuous SBC is the preferred protocol for achieving near-ground state cooling [75]. In this approach, a RSB is driven continuously on a narrow optical transition while optical pumping is accomplished by spontaneous emission from the excited state. Given the slow decay rate of narrow transitions, spontaneous emission may be enhanced by temporarily coupling the excited state to a dipole-allowed transition. In $^{40}\text{Ca}^+$, for instance, coupling the quadrupole $D_{5/2}$ qubit level to the dipole-allowed $P_{3/2}$ state can lead to cooling rates of $\dot{\bar{n}} = 5\ \text{ms}^{-1}$ when strongly saturating the RSB transition [75]. As we will show in Section 5.3, this rate is comparable to the pulsed SBC rate in hyperfine qubits driven by a carrier Rabi frequency $\Omega \approx 2\pi \times 10$ kHz. For our experiments in Section 7.5 we set $\Omega = 2\pi \times 65$ kHz, leading to an initial cooling rate of $\dot{\bar{n}} \approx 30\ \text{ms}^{-1}$.

Continuous SBC has been well-described via detailed theoretical models [60, 69] and validated in experiments [75]. For a given optical pumping rate, the optimum RSB parameters for achieving the lowest final $\bar{n}$ may be estimated from the full set of atomic rate equations [60], or determined experimentally by scanning over different values of RSB power and frequency [76]. In contrast, the discreteness of pulsed SBC protocols prevents a similar rate-equation type analysis while greatly expanding the parameter space of possible cooling sequences. For these reasons, finding a pulsed SBC model that allows for efficient determination of optimal sequences has remained elusive to date.

5.3 Optimized Pulsed SBC Protocols

For hyperfine qubits, the intuitive ‘classic’ protocol introduced in Section II is not the most *efficient* pulsed SBC method for reducing ion temperatures. Given a chosen n_i, which sets the number of pulses, there are no adjustable parameters that may be used to optimize the cooling rate per pulse or per unit time. When starting from small Doppler-cooled $\bar{n}_i$, only a few pulses are needed and the deviation from optimal is small; when $\bar{n}_i$ is large ($\gtrsim 10$), the deviation from optimal widens considerably. If $\bar{n}_i$ is large enough, the classic method will fail to prepare ions in the ground motional state as mentioned previously in Section 5.2.

In this section, we introduce two globally-optimized pulsed SBC protocols: a single-parameter protocol called the “fixed” method, and a full-parameter protocol called “optimal” method. For a given number of pulses, the optimal method provides the lowest possible $\bar{n}$ after first-order SBC. When $\bar{n}_i$ is large, we show how these protocols can be extended to higher-order SBC to avoid the limitations of first-order cooling. To compute these optimized SBC protocols we must first numerically simulate the complicated interplay between each $\pi-$pulse and its effect on the *entire* harmonic oscillator population $p(n)$. Below, we develop a graph-theoretic description of pulsed SBC to accomplish this task and provide a framework for fast optimization of pulse sequences.

5.3.1 Graph-Theoretic Description of Pulsed Sideband Cooling

We embed SBC into a graph $G = (V, E)$ with a set of vertices V and edges E. The vertices V represent a truncated set of the harmonic states $n = [0, n_{\text{max}}]$ where $n_{\text{max}} \gg \bar{n}_i$ is well satisfied. Each vertex is weighted by the probability corresponding to its harmonic state $V = \{p(0), p(1), \ldots, p(n_{\text{max}})\}$, as shown in Figure 5.1. Each vertex has an undirected edge loop weighted by the probability of not cooling: $a_n(t) = \cos^2(\Omega_{n,n-1}t/2)$ in the case of first-order cooling shown in Figure 5.1. The probability of cooling $b_n(t) = \sin^2(\Omega_{n,n-1}t/2)$ weights a directed edge from the n to $n-1$ vertices. For m^{th}-order cooling, the directed edges would connect to their m^{th} leftmost neighbor with the associated Rabi frequency $\Omega_{n,n-m}$.

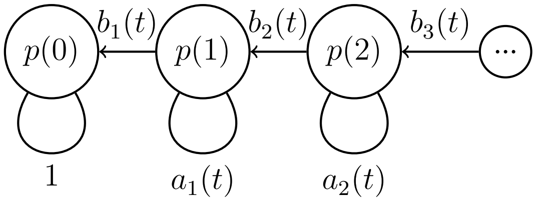

Figure 5.1: Graph G representing first-order SBC. The set of vertices V is represented by circles and weighted by the current harmonic probability distribution $p(n)$. The set of edges E is represented by lines: loops weighted by $a_n(t)$ and directed edges weighted by $b_n(t)$.

To model one SBC pulse of time t_0, all vertex weights take one traversal of their respective edges resulting a new set of vertex weights: $V_n^{(1)} = a_n(t_0)V_n^{(0)} + b_{n+1}(t_0)V_{n+1}^{(0)}$. To model N SBC pulses, the graph is traversed N times. In general, each traversal may have its own associated pulse time $\{t_0, t_1, \ldots, t_{N-1}\}$.

We numerically represent the graph and SBC process as a matrix equation. The initial vertex values map to the vector $\vec{p}_{\text{th}} = \{p_{\text{th}}(0), \ldots, p_{\text{th}}(n_{\text{max}})\}$, where $p_{\text{th}}(n)$ is the initial thermal distribution following Doppler cooling (Equation 5.2). One traversal of the graph maps to the upper triangular matrix

$$W(t) = \begin{pmatrix} 1 & b_1(t) & 0 & \ldots \\ 0 & a_1(t) & b_2(t) & \ldots \\ 0 & 0 & a_2(t) & \ldots \\ \vdots & \vdots & \vdots & \ddots \end{pmatrix} \tag{5.6}$$

which is shown graphically in Figure 5.2(a) for $t = 1.016 \times 2\pi/\Omega$. $W(t)$ acting on $\vec{p}_{\text{th}}$ results in an updated probability vector $\vec{p} = \{p(0), \ldots, p(n_{\text{max}})\}$

$$\begin{pmatrix} p(0) \\ p(1) \\ p(2) \\ \vdots \end{pmatrix} = \begin{pmatrix} 1 & b_1(t) & 0 & \ldots \\ 0 & a_1(t) & b_2(t) & \ldots \\ 0 & 0 & a_2(t) & \ldots \\ \vdots & \vdots & \vdots & \ddots \end{pmatrix} \begin{pmatrix} p_{\text{th}}(0) \\ p_{\text{th}}(1) \\ p_{\text{th}}(2) \\ \vdots \end{pmatrix}. \tag{5.7}$$

To encode the effects of multiple SBC pulses, all individual pulse matrices $W(t)$ are multiplied together: $W(t_{N-1}) \ldots W(t_1)W(t_0)$. In the simplest case, when all pulses are of the same duration

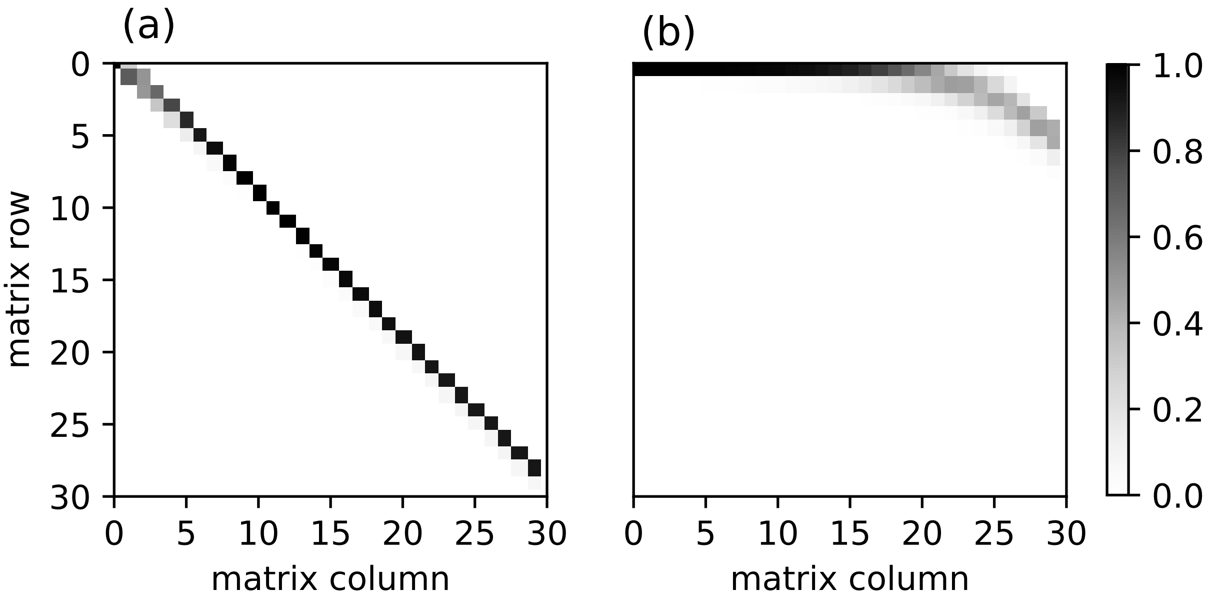

Figure 5.2: The first 30×30 matrix elements of the weight matrix (Equation 5.6) are shown graphically for (a) a single pulse and (b) 25 repetitions of the pulse applied in (a).

t_0, the SBC interaction is encoded as a matrix power of $W(t_0)$. For example, the final harmonic level occupation after 25 identical pulses can be calculated as $\vec{p} = W^{25}(t_0)\vec{p}_{\text{th}}$, with the low-$n$ matrix elements of W^{25} shown in Figure 5.2(b).

5.3.2 Fixed protocol

Optimized pulse sequences may be efficiently computed within the graph-theoretic framework introduced above. To begin, we consider a single-parameter optimization that we call the "fixed" protocol. Each of the SBC pulses is chosen to have the same duration $T_{\text{fixed}} = \{t_0, \ldots, t_0\}$, similar to SBC schemes implemented in some trapped-ion studies [77, 78, 73]. Here we explicitly seek to minimize the function

$$\bar{n}(t_0) = \sum_{n=0}^{n_{\max}} n \left[W^N(t_0)\vec{p}_{\text{th}} \right]_n \tag{5.8}$$

to find the time t_0 which yields the lowest possible $\bar{n}$ given N identical SBC pulses.

The optimal pulse time for the fixed method can be computed quickly since there is only one parameter to optimize for any number of pulses N. The most costly step in minimizing Equation 5.8 is the calculation of $[W^N(t_0)\vec{p}_{\text{th}}]_n$ for different t_0. However, standard numerical packages, such as Python's NumPy module [79], can exponentially reduce the number of matrix multiplications needed when computing a power of a matrix through binary decomposition. Assuming $N > 3$, a binary decomposition recursively squares the matrix, exponentially increasing the matrix power: 2, 4, 8, and so on. The implementation is adapted to allow for arbitrary matrix powers, with a computation time scaling with N as $\mathcal{O}(\log_2(N))$ and with system size n_{max} as $\mathcal{O}(n_{\text{max}}^3)$.

5.3.3 Optimal Protocol

We now consider the optimal protocol, which is a full-parameter optimization where each pulse time is treated as an independent variable. Given a set of experimental parameters, and restricting—for now—to first-order RSB pulses, the remaining degrees of freedom are the durations of each SBC pulse. The optimal protocol searches the full available parameter space of N distinct pulse times, yielding the lowest possible $\bar{n}$ for any given value of η, $\bar{n}_i$, Ω, and N.

The optimal protocol, using first-order RSBs, executes as follows. First, the initial harmonic populations $\vec{p}_{\text{th}}$ and Rabi frequencies $\Omega_{n,n-1}$ are calculated over a truncated range of harmonic states $[0, n_{\text{max}}]$ ($n_{\text{max}} \gg \bar{n}_i$), based on the experimental parameters η, $\bar{n}_i$, and Ω. Next, a gradient descent algorithm is applied to minimize the equation

$$\bar{n}(t_0, t_1, \ldots, t_{N-1}) = \sum_{n=0}^{n_{\text{max}}} n\left[W(t_{N-1})\ldots W(t_1)W(t_0)\vec{p}_{\text{th}}\right]_n \tag{5.9}$$

to find the pulse schedule $T_{\text{optimal}} = \{t_0, t_1, \ldots, t_{N-1}\}$ that gives the lowest average harmonic occupation $\bar{n}(t_0, t_1, \ldots, t_{N-1})$ following N SBC pulses.

Since each pulse time in the pulse schedule T_{optimal} is an independent variable, computing the optimal T_{optimal} scales exponentially with the number of pulses. For large n_{max} or N, this can cause calculations to exceed readily available computational resources. However, we find that careful bounding of the gradient descent minimization can help reduce computation times. For example, using a standard laptop we observe that a 50-pulse SBC optimization takes less than 90 seconds to compute, which is a factor of two faster than for the unbounded case.

The predicted performance of the optimal, fixed, and classic protocols are compared in Figure 5.3. Simulations are performed using the parameters $\bar{n}_i = 15.36$ and $\eta = 0.18$, which are similar to those of our experimental system described in Section 5.5. For fewer than ~ 50 SBC pulses, the classic method not only takes the longest absolute time to implement (Figure 5.3(a)), but also yields the highest final $\bar{n}$ (Figure 5.3(b)). In comparison, the fixed (solid black) and optimal (dashed gray) methods perform nearly identically, both in overall cooling time and final ion temperature. For larger $\bar{n}_i$, the classic method drifts further away from optimal, while the fixed method retains its near-optimal behavior.

5.3.4 Multiorder Optimization

When outside of the low η-$\bar{n}_i$ regime, the trapping of harmonic population in high-n states can limit first-order RSB cooling [78, 73, 67]. As shown in Figure 5.3(c), the first-order RSB Rabi frequency approaches zero for specific high-n harmonic levels (approximately $n = 112$ for our chosen parameters). As a consequence, any initial population $n \gtrsim 112$ will be trapped in these high-n states, even while the remaining population $n \lesssim 112$ is swept towards the ground state.

This population trapping effect is visible in Figure 5.3(d), which shows the harmonic population distribution following 50 first-order SBC pulses. A significant population near $n = 112$ remains uncooled, contributing approximately 0.3 motional quanta to the final value of $\bar{n}$: an order of magnitude higher than the SBC cooling limit and large compared to what is considered near-ground-state cooling. This effect also explains why the three first-order methods in Figure 5.3(a)-(b) begin to converge at large numbers of pulses: the trapped population contributions to $\bar{n}$ dominate at colder temperatures.

To avoid population trapping at high-n, higher-order RSB pulses can be incorporated into the SBC protocol. We refer to this scheme as "multiorder" cooling. Particularly in experimental regimes where η or $\bar{n}_i$ are large, trapped populations may be so significant that multiorder cooling is *required* to achieve near-ground-state temperatures [78, 73, 67]. This is because the harmonic

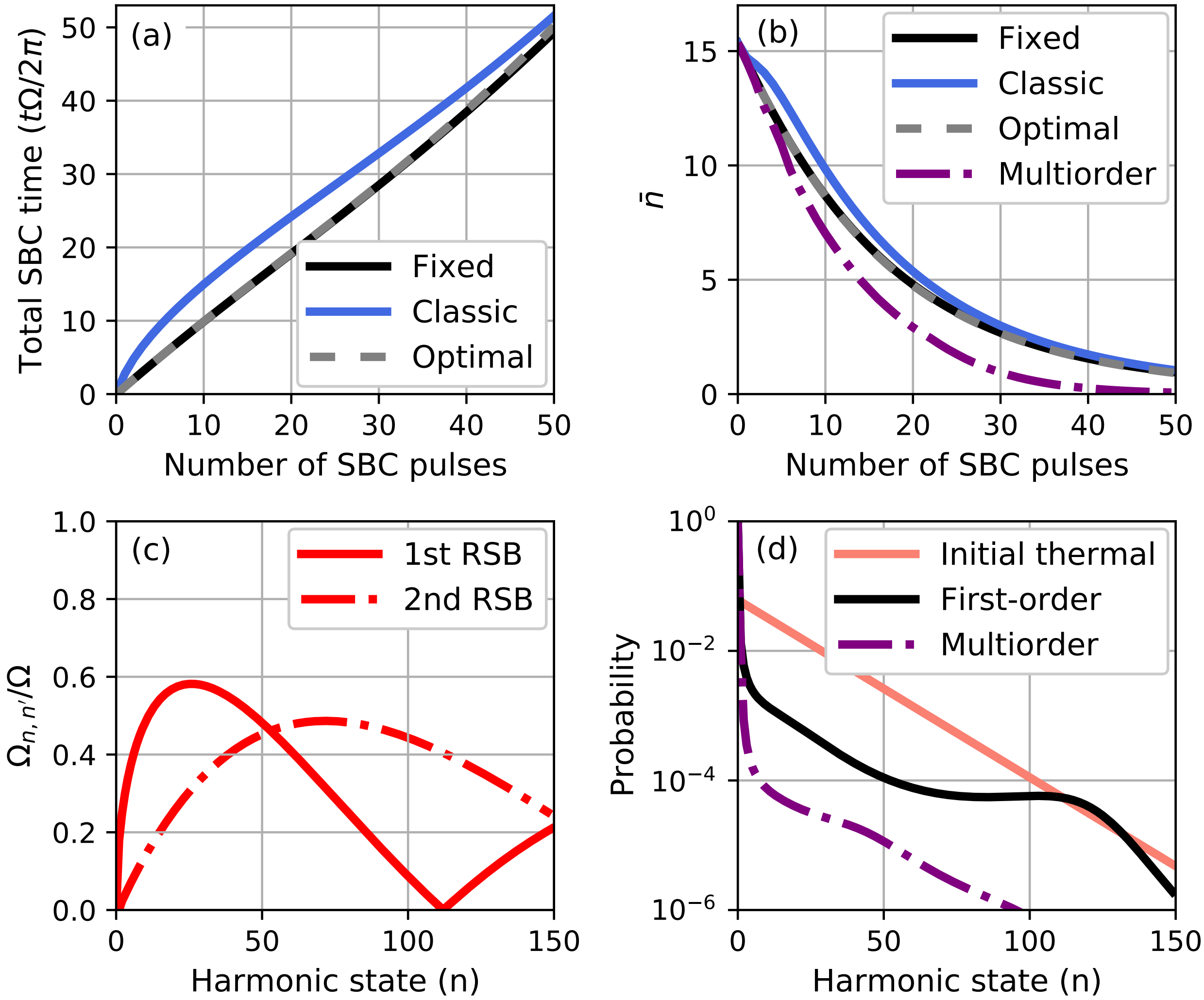

Figure 5.3: The classic, fixed, optimal, and multiorder protocols are compared for an initial temperature of $\bar{n}_i = 15.36$, and $\eta = 0.18$ (see text for definitions). (a) The total sideband cooling time (excluding optical pumping), and (b) the cooled $\bar{n}$ as a function of the number of SBC pulses. (c) Scaled frequencies for the first-order (solid) and second-order (dash-dot) RSB showing the near-zero frequency of the first-order RSB at $n = 112$. (d) Initial thermal distribution (solid light red) and distributions after 50 pulses of first-order fixed (solid black) and multiorder fixed (dash-dotted purple).

levels with near-zero RSB Rabi frequencies shift to smaller n as η increases, and because larger fractions of the initial population will be trapped at high-n as $\bar{n}_i$ increases.

Multiorder cooling circumvents population trapping since, for different RSB orders, the Rabi frequencies approach zero at different values of n. This is illustrated in Figure 5.3(c), where it can be seen that higher RSB orders exhibit their first zeros at higher values of n. This allows for multiorder pulse sequences which first move population from high- to intermediate-n, then employ first-order pulses to reach the ground state.

The graph-theoretic framework we introduced in Section 5.3.1 can easily incorporate higher-order pulses. For an m^{th} order pulse of time t, the probability of not cooling is $a_n(t) = \cos^2(\Omega_{n,n-m}t/2)$ and is mapped to the diagonal of the weight matrix $W(t)$. Likewise, the probability that the m^{th} order pulse takes $|n\rangle \to |n-m\rangle$ is $b_n(t) = \sin^2(\Omega_{n,n-m}t/2)$ and is mapped to the m^{th} upper diagonal of $W(t)$. Both the fixed and optimal protocols may then be calculated for multiorder cooling once the $W(t)$ matrices are constructed.

We simulate and optimize a multiorder fixed protocol with N_3 third-order pules, N_2 second-order pulses, and N_1 first-order pulses fixing the total number of SBC pulses $N = N_1 + N_2 + N_3$ and allowing the pulse time to vary per order

$$\bar{n}(t_1, t_2, t_3) = \sum_{n=0}^{n_{\text{max}}} n \left[W^{N_1}(t_1) W^{N_2}(t_2) W^{N_3}(t_3) \vec{p}_{\text{th}} \right]_n . \tag{5.10}$$

N_1, N_2, and N_3 were selected by brute force optimization of a block sequence (detailed in the next paragraph). Figure 5.3(b) shows multiorder cooling (dash-dotted purple) working significantly faster than the optimal first-order method, cooling from $\bar{n}_i = 15.36$ to a final $\bar{n} = 0.06$ after only 50 pulses. In addition, the multiorder protocol avoids the high-n population trapping present in the first-order sequences. This can be seen in Figure 5.3(d), where population is much more efficiently transferred from high-n to low-n when multiorder pulses are used.

Multiorder cooling introduces further optimization and experimental challenges. For an N pulse SBC protocol that includes k_m pulses of order m, there are a factorial number of permutations

$(N!/\prod k_m!)$ in which the pulse orders may be sequenced, and an exponential number of $\{k_m\}$ choices which satisfy $\sum k_m = N$. For small numbers of pulses ($N \lesssim 20$), we used a brute force computation to conclude that a "block" sequence is best: all k_m pulses of the same order m stay together in a "block," and higher-order m blocks are applied before lower orders. Under this restriction, the number of possible sequences becomes polynomial in the number of applied orders m, scaling as $\mathcal{O}(N^{m-1})$.

In practice, applying pulses with arbitrarily high orders is not experimentally feasible. Transition linewidths narrow for higher orders, making resonant excitation difficult. In addition, transition rates decrease, making pulse times impractically long (Equation 5.3). In our experimental demonstration (Section 5.5), we reliably address RSB transitions up to 3rd order. If higher RSB orders are needed, but not possible to apply, alternation between lower orders may still remove trapped population [73] at the cost of longer pulse sequences.

5.4 Thermometry of Sideband Cooled Distributions

In the quantum regime, full ion thermometry requires knowledge of the probabilities $p(n)$ for occupying each harmonic level n, so that the average occupation $\bar{n} = \sum np(n)$ may be calculated. Given the impracticality of measuring dozens or hundreds of probabilities $p(n)$ to high accuracy, thermometry techniques must make assumptions about the underlying distribution $p(n)$. The most common one is to assume that $p(n)$ is thermal, in which case $\bar{n}$ may be extracted by taking the ratio of first-order RSB and BSB transition probabilities [59]. However, Section 5.3 and Figure 5.3(d) demonstrated that sideband-cooled ions can have dramatically non-thermal distributions $p(n)$, depending on the cooling protocol, the number of RSB orders, and the number of cooling pulses. Thus common ion thermometry methods may give widely inaccurate results following extensive sideband cooling, motivating development of a new approach.

In this section, we begin by outlining two common ion thermometry methods, their underlying assumptions, and the reasons they fail to correctly measure ion temperatures following significant sideband cooling. We then introduce a new technique for ion thermometry which has been specifically tailored to reveal ion temperatures after sideband cooling and depends only on the time-averaged value of RSB transitions.

5.4.1 Existing Methods

Nearly all experiments measuring trapped-ion temperatures deep in the quantum regime follow the approach used in Ref. [59], which we call the “ratio” method. The ion is first initialized in the state $|{\downarrow}\rangle$, and the first-order red and blue sidebands are then driven with the same power for the same time. If the ion motional distribution is thermal, then the ratio of RSB to BSB transition probabilities can be related to the average harmonic level occupation $\bar{n}$ (Appendix C):

$$r \equiv \frac{P_{\uparrow}^{\mathrm{RSB}}(t)}{P_{\uparrow}^{\mathrm{BSB}}(t)} = \frac{\bar{n}}{\bar{n}+1}. \tag{5.11}$$

This ratio r may be experimentally determined by fitting absorption lineshapes to frequency scans over the red and blue sidebands (as in [59]), or by driving red and blue sidebands on resonance and taking the ratio of the resulting time series.

The ratio method is powerful due to its direct dependence on $\bar{n}$ and experimental ease. However, the ratio method relies on the assumption of a thermal harmonic distribution which is inherently mismatched to the motional distribution of ions following significant sideband cooling (see Figure 5.3(d)). As we will show in Section 5.5, this assumption can lead to an order-of-magnitude underestimate of the final $\bar{n}$ after only moderate sideband cooling.

When the underlying motional distribution is known to be non-thermal, alternative thermometry methods may provide a better estimate of $\bar{n}$. One popular method performs a frequency-domain analysis of a BSB Rabi oscillation, using singular value decomposition (SVD) to extract the harmonic level probabilities $p(n)$ [66]. In this method, a BSB oscillation is described as a matrix of transition probabilities $b_n(t_i) = \sin^2(\Omega_{n,n-1}t_i/2)$ acting on the level probability vector $\vec{p}$ to yield the measured fluorescence at each timestep t_i. SVD is then used to pseudo-invert the transition probability matrix and isolate the vector of $p(n)$’s (see Appendix B for more detail). This technique has been successfully implemented to measure $\bar{n}$ for both thermal states as well as coherent states [66].

Although SVD is a flexible method for measuring $\bar{n}$ in non-thermal distributions, there are several drawbacks. First, data acquisition can take a long time since long-oscillation time series are necessary to accurately determine as many harmonic state probabilities as possible. This is further compounded by the need to perform many thousands of repetitions to keep quantum projection noise low and avoid potential overfitting during the SVD. Additionally, the output probabilities from SVD have no physical boundary constraints such as $0 \leq p(n) \leq 1$ or $\sum p(n) = 1$. This has been found to produce large errors when applied to distributions with many non-negligible probabilities at high harmonic level n [66], as is the case for the distributions shown in Figure 5.3(d).

5.4.2 Modeling Post-SBC Distributions

The primary reason that the ratio and SVD methods fail to accurately estimate $\bar{n}$ following SBC is that they are not well-matched to the motional state distributions shown in Figure 5.3(d). After SBC, the largest contributions to $\bar{n}$ are often driven by the residual population remaining at large n, which is neglected when using a simple thermal approximation or when focusing on only the low-n populations. Thus, improved modeling of the probability distribution $p(n)$ following SBC is a prerequisite for higher-accuracy estimation of ion temperatures.

To date, the most detailed modelling of post-SBC motional distributions was outlined in [67]. Using simulated multi-order SBC pulses, it was found that the harmonic level populations were well-approximated by a double thermal distribution:

$$p_{\text{double}}(n) = \alpha p_{\text{th}}(n|\bar{n}_l) + (1-\alpha)\, p_{\text{th}}(n|\bar{n}_h) \tag{5.12}$$

where $\bar{n}_l$ captures the distribution for low n states, $\bar{n}_h$ captures the distribution for high n states, and the total average occupation is $\bar{n} = \alpha\bar{n}_l + (1-\alpha)\bar{n}_h$. Our numeric simulations of multiorder SBC in Figure 5.3(d) likewise demonstrate that the final state populations are well-described by this double-thermal model. In [67], $\bar{n}$ was experimentally determined by first fitting the simulated distribution to extract $\bar{n}_h$, then fitting the experimental data to Equation 5.12 with $\bar{n}_h$ as a fixed parameter.

Here, we seek to generalize Equation 5.12 and develop a measurement protocol that avoids dependence on numeric simulations. To begin, we propose direct measurement to find the harmonic level populations $p_{\text{meas}}(n)$ up to $n = k$, where $k > \bar{n}_l$. Using this, we compute the remaining population fraction in all levels $n > k$:

$$p_{\text{rem}}(n > k) = 1 - \sum_{n=0}^{k} p_{\text{meas}}(n). \tag{5.13}$$

Next, we propose direct measurement of the initial thermal state $\bar{n}_i$ before SBC, which we identify as $\bar{n}_h$ in Equation 5.12. Once again the quantity $p(n > k)$ is calculated, this time for the initial thermal distribution

$$p_{\text{th}}(n > k) = \sum_{n=k+1}^{\infty} \frac{\bar{n}_i^n}{(\bar{n}_i + 1)^{n+1}} \tag{5.14}$$

The ratio of Eqns. 5.13 and 5.14 estimates the fraction of states remaining in an approximate thermal distribution of average occupation $\bar{n}_i$. The final $\bar{n}$ is then estimated as

$$\bar{n} \approx \sum_{n=0}^{k} n p_{\text{meas}}(n) + \frac{p_{\text{rem}}(n > k)}{p_{\text{th}}(n > k)} \sum_{n=k+1}^{\infty} n \frac{\bar{n}_i^n}{(\bar{n}_i + 1)^{n+1}}. \tag{5.15}$$

The advantage of Equation 5.15 is that it leverages the most information available from measurement with no direct dependence on simulation. The only remaining element needed is a robust method to measure the individual probabilities of the low-lying harmonic levels, $p(n \leq k)$. In the following section, we introduce a simple technique that reveals these desired motional state populations.

5.4.3 Time-averaged Thermometry

We propose a "time-average" measurement protocol which, when combined with Equation 5.15, provides a high-accuracy estimate of $\bar{n}$ following SBC. This approach is constructed to measure the individual probabilities of the first few harmonic levels. Suppose a trapped ion is initialized in the state $|{\downarrow}\rangle$. Then, the expected probability of finding the ion in the $|{\uparrow}\rangle$ state when driven with an m^{th} order RSB is given by:

$$P_{\uparrow,m}^{\text{RSB}}(t) = \sum_{n=0}^{\infty} \frac{1}{2}\left[1 - e^{-\gamma t}\cos(\Omega_{n+m,n}t)\right] p(n+m). \tag{5.16}$$

where no assumptions have been made about the probability distribution $p(n)$, and decoherence effects at rate γ have been included for generality.

The running time average of Equation 5.16 is

$$\begin{aligned}\bar{P}_{\uparrow,m}^{\text{RSB}}(t) &= \frac{1}{t}\int_0^t P_{\uparrow,m}^{\text{RSB}}(t')dt' \\ &= \frac{1}{2}\sum_{n=0}^{\infty} p(n+m)\left[1 - \frac{\gamma}{\left(\Omega_{n+m,n}^2 + \gamma^2\right)t}\right. \\ &\left.+\frac{e^{-\gamma t}(\gamma\cos(\Omega_{n+m,n}t') - \Omega_{n+m,n}\sin(\Omega_{n+m,n}t))}{\left(\Omega_{n+m,n}^2 + \gamma^2\right)t}\right].\end{aligned} \tag{5.17}$$

We observe that for long times ($t \gg 1/(\Omega_{n+m,n}^2 + \gamma^2)$), the time average converges to a partial sum of motional state probabilities

$$\bar{P}_{\uparrow,m}^{\text{RSB}}(t) \approx \frac{1}{2}\sum_{n=0}^{\infty} p(n+m). \tag{5.18}$$

To extract the individual harmonic probabilities, consider driving with a first-order RSB:

$$\begin{aligned}\bar{P}_{\uparrow,1}^{\text{RSB}}(t) &\approx \frac{1}{2}\sum_{n=0}^{\infty} p(n+1) \\ &\approx \frac{1}{2}\left[1 - p(0)\right]\end{aligned} \tag{5.19}$$

from which $p(0)$ can be directly estimated

$$p(0) \approx 1 - 2\bar{P}^{\mathsf{RSB}}_{\uparrow,1}(t). \tag{5.20}$$

Higher harmonic state probabilities may then be estimated by driving with sequentially higher-order RSBs and applying the recursion relation

$$p(m-1) \approx 2(\bar{P}_{\uparrow,m-1} - \bar{P}_{\uparrow,m}). \tag{5.21}$$

This time-average approach provides an efficient and robust method for extracting motional state populations. Compared with existing methods, relatively few points are needed to determine the time average of the RSB oscillation. Although these points should be taken at long times (relative to the RSB Rabi frequency), we note that Equation 5.18 does not depend on the decoherence rate γ, and indeed converges *faster* when decoherence is included. Rather, we anticipate that the largest errors in time-average measurements will arise from real-time changes in $p(n)$ driven by motional heating. Such trap heating effects have been comprehensively studied [65] and can be incorporated into the motional state analysis if needed.

5.5 Experimental Results

In this section, we experimentally demonstrate the effectiveness of our time-averaged thermometry method. We begin by measuring the temperature of a trapped ion following Doppler cooling and comparing the time-average method to several existing techniques. We then repeat our measurements and comparisons using an optimized sideband cooling sequence from Section 5.3, finding that the time-average method most closely agrees with theory predictions.

Thermometry experiments are performed on a single $^{171}\mathrm{Yb}^+$ ion confined in the rod-style Paul trap described in Section 3.2.1, with axial frequency $\omega_z = 2\pi \times 0.670 \pm 0.008$ MHz. In our setup, the Lamb-Dicke parameter $\eta = 0.18 \pm 0.01$, the Rabi carrier frequency $\Omega = 2\pi \times 64.9 \pm 0.5$ kHz, and the optical pumping time is $5\ \mu$s. Doppler cooling is performed with 369.5 nm light along the ${}^2S_{1/2}|F = 0\rangle \rightarrow {}^2P_{1/2}|F = 1\rangle$ and ${}^2S_{1/2}|F = 1\rangle \rightarrow {}^2P_{1/2}|F = 0\rangle$ transitions (linewidth $\Gamma = 2\pi \times 19.6$ MHz), while red and blue sideband transitions are performed with far-detuned Raman beams at 355 nm. After each experiment, the qubit state is determined by irradiating the ion with 369.5 nm light resonant with the ${}^2S_{1/2}|F = 1\rangle \rightarrow {}^2P_{1/2}|F = 0\rangle$ transition and capturing the spin-dependent fluorescence on a photomultiplier tube.

5.5.1 Thermal Distribution

When an ion is cooled to its Doppler-limited temperature, the motional state is well-characterized by a thermal distribution (Equation 5.2). Given our axial trap frequency, this temperature corresponds to an average harmonic occupation $\bar{n}_{\text{Dop}} = 14.6 \pm 0.2$ (Equation 5.1). We take this value as the theoretical prediction, against which we compare several different methods for trapped-ion thermometry.

We begin by using the ratio method to estimate the Doppler-cooled ion temperature. Figure 5.4(a)-(b) show frequency scans over the red and blue sidebands, respectively, with error bars smaller than the size of the markers. Sinc squared functions are fit to the data with excellent agreement and shown as solid lines. Taking the ratio of the RSB and BSB transition strengths (Equation C.3) yields $\bar{n}_{\text{ratio}} = 14.3 \pm 1.5$, in good agreement with the Doppler-limited prediction.

Two additional estimates of the Doppler-limited temperature may be extracted by driving a first-order BSB oscillation. In the first method, the data is fit to a thermally-weighted Rabi oscillation $P_{\uparrow}^{\text{BSB}}(t) = \sum_{n=0}^{800} p_{\text{th}}(n) \sin^2(\Omega_{n,n+1}t/2)$, shown as the solid light blue curve in Figure 5.4(c). This single-parameter fit finds an estimated $\bar{n}_{\text{thermal fit}} = 14.9 \pm 0.7$. Using the same BSB data set, we also employ the SVD method to estimate $\bar{n}_{\text{SVD}} = 16.4 \pm 2.1$. In Figure 5.4(c), the dashed black curve is calculated by weighting a BSB oscillation function $P_{\uparrow}^{\text{BSB}}(t) = \sum_{n=0}^{n_{\text{SVD}}} p_{\text{SVD}}(n) \sin^2(\Omega_{n,n+1}t/2)$ with the SVD-computed probabilities $p_{\text{SVD}}(n)$.

Finally, the first (dark green) and second (dark purple) RSBs are driven over a long period of time, with their respective running time averages (light green and light purple) shown in Figure 5.4(d)-(e). We take an excess of data points in our demonstration to confirm the accuracy of

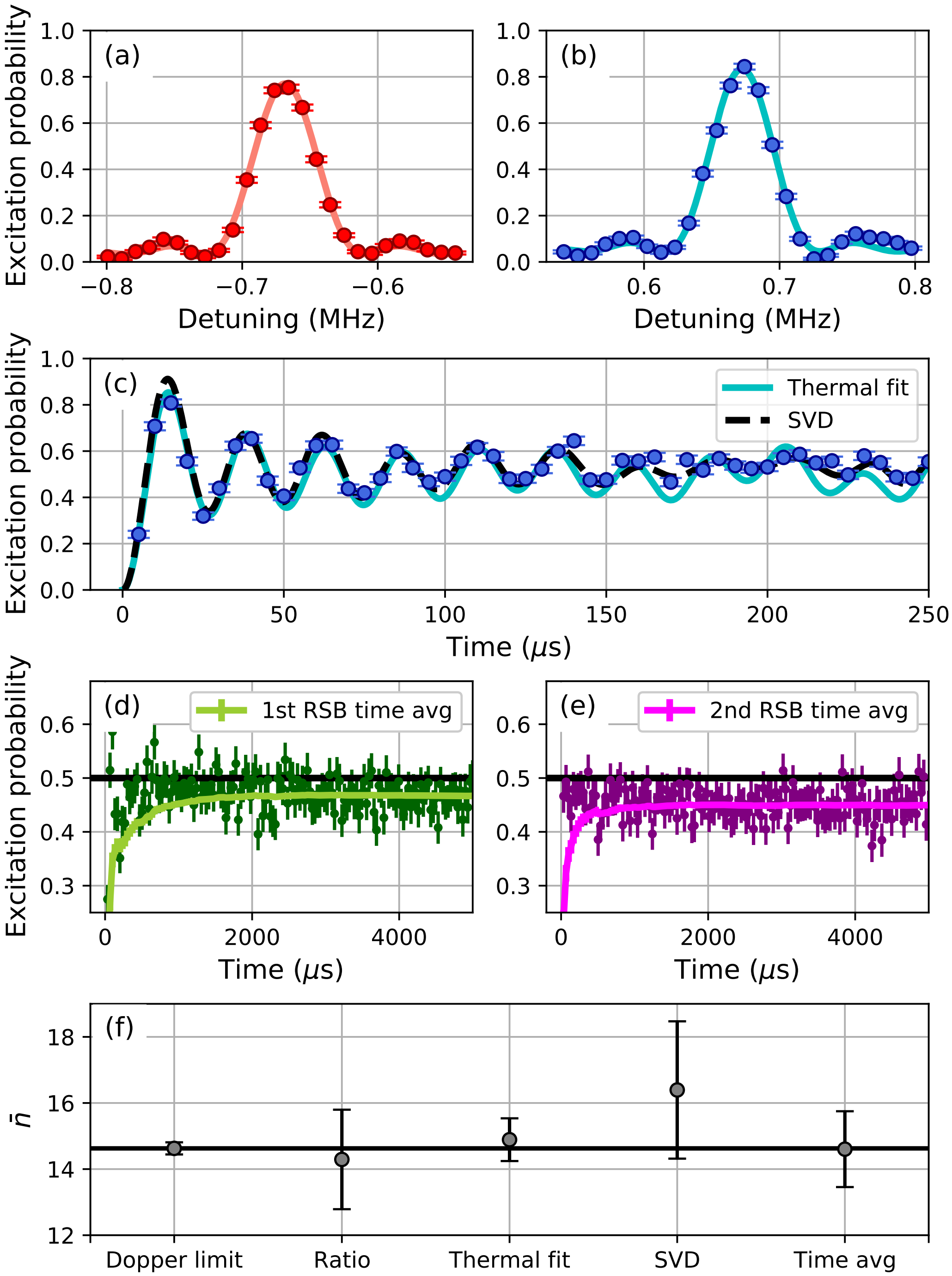

Figure 5.4: Thermometry comparisons of thermally-distributed ion motional states. (a) and (b) are red and blue sideband frequency scans used to determine $\bar{n}$ from the ratio method. (c) shows BSB Rabi oscillation data (blue points) fit by both a thermally-weighted Rabi oscillation function (solid blue) and a SVD analysis (dashed black). (d) and (e) are long Rabi oscillations of the first- and second-order RSBs, respectively, with their running time-average values shown as solid lines. (f) compares these different thermometry methods against the calculated Doppler cooling limit of $\bar{n}_{\text{Dop}} = 14.6$.

this new technique, though we note that only ~ 20 data points at long times are needed to find the same $\bar{n}$ to within 5%. From the first-order RSB time average in Figure 5.4(d), we estimate $p(0)$ using Equation 5.20. Using the second-order RSB time average in Figure 5.4(e) and the value for $p(0)$, $p(1)$ may be obtained from Equation 5.21. Finally, fitting $p(0)$ and $p(1)$ to a thermal distribution yields $\bar{n}_{\text{time avg}} = 14.6 \pm 1.2$.

All extracted values of $\bar{n}$ are compared to the Doppler-limited prediction in Figure 5.4(f). We conclude that all approaches studied here are viable methods for extracting the average harmonic occupation $\bar{n}$ when applied to thermal distributions. In the following subsection, we will re-apply these measurement techniques to sideband cooled ions, whose motional distributions are predicted to be significantly non-thermal.

5.5.2 Sideband Cooled Distribution

In this set of experiments, the ion is initially cooled to the Doppler limit of $\bar{n} = 14.6$, then further cooled using 25 first-order fixed SBC pulses (see Section 5.3.2). As shown in Figure 5.3(b), this small number of pulses cannot reach the ground state using any SBC protocol when starting from such a large initial $\bar{n}$. Nevertheless, we will show that 25 SBC pulses is already sufficient to induce large discrepancies between different thermometry techniques.

The inherent nonthermal distribution of the sideband cooled ion is predicted to cause a significant bias in the ratio method's estimation of $\bar{n}$. Figure 5.5 illustrates this point for the given experimental parameters. In Figure 5.5(a), a simulated distribution after 25 first-order fixed SBC pulses (solid) is compared to a thermal distribution with the same $\bar{n}$ (dashed). The wide discrepancy indicates that a thermal state is a poor approximation for the post-SBC distribution.

To quantify the potential error in assuming a thermal distribution, Figure 5.5(b) compares the $\bar{n}$ of the simulated distribution (solid) to the predicted result from the ratio method (dashed). The ratio method drastically underestimates $\bar{n}$ after just a few pulses, with almost a full order of magnitude difference by 25 pulses. We caution that when ratio-method thermometry is applied after significant SBC, it may result in misleadingly low estimates of ion temperatures and motional

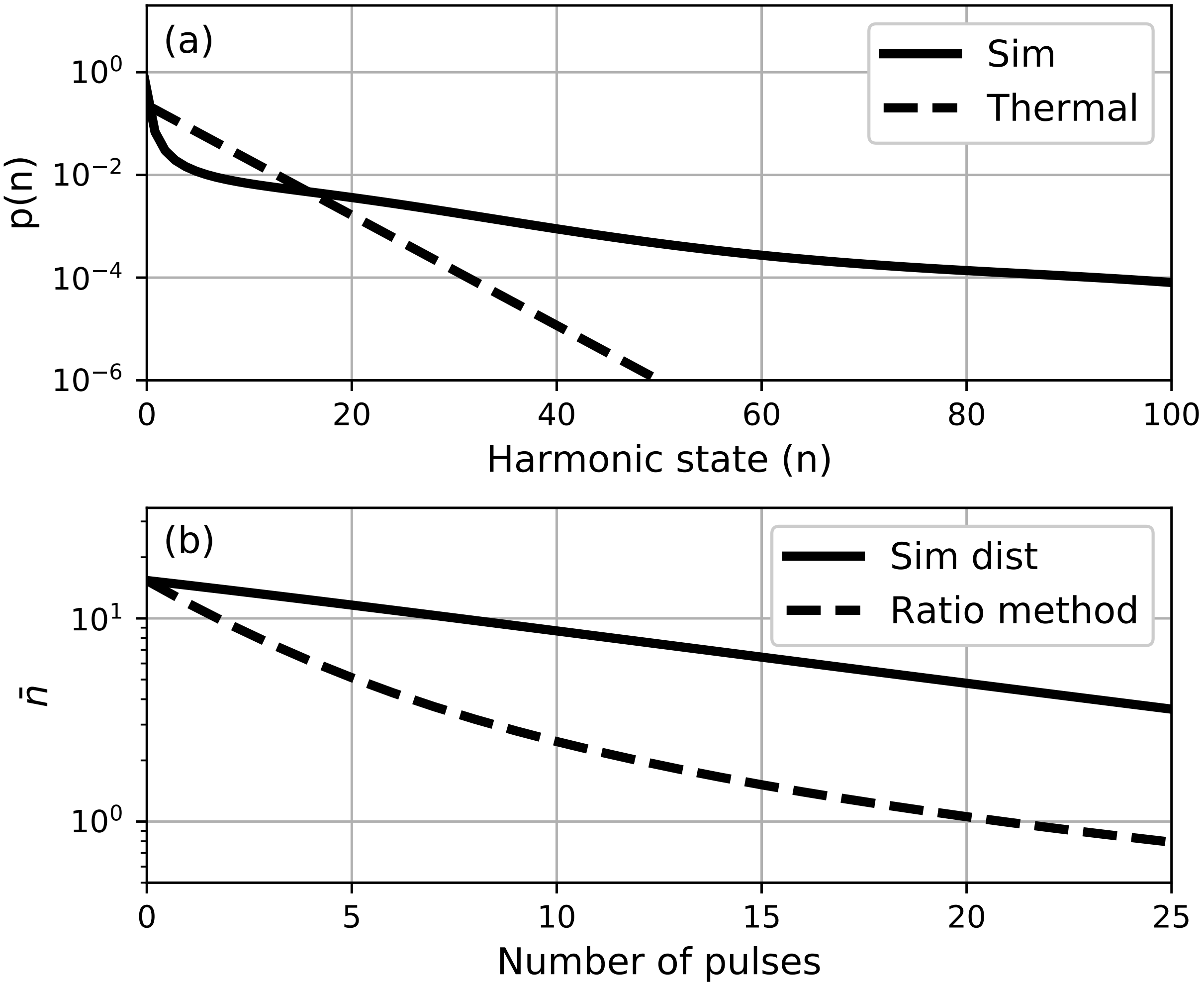

Figure 5.5: (a) Simulated motional state distribution after 25 first-order fixed pulses (solid), and a thermal distribution with the same $\bar{n}$ (dashed). (b) For any number of SBC pulses, the estimated $\bar{n}$ from the ratio method (dashed) is predicted to significantly underestimate the true $\bar{n}$ as calculated from the simulated distribution (solid).

heating rates.

Following SBC, we show the Rabi oscillations of first-order red and blue sidebands in Figure 5.6(a). The data points are connected (not fitted) to guide the eye, and errors at each point are the size of the marker. Under the assumptions of the ratio method, the ratio of the RSB to BSB at any point in the time provides a valid estimate of $\bar{n}$. We have calculated this ratio for all points in Figure 5.6(a), and have plotted the corresponding $\bar{n}$ in Figure 5.6(b).

For thermal distributions, as assumed by the ratio method, $\bar{n}$ should be constant at all times. In Figure 5.6(b), the substantial differences in extracted $\bar{n}$ with time provide experimental evidence that the underlying state distribution is nonthermal. To estimate $\bar{n}$ in Figure 5.6(b), we average over the varying $\bar{n}$ to find $\bar{n}_{\text{ratio}} = 0.58 \pm 0.56$. This value is a drastic *underestimate* of the predicted value $\bar{n}_{\text{sim}} = 3.57 \pm 0.58$, by almost a full order of magnitude. Furthermore, the simulated $\bar{n}$ does not account for ion heating or noise effects, which if included would make the discrepancy even larger.

Next, we applied a SVD analysis to the first-order BSB in Figure 5.6(a). Since the tail of the SBC distribution is predicted to be long, we chose the length of the level probability vector $\vec{p}$ to maximize the number of physically constrained probabilities, $0 \leq p(n) \leq 1$. Nevertheless, the BSB time-series data remained poorly fit for any length of $\vec{p}$, and the most accurate SVD result ($\bar{n}_{\text{SVD}} = 8.0 \pm 1.3$) still significantly disagrees with the simulated average harmonic occupation.

Lastly, we apply our time-average measurement technique to a sideband cooled ion. We begin by driving the the first (dark green), second (dark purple), and third (dark orange) RSBs for a long time period, as shown in Figure 5.6(c)-(e). Following the time average procedure outlined in Section 5.4.3, $p(0)$, $p(1)$, $p(2)$, and $p(n > 2)$ are estimated from the measured time averages. Substituting these probabilities into Equation 5.15 results in a measured $\bar{n}_{\text{time avg}} = 4.1 \pm 0.7$.

The estimated level distributions from the simulation, time average method, and SVD method are compared in Figure 5.6(f). The numerically simulated distribution (black) follows a monotonic decrease in population for increasing n. The time average method (blue) finds similar monotonic behavior, with a relative excess of population in the $n = 1$ and $n = 2$ levels which we attribute

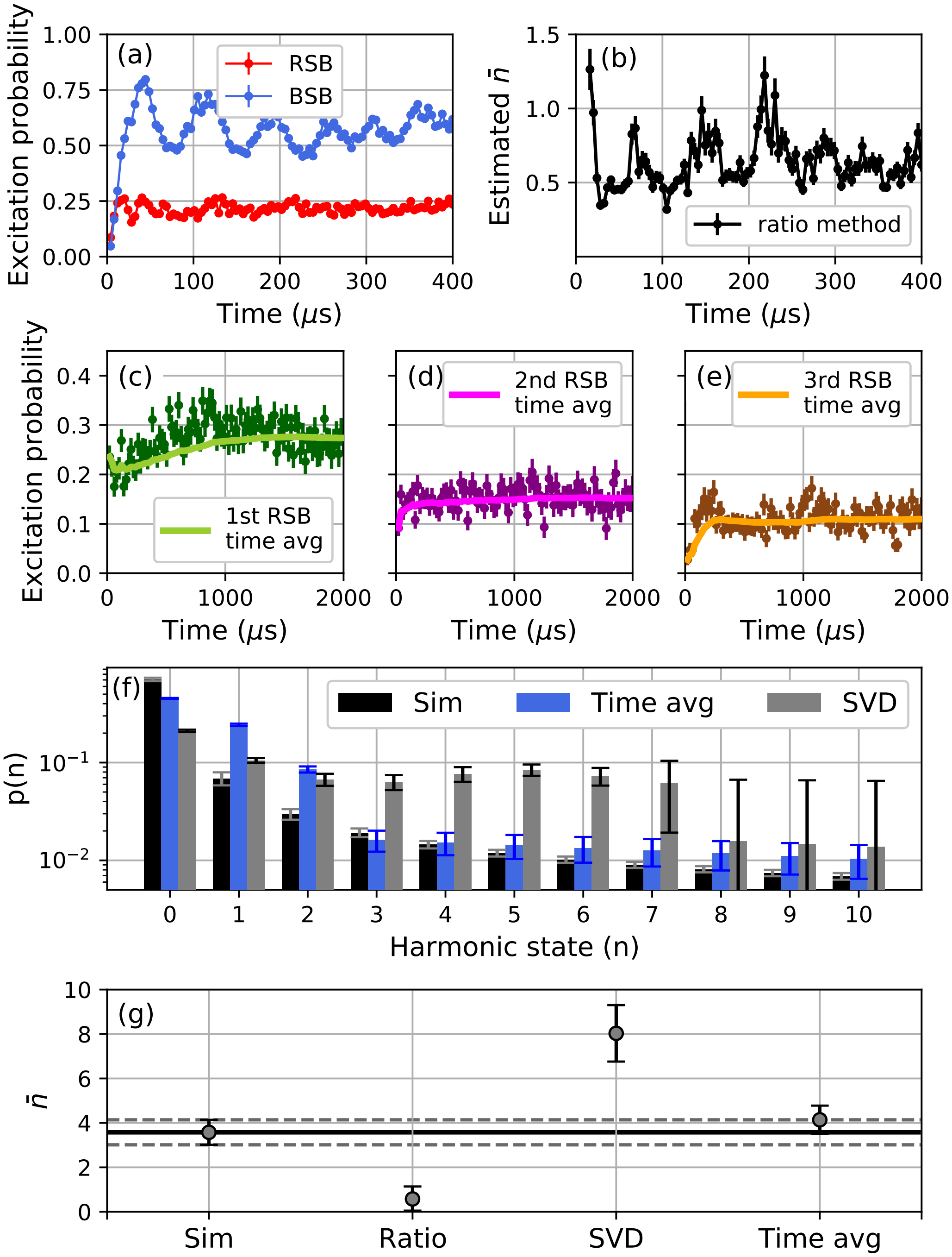

Figure 5.6: Thermometry comparisons of a sideband cooled ion. (a) the measured first-order RSB and BSB time series. Points are connected to guide the eye. (b) $\bar{n}$ estimation at each time point using the ratio method (excluding the first few time steps). (c)-(e) long-time Rabi oscillations for the first, second, and third RSBs, respectively, with their running time averages drawn as solid lines. (f) population distributions as estimated by numeric simulation (black), time-averaged method (blue), and SVD (gray). (g) $\bar{n}$ measurements from the ratio method, SVD, and the time-average method are compared to a numeric simulation of SBC. Only the time-average method closely estimates $\bar{n}_{\text{sim}}$.

to ion motional heating out of the $n = 0$ state [65]. In contrast, the distribution estimated by the SVD method (gray) is non-monotonic and exhibits a steep drop-off in population between $n = 7$ and $n = 8$, suggesting unphysical behavior which cannot be explained by standard heating models [65]. Of all the considered thermometry techniques, the time average method best matches the simulated level distributions, and it is the only method that does not significantly disagree with the simulated prediction $\bar{n}_{\text{sim}}$ (Figure 5.6(g)).

5.6 Conclusion

Sideband cooling has been a popular and powerful technique for the near ground-state preparation of trapped ions. Yet, historical approaches to SBC can be made more efficient, and the measurement of cooled ion temperatures can be performed with less error. In this work, we have shown how to calculate the optimal pulsed SBC protocol for any experimental setup characterized by a cooling laser geometry and wavelength, an ion wavepacket width (which depends upon the ion mass and trap frequency), and an initial ion temperature (which depends on the trap frequency and atomic linewidth). We have additionally argued that careful understanding of the expected state distributions is a necessary precondition for accurate thermometry.

Our efficient numeric simulations and optimizations were enabled by expressing pulsed SBC within a graph-theoretic framework. This approach is powerful for optimizing SBC pulse sequences, and is particularly important in regimes with high Doppler-limited initial temperatures $\bar{n}_i$, or extended ion wavepackets (which correspond to a large η). We observe that repeated SBC pulses with a single optimized time perform nearly-identically to fully-optimized pulse sequences, while traditional protocols were the least efficient per pulse and per unit time. We have likewise introduced a new thermometry technique which more closely models the state distribution after SBC, and experimentally validated its performance. In contrast, we observe that the most common measurement technique can severely underestimate ion temperatures if extensive SBC is performed.

In future work we anticipate that the graph representation of pulsed SBC may be expanded to include noise models for ion heating, decoherence, off-resonant couplings, and effects of rf-driven micromotion. Such additions could be smoothly incorporated into the matrix formalism and would allow for further SBC optimization in the face of realistic experimental imperfections. Extension to multiple ions and multiple modes is another natural direction that fits nicely within the matrix representation of pulsed SBC.

Finally, the time-average technique can open new possibilities for improved thermometry. With this method, for instance, it should be possible to probe the time-dependent population dynamics of trapped-ion motional states and observe how the harmonic level distribution changes in response to external noise sources. Such experiments would provide an additional set of characterizations which may help elucidate mechanisms responsible for anomalous ion heating.

CHAPTER 6

SUSCEPTIBILITY OF TRAPPED-ION QUBITS TO LOW-DOSE RADIATION SOURCES

6.1 Section Overview

Understanding the degree to which radiation-induced errors arise in ion-trap processors will be crucial for mitigating potential failure mechanisms of trapped-ion quantum protocols. Recently, experiments with superconducting qubits have found that ionizing radiation from small-scale sources [80] and from cosmic rays [81] can limit the qubit coherence times and destroy quantum information stored throughout the chip. In both cases, it is believed that ionizing radiation generates phonons in the chip substrate, breaking Cooper-paired electrons and producing large quasiparticle densities which lead to qubit decoherence [82, 83]. Since such radiation events may lead to widespread correlated errors between qubits, they may be difficult or impossible to correct using standard fault-tolerant methods [84].

To date, no comparable studies of radiation effects have been performed using trapped-ion quantum processors. Although Cooper-pair breaking and quasiparticle generation are not applicable to ion-based qubits, ions may instead be susceptible to alternative radiation-induced effects. For instance, most ionizing radiation contains enough energy to increase the charge state of trapped ions and thereby destroy the qubit [85]. Even if the qubit survives, the presence of high-energy x-ray or γ photons may induce Stark shifts [86] or energy level fluctuations which reduce the qubit coherence time. Furthermore, high-energy radiation has the potential to ionize background gases or release adsorbed atoms and photoelectrons from the vacuum chamber walls [87], which may lead to increased collisions or motional heating of the ions.

In this chapter, we study the effects of low-dose radiation on trapped-ion qubits. We first expose an ion-trap apparatus to an array of laboratory-scale α, β and γ radiation sources to observe whether the ion trapping lifetime is reduced. In the presence of those same sources, we next set limits on the changes in qubit coherence time and single-qubit rotation fidelity during exposure. Finally, we investigate whether low-dose radiation leads to increased motional heating rates of trapped ions. In all cases, our measurements of radiation effects are performed while the ion-trap is in operation, rather than irradiating the trap and testing afterwards.

In Section 6.2 below, we expand on the rod trap used in this work. We describe the α, β, and γ sources integrated with the apparatus and list their activity and estimated irradiance at the ion position. Section 6.3 provides lifetime, coherence time, gate fidelity, and motional heating rate results, and concluding remarks are provided in Section 6.4.

6.2 Experimental Apparatus and Radiation Sources

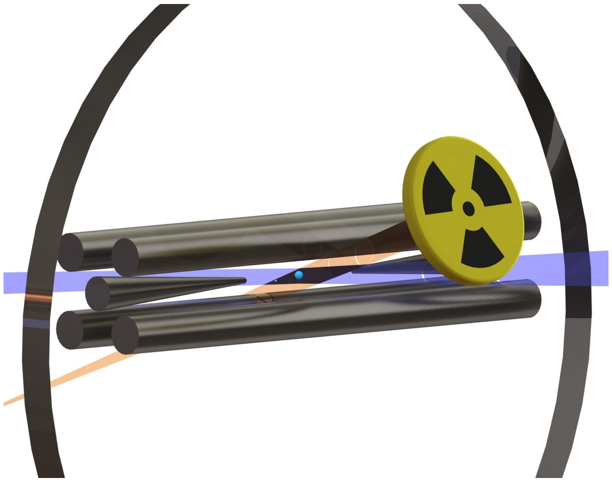

Figure 6.1: Sketch of the experimental arrangement (not to scale). Ions are confined in a “needle”-style RF trap housed inside a vacuum chamber. Laser beams (blue) are used for cooling and state-detection of the ions. Radiation (orange) emanates from a source outside the vacuum chamber and must pass through 4.65 mm of glass before interacting with the ions.

Ions are confined in the rod-style Paul trap described in Section 3.2.1. Typical axial and radial trap frequencies for these experiments are $2\pi \times 390$ kHz and $2\pi \times 720$ kHz, respectively. Vacuum pressures remain below 10^{-10} Torr, and the walls of the vacuum chamber are made from 316L stainless steel, with three Corning 7056 glass viewports providing optical access to the ions. As shown in Fig. 1, radiation must pass through one of the viewports before interacting with the ions. The trapping, cooling, state initialization, and detection processes of the $^{171}\mathrm{Yb}^+$ qubits are all performed using lasers as described in Ch. 3. Qubit state manipulation in these experiments is performed by broadcasting 12.6 GHz radiation, resonant with the qubit state separation, using a microwave horn just outside the vacuum chamber.

We subject the ion trap hardware to an array of α, β, and γ radiation sources. Table 6.1 lists each of the isotopes used in these experiments, along with their radiation type, activity, and primary decay energies. Each source is encapsulated in a 1-inch "button" package, of U.S. Nuclear Regulatory Commission exempt quantity, and is mounted just outside the ion trap vacuum chamber (Fig. 6.1). To reach the ions, the radiation must pass through 45.5 mm of air, 4.65 mm of glass, and 10.5 mm of vacuum.

The presence of the glass vacuum window is expected to cause significant variations in the radiation dose at the ion, depending on the radiation type. For instance, it is known that α-radiation can be stopped by a piece of paper, while thick lead shielding is often required to attenuate γ-rays [87]. Consequently, the source activity alone is not sufficient to determine the radiation dose at the ion; interactions between the radiation and the vacuum window must be considered as well.

We estimate the irradiance at the ion for each source in Table 6.1, which is equivalent to the radiative energy flux passing through the trapping region inside the vacuum chamber. Several different numerical methods were implemented to estimate the attenuation of α, β, and γ particles through the vacuum window. Since α particles are positively charged, we simulated their trajectories using the Monte-Carlo based Stopping and Range of Ions in Matter (SRIM) code [88]. For the decay energies of $^{210}\mathrm{Po}$ and $^{241}\mathrm{Am}$ used in these experiments, a typical α-particle is estimated to penetrate only $\sim 20 - 30$ μm into the 4.65 mm glass window, with negligible probability to pass through the full thickness. Similarly, β-attenuation was estimated using a Monte-Carlo simulation of electrons in solids (CASINO) [89], with non-negligible transmission probabilities found for only the highest-energy β-particles. In contrast, high transmission probabilities were found for γ-rays of the energies used in these experiments, as estimated using the NIST XCOM photon

Table 6.1: Low-dose α, β, and γ sources integrated with the ion trap experimental apparatus. For each source, the activity and primary decay energies are listed, as well as the estimated irradiance at the location of the trapped ion. The presence of the vacuum window between the sources and the trapped ion shields essentially all α particles and most β particles.

Source	**Type**	**Activity**	**Energy (keV)**	**Irradiance (W/m^{-2})**
Polonium-210	α	0.1 μCi	5300	≈ 0
Americium-241	α	1 μCi	5490	≈ 0
Strontium-90	β	0.1 μCi	546	2×10^{-15}
Thallium-204	β	10 μCi	764	2×10^{-8}
Cobalt-60	β, γ	1 μCi	β: 318; γ: 1170, 1330	β: 1×10^{-18}; γ: 2×10^{-4}
Cesium-137	β, γ	5 μCi	β: 512, 1170; γ: 662	β: 4×10^{-7}; γ: 2×10^{-4}
Cadmium-109	γ	10 μCi	88	6×10^{-5}
Barium-133	γ	10 μCi	81, 276, 304, 356, 384	3×10^{-4}

cross-section database [90].

6.3 Results

6.3.1 Lifetime Measurements

As an initial investigation of the effects of radiation on trapped ion qubits, we measure the trapping lifetime of ions exposed to radiation sources. The "ion lifetime" refers to the $1/e$ time for which an ion qubit remains confined within the RF trap in the absence of cooling mechanisms. If radiation induces fast depopulation of the ion trap, it may prove uncorrectable by both standard quantum error-correcting codes [91, 92, 93, 94, 95] or by more specialized codes which account for qubit loss [96, 97].

Although ions have been confined in many systems for months, this requires continuous laser cooling which is forbidden while a quantum computation is in process [98]. Without active cooling, there is the potential for collisions to cause unmitigated ion heating and eventual loss of the qubit. Radiation effects may further increase the local background gas pressure and collision rate, as well as further ionize Yb^{+}, which in both cases would lead to reduced trapping lifetimes.

Our measurements find that ion lifetimes remain in excess of one second when exposed to every source of radiation listed in Table 6.1. For each experiment, one ion is initially Doppler cooled to

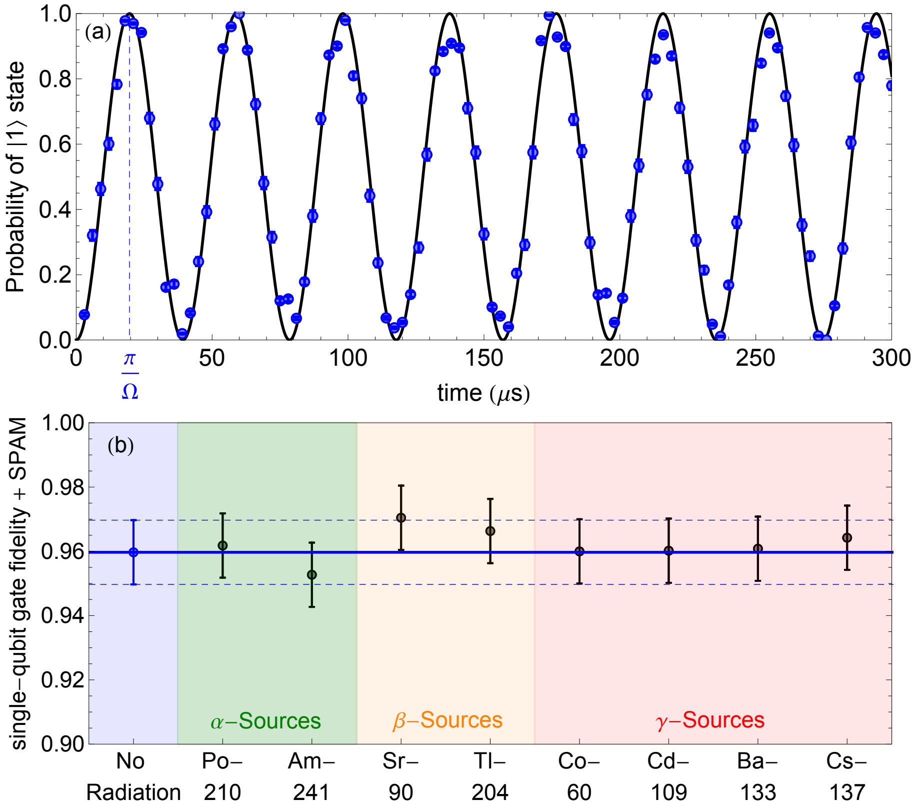

Figure 6.2: (a) Oscillations between qubit states $|0\rangle$ and $|1\rangle$ when driven with microwave pulses at 12.6 GHz, with no radiation present. (b) The single-qubit X-gate fidelities (including all state-preparation and measurement errors) remain unchanged to within experimental error when various types of low-dose radiation are introduced. The blue solid line indicates the results of the control (no radiation) trial; blue dashed lines indicate 1 s.d. statistical measurement uncertainty.

0.5 mK, confined without any cooling for 1 second, then illuminated to confirm its survival in the trap. Each experiment is repeated for 10 trials per data point. The 100% measured survival probability at one second indicates that the true $1/e$ lifetime is longer than one minute in all cases. We note that for ion-trap experiments, one second is already orders of magnitude longer than the typical $\sim 1-10$ millisecond timescales of quantum computation and simulation studies [99, 100].

6.3.2 Coherence time and Single-Qubit Gate Fidelity Measurements

In this next round of experiments, we investigate whether (a) the coherence time of our system is sufficiently long to apply a single-qubit rotation in the presence of radiation, and if so, (b) whether the single-qubit gate fidelity is measurably impacted by the radioactive sources. Radiation-induced Stark shifts have the potential to cause uncontrolled variations in the phase evolution of the quantum bit [86], resulting in lowered T_2 coherence times and gate fidelities. If no decrease in fidelity is observed, then we can simultaneously conclude that (a) the coherence time is sufficiently long for single-qubit gate operations, and (b) radiation does not affect single-qubit rotations to within experimental error.

The single-qubit gates implemented here take the form of rotations around the $\hat{x}$ axis of the Bloch Sphere, $U(t) = e^{-i\sigma_x \Omega t/2}$, where σ_x is the Pauli X matrix and Ω is the Rabi frequency. Rotations are driven using microwaves resonant with the 12.6 GHz frequency splitting between qubit levels. When the qubit is initialized in $|0\rangle$ and microwaves are left on continuously, the qubit state oscillates between the $|0\rangle$ and $|1\rangle$ states at Rabi frequency $\Omega \approx 25$ kHz, as shown in Figure 6.2(a). To estimate the average single-qubit X-gate fidelity, we apply the 12.6 GHz radiation for a time $t = \pi/\Omega$ and measure the population fraction transferred from the $|0\rangle \rightarrow |1\rangle$ state.

As described, such measurements underestimate the true single-qubit gate fidelity since they include the effects of State Preparation and Measurement (SPAM) errors. These errors account include the possibilities that the initial preparation is not purely $|0\rangle$, but contains some small fraction of $|1\rangle$, and that the measurement fidelity of distinguishing $|0\rangle$ from $|1\rangle$ is not 100%. An independent characterization of our total SPAM error yielded $3.3 \pm 1.3\%$, which is the dominant source of infidelity for the measurements in Figure 6.2(b).

The measured single-qubit X-gate fidelities, including SPAM errors, is shown in Figure 6.2(b). Each experimental trial was repeated 10,000 times to keep quantum projection noise errors at the level of $\sim 10^{-2}$. To within experimental error, we observed no radiation-induced change during the combined operations of state preparation, single qubit rotations, and measurement when compared with our control trial. Independently, by performing multiple concatenated $X-$gates, we bound the maximum radiation-induced single-qubit fidelity error (in the absence of SPAM) at the $< 0.3\%$ level. We therefore conclude that (a) the coherence time of the trapped ion remained sufficient for single-qubit gate operations, and (b) if radiation effects were indeed present, they would be well under the $\sim 1\%$ error threshold needed for correction under fault-tolerant schemes.

6.3.3 Heating Rate Measurements

In a final set of experiments, we quantify the effects of radiation on the trapped ion temperature. Quantum entangling operations rely on cooling ions to near their ground state of motion [51], such that their motion is quantized in a global harmonic oscillator potential. Since dissipative cooling is forbidden during quantum gate operations, ion heating during the computation may compromise the overall fidelity [65]. If this heating rate is exacerbated by the presence of radiation, either through direct or induced collisions with background particles or by increased charge fluctuations on nearby surfaces, two-qubit gate fidelities will be negatively affected.

Our measurements of the ion temperature begin by Doppler-cooling the ion to ≈ 0.5 mK. The cooling laser is then turned off, and the ion is allowed to heat for 100 ms (much longer than the typical gate time of an ion-trap quantum computer [99]). Finally, the temperature is re-measured after 100 ms such that the heating rate may be determined. We then repeat this sequence in the presence of all radioactive sources listed in Table 6.1.

Temperature measurements of a trapped ion are performed by observing its fluorescence as a function of detuning δ from resonance (Appendix B). Such resonance lineshapes have two primary contributions. The first is the power-broadened Lorentzian linewidth of the atom, given by $\Gamma' = \Gamma\sqrt{1+s}$, where $\Gamma = (2\pi) \times 19.6$ MHz is the natural linewidth of the Yb$^+$ 369 nm transition, and $s = 0.3$ is the laser saturation parameter used in these experiments. The second major contribution to the linewidth comes from the Doppler-broadened temperature of the ions, which is a Gaussian lineshape with standard deviation $\sigma = \sqrt{k_B T / m\lambda^2}$, where $\lambda = 369$ nm, k_B is Boltzmann's constant, and T is the ion temperature.

Given these two contributions to the linewidth, the fluorescence profile is most appropriately fit to a Voigt function, which is the convolution of a Gaussian lineshape G and Lorentzian lineshape

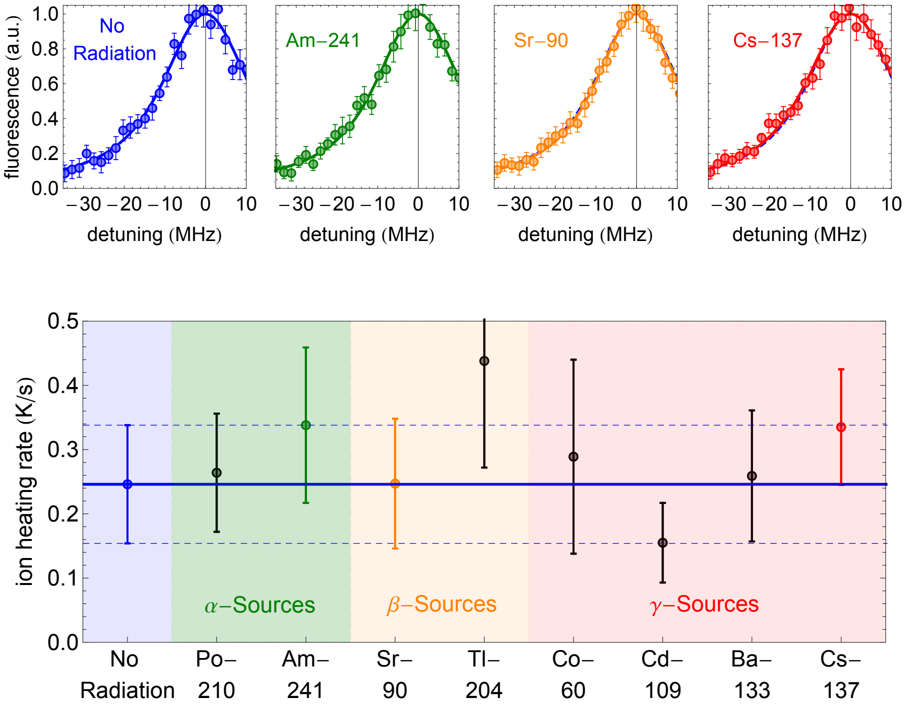

Figure 6.3: (Insets): measured ion fluorescence vs. detuning from resonance. The width of the lineshape determines the ion temperature. (Bottom) The extracted ion heating rates for various radiation sources. No statistically significant deviation in the heating rate is observed compared to the no-radiation case. The blue solid line indicates the results of the control (no radiation) trial; blue dashed lines indicate 1 s.d. measurement uncertainty.

L:

$$V(\delta;\sigma,\Gamma') = \int_{-\infty}^{\infty} G(\delta';\sigma)L(\delta-\delta';\Gamma')d\delta' \tag{6.1}$$

By fitting this lineshape to the measured fluorescence as a function of laser detuning, the only free parameter is the Gaussian width σ which uniquely determines the ion temperature T.

Characteristic lineshapes for the control case (no radiation) and for α, β, and γ sources are shown in the top insets of Figure 6.3. For the no-radiation case, the linewidth yields a fitted temperature of 25 mK after 100 ms of heating, corresponding to a heating rate of 0.25 K/s (6.0 quanta/ms). This lineshape is replicated as a blue dashed line in the other 3 inset panels but is almost entirely covered by the radiation-present data. For each isotope and dose of radiation we have fit a lineshape profile to extract a temperature and heating rate, plotting the summary of results in the bottom panel of Figure 6.3.

We observe no statistically significant increase in the heating rates when the ion trap is irradiated with low-dose α, β, or γ-sources. Likewise, we observe no increase in the background gas pressure at the 10^{-10} Torr level (which would increase the collisional heating rate), nor do we find that the ion shifts position in the trap due to unwanted charge accumulation (which would increase the electric field noise heating rate). We therefore conclude that much higher doses of radiation may be necessary to cause measurable increases in ion heating rates and their associated entangling gate infidelities.

6.4 Conclusion

This work measured the *in-situ* changes in ion-trap qubit lifetimes, coherence times, single-site rotation fidelities, and motional heating rates when exposed to an array of laboratory-scale α, β and γ radiation sources. Since the ion trap was in operation during these measurements, the effects of radiation were tested on the ion qubit and surrounding trap hardware simultaneously. If radiation-induced errors were found to exceed fault-tolerant thresholds, it would indicate serious future challenges for the ability to perform large-scale quantum computations using unshielded ion-trap-based hardware.

For the small-scale doses used in this study, we found no quantifiable degradation of ion-based qubits in the presence of radiation, for any of the measurements performed. This finding is an early first step for demonstrating the long-term prospects of using ion-based quantum information systems in space or other extreme environments. However, exposure to higher-dose sources will be required to fully quantify possible points of failure and guide future design requirements for system shielding. In addition, future work should also more accurately quantify the single-qubit gate errors using randomized benchmarking, and determine whether high-dose radiation induces correlated ion-qubit errors which cannot be easily corrected using standard fault-tolerant protocols.

CHAPTER 7

CHARACTERIZATION OF RADIAL-2D CRYSTALS IN A LINEAR PAUL TRAP

7.1 Section Overview

This chapter details an experimental study of 2D Coulomb crystals in the “radial-2D” phase of a linear Paul trap [37], establishing radial-2D ion crystals as a robust experimental platform for realizing a variety of theoretical proposals in quantum simulation and computation. Section 7.2 provides relevant background on experiments with Coulomb crystals and motivates the study. Section 7.3 describes the trap geometry and identifies a radial-2D crystal as an ion lattice aligned entirely with the radial plane, created by imposing a large ratio of axial to radial trapping potentials. This section contrasts the radial-2D phase with the “lateral-2D” phase which can also be used for quantum simulation.

Section 7.4 demonstrates, using arrays of up to 19 $^{171}\mathrm{Yb}^{+}$ ions, that the structural phase boundaries of radial-2D crystals are well-described by the pseudopotential approximation, despite the time-dependent ion positions driven by intrinsic micromotion. Section 7.5 uses heating rate measurements to observe that micromotion-induced heating of the radial-2D crystal is confined to the radial plane. Here we verify that the transverse motional modes, which are used in most ion-trap quantum simulation schemes, are well-predictable numerically and remain decoupled and cold in this geometry.

7.2 Coulomb Crystals

Over the last decade, one-dimensional (1D) ion chains in RF traps have seen remarkable success in engineering high-fidelity quantum gates [101, 102] and simulating 1D quantum spin systems [9]. If a comparable ability to control and probe two-dimensional (2D) crystals in RF traps can be achieved, then the native 2D interactions between ions would provide an inherent advantage over

1D systems for the quantum simulation of complex 2D materials [27, 26, 25, 23]. In addition, 2D arrays can hold larger numbers of qubits more efficiently than 1D strings, with a higher error threshold for fault-tolerance [28, 29], and may simplify preparations of 2D cluster states for one-way quantum computing [30, 31]. Already, 2D arrays of ions in Penning traps have led to successes in simulating and studying quantum spin models [19, 32], though the fast crystal rotation in such traps poses a significant challenge to individual ion addressing.

Achieving the desired level of control in Coulomb crystals has typically required an initial characterization of ion positions, structural phases, normal mode frequencies, and sources of crystal heating. In this chapter, we report the experimental characterization and coherent control of radial-2D crystals in a linear Paul trap. We map the full range of structural phases for Coulomb crystals as a function of ion number using arrays of up to 19 ions, and we investigate the transverse vibrational mode spectrum in the radial-2D phase. Next, we measure the time-dependent temperature of the crystal as it experiences micromotion-induced heating, and we extract the center-of-mass heating rate along the micromotion-free direction perpendicular to the radial plane. Finally, we discuss the implications for future quantum information processing experiments.

7.3 Two-Dimensional Ion Crystals

7.3.1 Lateral-2D Crystals

In RF traps, there are two distinct methods of orienting an ion lattice: the lateral-2D configuration and the radial-2D configuration. The first orientation is an extension of the well-known "zig-zag" phase, spanning a 2D plane defined by one radial and one axial trap direction. In this case, rf-driven micromotion is present along one of the in-plane directions as well as transverse to the plane. Ion crystals in this phase, which we refer to as the "lateral-2D" geometry, were first realized in RF traps over 20 years ago [103]. More recent work has measured the vibrational spectrum of lateral-2D crystals [104], and further experiments have demonstrated coherent operations in this regime [105].

7.3.2 Radial-2D Crystals

In the “radial-2D” phase, the longitudinal in-plane modes lie along the radial direction and experience micromotion, while the transverse modes lie along the axial direction and remain micromotion-free. This radial-2D phase has been the primary interest for most theoretical studies of 2D ion crystals, which have made predictions of crystal stability, lifetimes, heating rates, phase boundaries, and gate fidelities [27, 26, 25, 106, 107, 28, 29]. Prior to 2021, however, experiments performed with radial-2D crystals had only demonstrated Doppler cooling [108] and probed the radial-2D phase boundary with 3-4 ions [104].

Since lateral-2D and radial-2D crystals have different relative orientations of micromotion with respect to the crystal plane, studies of the structural and dynamical properties of lateral-2D crystals are not directly applicable to the radial-2D regime. There also may be differences in the degree to which micromotion may obscure site-specific imaging resolution, or worse, lead to fast absorption of energy from the RF drive [109, 110, 106] and melting of the ion lattice [111].

7.4 Experimental Setup

Experiments are performed with $^{171}\mathrm{Yb}^+$ ions confined in the four-rod linear Paul trap described in Section 3.2.1. A slight asymmetry is introduced between the radial $\hat{x}$- and $\hat{y}$- directions to prevent a zero-frequency rotational mode; for specificity, we define the radial secular trap frequency as $\omega_r \equiv \mathrm{Max}[\omega_x, \omega_y]$. The RF voltage V_0 is held constant at 340 V throughout experiments, yielding a Mathieu parameter of $q = 0.10$, while the DC voltage U_0 is varied between $0.012 - 30$ V. As the DC voltage is raised, the aspect ratio $\alpha = \omega_z/\omega_r$ increases. At large values of α, ions are squeezed into the xy plane and self-assemble into a triangular lattice.

7.4.1 Raman Spectrosocpy

Raman beam spectroscopy is used for axial mode determination and axial heating rate measurements. The two Raman beams have a frequency difference near the $^{171}\mathrm{Yb}^+$ hyperfine ground state

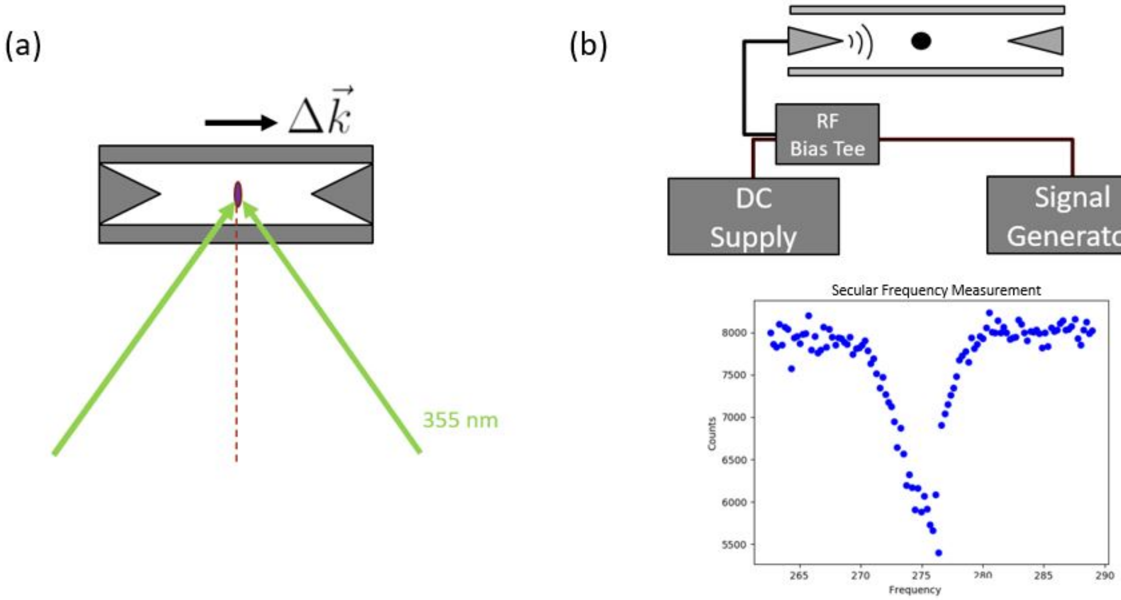

Figure 7.1: (a) Raman beam configuration: two 355 nm Raman beams oriented in the yz plane enter from the front of the trap at 53 degree angles to the left and right of the y axis, creating a resultant k-vector along z. (b) RF is injected onto a DC endcap via a bias tee. Scanning the RF frequency until it is on resonance with the ion's center of mass mode creates a dip in the ion's fluorescence profile, allowing us to find a secular trap frequency accurate to within 1 kHz.

splitting ω_{hf}, with the precise frequencies, amplitudes, and relative phase controlled by AOMs, as described in Chapter 3. Two 355 nm Raman beams oriented in the yz plane enter from the front of the trap, at 53 degree angles to the left and right of the y axis respectively as shown in Figure 7.1(a). In the measurements presented in this chapter, for which $\omega_z = 2\pi \times 900$ kHz, this leads to a dimensionless Lamb-Dicke parameter

$$\eta = 2\sin(53^{\circ})\frac{2\pi}{\lambda}\sqrt{\frac{\hbar}{2m\omega_z}} = 0.16 \tag{7.1}$$

and a resultant wavevector $\vec{k} = \vec{k_2} - \vec{k_1}$ along the axial ($\hat{z}$) direction. For a radial-2D crystal, oriented in the xy plane, this geometry results in strong coupling to the axial (transverse) motional modes and suppression of coupling to the radial (in-plane) modes.

7.4.2 Secular Frequency Determination

Since our Raman beams don't couple to the radial modes, we use RF injection to measure secular frequencies along all three axes [112]. To measure along the $\hat{z}$ axis, we attach an RF bias tee into one of our DC lines and use a signal generator to inject RF jointly with the DC endcap voltage, as shown in Figure 7.1(b). Then we scan the RF frequency until it is on resonance with the ion's center of mass mode and heats the ion, resulting in a dip in collected fluorescence accurate to within a kHz. A second bias tee, in line with a compensation rod, injects RF equally along the $\hat{x}$ and $\hat{y}$ trap directions and is used to perform identical frequency measurements along the radial directions.

7.4.3 Note on Micromotion Amplitude

Critical measurements are performed with crystals of 7, 13, and 19 ions. As the number of ions N grows larger, the outer radius of the crystal scales as $\sim d\sqrt{N}/2$ for ions separated by distance d. The maximum micromotion amplitude therefore also scales with the square-root of ion number, $|\vec{r_1}|_{\text{max}} \sim qd\sqrt{N}/4$ [26]. For a seven-ion crystal with our trap parameters, the outermost ions are approximately 6 μm from the trap center, giving a micromotion amplitude of ≈ 300 nm. For the 13-ion crystals, we find micromotion amplitudes $|\vec{r_1}| \approx 430$ nm, and for the largest examined crystal of 19 ions, we find $|\vec{r_1}| \approx 500$ nm. In each case, we note that the micromotion amplitude is small compared to the 5 μm inter-ion spacing of the crystal.

7.5 Phase Boundaries and Transverse Mode Spectrum

7.5.1 Structural Phase Boundaries

When the aspect ratio $\alpha \equiv \omega_z/\omega_r$ of the trap's axial and radial secular frequencies is small, ions form a 1D chain along the trap's central axis (Figure 7.2(a)). As α is increased (by increasing the axial frequency), the ions pass through a zig-zag phase (Figure 7.2(b)) and a number of three-dimensional (3D) spheroidal configurations (Figure 7.2(c)), before forming a radial-2D crystal.

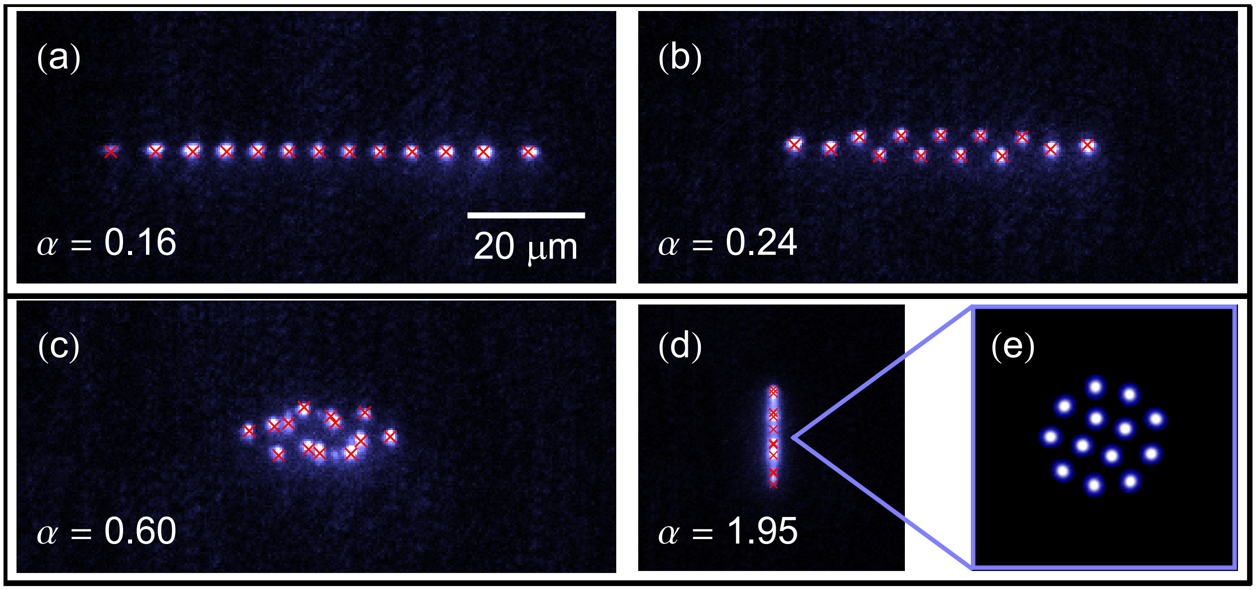

Figure 7.2: Crystals of 13 ions are shown for increasing values of the trap aspect ratio $\alpha \equiv \omega_z/\omega_r$. The structure transforms from a 1D chain (a) to zig-zag (b) and 3D spheroidal phases (c), before ending in a 2D triangular lattice in the radial plane (d). Crosses show the ion positions predicted by the pseudopotential approximation. Panel (e) shows the same calculation as the crosses in (d), rotated to better display the lattice structure. Simulated ion sizes in (e) correspond to the diffraction-limited spot size of our imaging optics and include effects from rf-driven micromotion.

This last configuration occurs in Figure 7.2(d), where the single plane of ions is viewed on-edge. Figure 7.2(e) simulates the same crystal rotated perpendicularly to the plane. For these higher-α phases, ions that lie away from the trap's central axis are subject to rf-driven micromotion, the amplitude of which increases linearly with an ion's radial coordinate. Though the equilibrium ion positions are no longer stationary due to micromotion, the observed time-averaged positions closely correspond to predictions obtained from pseudopotential theory calculations (red crosses in Figure 7.2).

Varying the axial confinement over such a large range enables the precise experimental determination of structural phase transition boundaries at both small and large α, as shown in Figure 7.3(a). Ions starting in a 1D chain exhibit a sudden transition to a zig-zag configuration at a critical value of α dependent on particle number N. The 1D to zig-zag transition only occurs due to non-degenerate radial frequencies and is quite close to the zig-zag to 3D boundary for our near-degenerate trap. Numerous unmapped subtransitions occur within the 3D Coulomb crystal phase;

the richness of 3D geometries that arises with even 3-4 ions is detailed in [104]. Since micromotion plays no role in this transition, numerical estimates of the phase boundary are straightforward [40, 113, 114]. The predicted transition

$$\alpha = \frac{1}{.73N^{.86}} \tag{7.2}$$

has been previously verified with up to 10 ions [115]. Our measurements confirm this behavior for up to 19 ions and are compared to the theoretical prediction (lowest blue dashed line) in Figure 7.3(a).

For the 3D to radial-2D transition, the presence of micromotion complicates theoretical estimates of the phase boundary. One calculation, shown as the upper blue dashed line in Figure 7.3(a), predicts the phase transition at

$$\alpha = (2.264N)^{.25} \tag{7.3}$$

using only the time-averaged pseudopotential [40]. A more complete description, which accounts for the fully-coupled and time-dependent dynamics of the ion positions, is shown as the solid red line in Figure 7.3(a). Here, a Floquet-Lyapunov (FL) transformation, detailed in Appendix A, is invoked to convert the periodic, time-dependent problem to a time-independent formulation and find the decoupled modes of oscillation [117, 116].

A third analysis of this phase boundary, shown as the orange dotted line in Figure 7.3(a), suggests the existence of a micromotion-destabilized region due to a downward shift in transverse mode frequencies [28]. Our measurements of the 3D to radial-2D phase boundary in Figure 7.3(a) confirm the validity of the FL approach in this regime, as opposed to the micromotion-destabilized theory. In addition, our data demonstrate that the pseudopotential approach provides a close approximation of the transition for up to 19 ions, even in the presence of increasing radial micromotion with larger crystal sizes.

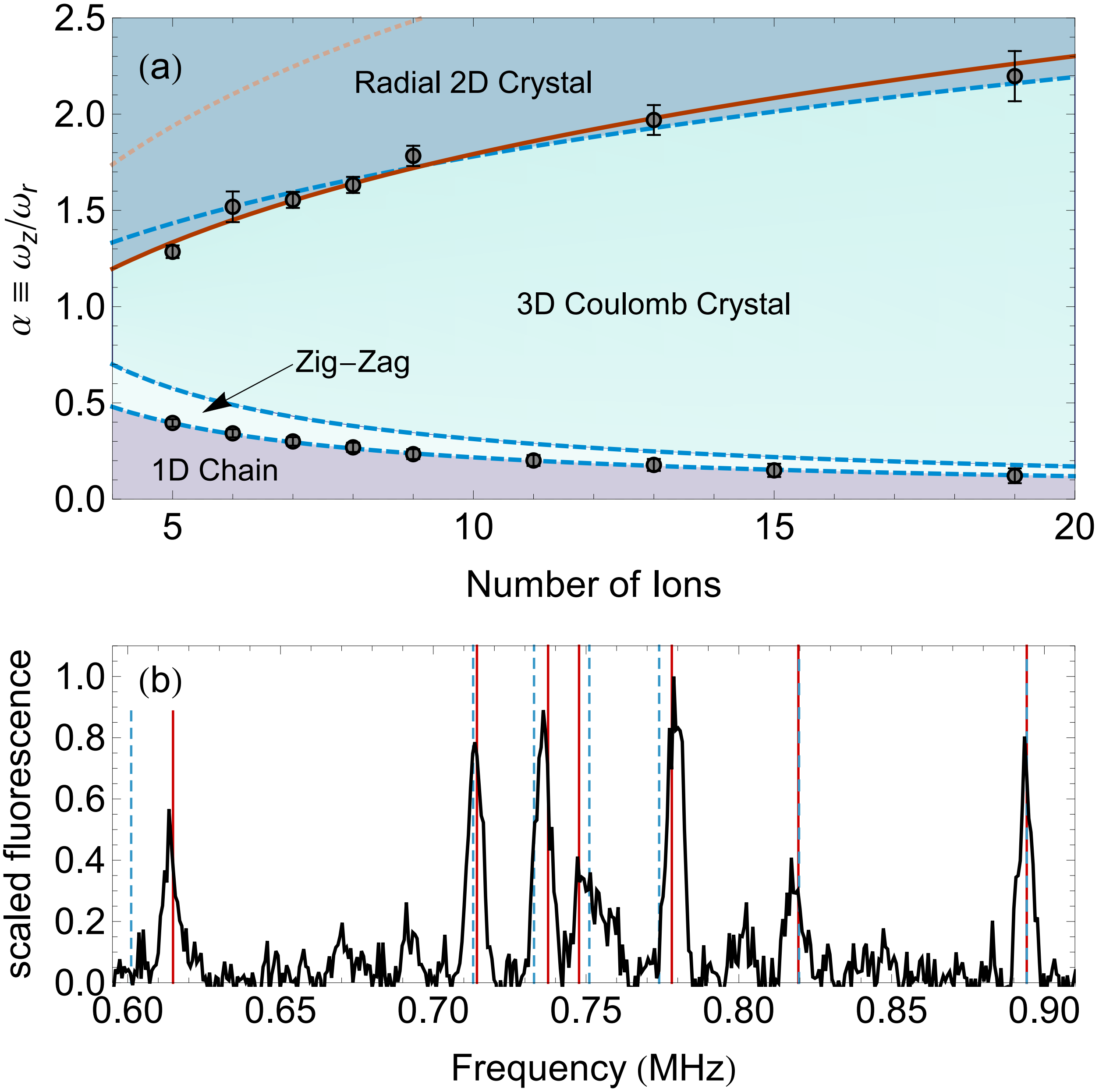

Figure 7.3: (a) Phase diagram of ion Coulomb crystals in a linear Paul trap. Data show the measured α that separate the 1D/zig-zag and 3D/radial-2D phases as a function of ion number. Three theory predictions (with no adjustable parameters) are plotted for comparison. Blue dashed, pseudopotential [40]; Red solid, Floquet-Lyapunov [116]; Orange dotted, micromotion-destabilized [28]. (b) Axial mode spectrum for 7 ions in a radial-2D crystal at $\alpha = 2$. Vertical lines show predicted mode frequencies. Blue dashed, pseudopotential; Red solid, Floquet-Lyapunov.

7.5.2 Axial Mode Spectrum

As a further investigation of micromotion effects, we measure the vibrational spectrum of a 7-ion crystal deep in the radial-2D regime. Global, far-detuned Raman transitions at 355 nm allow for spin-motion coupling and coherent excitation of the crystal modes [118]. In Figure 7.3(b), we compare the measured axial mode frequency spectrum to frequencies calculated using the pseudopoential (blue dashed) and FL (red solid) approaches. These methods largely agree with the measured data and with each other to within 2 kHz, though the pseudopotential approximation mispredicts the lowest frequency mode by over 10 kHz. Nevertheless, the pseudopotential approximation may still provide reasonable accuracy for many experiments. For instance, in quantum simulations of spin-lattice Hamiltonians [9], the pseudopotential approach correctly predicts the 2D-Ising interaction range to within 0.5% for up to 19 ions.

7.6 Micromotion-Induced Heating

The presence of micromotion may have strong effects on crystal lifetimes and temperatures. When multiple ions are confined in an RF trap, ion-ion collisions can transfer micromotion energy into secular kinetic energy and result in rapid RF heating [109, 110]. As the collision rate increases, ion motion becomes less correlated, and a sudden jump in temperature occurs at an inflection point which corresponds to a ‘melting’ of the crystal [111]. This RF heating mechanism is expected to dominate over other sources of noise, such as electric field fluctuations [65] and collisions with background gas molecules [106]. Though molecular dynamics simulations indicate that large numbers of ions could be maintained for long times without continuous cooling [106], this presumes the existence of ideal traps; no prior studies have established the lifetime and heating rates of radial-2D crystals in experimentally-realizable systems.

7.6.1 Crystal Lifetime Measurements

To begin investigating the effects of micromotion-induced heating, we measure the trapping lifetimes of radial-2D crystals in the absence of active cooling. After the ions are Doppler cooled, the cooling beams are switched off and the ions are allowed to heat for a specified amount of time. If the crystal melts during this period, one or more ions may escape the trap confining potential or remain uncooled when the Doppler beams are re-applied. We define the trapping lifetime as the time for which all ions remain in the crystal with 1/e probability, and find that it is in excess of 5 seconds for lattices of up to 19 ions. This lifetime is exceptionally long compared to the typical $\sim$millisecond timescales of quantum computation or simulation experiments [100, 99].

7.6.2 Voigt Fluorescence Profiles

The overall 3D temperature of an ion crystal, related to thermal energy by $E = \frac{3}{2}k_B T$, can be determined by measuring fluorescence as a function of the cooling laser's detuning. The ion resonance, which is described by a Voigt distribution (Appendix B), is a convolution of Lorentzian and Gaussian profiles. The Lorentzian contribution comes from the power-broadened natural linewidth

$$\Delta\nu_L = \Gamma\sqrt{1+s} = 2\pi \times 22 \text{ MHz}, \tag{7.4}$$

where $\Gamma = 2\pi \times 19.6$ MHz is the natural linewidth of the $^{171}\text{Yb}^+$ 369.5 nm $^2\text{S}_{1/2} \rightarrow {}^2\text{P}_{1/2}$ transition and $s = 0.3$ is the laser saturation parameter. The Gaussian contribution results from Doppler broadening, with a full-width at half-maximum of

$$\Delta\nu_G = 2\sqrt{\frac{(2\ln 2)k_B}{m\lambda^2}}\sqrt{T_r\cos^2\theta + T_z\sin^2\theta}. \tag{7.5}$$

This expression arises since our fluorescence beam intersects the crystal plane at an angle ($\theta = 45^\circ$) and is therefore sensitive to both the radial and axial temperatures T_r and T_z. Later we will show that keeping independent radial and axial temperatures is well-justified, and that the axial

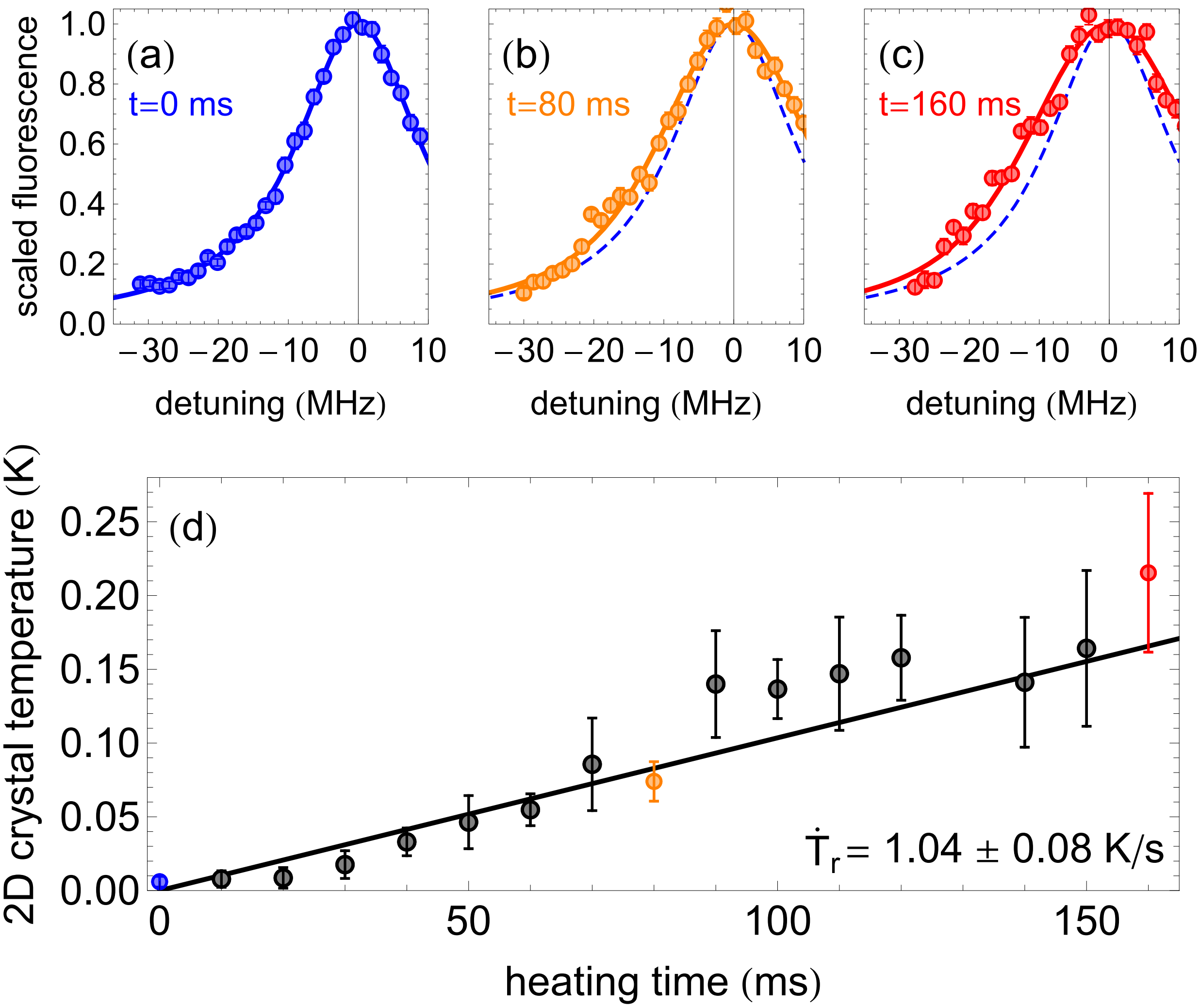

Figure 7.4: Voigt fluorescence lineshapes of a 7 ion crystal exposed to RF heating are shown for heating times of (a) 0 ms, (b) 80 ms, and (c) 160 ms. The lineshape widens at later times due to increasing contributions from Doppler broadening. The 0 ms profile (3 mK temperature) is indicated by a dashed blue line in panels (b) and (c) for reference. (d) A radial heating rate of $\dot{T}_r = 1.04 \pm .08$ K/s is extracted from Voigt profile fits to ion fluorescence data.

temperature adds negligible contribution to the overall linewidth.

When the crystal is Doppler cooled to 3 mK (as confirmed with sideband Raman spectroscopy), the Doppler width $\Delta\nu_G$ is 1 MHz, which has no noticeable effect on the fluorescence profile (Figure 7.4(a)). However, if the cooling beams are extinguished and the crystal acquires radial energy through RF heating, the fluorescence profile spreads due to an increase in thermal motion (Figure 7.4(b,c)). To extract the radial crystal temperature, we fit the measured Voigt fluorescence profile to a Lorentzian of constant width $\Delta\nu_L$ and a Gaussian of variable width $\Delta\nu_G$, weighting point averages by 1/variance. By performing many temperature measurements at increasing heating times, as shown in Figure 7.4(d), we determined the radial heating rate to be $\dot{T}_r = 1.04 \pm .08$ K/s. Previous work has predicted nonlinear heating near the melting point of Coulomb crystals; the linear nature of our data implies that short time scales, large ion masses, and low initial temperatures keep crystals far from this limit [111, 110].

7.6.3 Axial Heating Rate

To look for evidence of heat transfer between the radial and axial directions, we measure the heating rate of the axial center-of-mass (COM) mode using resolved sideband spectroscopy [50]. Following Doppler cooling, our 355 nm Raman beams are used to sideband cool the axial COM mode to $\bar{n} \leq 2.5$ as well as to induce stimulated Raman transitions at the axial COM red and blue sideband frequencies, $\omega_{\text{hf}} \pm \omega_z$. Coherent oscillations of these sidebands result in profiles like those shown in Figure 7.5(a), which are performed on a radial 2D crystal of 7 ions immediately after sideband cooling. The number of quanta in the axial COM mode is determined by taking the ratio r of red to blue sideband transition probability amplitudes (Figure 7.5(a)) for several different sideband drive times and finding the mean occupation number

$$\bar{n} = \frac{r}{1-r}. \tag{7.6}$$

The ratio method is further described in Appendix C. Finally, the axial COM heating rate $\dot{\bar{n}}$ is determined by leaving the crystal uncooled for increasing time periods and repeating the sideband measurements.

We compare the axial COM heating rate of a single ion to that of a radial-2D crystal with 7 ions, under the same trapping conditions ($\omega_z \approx 2\pi \times 900$ kHz and $\alpha = 2$). As shown in Figure 7.5(b), we find a single-ion ambient heating rate of $\dot{\bar{n}} = 100 \pm 20$ motional quanta/s. This measurement, which corresponds to temperature heating rate $\dot{T}_z = 0.004 \pm 0.001$ K/s and a spectral density of electric field noise $S_E = 2.65 \times 10^{-12}$ V^{2}m^{-2}Hz^{-1}, is comparable to heating rates

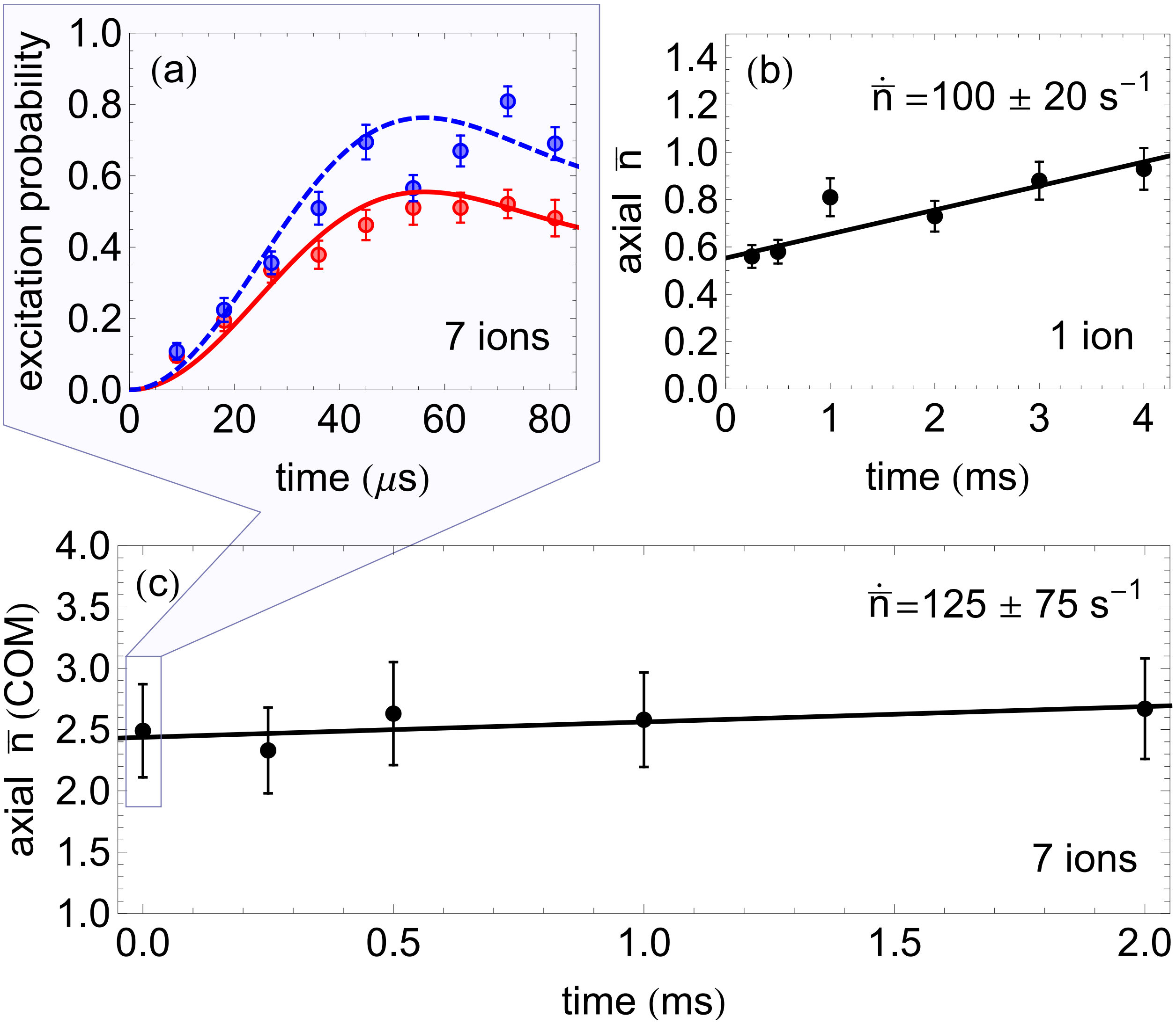

Figure 7.5: (a) A comparison of red (solid) and blue (dashed) sideband probability amplitudes are shown for a 7 ion crystal immediately following sideband cooling. The heating rate of the axial (transverse) COM mode for a single ion (b) is comparable to that of a 7 ion crystal (c). In both cases, the absolute heating rate is low compared to traps of similar size.

observed in other room-temperature RF traps of similar size [65]. We then repeat these measurements for the axial COM mode of a 7-ion crystal, finding a heating rate of $\dot{\bar{n}} = 125 \pm 75$ quanta/sec (Figure 7.5(c)). In temperature units, this rate is over 200 times smaller than the measured radial heating (Figure 7.4) and justifies our earlier assumption of non-equilibration between axial and radial directions.

Our measurements with one and seven ions further suggest that electric field noise is not the dominant heating mechanism in our trap. This is because electric field fluctuations, which are largely correlated across the ions, are expected to preferentially heat the COM mode and scale linearly with ion number [65]. Our results instead indicate largely uncorrelated noise, which has likewise been observed in Penning traps using the analog of a radial-2D crystal [119]. In the limit of perfectly uncorrelated noise, we would expect other axial modes (indexed by k) to exhibit heating rates $\dot{\bar{n}}_{(k)} = (\omega_{\text{COM}}/\omega_k)\dot{\bar{n}}_{\text{COM}}$ [65], giving at worst an estimated $\sim 50\%$ larger heating rate for the lowest-frequency (zig-zag) axial mode. Whether the noise in our system is correlated or not, our observations of objectively low axial temperatures in the presence of rapid radial heating demonstrate that the axial modes of a radial-2D crystal remain cold, isolated, and well-suited for quantum simulation experiments.

7.7 Conclusion

The experiments described in this chapter establish that micromotion effects on radial-2D crystals can be largely constrained to the radial plane, with phase boundaries and axial vibrational spectra well-predicted by micromotion-free pseudopotential theory and only the in-plane radial degrees of freedom experiencing micromotion-induced heating. In contrast, the axial (transverse) degrees of freedom can remain decoupled and cold. Furthermore, the $\sim$5-μm ion-ion spacings enacted by this geometry would enable fast ion-ion coupling rates while allowing for future individual addressing with low cross-talk.

This demonstration of stable, isolated, and low-noise axial modes establishes radial-2D crystals in linear Paul traps as a realistic platform for implementing several proposals in quantum simulation [26, 27]. This system is especially well-suited for studies of highly-frustrated quantum spin models [23, 26, 25, 120], since long-range antiferromagnetic interactions are routinely implemented between co-trapped ions [9], and since ions in the radial-2D phase self-assemble into a triangular lattice.

The realization of such proposals demands several developments. First, the trap used for this study did not facilitate site-resolved detection of the ion lattice. Next, methods to cool radial-2D crystals near the motional ground-state should be applied [121, 122]. Evidence of entanglement generation via Mølmer-Sørensen interactions [51] (or equivalent) should then be demonstrated before implementing full spin-lattice simulations. Finally, the possibility of maintaining 100+ ions in the radial-2D crystal phase for long times [106], and the limits of crystal stability in the presence of RF heating, should be experimentally explored as the system is scaled to larger sizes.

CHAPTER 8

AN OPEN-ENDCAP BLADE TRAP FOR RADIAL-2D ION CRYSTALS

8.1 Section Overview

In Ch. 7, we studied radial-2D ion crystals, for which the out-of-plane modes are co-aligned with the trap axis and remain micromotion-free. These crystals were found to have long lifetimes, well-characterized vibrational modes, and low heating rates in the out-of-plane (transverse) direction, validating their use for quantum simulation experiments. However, the rod-style Paul trap used to confine the crystals blocked optical access along the trap axis perpendicular to the radial plane, such that it was only possible to view the radial-2D crystals from the side. In order to achieve full site-resolved imaging and enable the possibility of individual addressing for this crystal geometry, it is necessary to develop a Paul trap with open line-of-sight along its central axis.

In this chapter, we describe the development of an open-endcap linear RF trap that is capable of confining and resolving large numbers of ions in the radial-2D crystal phase. We begin in Section 8.2 with the design requirements for trapping and imaging radial-2D crystals as well as a simulation of our trap design. In Section 8.3, we discuss the trap fabrication and assembly while Section 8.4 covers the RF and DC electronics and voltage control. We demonstrate and characterize the performance of the open-endcap trap in Section 8.5, followed by concluding remarks in Section 8.6.

8.2 Open-Endcap Trap Design

8.2.1 Linear Paul Traps

Linear Paul traps are capable of confining ion crystals in one, two, or three dimensions [37, 104], but require significantly different parameters (such as trap sizes and applied voltages) to achieve each of these geometries. Thus, trap designs that have been optimized for holding 1D chains may prove incapable of (or impractical for) confining ions in the radial-2D phase. In this section, we review the linear Paul trap and consider the requirements for the stable trapping of radial-2D ion crystals while ensuring sufficient optical access for site-resolved imaging.

The time-dependent potential provided by a linear quadrupole RF trap can be written as [50]

$$\begin{aligned}\Phi(\vec{r},t) &= \Phi_{DC}(\vec{r}) + \Phi_{rf}(\vec{r},t)\\ &= \frac{\kappa U_0}{2z_0^2}(2z^2 - \chi x^2 - \gamma y^2) + \frac{V_0\cos(\Omega_t t)}{2d_0^2}(x^2 - y^2)\end{aligned} \tag{8.1}$$

where U_0 is the DC voltage, V_0 is the amplitude of an RF voltage with oscillation frequency Ω_t, d_0 and z_0 are the radial and axial trap dimensions, and κ is a geometric factor of order one determined by the trap electrodes. In Equation 8.1, we have also introduced the radial anisotropic factors χ and γ, which we experimentally choose to deviate slightly from one. This small asymmetry breaks the degeneracy of the x and y radial axes, thereby preventing radial-2D crystals from rotating freely in the xy plane.

Near the center of the trap, the potential can be approximated as a harmonic pseudopotential well

$$\Phi(\vec{r}) = \frac{1}{2}m\left(\omega_x^2 x^2 + \omega_y^2 y^2 + \omega_z^2 z^2\right), \tag{8.2}$$

where the secular resonance frequencies in the radial and axial directions can be written as

$$\omega_x = \sqrt{\frac{Q}{m}\left(\frac{qV_0}{4d_0^2} - \frac{\kappa\chi U_0}{z_0^2}\right)}\,;\ \omega_y = \sqrt{\frac{Q}{m}\left(\frac{qV_0}{4d_0^2} - \frac{\kappa\gamma U_0}{z_0^2}\right)}, \tag{8.3}$$

$$\omega_z = \sqrt{\frac{Q}{m}\frac{2\kappa U_0}{z_0^2}} \tag{8.4}$$

with ion charge Q, ion mass m, and the Mathieu “q” parameter $q = 2QV_0/md_0^2\Omega_t^2$. Within this pseudopotential framework, we can account for RF driven micromotion by expanding the ions’ motion about their equilibrium positions [50, 29]. To leading order, the coordinates of each ion varies in time as

$$\vec{r}(t) = \vec{r}^{(0)} + \vec{r}^{(1)}\cos(\Omega_t t) + \vec{r}^{(2)}\cos(2\Omega_t t) + ... \tag{8.5}$$

where $\vec{r^{(0)}}$ is the time-averaged ion position, $\vec{r^{(1)}} = (q_x\hat{x} + q_y\hat{y} + q_z\hat{z})r^{(0)}/2)$, and $\vec{r^{(2)}} = (q_x^2\hat{x} + q_y^2\hat{y} + q_z^2\hat{z})r^{(0)}/32$ are the amplitudes of the first two micromotion terms.

8.2.2 Design Considerations

Under the pseudopotential approximation, the criteria for achieving a radial-2D ion crystal is [40]

$$\omega_z/\omega_r > (2.264N)^{\frac{1}{4}}. \tag{8.6}$$

The primary design challenge for trapping crystals in the radial-2D phase is to choose the appropriate trap dimensions, voltages, and frequencies that ensure Equation 8.6 is strongly obeyed for large numbers of ions, while keeping all parameters experimentally reasonable.

Several principles guide the selection of optimal trap parameters for radial-2D crystals. Satisfying Equation 8.6 is most easily accomplished when ω_z is large, which requires large U_0 and/or small z_0. Yet, large U_0 and small z_0 have a deconfining effect in the radial direction: if the second term under the square root in Equation 8.3 grows too large, the ions will escape. To counter this effect, V_0 must also be moderately large while keeping d_0 small. Furthermore, since it is desirable to have small micromotion amplitudes, the trap drive frequency Ω_t should be made large to keep the Mathieu q parameter small. Overall, these observations lead to a set of self-consistent design choices: small trap dimensions d_0 and z_0, large DC voltage U_0, moderately large RF voltage V_0, and relatively large trap frequency Ω_t. For specificity, the experimental demonstration presented in Section 5 used the parameters $d_0 = 230$ m, $z_0 = 200$ m, $U_0 = 14.4$ V, $V_0 = 150V$, and $\Omega_t = 2\pi \times 27.51$ MHz.

In addition to selecting the above parameters, we also choose to implement a segment-blade design for our linear Paul trap [123, 124]. We consider three advantages of this trap geometry: 1) the open endcaps of the blades ensure that imaging is possible perpendicular to 2D ion plane; 2) the trap dimensions d_0 and z_0 can be made quite small to avoid unreasonably high voltages V_0 and U_0; 3) the blades can be designed such that they do not compromise the numerical aperture (NA) of the imaging optics. In our trap, we have angled the edges of the RF and DC blades to ensure that there are no obstructions to light collection using a NA = 0.28 imaging objective (Special Optics 54-17-29-369nm).

Images of our blade-trap design are shown in Figure 8.1. The center of the trap assembly is located 11.5 mm away the vacuum viewport to allow for a large solid angle for imaging. In this design, the DC blades are segmented into two endcaps plus one central electrode (Figure 8.1c); the RF blades are continuous and of the same total length as the three DC blade segments, providing translational symmetry for the RF potential. All blades (including the rf) can be DC biased to allow for translation along all 3 principal axes. Finally, two compensation electrodes are mounted above and below the trap to provide additional voltage compensation along the vertical/horizontal directions.

8.2.3 Finite-Element Simulations

Following the discussion above, trapping ions in the radial-2D crystal phase relies on a delicate balance between the trap geometry and the applied voltages U_0 and V_0. Equation 8.3 shows that this balance also relies on the value of the geometric factor κ. Since the blade-style electrodes are not perfect hyperbolas (for which $\kappa = 1$), it is necessary to perform numeric simulations to determine the trap secular frequencies and ensure stable trapping in the radial-2D phase.

We numerically calculate the potentials within the trap using finite-element simulations. First, we calculate the effective potentials $\phi_{DC}(\vec{r})$ and $\phi_{rf}(\vec{r})$ which arise from the application of 1 Volt to each individual electrode (with the others grounded). Using this set of potential basis functions, the total potential near the center of our trap can be written in the form $\Phi_{tot}(\vec{r},t) = \Phi_{rf}(\vec{r},t) + \Phi_{DC}(\vec{r})$, where the RF contribution is given by:

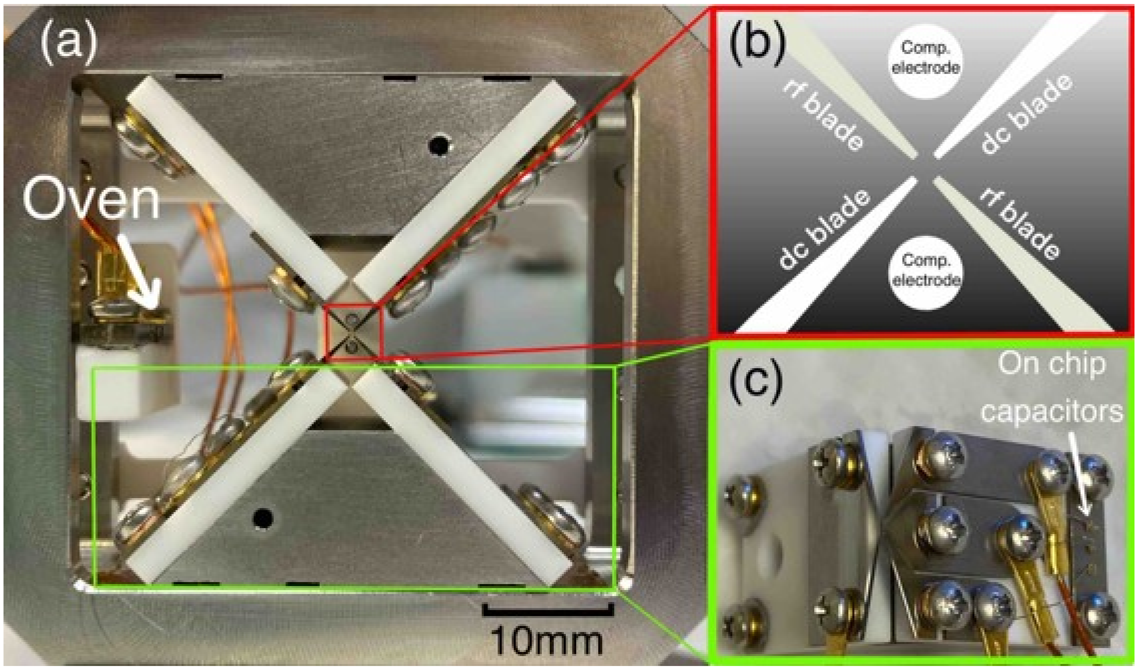

Figure 8.1: Assembled blade trap mounted in its vacuum chamber, taken along the imaging direction. The blades are mounted on insulating Macor plates, which are fastened to a stainless steel frame and support structure (connected to ground). ^{171}Yb and ^{174}Yb ovens are placed to the left of the trap. (b) Sketch of the blade configuration near the trap center. RF and segmented DC blades provide the trap potentials; two rod-style electrodes provide compensation in the vertical/horizontal directions. (c) Image of an RF blade and segmented DC blade mounted on their Macor supports. Blades are machined from a 500 μm-thick piece of solid tungsten and polished after machining. On-chip capacitors (800 pF) on each DC segment provide filtering of RF pickup.

$$\begin{aligned}\Phi_{rf}(\vec{r},t) &= V_0\cos(\Omega_t t)\phi_{rf}(\vec{r})\\ &= V_0\cos(\Omega_t t)(\eta^x_{rf}x^2 + \eta^y_{rf}y^2 + \eta^z_{rf}z^2),\end{aligned} \tag{8.7}$$

and the DC component is

$$\begin{aligned}\Phi_{DC}(\vec{r}) &= U_0\phi_{DC}(\vec{r})\\ &= U_0(\eta^x_{DC}x^2 + \eta^y_{DC}y^2 + \eta^z_{DC}z^2),\end{aligned} \tag{8.8}$$

where the factors η^α in Equation 8.7 and Equation 8.8 indicate the curvatures in the α direction for the RF and DC potentials. Comparing these equations to the form of Equation 8.1, we extract the geometric factor $\kappa = z_0^2\eta^z_{DC}$, as well as the anisotropic factors $\chi = -2z_0^2\eta^x_{DC}/\kappa$ and $\gamma = -2z_0^2\eta^y_{DC}/\kappa$. The resulting trap potential, along with its associated electric field, is shown in Figure 8.2(a).

For a single trapped ion, the action of this simulated potential $\Phi(\vec{r},t)$ gives rise to the time evolution described by the Mathieu equations

$$\frac{d^2u_i}{d\zeta^2} + a_i - 2q_i\cos(2\zeta)]u_i = 0 \tag{8.9}$$

where $i \epsilon \{x,y,z\}$ and the dimensionless parameters $\zeta = \Omega_t t/2, a_i = 8QU_0\eta^i_{DC}/m\Omega_t^2, q_i = 4QV^i_{0\,rf}/m\Omega_t^2$. Under the pseudopotential approximation, which is valid when $a_i < q_i^2 \ll 1$, the ion secular frequencies are then defined by $\omega_i = \beta_i\Omega_t/2$, where $\beta_i \approx \sqrt{a_i + q_i^2/2}$ are the characteristic exponents of the Mathieu equation [28, 50].

Having extracted the secular trap frequencies from the finite-element simulation, we can apply the harmonic pseudopotential approximation to estimate the ion positions for large radial-2D crystals. For N trapped ions, the total potential energy depends on both the trapping potential as well

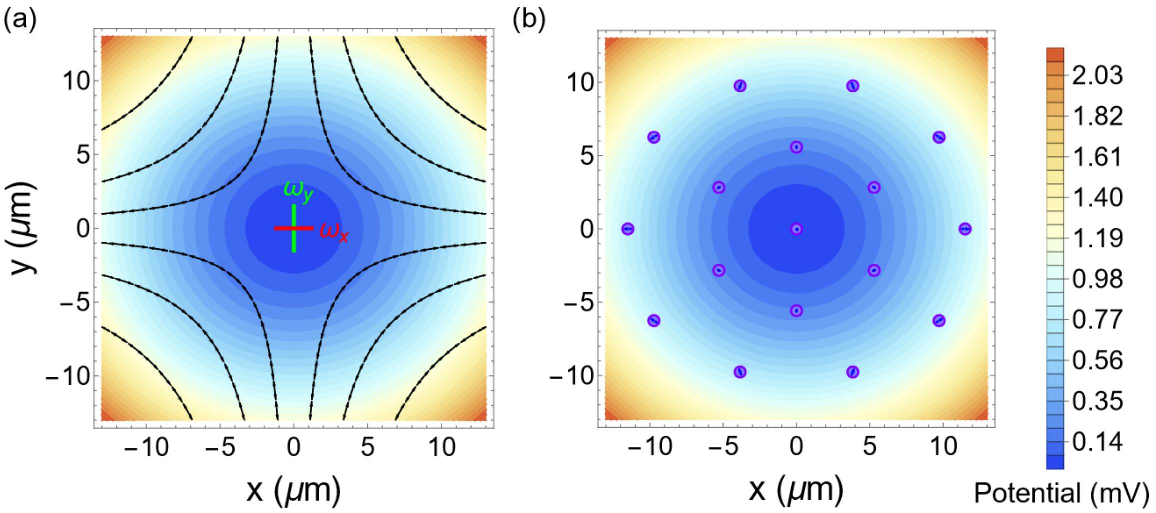

Figure 8.2: (a) The radial trapping potential for our open-endcap geometry, calculated using finite-element simulation methods. The two radial frequencies are made slightly non-degenerate to prevent rotation of the ion crystal. The associated electric field lines are shown in black. (b) Simulated equilibrium ion positions in for 17 $^{174}\text{Yb}^+$ ions in the potential of (a). Ions away from the central axes experience driven micromotion, whose amplitude can be calculated using the Floquet-Lyapunov transformation. For the 17-ion crystal, these amplitudes (shown as small arrows in (b)) are predicted to be small compared to the inter-ion spacing.

as the Coulomb interaction between every pair of ions:

$$V(x,y,z) = \sum_{n=1}^{N} \frac{1}{2} m(\omega_x^2 x_i^2 + \omega_y^2 y_i^2 + \omega_z^2 z_i^2) \\ + \frac{Q^2}{4\pi\epsilon_0} \sum_{i \neq j}^{N} \sum_{j}^{N} \frac{1}{\sqrt{(x_i - x_j)^2 + (y_i - y_j)^2 + (z_i - z_j)^2}}.$$

The equilibrium position of each ion can be found by simulating the full equations of motion with an added friction (cooling) term [28]. The results of one such calculation, for 17 ions, are shown in Figure 8.2(b). After finding the equilibrium positions, the vibrational modes and micromotion trajectory of each ion can be calculated using the Floquet–Lyapunov transformation [117, 116] which is discussed in Appendix A. The small arrows in Figure 8.2(b) show the resulting micromotion amplitude for the off-axis ions, which to first order scales linearly as the ions' radial distance from the trap center.

8.3 Trap Fabrication

8.3.1 Material Selection

Micro-fabricated, gold-coated blades are a popular choice for constructing ion trap electrodes [125, 126]. However, the gold coating on such electrodes are often susceptible to damage from resistive heating or from large electric fields which arise during operation of the trap [127]. For instance, tests in our lab demonstrated that the large RF voltages required for creating the radial-2D crystal phase quickly led to melting and evaporation of the gold layer. To ensure more robust performance in the presence of large RF voltages, we fabricated our electrodes from solid tungsten. Tungsten is an easily available, strong, and low resistivity metal that has been used in a variety of earlier RF traps [128, 129, 130, 131, 132]. Compared with more common metals (such as stainless steel), we consider tungsten advantageous for our trap since its low resistivity will limit blade heating and any associated vacuum pressure increases when large RF voltages are applied.

8.3.2 Blade Fabrication and Assembly

The blade electrodes are fabricated from a sheet of 500 μm-thick pure tungsten using a wire-EDM (Electrical Discharge Machining) process. This technique allows for fairly complex electrode geometries (such as the segmented DC blades) to be machined to within $\sim$ 10 μm tolerances. In our design, the three DC blade segments are each 300 μm long and separated by a 50 μm gap; the RF blades have a total length of 1 mm. The final processed tip thickness is 100 μm for all blades; however, for reasons explained below, we target an initial 300 μm tip thickness during wire-EDM machining.

For sintered materials like tungsten, the exposed surface following wire-EDM processing can be markedly rough. This can be problematic for trapped-ion systems, since there is evidence that large surface roughness could significantly affect motional heating rates [133, 134, 135, 65]. In addition, rough electrode surfaces could increase unwanted laser beam reflections, increasing the background light collected by the imaging optics. Figure 8.3a shows an image of a blade electrode

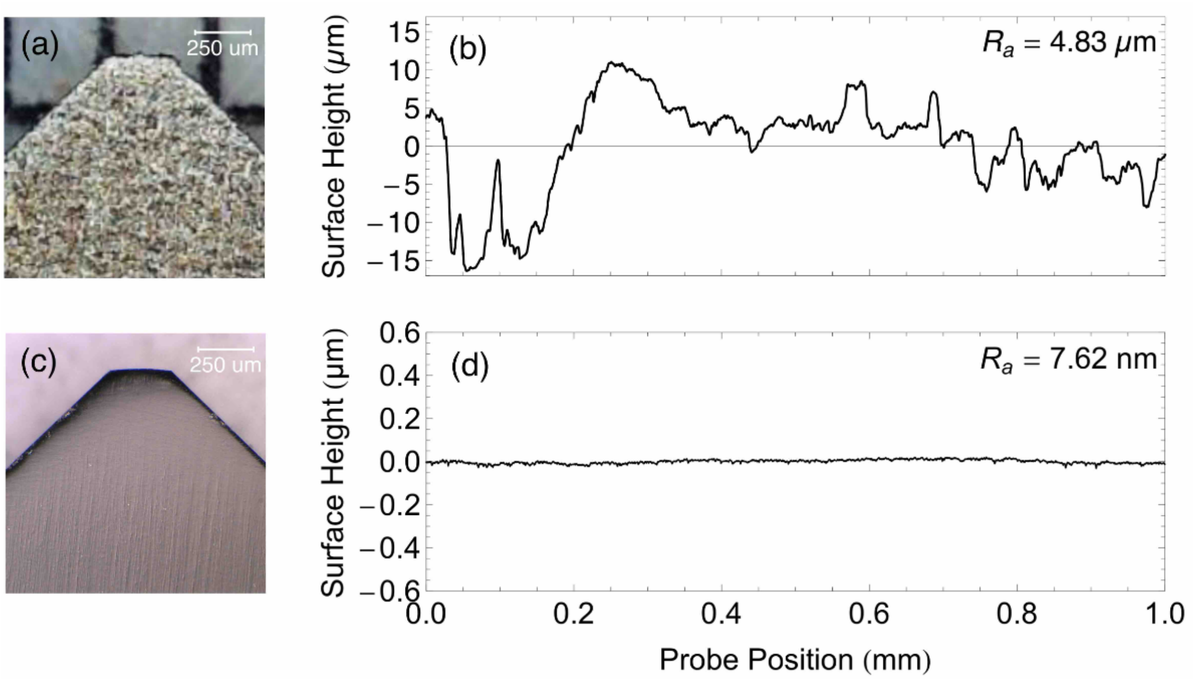

Figure 8.3: a) Image of a blade electrode directly after wire-EDM machining. (b) Using a stylus profilometer near the tip of the blade, we characterize the average surface roughness R_a. (c) After electropolishing and hand polishing, the blade has a smooth mirror-like surface. (d) The surface roughness of the polished blade is reduced by nearly three orders of magnitude compared to the unprocessed blade.

just after wire-EDM machining. Using a stylus profilometer (Bruker DektakXT), we characterized the arithmetic average surface roughness R_a of this blade to be approximately 5 μm over a 1 mm region near the tip (Figure 8.3b).

To smooth the tungsten blade surface after machining, we implement a two-stage polishing process. First, we use self-terminated electrochemical etching to remove the largest surface features [136]. The blade is immersed into sodium hydroxide solution (NaOH, 400 ml of 2 mol/L) and connected to the cathode of a power supply (10 V, 1.5 A) for 2 minutes of etching. This process lowers the surface roughness to $R_a < 1\mu$m and reduces the tip thickness from 300μm to $\sim 100\mu$m. Following this electropolishing stage, the electrodes are hand-polished using 3 μm, 1 μm, and 0.3 μm stages of Aluminum Oxide polishing paper. Figure 8.3c shows an image of the blade electrode after processing. As measured by a profilometer, the surface roughness is reduced from $R_a \approx 5\mu$m to $R_a \approx 8$ nm after these polishing processes (Figure 8.3d).

Following machining and polishing of the blades, the trap is assembled in a clean room to avoid dust contamination. As shown in Figure 8.1a, the blades are mounted on Macor plates fastened to trapezoidal stainless-steel blocks. The DC segments are handaligned under a microscope to keep a 50 μm gap between segments, and the RF blade is mounted parallel to the DC segments with a gap of 280 μm (Figure 8.1c). Two assembled triangular blocks are placed in a stainless steel frame in a vertex-to-vertex orientation, with a vertical gap between blades of 300 μm. All DC electrodes are mechanically connected to gold-plated lugs, which are crimped to Kapton-coated wire and connected to a Sub-C 9-pin feedthrough. The RF blades and atomic ovens connect with separate high-power electrical feedthroughs. To reach UHV pressures, the vacuum system was initially pumped to 10^{-7} Torr, then baked for two weeks at 200° C; the final pressure of the chamber at room temperature is below 10^{-11} Torr.

8.4 Electronics and Voltage Control

8.4.1 Helical Resonator

Ions confined by a Paul trap require a stable, high voltage, and low noise RF potential. A helical resonator allows impedance matching between the RF source and the ion trap, amplifying voltage while filtering noise injected into the system [54]. We opt to build a two-coil resonator, since this allows for independent DC biasing of the RF blades so that the trap may be compensated in all directions[1]. In order to construct a resonator to operate at a desired frequency, we first measure the capacitance of the connection wire and ion trap C_{trap} at the trap feedthrough. Once these are known, we build the shield and helical resonator coils following the procedure outlined in [54]. A cross-sectional drawing of the two-coil resonator is shown in Figure 8.4a along with our chosen design parameters. Under these conditions, the resulting resonant frequency is $\Omega_t = 2\pi \times 27.51$ MHz when connected to our blade trap.

Due to our implementation of a two-coil resonator, we designed the circuit shown in Figure 8.4b to appropriately sample the transmitted RF voltage. To begin, we use two capacitors C_1 and C_2 (KEMET, SMD Comm X5R series, 10 μF) to bridge between the resonator's two outputs V_{rf1} and V_{rf2}. With this configuration, we can accomplish two goals. First, combining the two RF outputs with capacitors balances any potential phase differences caused by mechanical asymmetry of the resonator. Second, the potential at the point S is the average value of the outputs which can be used as a voltage probing point for sampling. A capacitive divider connected to point S is used to scale down the high rf-voltage for sampling. The divider consists of two high voltage-tolerance capacitors, C_3 (AVX Corporation, SQ series, 0.2 μF) and C_4 (AVX Corporation, UQ series, 20 μF). This combination picks off 1% of the high voltage signal (down to the ~ 1 V range) so that the later rectifier design requirements are less stringent. We measured the RF pickup signal as a

---

[1] At this time, the two-coil resonator has been removed from the system due to its introduction of unexplained motional modes in the axial frequency spectrum. It has been replaced with a single-coil can of the same resonant frequency. Though the single-coil resonator does not allow independent biasing of the RF blades, we are still able to compensate in all directions due to the rod-style electrodes located above and below the trap. Though we may or may not choose to re-implement a double-coil resonator design in the future, I have chosen to leave the relevant section (8.4.1 of this thesis) of [38] unedited.

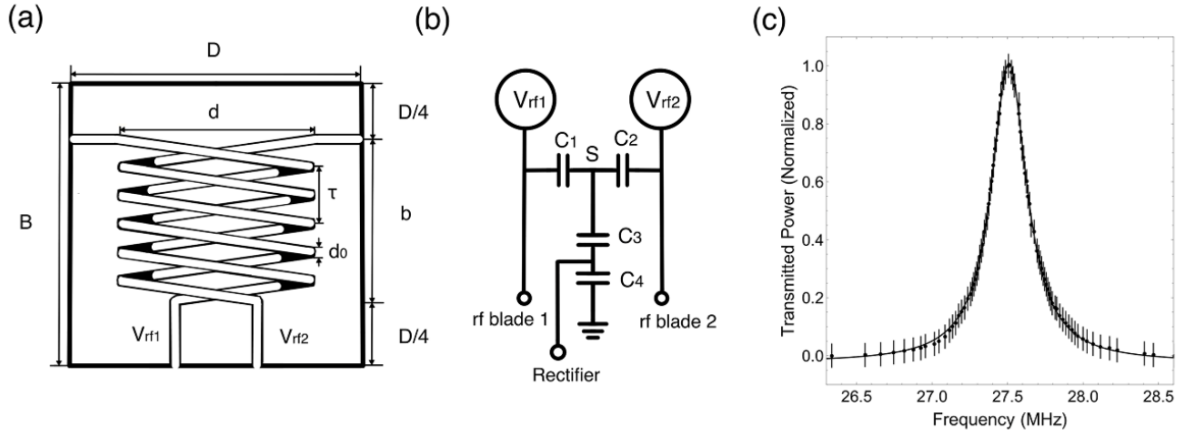

Figure 8.4: (a) Sketch of the two-coil resonator design. The shield diameter $D = 102$ mm, shield height $B = 101$ mm, coil diameter $d = 64$ mm, coil height $b = 68$ mm, winding pitch $\tau = 10$ mm, and the coil wire diameter $d_0 = 2.5$ mm provides a $\Omega_t = 2\pi \times 27.51$ MHz drive frequency when connected to a trap with capacitance $C_{trap} = 10$ pF. (b) Schematics of the voltage sampler and capacitive divider. C_1 and C_2 are placed across the outputs to balance V_{rf1} and V_{rf2}; C_3 and C_4 form the capacitive divider. C_1, C_2, C_3 and C_4 are on the same circuit board housed within the resonator cylinder. The voltage-reduced sampling signal is sent out through a BNC connector. The rectifier circuit is right next to the BNC connector to avoid electromagnetic interference. (c) We measure a resonator Q factor of ≈ 100 by sampling the output of the capacitive divider as a function of RF input frequency.

function of input RF frequency, from which we determined the Q factor of the resonator to be ~ 100 (as shown in Figure 8.4c).

8.4.2 rf Locking and Stability

The fidelity of quantum operations within ion traps is sensitive to fluctuations in the RF frequency, which may be driven by noise in the input RF amplifier, mechanical vibrations of the resonator, and temperature drifts (to name a few sources). Since the trap secular frequencies depend on the ratio of V_0/Ω_t (Equation 8.3), and since the RF drive frequency Ω_t is typically well-stabilized at the RF source, active RF amplitude stabilization is a crucial tool for keeping the trap secular frequency consistent. In our case, we actively stabilize the RF voltage amplitude following the techniques outlined in [137][2].

---

[2] The single-coil replacement resonator does not presently have a capacitive divider as referenced in section 8.4.2, and at the time of writing we are working with free-running RF voltage. Drift in our motional sidebands is measurable

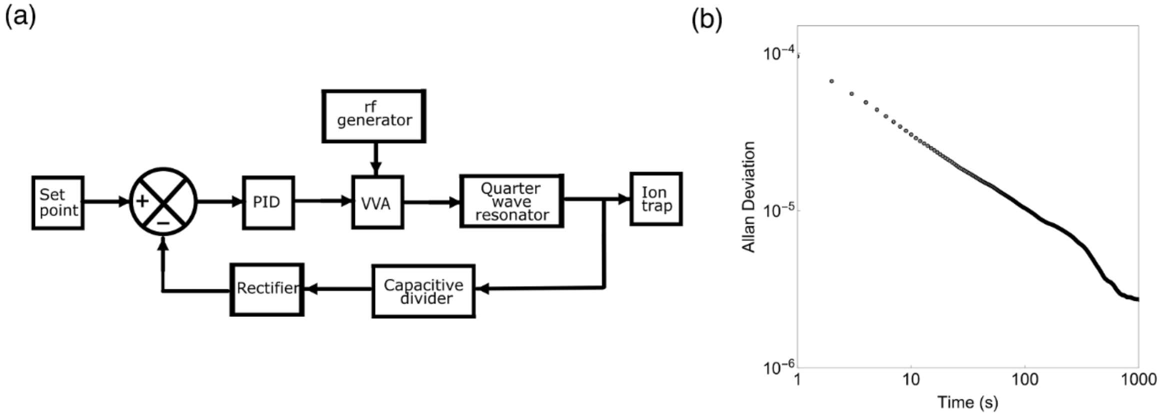

Figure 8.5: (a) Servo loop block diagram for active stabilization of the RF voltage amplitude. VVA: Voltage Variable Attenuator, PID: proportional-integral-derivative controller. (b) Allan deviation of the RF signal amplitude during operation of the servo loop in (a).

Our servo loop block diagram is shown in Figure 8.5a. The RF generator produces a signal at frequency $\Omega_t = 2\pi \times 27.51$ MHz and power -8 dBm, which passes through a voltage variable attenuator (VVA) and is amplified before being sent to the helical resonator. The picked-off signal from the resonator passes through a rectifier circuit and is fed as the input of a closed proportional–integral–derivative (PID) loop. The RF amplitude is thus stabilized with respect to the set point value.

We performed long-term monitoring of the DC signal after the rectifier when the servo is engaged. These measurements represent the scale of RF amplitude fluctuations over time. We find that the Allan deviation of RF amplitude scales with time τ as $\approx 1/\sqrt{\tau}$; at 1000 s, the relative stability is $2.74 \pm 0.04 \times 10^{6}$, which translates to a $\sim$ 30 Hz rms fluctuation of the radial secular frequencies.

8.4.3 DC Control

In addition to RF control, we desire stable, low noise voltages applied to the DC trap electrodes. We apply these voltages using static DC power supplies (Matsusada R4G series) that can output 0-120

---

over experiment timescales, and in the near future, RF frequency locking will need to be implemented with the single-coil resonator either by adding a capacitive divider or using a bidirectional coupler for voltage sampling.

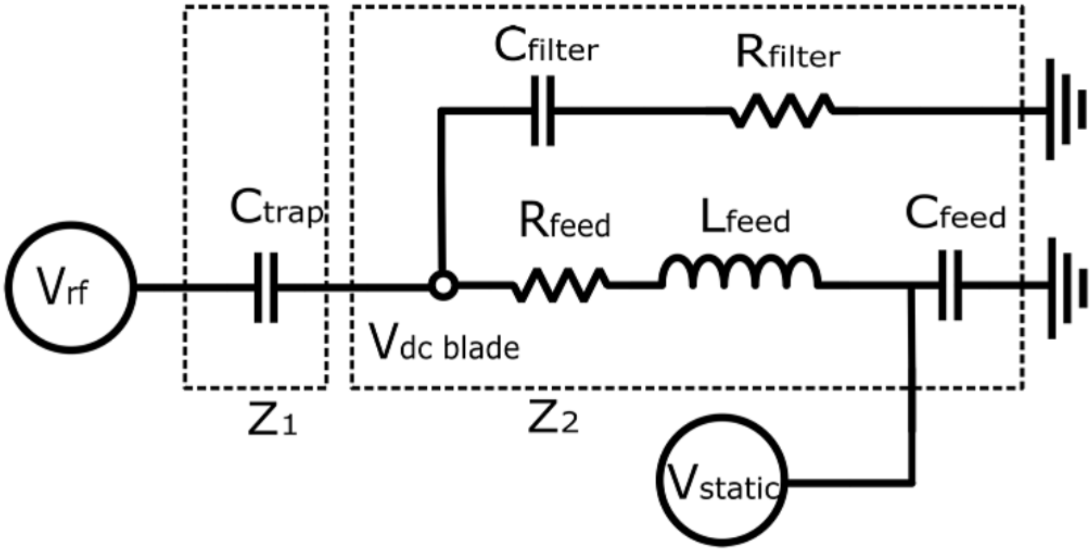

Figure 8.6: DC circuit diagram of our ion trap. The in-vacuum filter is designed to reduce the RF pickup on the static DC blades.

V with 1 mVrms ripple. To prevent noise pickup from various ancillary electronic devices, each DC channel is externally RC-filtered before being connected to a 9-pin feedthrough at the trap vacuum chamber. Given the small dimensions of our blade trap, one additional concern is unwanted RF pickup on the DC blades. To mitigate this effect, each DC blade segment is wirebonded to an 800 pF capacitor to shunt RF pickup to ground (see image in Figure 8.1c). To model the effective in-vacuum circuit, we treat the ion trap as a capacitor (C_{trap}) and consider the contributions from the on-trap filter elements and vacuum feedthroughs, as shown in Figure 8.6. Using this model, we can estimate the RF pickup on the static DC blades by first calculating the complex impedance

$$Z_2 = \left(\frac{1}{Z_{C,filter} + Z_{R,filter}} + \frac{1}{Z_{C,feed} + Z_{R,feed} + Z_{L,feed}} \right)^{-1} \tag{8.10}$$

where for our system, $Z_{R,feed} \approx R_{feed} \ll 1\Omega$, $|Z_{C,feed} = \frac{1}{\Omega_t C_{feed}} \approx 1.8\Omega$ and $|Z_{L,feed}| = \Omega_t L_{feed} \approx 52\Omega$. The resistance of the filter $R_{filter} \ll 1\Omega$, which is negligible compared with the capacitive filter impedance $|Z_{C,filter}| = \frac{1}{\Omega_t C_{filter}} = 7.2\Omega$. Thus, we estimate the impedance $|Z_2| = 6.4\Omega$. The measured trap capacitance of 10 pF leads to an impedance $|Z_1| = 600\Omega$ at our trap drive frequency. Therefore, the estimated RF pickup on the DC blades is then $\frac{|Z_2|}{|Z_1|+|Z2|}V_{RF} = 0.01V_{RF}$.

We note that in the absence of the on-trap filter capacitors, the RF pickup on the DC blades would be approximately a factor of 8 larger.

8.5 Experimental Demonstration

8.5.1 Laser Access and Internal States

Our blade trap and vacuum system have been designed to ensure sufficient optical access for state preparation, manipulation, and measurement. As shown in Figure 8.7, ^{174}Yb^{+} ions are loaded into the trap via photo-ionization of neutral ^{171}Yb using 399 nm and 369.5 nm light. Ions are Doppler cooled by 369.5 nm light that is $\approx$ 10 MHz red-detuned of the $^{2}S_{1/2}$ $^{2}P_{1/2}$ transitions, and co-aligned with the 399 nm beam. Additional wavelength components near 369.5 nm are used for optical pumping and detection of the qubit state, while co-aligned light at 935 nm is used to repump population out of the metastable $^{2}D_{3/2}$ state [138]. A 5 G magnetic field along the vertical direction breaks the degeneracy of the hyperfine triplet. Finally, two-photon stimulated Raman transitions for quantum state manipulation are driven by shining two 355 nm beams such that their wave vector difference $\Delta\vec{k}$ is aligned along the transverse direction of the radial-2D crystal (which is the axial direction of the trap).

8.5.2 Confinement and Imaging of Radial-2D Crystals

Ions may be confined in radial-2D crystals once the trap secular frequencies satisfy the inequality in Equation 8.6. To create this ion geometry experimentally, we load the desired number of ions at low axial frequency ω_z, then increase the endcap voltages (DC1, DC3, DC4, DC6) to push the ions into the radial-2D phase. In practice, imperfect electrode fabrication, trap misalignments, and stray electric fields could cause ion heating during the transitions through different structural phases. To avoid losing ions, and to minimize any excess micromotion, we compensate by applying small bias voltages to blade segments as needed. Once ions are in the 2D regime and Doppler cooled to milliKelvin temperatures, they form a Wigner crystal as the system minimizes its configuration energy. As shown in Figure 8.8, the final crystal geometry takes the form of a triangular lattice in

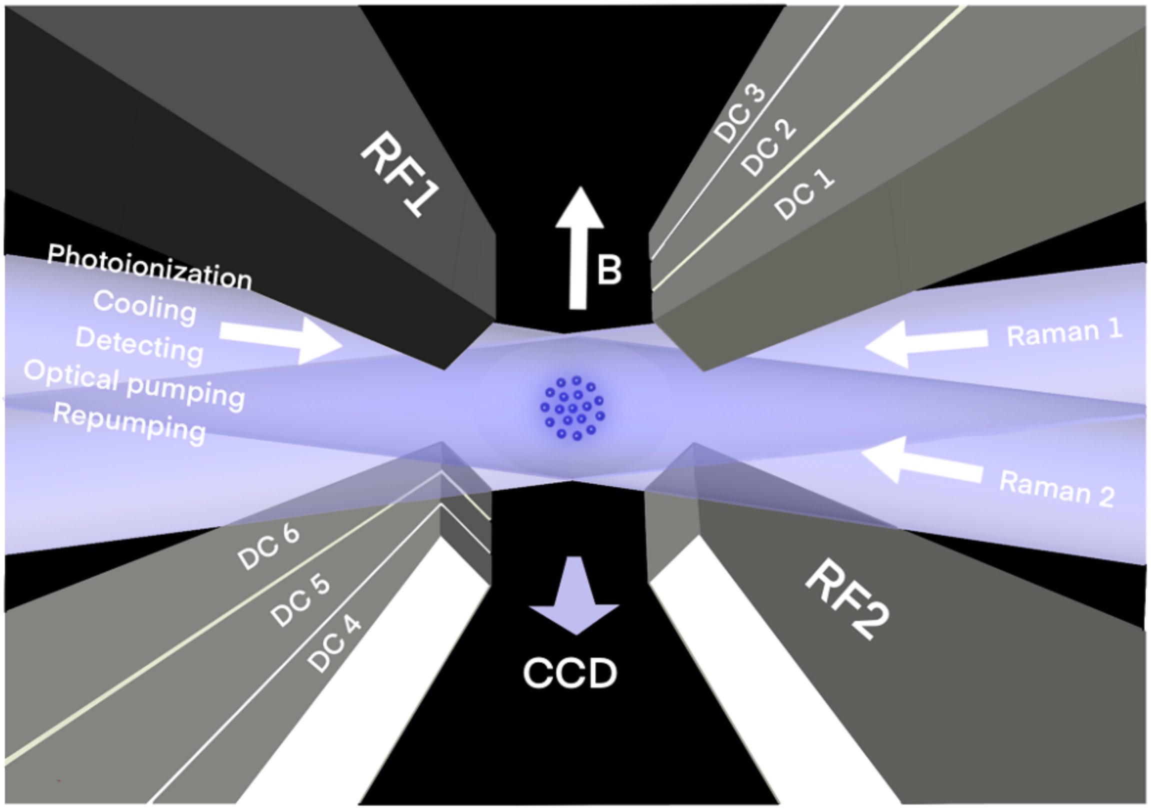

Figure 8.7: Concept drawing of the trap and laser beam configurations for photoionization (399 nm), cooling, optical pumping, and detection (369.5 nm), repumping (935nm), and two-photon Raman transitions (355nm). The CCD camera faces the crystal plane and the magnetic field is oriented vertically. Oscillating voltages on electrodes RF1 and RF2 provide the radial confinement, while static voltages applied to electrodes DC1, DC3, DC4, and DC6 provide axial confinement.

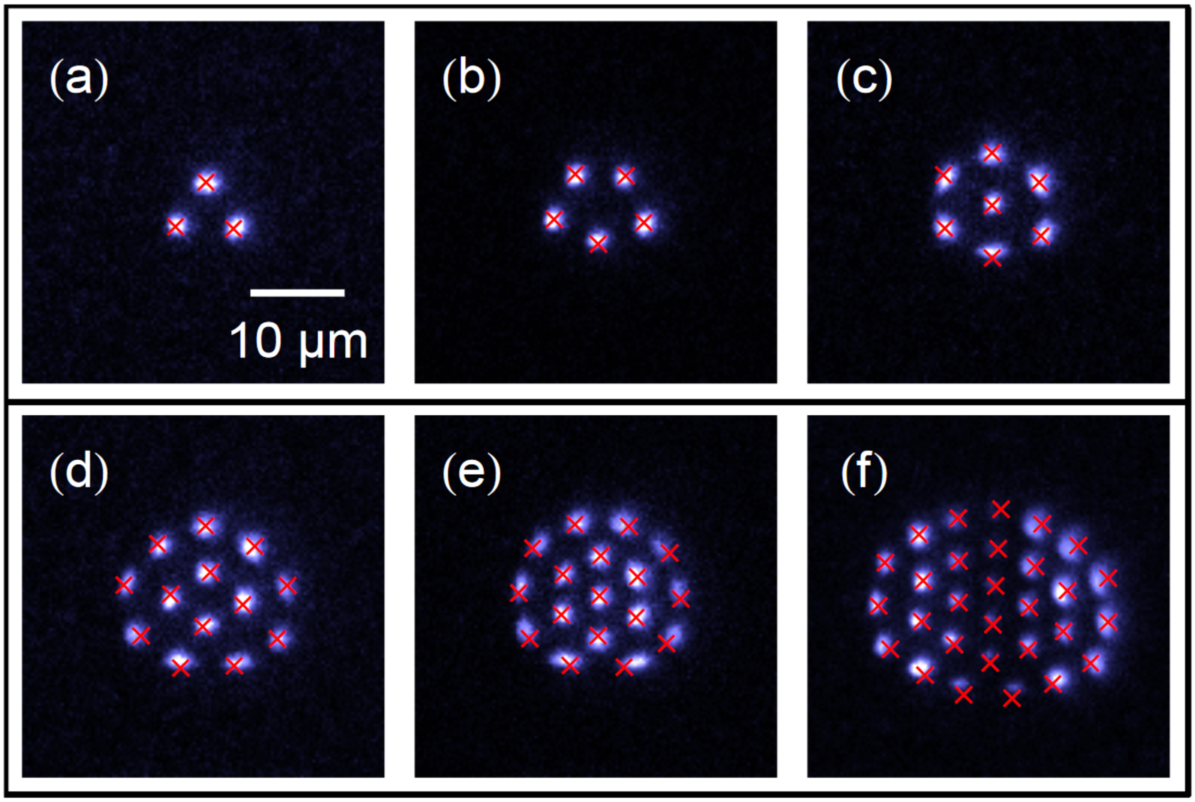

Figure 8.8: CCD images of crystals with 3, 5, 7, 13, 17, and 29 ions trapped in the radial-2D crystal phase, with measured center-of-mass frequencies $\omega_x = 2\pi \times 0.416$ MHz, $\omega_y = 2\pi \times 0.446$ MHz, $\omega_z = 2\pi \times 1.124$ MHz. Red crosses show the ion positions predicted under the pseudopotential approximation

the radial plane.

The ion positions can be predicted under the pseudopotential approximation once the trap frequencies are experimentally known. To measure the ion secular frequencies for a set of applied trap voltages, we inject an additional small RF voltage on the trap electrode DC 3 following Doppler cooling. This electrode is chosen since its contribution to the electric field at the ion has components along the x, y, and z directions. If the injected RF drive is in resonance with the ion's oscillation frequency, the ion will absorb energy and heat up, decreasing its fluorescence when probed with a detection laser beam [112]. Once the frequencies are determined, we use the procedure outlined in Sec 2.3 to predict the ion positions in the radial-2D crystal; results are shown as red crosses in Figure 8.8.

More complex processes are involved when laser cooling ion crystals in two- and three-dimensions as compared to the one-dimensional case. Ions away from the trap center experience micromotion, which leads to Doppler-shifted cooling transitions which depend on the micromotion amplitude at each ion position. For large crystals, this micromotion-induced Doppler shift can lead to dramatically different cooling rates for a crystal's outermost ions as compared to the inner ions [45]. Optimum Doppler cooling is often found further red-detuned than the typical single-ion detuning, which may result in relatively decreased fluorescence for the innermost ions (as seen in Figure 8.8f). For very large crystals, it may ultimately prove necessary to introduce multi-tone Doppler cooling to frequency-address ions at different radii, or to power-broaden the resonant transition as suggested in [45].

8.5.3 Ion Trajectory Analysis

In radial-2D crystals, ions located far from the origin experience the largest amplitude of micromotion. Following the process outlined in Sec 2.3 (and Appendix A), we calculate that the maximum radial micromotion amplitude in a 17-ion radial-2D crystal is < 650 nm, which is small compared to the $\sim 1\mu$m diffraction-limited spot size of our imaging system as well as the 5μm inter-ion spacing. The micromotion along the axial direction is calculated to be negligible due to the small Mathieu q_z parameter; this was confirmed in prior measurements using the "needle trap" geometry, where the radial-2D crystal was imaged from the side. Since the out-of-plane axial modes remain micromotion free in this geometry, these modes will be preferable for performing future quantum simulation experiments.

Close inspection of the ion trajectories in Figure 8.8 reveals a convex curvature, rather than the concave curvature which would be expected from driven micromotion (see calculation in Figure 8.2b). We attribute this result to thermally-driven, small-angle rotations of the ion crystal. Consider, for instance, a radial-2D crystal in a perfectly symmetric potential with degenerate radial secular frequencies. The crystal will be free to rotate with no energy penalty; when imaged on a CCD camera, the ions will appear as concentric rings. Although in our trap this degeneracy is explicitly broken, residual thermal energy in the crystal may still induce small azimuthal oscillations. We calculate that the ion excursions observed in Figure 8.8(e)-(f) are consistent with crystal temperatures of only ≈ 20 mK. We anticipate that this effect can be reduced by further breaking the degeneracy between the radial secular frequencies, by introducing multi-tone Doppler cooling [57], or by applying sub-Doppler cooling techniques such as resolved sideband cooling [50, 139] or Electromagnetically-Induced Transparency (EIT) cooling [121, 122].

8.6 Conclusion

Radial-2D crystals hold great promise as a platform for quantum simulation of exotic many-body materials but require carefully-designed RF traps to realize a robust implementation. In this work, we have presented the design of an open-endcap blade trap which allows for both stable confinement of radial-2D crystals as well as site resolved imaging of the triangular 2D lattice. The electrode geometry has been chosen so that the required trap potentials are accessible using reasonable laboratory voltages, and the use of tungsten as an electrode material limits potential damage from resistive heating or voltage flashover. Furthermore, we have implemented RF and DC electronics which lead to stable and low-noise operation of the trap.

CHAPTER 9

CONCLUSION AND OUTLOOK

In this thesis, I presented an experimental platform for performing quantum simulation protocol on a radial-2D lattice of $^{171}\mathrm{Yb}^+$ ions in an RF trap. Our characterization of a rod-style linear Paul trap shows that radial-2D crystals can be a robust platform, in which micromotion effects are essentially constrained to the radial plane, and axial vibrational modes remain cold and decoupled. The design and implementation of a blade-style RF trap tailored to optimal (and experimentally reasonable) trap parameters, permits site-resolved imaging of large radial-2D crystals. Our experimental observations of up to 29 ions in radial-2D arrays, imaged perpendicularly to the crystal plane, pave the way for 2D quantum simulation experiments. An integral component of quantum simulation yet to be demonstrated for radial-2D crystals is the creation and characterization of entangled states. System decoherence has thus far prevented us from providing definite proof of entanglement creation, though near-term hardware improvements are expected to increase coherence times past the entanglement detection threshold.

After verifying entanglement protocol, we will be able to use global laser beams to characterize the ground state and dynamical properties of frustrated 2D spin-models by measuring their excitations [23] and correlation functions (which can distinguish, for instance, between Néel states or Valence Bond Solid states [140]), and by tuning the relative contributions of inherent geometric and long-range frustration. In future work, we also anticipate implementing individual-ion addressing, which will further expand the classes of quantum materials that may be simulated using radial-2D crystals in linear RF traps. Shelving of specific ions will allow for the quantum simulation of more complex lattice geometries, such as Kagome, which are believed to support spin-liquid phases [26, 23, 25, 141, 142]. In the long term, radial crystals with individual addressing may provide a naturally scalable solution for fault-tolerant quantum computing [28, 29] or simplify preparations for one-way quantum computing schemes [30, 31].

An optimized protocol for pulsed SBC was presented, along with a time-averaged thermometry method which more accurately measures ion temperature after extensive SBC compared to standard techniques. This time-average technique opens new possibilities for noise characterization in trapped ion systems, and the SBC graph representation method may be extended to multiple ions and multiple modes. However, even with optimized protocol, SBC will remain the longest experiment time component by a large margin. For one ion, a typical experiment can require minutes of sideband cooling. When ion number is increased, the SBC time also increases as 1) we must cool along more motional modes, 2) we start from a higher temperature due to micromotion effects on Doppler cooling, and 3) we cannot simultaneously cool multiple motional modes with SBC, meaning the COM mode heats while the other modes are being cooled. We plan to significantly reduce the amount of SBC pulses required by introducing an intermediate round of Electromagnetically-Induced Transparency (EIT) cooling in between the Doppler cooling and SBC sequences. EIT cooling provides fast sub-Doppler cooling over all motional modes in < 1 ms and has been successfully implemented in $^{171}\mathrm{Yb}^{+}$ systems [122, 121].

Finally, we have measured qubit susceptibility to small-dose radiation and found no quantifiable degradation for any of the measurements performed. This finding is encouraging for the long-term prospects of using ion-based quantum information systems in hostile environments. In future experiments, we will work with higher-dose radiation sources to better quantify possible points of failure and guide design requirements for system shielding or alternative quantum information protocols robust to radiation-induced errors. Such investigations are primarily complicated by the difficulty of integrating high-dose radiation sources within standard atomic-physics laboratories. To circumvent this difficulty, we are developing a portable ion trap based on laser-cooled $^{171}\mathrm{Yb}^{+}$ ions. The entire system is accommodated into two mobile rack units comprised of laser, electronics, and physics package subsystems, including a lumped circuit RLC resonator. The compact and robust package is specifically designed to fit within test chambers located at high-dose radiation test facilities, and will support future ion-trap-based quantum science in extreme environments.

APPENDIX A

FLOQUET-LYAPUNOV SOLUTION OF ION MOTION

A.1 Dynamic Solution of Ion Motion

In this section, we precisely solve the normal modes and micromotion of N ions in a 2D crystal by the Floquet–Lyapunov transformation [116, 117].

The potential energy of the ions in our Paul trap can be written as

$$\begin{aligned} V &= V_{trap} + V_{coulomb} \\ &= \sum_{i}^{n} \frac{1}{2}(\Lambda_x x_i^2 + \Lambda_y y_i^2 + \Lambda_z z_i^2) + \sum_{i \neq j} \frac{1}{2} \frac{q^2}{4\pi\epsilon_0} \|r_i - r_j\|^{-1} \end{aligned} \tag{A.1}$$

where $r_i = \{x_i, y_i, z_i\}$ is the vector coordinate of ion i, and the time-dependent trapping terms are given by

$$\Lambda_\alpha = B_\alpha + A_\alpha \cos(\Omega_t t),\ \alpha \in \{x, y, z\} \tag{A.2}$$

A_α, B_α represent the real trap electric potential coefficients. In Sec 2.3 we calculated the secular frequencies under the pseudopotential approximation, which may be expressed as

$$V_{pseudo} = \frac{1}{2} m \sum_{i}^{n} (\omega_x^2 x_i^2 + \omega_y^2 y_i^2 + \omega_z^2 z_i^2) \tag{A.3}$$

The total potential energy could then be written as

$$\begin{aligned} V &= V_1 + V_2 \\ &= (V_{pseudo} + V_{coulomb}) + (V_{trap} - V_{pseudo}) \end{aligned} \tag{A.4}$$

Treating V_2 as the perturbation, we expand the time-dependent positions $\{R_{i,\alpha}(t)\}$ around the minimum-configuration locations $\{R_{i,\alpha}^0\} = (x_1^{(0)}, y_1^{(0)}, z_1^{(0)}, \ldots, x_N^{(0)}, y_N^{(0)}, z_N^{(0)})$ that are obtained from the secular part of $V_1 = V_{pseudo} + V_{coulomb}$. The time-dependent positions can then be written in terms of the normal modes S_j by setting

$$R_{i,\alpha}(t) = R^0_{i,\alpha} + r_{i,\alpha} = R^0_{i,\alpha} + \sum_j^{3N} \Gamma_{i,j} S_j(t) \tag{A.5}$$

where $\Gamma_{i,j}$ are the matrix elements of the normal mode vectors, with rows indexed by the N ions i in the three directions α, and columns indexed by the $3N$ normal modes j.

We then plug Equation A.5 into Equation A.4, write the potential in terms of the normal modes, and keep the first two terms:

$$\begin{aligned} V &= \frac{1}{2}\vec{S}^T \Lambda \vec{S} + \sum_{i,\alpha}^{N} (\Lambda_\alpha - \frac{1}{2} m\omega_\alpha^2)(R^0_{i,\alpha} + \sum_j^{3N} \Gamma_{i,j} S_j)^2 + \ldots \\ &\approx \frac{1}{2}\vec{S}^T \Lambda \vec{S} + ((\vec{R}^0)^T + \vec{S}^T \Gamma)(W_1 + W_2 cos\Omega t)(\vec{R}^0 + \Gamma^T \vec{S}) \end{aligned} \tag{A.6}$$

where $\Lambda = \text{diag}\{\Omega^2_{i\alpha}\}$, $W_1 = \text{diag}\{B_\alpha - \frac{1}{2} m\omega_\alpha^2\}$, $W_2 = \text{diag}\{A_\alpha\}$, and Ω_i is the ith normal frequency in α direction. The linearized equation of motion derived from Equation A.6 is

$$mS'' + (\Lambda + J) \cdot S + P + (L + Y \cdot S) \cos \Omega t = 0 \tag{A.7}$$

where

$$\begin{aligned} \vec{P} &= \Gamma \cdot W_1 \cdot \vec{R}^0 + (\vec{R}^0)^T \cdot W_1 \Gamma^T \\ \vec{L} &= \Gamma \cdot W_2 \cdot \vec{R}^0 + (\vec{R}^0)^T \cdot W_2 \Gamma^T \\ J &= \Gamma \cdot W_1 \cdot \Gamma^T + (\Gamma \cdot W_1 \cdot \Gamma^T)^T \\ Y &= \Gamma \cdot W_2 \cdot \Gamma^T + (\Gamma \cdot W_2 \cdot \Gamma^T)^T \end{aligned} \tag{A.8}$$

Let

$$\begin{aligned} A &= (\Lambda + J)\frac{4}{\Omega^2 m} \\ Q &= -\frac{1}{2}Y\frac{4}{\Omega^2 m} \\ \vec{G} &= -\vec{P}\frac{4}{\Omega^2 m} \\ \vec{F} &= -\frac{1}{2}\vec{L}\frac{4}{\Omega^2 m} \end{aligned} \tag{A.9}$$

We then have a simplified inhomogeneous Mathieu Matrix Equation from Equation A.7

$$\vec{S}'' + (A - 2Q\cos\Omega t)\cdot\vec{S} = \vec{G} + 2\vec{F}\cos\Omega t \tag{A.10}$$

where F and G are $3N$-component constant vectors. We assign the basic π periodic solution $\vec{S} = \sum_{-\infty}^{\infty}\vec{B}_{2n}e^{i(2n)t}$ in the equations of motion (Equation A.10) to obtain

$$\begin{gathered} (A - 4n^2)\vec{B}_{2n} - Q(\vec{B}_{2n-2} + \vec{B}_{2n+2}) = \\ \vec{G}\delta_{1,n} + \vec{F}(\delta_{n,1} + \delta_{n,-1}) \end{gathered} \tag{A.11}$$

By defining $C_{2n} = A - 4n^2$ and using $B_{2n} = B_{-2n}$, we can write infinite recursion relations for $\vec{B}_{2n}$,

$$A\vec{B}_0 - 2Q\vec{B}_2 = \vec{G} \tag{A.12}$$

$$C_2\vec{B}_2 - Q(\vec{B}_0 + \vec{B}_4) = \vec{F} \tag{A.13}$$

$$C_{2n}\vec{B}_{2n} - Q(\vec{B}_{2n-2} + \vec{B}_{2n+2}) = 0, (n \geq 2) \tag{A.14}$$

Equation A.14 immediately gives a recursion relation in the form of Equation A.10, which allows us to get the infinite inversions expression

$$\vec{B}_4 = T_2Q\vec{B}_2 \tag{A.15}$$

where

$$T_2 = [C_4 - Q[C_6 - Q[C_8 - ...]^{-1}Q]^{-1}Q]^{-1} \tag{A.16}$$

Substituting Equation A.15 into Equation A.12 and Equation A.13 we obtain the linear system

$$\begin{pmatrix} A & -2Q \\ -Q & R_2 - QT_2Q \end{pmatrix} \begin{pmatrix} \vec{B}_0 \\ \vec{B}_2 \end{pmatrix} = \begin{pmatrix} \vec{G} \\ \vec{F} \end{pmatrix} \tag{A.17}$$

which can be solved to find the coefficients of the normal modes $\vec{S}$, and the micromotion terms $\vec{r} = \Gamma^T \cdot \vec{S}$.

APPENDIX B

VOIGT DISTIBUTION

A Voigt function is the convolution of a Gaussian lineshape G and Lorentzian lineshape L:

$$V(\delta;\sigma,\Gamma)=\int_{-\infty}^{\infty}G(\delta';\sigma)L(\delta-\delta';\Gamma)d\delta' \tag{B.1}$$

where δ is the detuning and $G(\delta;\sigma)$ is the centered Gaussian profile

$$\frac{1}{\sqrt{2\pi\sigma}}\exp(-\frac{\delta^2}{2\sigma^2}) \tag{B.2}$$

with Doppler width

$$\sigma\equiv\Delta\nu_G=\sqrt{\frac{k_BT}{m\lambda^2}}, \tag{B.3}$$

where $\lambda = 369$ nm, k_B is Boltzmann's constant, and T is the ion temperature. For our trap geometry,

$$\Delta\nu_G=2\sqrt{\frac{(2\ln 2)k_B}{m\lambda^2}}\sqrt{T_r\cos^2\theta+T_z\sin^2\theta}, \tag{B.4}$$

since our fluorescence beam intersects the crystal plane at an angle ($\theta = 45°$) and is therefore sensitive to both the radial and axial temperatures T_r and T_z.

The Lorentzian contribution

$$L(\delta;\Gamma)=\frac{1}{\pi}\frac{\Gamma}{\delta^2+\Gamma^2} \tag{B.5}$$

comes from the power-broadened natural linewidth

$$\Delta\nu_L=\Gamma\sqrt{1+s}=2\pi\times 22\text{ MHz}, \tag{B.6}$$

where $\Gamma = 2\pi\times 19.6$ MHz is the natural linewidth of the ^{171}Yb^{+} 369.5 nm $^2S_{1/2}\rightarrow^2P_{1/2}$ transition and $s = .3$ is the laser saturation parameter.

APPENDIX C

THERMOMETRY

C.1 Ratio Thermometry

The ratio method [59] estimates the average harmonic state $\bar{n}$ of a thermal distribution $p_{\text{th}}(n) = \bar{n}^n/(\bar{n}+1)^{n+1}$ by using the unique property $p_{\text{th}}(n+1) = p_{\text{th}}(n)\bar{n}/(\bar{n}+1)$.

Given a RSB Rabi oscillation

$$\begin{aligned} P_{\uparrow}^{\text{RSB}}(t) &= \sum_{n=1}^{\infty} p_{\text{th}}(n) \sin^2\left(\frac{\Omega_{n,n-1}t}{2}\right) \\ &= \frac{\bar{n}}{\bar{n}+1} \sum_{n=0}^{\infty} p_{\text{th}}(n) \sin^2\left(\frac{\Omega_{n,n+1}t}{2}\right) \end{aligned} \tag{C.1}$$

and a BSB Rabi oscillation

$$P_{\uparrow}^{\text{BSB}}(t) = \sum_{n=0}^{\infty} p_{\text{th}}(n) \sin^2\left(\frac{\Omega_{n,n+1}t}{2}\right) \tag{C.2}$$

their ratio is a function $\bar{n}$ for any time t or frequency detuning

$$r \equiv \frac{P_{\uparrow}^{\text{RSB}}(t)}{P_{\uparrow}^{\text{BSB}}(t)} = \frac{\bar{n}}{\bar{n}+1}. \tag{C.3}$$

C.2 SVD Thermometry

The SVD method [66] is a frequency-domain analysis of a RSB or BSB Rabi oscillation. In this method, $\Omega_{n,n'}$ is independently calculated, and its contribution to the overall Rabi oscillation is constructed into a rectangular matrix (dimension $M \times N$) with M time steps taken in the experiment, considering N harmonic states of interest, and elements $b_n(t) = \sin^2(\Omega_{n,n-1}t/2)$. This matrix acts on the harmonic distribution vector ($N \times 1$) to produce a vector representing the measured fluorescence at each experimental time step. For example, a BSB oscillation would be constructed as follows

$$\begin{pmatrix} b_1(t_0) & b_2(t_0) & \dots \\ b_1(t_1) & b_2(t_1) & \dots \\ b_1(t_2) & b_2(t_2) & \dots \\ \vdots & \vdots & \ddots \end{pmatrix} \begin{pmatrix} p(0) \\ p(1) \\ p(2) \\ \vdots \end{pmatrix} = \begin{pmatrix} P_\uparrow^{\mathrm{BSB}}(t_0) \\ P_\uparrow^{\mathrm{BSB}}(t_1) \\ P_\uparrow^{\mathrm{BSB}}(t_2) \\ \vdots \end{pmatrix}. \tag{C.4}$$

Using singular value decomposition (SVD), the rectangular matrix is pseudo-inverted to solve for the harmonic distribution vector. Once this vector of $p(n)$ is known, the average occupation is found by calculating $\bar{n} = \sum np(n)$.

REFERENCES

[1] A. Aspect, J. Dalibard, and G. Roger, “Experimental test of bell’s inequalities using time-varying analyzers,” *Physical review letters*, vol. 49, no. 25, p. 1804, 1982.

[2] R. P. Feynman, “Simulating physics with computers,” in *Feynman and computation*, CRC Press, 2018, pp. 133–153.

[3] S. Lloyd, “Universal quantum simulators,” *Science*, pp. 1073–1078, 1996.

[4] D. Deutsch, “Quantum theory, the church–turing principle and the universal quantum computer,” *Proceedings of the Royal Society of London. A. Mathematical and Physical Sciences*, vol. 400, no. 1818, pp. 97–117, 1985.

[5] D. P. DiVincenzo, “The physical implementation of quantum computation,” *Fortschritte der Physik: Progress of Physics*, vol. 48, no. 9-11, pp. 771–783, 2000.

[6] K. Bharti *et al.*, “Noisy intermediate-scale quantum (nisq) algorithms,” *arXiv preprint arXiv:2101.08448*, 2021.

[7] M. Suzuki, “Generalized trotter’s formula and systematic approximants of exponential operators and inner derivations with applications to many-body problems,” *Communications in Mathematical Physics*, vol. 51, no. 2, pp. 183–190, 1976.

[8] I. Buluta and F. Nori, “Quantum simulators,” *Science*, vol. 326, no. 5949, pp. 108–111, 2009.

[9] C. Monroe *et al.*, “Programmable quantum simulations of spin systems with trapped ions,” *Reviews of Modern Physics*, vol. 93, no. 2, p. 025 001, 2021.

[10] F. Schäfer, T. Fukuhara, S. Sugawa, Y. Takasu, and Y. Takahashi, “Tools for quantum simulation with ultracold atoms in optical lattices,” *Nature Reviews Physics*, vol. 2, no. 8, pp. 411–425, 2020.

[11] C. Qiu, X. Nie, and D. Lu, “Quantum simulations with nuclear magnetic resonance system,” *Chinese Physics B*, vol. 30, no. 4, p. 048 201, 2021.

[12] G.-S. Paraoanu, “Recent progress in quantum simulation using superconducting circuits,” *Journal of Low Temperature Physics*, vol. 175, no. 5, pp. 633–654, 2014.

[13] J. I. Cirac and P. Zoller, “Quantum computations with cold trapped ions,” *Physical review letters*, vol. 74, no. 20, p. 4091, 1995.

[14] C. Monroe, D. M. Meekhof, B. E. King, W. M. Itano, and D. J. Wineland, "Demonstration of a fundamental quantum logic gate," *Physical review letters*, vol. 75, no. 25, p. 4714, 1995.

[15] F. Schmidt-Kaler *et al.*, "Realization of the cirac–zoller controlled-not quantum gate," *Nature*, vol. 422, no. 6930, pp. 408–411, 2003.

[16] J. M. Pino *et al.*, "Demonstration of the qccd trapped-ion quantum computer architecture," *arXiv preprint arXiv:2003.01293*, 2020.

[17] C. D. Bruzewicz, J. Chiaverini, R. McConnell, and J. M. Sage, "Trapped-ion quantum computing: Progress and challenges," *Applied Physics Reviews*, vol. 6, no. 2, p. 021 314, 2019.

[18] L. Egan *et al.*, "Fault-tolerant control of an error-corrected qubit," *Nature*, vol. 598, no. 7880, pp. 281–286, 2021.

[19] J. W. Britton *et al.*, "Engineered two-dimensional ising interactions in a trapped-ion quantum simulator with hundreds of spins," *Nature*, vol. 484, no. 7395, pp. 489–492, 2012.

[20] A. Friedenauer, H. Schmitz, J. T. Glueckert, D. Porras, and T. Schätz, "Simulating a quantum magnet with trapped ions," *Nature Physics*, vol. 4, no. 10, pp. 757–761, 2008.

[21] P. Wang *et al.*, "Single ion qubit with estimated coherence time exceeding one hour," *Nature communications*, vol. 12, no. 1, pp. 1–8, 2021.

[22] D. Leibfried, R. Blatt, C. Monroe, and D. Wineland, "Quantum dynamics of single trapped ions," *Reviews of Modern Physics*, vol. 75, no. 1, p. 281, 2003.

[23] L. Balents, "Spin liquids in frustrated magnets," *Nature*, vol. 464, no. 7286, pp. 199–208, 2010.

[24] A. Bermudez, J. Almeida, F. Schmidt-Kaler, A. Retzker, and M. B. Plenio, "Frustrated quantum spin models with cold coulomb crystals," *Physical review letters*, vol. 107, no. 20, p. 207 209, 2011.

[25] R. Nath, M. Dalmonte, A. W. Glaetzle, P. Zoller, F. Schmidt-Kaler, and R. Gerritsma, "Hexagonal plaquette spin–spin interactions and quantum magnetism in a two-dimensional ion crystal," *New Journal of Physics*, vol. 17, no. 6, p. 065 018, 2015.

[26] P. Richerme, "Two-dimensional ion crystals in radio-frequency traps for quantum simulation," *Physical Review A*, vol. 94, no. 3, p. 032 320, 2016.

[27] B. Yoshimura, M. Stork, D. Dadic, W. C. Campbell, and J. K. Freericks, “Creation of two-dimensional coulomb crystals of ions in oblate paul traps for quantum simulations,” *EPJ Quantum Technology*, vol. 2, no. 1, p. 2, 2015.

[28] S.-T. Wang, C. Shen, and L.-M. Duan, “Quantum computation under micromotion in a planar ion crystal,” *Scientific Reports*, vol. 5, p. 8555, 2015.

[29] C. Shen and L.-M. Duan, “High-fidelity quantum gates for trapped ions under micromotion,” *Physical Review A*, vol. 90, no. 2, p. 022 332, 2014.

[30] R. Raussendorf and H. J. Briegel, “A one-way quantum computer,” *Physical Review Letters*, vol. 86, no. 22, p. 5188, 2001.

[31] H. Wunderlich, C. Wunderlich, K. Singer, and F. Schmidt-Kaler, “Two-dimensional cluster-state preparation with linear ion traps,” *Physical Review A*, vol. 79, no. 5, p. 052 324, 2009.

[32] M. Gärttner, J. G. Bohnet, A. Safavi-Naini, M. L. Wall, J. J. Bollinger, and A. M. Rey, “Measuring out-of-time-order correlations and multiple quantum spectra in a trapped-ion quantum magnet,” *Nature Physics*, vol. 13, no. 8, pp. 781–786, 2017.

[33] M. Mielenz *et al.*, “Arrays of individually controlled ions suitable for two-dimensional quantum simulations,” *Nature communications*, vol. 7, no. 1, pp. 1–9, 2016.

[34] F. Rajabi *et al.*, “Dynamical hamiltonian engineering of 2d rectangular lattices in a one-dimensional ion chain,” *npj Quantum Information*, vol. 5, no. 1, pp. 1–7, 2019.

[35] A. Rasmusson, M. D’Onofrio, Y. Xie, J. Cui, and P. Richerme, “Optimized pulsed sideband cooling and enhanced thermometry of trapped ions,” *Physical Review A*, vol. 104, no. 4, p. 043 108, 2021.

[36] J. Cui, A. Rasmusson, M. D’Onofrio, Y. Xie, E. Wolanski, and P. Richerme, “Susceptibility of trapped-ion qubits to low-dose radiation sources,” *Journal of Physics B: Atomic, Molecular and Optical Physics*, vol. 54, no. 13, 13LT01, 2021.

[37] M. D’Onofrio, Y. Xie, A. Rasmusson, E. Wolanski, J. Cui, and P. Richerme, “Radial two-dimensional ion crystals in a linear paul trap,” *Physical Review Letters*, vol. 127, no. 2, p. 020 503, 2021.

[38] Y. Xie, J. Cui, M. D’Onofrio, A. Rasmusson, S. W. Howell, and P. Richerme, “An open-endcap blade trap for radial-2d ion crystals,” *Quantum Science and Technology*, vol. 6, no. 4, p. 044 009, 2021.

[39] W. Paul, “Electromagnetic traps for charged and neutral particles,” *Reviews of modern physics*, vol. 62, no. 3, p. 531, 1990.

[40] D. H. Dubin, "Theory of structural phase transitions in a trapped coulomb crystal," *Physical review letters*, vol. 71, no. 17, p. 2753, 1993.

[41] D. Berkeland and M. Boshier, "Destabilization of dark states and optical spectroscopy in zeeman-degenerate atomic systems," *Physical Review A*, vol. 65, no. 3, p. 033 413, 2002.

[42] M. Johanning *et al.*, "Resonance-enhanced isotope-selective photoionization of ybi for ion trap loading," *Applied Physics B*, vol. 103, no. 2, pp. 327–338, 2011.

[43] H. J. Metcalf and P. van der Straten, "Laser cooling and trapping of atoms," *JOSA B*, vol. 20, no. 5, pp. 887–908, 2003.

[44] W. M. Itano and D. Wineland, "Laser cooling of ions stored in harmonic and penning traps," *Physical Review A*, vol. 25, no. 1, p. 35, 1982.

[45] R. DeVoe, J. Hoffnagle, and R. Brewer, "Role of laser damping in trapped ion crystals," *Physical Review A*, vol. 39, no. 9, p. 4362, 1989.

[46] A. Kato *et al.*, "Two-tone doppler cooling of radial two-dimensional crystals in a radiofrequency ion trap," *Physical Review A*, vol. 105, no. 2, p. 023 101, 2022.

[47] R. Islam, "Quantum simulation of interacting spin models with trapped ions," *PhD Thesis*, 2012.

[48] C. Lee, "Ytterbium ion qubit state detection on an iccd camera," *Honors Thesis*, 2012.

[49] C. Senko, "Dynamics and excited states of quantum many-body spin chains with trapped ions," *PhD Thesis*, 2014.

[50] D. J. Wineland, C. Monroe, W. M. Itano, D. Leibfried, B. E. King, and D. M. Meekhof, "Experimental issues in coherent quantum-state manipulation of trapped atomic ions," *Journal of Research of the National Institute of Standards and Technology*, vol. 103, no. 3, p. 259, 1998.

[51] K. Mølmer and A. Sørensen, "Multiparticle entanglement of hot trapped ions," *Physical Review Letters*, vol. 82, no. 9, p. 1835, 1999.

[52] A. Sørensen and K. Mølmer, "Quantum computation with ions in thermal motion," *Physical review letters*, vol. 82, no. 9, p. 1971, 1999.

[53] A. Sorensen and K. Molmer, "Entanglement and quantum computation with ions in thermal motion," *Physical Review A*, vol. 62, no. 2, p. 022 311, 2000.

[54] J. Siverns, L. Simkins, S. Weidt, and W. Hensinger, "On the application of radio frequency voltages to ion traps via helical resonators," *Applied Physics B*, vol. 107, no. 4, pp. 921–934, 2012.

[55] M. W. van Mourik *et al.*, "Rf-induced heating dynamics of noncrystallized trapped ions," *Physical Review A*, vol. 105, no. 3, p. 033 101, 2022.

[56] R. Islam *et al.*, "Beat note stabilization of mode-locked lasers for quantum information processing," *Optics letters*, vol. 39, no. 11, pp. 3238–3241, 2014.

[57] M-Labs, "Artiq manual," *https://m-labs.hk/artiq/manual/index.html*,

[58] M. OpenCourseWare, "Doppler-free spectroscopy," *https://ocw.mit.edu/courses/8-13-14-experimental-physics-i-ii-junior-lab-fall-2016-spring-2017/pages/experiments/doppler-free-laser-spectroscopy/*,

[59] F. Diedrich, J. C. Bergquist, W. M. Itano, and D. J. Wineland, "Laser cooling to the zero-point energy of motion," *Physical Review Letters*, vol. 62, pp. 403–406, 4 Jan. 1989.

[60] I. Marzoli, J. I. Cirac, R. Blatt, and P. Zoller, "Laser cooling of trapped three-level ions: Designing two-level systems for sideband cooling," *Physical Review A*, vol. 49, no. 4, p. 2771, 1994.

[61] C. Monroe *et al.*, "Resolved-sideband raman cooling of a bound atom to the 3d zero-point energy," *Physical Review Letters*, vol. 75, no. 22, p. 4011, 1995.

[62] B. E. King *et al.*, "Cooling the collective motion of trapped ions to initialize a quantum register," *Physical Review Letters*, vol. 81, no. 7, p. 1525, 1998.

[63] J.-S. Chen *et al.*, "Efficient-sideband-cooling protocol for long trapped-ion chains," *Phys. Rev. A*, vol. 102, p. 043 110, 4 Oct. 2020.

[64] J. Pino *et al.*, "Demonstration of the trapped-ion quantum ccd computer architecture," *Nature*, vol. 592, no. 7853, pp. 209–213, 2021.

[65] M. Brownnutt, M. Kumph, P. Rabl, and R. Blatt, "Ion-trap measurements of electric-field noise near surfaces," *Reviews of Modern Physics*, vol. 87, no. 4, p. 1419, 2015.

[66] D. M. Meekhof, C. Monroe, B. E. King, W. M. Itano, and D. J. Wineland, "Generation of nonclassical motional states of a trapped atom," *Physical Review Letters*, vol. 76, no. 11, p. 1796, 1996.

[67] J.-S. Chen, S. M. Brewer, C. W. Chou, D. J. Wineland, D. R. Leibrandt, and D. B. Hume, "Sympathetic ground state cooling and time-dilation shifts in an al 27+ optical clock," *Physical Review Letters*, vol. 118, no. 5, p. 053 002, 2017.

[68] S. Stenholm, “The semiclassical theory of laser cooling,” *Reviews of Modern Physics*, vol. 58, no. 3, p. 699, 1986.

[69] J. Eschner, G. Morigi, F. Schmidt-Kaler, and R. Blatt, “Laser cooling of trapped ions,” *J. Opt. Soc. Am. B*, vol. 20, no. 5, pp. 1003–1015, May 2003.

[70] D. J. Wineland and W. M. Itano, “Laser cooling of atoms,” *Physical Review A*, vol. 20, no. 4, p. 1521, 1979.

[71] W. Neuhauser, M. Hohenstatt, P. Toschek, and H. Dehmelt, “Optical-sideband cooling of visible atom cloud confined in parabolic well,” *Physical Review Letters*, vol. 41, no. 4, p. 233, 1978.

[72] D. J. Wineland and W. M. Itano, “Laser cooling,” *Physics Today*, vol. 40, no. 6, pp. 34–47, 1987.

[73] H. Che, K. Deng, Z. T. Xu, W. H. Yuan, J. Zhang, and Z. H. Lu, “Efficient raman sideband cooling of trapped ions to their motional ground state,” *Phys. Rev. A*, vol. 96, p. 013 417, 1 Jul. 2017.

[74] M. D’Onofrio, Y. Xie, A. J. Rasmusson, E. Wolanski, J. Cui, and P. Richerme, “Radial two-dimensional ion crystals in a linear paul trap,” *Physical Review Letters*, vol. 127, no. 2, p. 020 503, 2021.

[75] C. Roos *et al.*, “Quantum state engineering on an optical transition and decoherence in a paul trap,” *Physical Review Letters*, vol. 83, no. 23, p. 4713, 1999.

[76] C. Hempel, “Digital quantum simulation, schrödinger cat state spectroscopy and setting up a linear ion trap,” *Universität Innsbruck, Ph.D. Dissertation*, 2014.

[77] L. Deslauriers *et al.*, “Zero-point cooling and low heating of trapped cd+ 111 ions,” *Physical Review A*, vol. 70, no. 4, p. 043 408, 2004.

[78] Y. Wan, F. Gebert, F. Wolf, and P. O. Schmidt, “Efficient sympathetic motional-ground-state cooling of a molecular ion,” *Physical Review A*, vol. 91, no. 4, p. 043 425, 2015.

[79] C. R. Harris *et al.*, “Array programming with NumPy,” *Nature*, vol. 585, no. 7825, pp. 357–362, Sep. 2020.

[80] A. P. Vepsäläinen *et al.*, “Impact of ionizing radiation on superconducting qubit coherence,” *Nature*, vol. 584, no. 7822, pp. 551–556, 2020.

[81] M. McEwen *et al.*, “Resolving catastrophic error bursts from cosmic rays in large arrays of superconducting qubits,” *arXiv preprint arXiv:2104.05219*, 2021.

[82] J. M. Martinis, M. Ansmann, and J. Aumentado, "Energy decay in superconducting josephson-junction qubits from nonequilibrium quasiparticle excitations," *Physical Review Letters*, vol. 103, no. 9, p. 097 002, 2009.

[83] A. Kozorezov, A. Volkov, J. Wigmore, A. Peacock, A. Poelaert, and R. Den Hartog, "Quasiparticle-phonon downconversion in nonequilibrium superconductors," *Physical Review B*, vol. 61, no. 17, p. 11 807, 2000.

[84] A. G. Fowler and J. M. Martinis, "Quantifying the effects of local many-qubit errors and nonlocal two-qubit errors on the surface code," *Physical Review A*, vol. 89, no. 3, p. 032 316, 2014.

[85] S. Heugel, M. Fischer, V. Elman, R. Maiwald, M. Sondermann, and G. Leuchs, "Resonant photo-ionization of yb+ to yb2+," *Journal of Physics B: Atomic, Molecular and Optical Physics*, vol. 49, no. 1, p. 015 002, 2015.

[86] G. W. Drake, *Atomic, molecular and optical physics handbook*. Oxford Univ. Press, 1996.

[87] J. E. Turner, *Atoms, radiation, and radiation protection*. Weinheim: John Wiley & Sons, 2008.

[88] J. F. Ziegler, M. D. Ziegler, and J. P. Biersack, "Srim–the stopping and range of ions in matter (2010)," *Nuclear Instruments and Methods in Physics Research Section B: Beam Interactions with Materials and Atoms*, vol. 268, no. 11-12, pp. 1818–1823, 2010.

[89] P. Hovington, D. Drouin, and R. Gauvin, "Casino: A new monte carlo code in c language for electron beam interaction—part i: Description of the program," *Scanning*, vol. 19, no. 1, pp. 1–14, 1997.

[90] M. Berger, "Xcom: Photon cross sections database," *http://www.nist.gov/pml/data/xcom/index.cfm*, 2010.

[91] E. Knill, "Quantum computing with realistically noisy devices," *Nature*, vol. 434, no. 7029, pp. 39–44, 2005.

[92] R. Raussendorf and J. Harrington, "Fault-tolerant quantum computation with high threshold in two dimensions," *Physical Review Letters*, vol. 98, no. 19, p. 190 504, 2007.

[93] D. Nigg *et al.*, "Quantum computations on a topologically encoded qubit," *Science*, vol. 345, no. 6194, pp. 302–305, 2014.

[94] N. M. Linke *et al.*, "Fault-tolerant quantum error detection," *Science Advances*, vol. 3, no. 10, e1701074, 2017.

[95] L. Egan *et al.*, “Fault-tolerant operation of a quantum error-correction code,” *arXiv preprint arXiv:2009.11482*, 2020.

[96] T. M. Stace, S. D. Barrett, and A. C. Doherty, “Thresholds for topological codes in the presence of loss,” *Physical Review Letters*, vol. 102, no. 20, p. 200 501, 2009.

[97] R. Stricker *et al.*, “Experimental deterministic correction of qubit loss,” *Nature*, vol. 585, no. 7824, pp. 207–210, 2020.

[98] C. Monroe and J. Kim, “Scaling the ion trap quantum processor,” *Science*, vol. 339, no. 6124, pp. 1164–1169, 2013.

[99] N. M. Linke *et al.*, “Experimental comparison of two quantum computing architectures,” *Proceedings of the National Academy of Sciences*, vol. 114, no. 13, pp. 3305–3310, 2017.

[100] P. Richerme *et al.*, “Non-local propagation of correlations in quantum systems with long-range interactions,” *Nature*, vol. 511, no. 7508, pp. 198–201, 2014.

[101] J. P. Gaebler *et al.*, “High-fidelity universal gate set for be 9+ ion qubits,” *Physical Review Letters*, vol. 117, no. 6, p. 060 505, 2016.

[102] C. J. Ballance, T. P. Harty, N. M. Linke, M. A. Sepiol, and D. M. Lucas, “High-fidelity quantum logic gates using trapped-ion hyperfine qubits,” *Physical Review Letters*, vol. 117, no. 6, p. 060 504, 2016.

[103] M. Block, A. Drakoudis, H. Leuthner, P. Seibert, and G. Werth, “Crystalline ion structures in a paul trap,” *Journal of Physics B: Atomic, Molecular and Optical Physics*, vol. 33, no. 11, p. L375, 2000.

[104] H. Kaufmann *et al.*, “Precise experimental investigation of eigenmodes in a planar ion crystal,” *Physical Review Letters*, vol. 109, no. 26, p. 263 003, 2012.

[105] Y. Wang *et al.*, “Coherently manipulated 2d ion crystal in a monolithic paul trap,” *Advanced Quantum Technologies*, vol. 3, no. 11, p. 2 000 068, 2020.

[106] I. M. Buluta, M. Kitaoka, S. Georgescu, and S. Hasegawa, “Investigation of planar coulomb crystals for quantum simulation and computation,” *Physical Review A*, vol. 77, no. 6, p. 062 320, 2008.

[107] I. Buluta and S. Hasegawa, “The structure of planar coulomb crystals in rf traps,” *Journal of Physics B: Atomic, Molecular and Optical Physics*, vol. 42, no. 15, p. 154 004, 2009.

[108] M. Ivory, A. Kato, A. Hasanzadeh, and B. Blinov, “A paul trap with sectored ring electrodes for experiments with two-dimensional ion crystals,” *Review of Scientific Instruments*, vol. 91, no. 5, p. 053 201, 2020.

[109] V. L. Ryjkov, X. Z. Zhao, and H. A. Schuessler, "Simulations of the rf heating rates in a linear quadrupole ion trap," *Physical Review A*, vol. 71, no. 3, p. 033 414, 2005.

[110] C. B. Zhang, D. Offenberg, B. Roth, M. A. Wilson, and S. Schiller, "Molecular-dynamics simulations of cold single-species and multispecies ion ensembles in a linear paul trap," *Physical Review A*, vol. 76, no. 1, p. 012 719, 2007.

[111] K. Chen, S. T. Sullivan, W. G. Rellergert, and E. R. Hudson, "Measurement of the coulomb logarithm in a radio-frequency paul trap," *Physical Review Letters*, vol. 110, no. 17, p. 173 003, 2013.

[112] H. Nägerl, D. Leibfried, F. Schmidt-Kaler, J. Eschner, and R. Blatt, "Coherent excitation of normal modes in a string of ca+ ions," *Optics Express*, vol. 3, no. 2, pp. 89–96, 1998.

[113] J. P. Schiffer, "Phase transitions in anisotropically confined ionic crystals," *Physical Review Letters*, vol. 70, no. 6, p. 818, 1993.

[114] A. Steane, "The ion trap quantum information processor," *Applied Physics B*, vol. 64, no. 6, pp. 623–643, 1997.

[115] D. Enzer *et al.*, "Observation of power-law scaling for phase transitions in linear trapped ion crystals," *Physical Review Letters*, vol. 85, no. 12, p. 2466, 2000.

[116] H. Landa, M. Drewsen, B. Reznik, and A. Retzker, "Modes of oscillation in radiofrequency paul traps," *New Journal of Physics*, vol. 14, no. 9, p. 093 023, 2012.

[117] H. Landa, "Classical and quantum modes of coupled mathieu equations," *Journal of Physics A: Mathematical and Theoretical*, vol. 45, p. 455 305, 2012.

[118] W. C. Campbell *et al.*, "Ultrafast gates for single atomic qubits," *Physical Review Letters*, vol. 105, no. 9, p. 090 502, 2010.

[119] B. C. Sawyer, J. W. Britton, and J. J. Bollinger, "Spin dephasing as a probe of mode temperature, motional state distributions, and heating rates in a two-dimensional ion crystal," *Physical Review A*, vol. 89, no. 3, p. 033 408, 2014.

[120] H. Diep *et al.*, *Frustrated spin systems*. Singapore: World Scientific, 2013.

[121] M. Qiao *et al.*, "Double-electromagnetically-induced-transparency ground-state cooling of stationary two-dimensional ion crystals," *Physical Review Letters*, vol. 126, no. 2, p. 023 604, 2021.

[122] L. Feng *et al.*, "Efficient ground-state cooling of large trapped-ion chains with an electromagnetically induced transparency tripod scheme," *Physical Review Letters*, vol. 125, no. 5, p. 053 001, 2020.

[123] J. D. Siverns and Q. Quraishi, “Ion trap architectures and new directions,” *Quantum Information Processing*, vol. 16, no. 12, pp. 1–42, 2017.

[124] S. Gulde, “Ph.d dissertation,” *Universitt Innsbruck*, 2003.

[125] G. Pagano *et al.*, “Cryogenic trapped-ion system for large scale quantum simulation,” *Quantum Science and Technology*, vol. 4, no. 1, p. 014 004, 2018.

[126] D. Hucul *et al.*, “Modular entanglement of atomic qubits using photons and phonons,” *Nature Physics*, vol. 11, no. 1, pp. 37–42, 2015.

[127] R. Sterling, M. Hughes, C. Mellor, and W. Hensinger, “Increased surface flashover voltage in microfabricated devices,” *Applied Physics Letters*, vol. 103, no. 14, p. 143 504, 2013.

[128] L. Deslauriers, S. Olmschenk, D. Stick, W. Hensinger, J. Sterk, and C. Monroe, “Scaling and suppression of anomalous heating in ion traps,” *Physical Review Letters*, vol. 97, no. 10, p. 103 007, 2006.

[129] I. Zalivako *et al.*, “Nonselective paul ion trap loading with a light-emitting diode,” *Applied Physics Letters*, vol. 115, no. 10, p. 104 102, 2019.

[130] D. Cruz, J. Chang, and M. Blain, “Field emission characteristics of a tungsten microelectromechanical system device,” *Applied Physics Letters*, vol. 86, no. 15, p. 153 502, 2005.

[131] C. L. Arrington *et al.*, “Micro-fabricated stylus ion trap,” *Review of Scientific Instruments*, vol. 84, no. 8, p. 085 001, 2013.

[132] T. Ray, S. Jyothi, N. B. Ram, and S. Rangwala, “A thin wire ion trap to study ion–atom collisions built within a fabry–perot cavity,” *Applied Physics B*, vol. 114, no. 1, pp. 267–273, 2014.

[133] K.-Y. Lin, G. H. Low, and I. L. Chuang, “Effects of electrode surface roughness on motional heating of trapped ions,” *Physical Review A*, vol. 94, no. 1, p. 013 418, 2016.

[134] D. A. Hite *et al.*, “100-fold reduction of electric-field noise in an ion trap cleaned with in situ argon-ion-beam bombardment,” *Physical review letters*, vol. 109, no. 10, p. 103 001, 2012.

[135] D. Hite *et al.*, “Surface science for improved ion traps,” *MRS bulletin*, vol. 38, no. 10, pp. 826–833, 2013.

[136] Z. Wang, L. Luo, K. Thadasina, K. Qian, J. Cui, and Y. Huang, “Fabrication of ion-trap electrodes by self-terminated electrochemical etching,” *EPJ Techniques and Instrumentation*, vol. 3, pp. 1–9, 2016.

[137] K. Johnson *et al.*, “Active stabilization of ion trap radiofrequency potentials,” *Review of Scientific Instruments*, vol. 87, no. 5, p. 053 110, 2016.

[138] S. Olmschenk, K. C. Younge, D. L. Moehring, D. N. Matsukevich, P. Maunz, and C. Monroe, “Manipulation and detection of a trapped yb+ hyperfine qubit,” *Physical Review A*, vol. 76, no. 5, p. 052 314, 2007.

[139] F. Diedrich, J. Bergquist, W. M. Itano, and D. Wineland, “Laser cooling to the zero-point energy of motion,” *Physical review letters*, vol. 62, no. 4, p. 403, 1989.

[140] C. Lhuillier, “Frustrated quantum magnets,” *arXiv preprint cond-mat/0502464*, 2005.

[141] S. Yan, D. A. Huse, and S. R. White, “Spin-liquid ground state of the s= 1/2 kagome heisenberg antiferromagnet,” *Science*, vol. 332, no. 6034, pp. 1173–1176, 2011.

[142] K. Kumar, K. Sun, and E. Fradkin, “Chiral spin liquids on the kagome lattice,” *Physical Review B*, vol. 92, no. 9, p. 094 433, 2015.

Marissa Danielle D'Onofrio

EDUCATION

Indiana University, Bloomington, IN
PhD, Physics, August 2017-December 2022

Indiana University, Bloomington, IN
Masters, Physics, August 2017

Berry College, Mount Berry, GA
Bachelor of Science, Physics, May 2016

PROFESSIONAL EXPERIENCE

Postdoctoral Researcher Duke Quantum Center
Aug 2022-Present Durham, NC
Advisor: Ken Brown

Research Assistant Indiana University Physics Department
May 2017-Aug 2022 Bloomington, IN
Advisor: Phil Richerme

Physics Instructor Foundations in Science and Math
June 2018 Bloomington, IN
Organizer: Melene Thompson

Associate Instructor Indiana University Physics Department
Aug 2016-May 2017 Bloomington, IN
Director: Dan Beeker
Sections: General Physics I Discussion; Physics in the Modern World Lab

Research Assistant Indiana University Physics Department
June 2016-Aug 2016 Bloomington, IN
Advisor: Rex Tayloe

Student Researcher Berry College Physics Department
Jan 2015-May 2016 Mount Berry, GA
Advisor: Shawn Hilbert

Resident Assistant Berry College Residence Life
Aug 2014-May 2016 Mount Berry, GA
Director: Matt Mixer

Robotics Instructor Club Scientific
May 2014-Aug 2014 Marietta, GA
Director: Bob Hagan

PUBLICATIONS

A.J. Rasmusson, M. D'Onofrio, Y. Xie, J. Cui, and P. Richerme, "Optimized Sideband Cooling and Enhanced Thermometry of Trapped Ions," *Physical Review A*, **104**, 043108, (2021).

Y. Xie, J. Cui, M. D'Onofrio, A.J. Rasmusson, S. Howell, and P. Richerme, "An Open-Endcap Blade Trap for Radial-2D Ion Crystals," *Quantum Science and Technology*, **6**, 044009, (2021).

J. Cui, A.J.Rasmusson, M. D'Onofrio, Y. Xie, E. Wolanski, and P. Richerme, "Susceptibility of Trapped-Ion Qubits to Low-Dose Radiation Sources," *Journal of Physics B*, **54**, 13LT01, (2021).

M. D'Onofrio, Y. Xie, A.J.Rasmusson, E. Wolanski, J. Cui, and P. Richerme, "Radial Two- Dimensional Ion Crystals in a Linear Paul Trap," *Physical Review Letters*, **127**, 020503, (2021).

D. Akimov, et al. "First Constraint on Coherent Elastic Neutrino-Nucleus Scattering in Argon," *Physical Review D*, **100**, 115020, (2019).

D. Akimov, et al. "COHERENT 2018 at the spallation neutron source," arXiv:1803.09183, (2018).

M. D'Onofrio, M. Crum, T. Canalichio, T. Bull, H. Batelaan, and S.A. Hilbert,"An Acoustic Analog for a Quantum Mechanical Level-Splitting Route to Band Formation," *American Journal of Physics*, **84**, 841, (2016).

INVITED TALKS

Duke University, Durham, NC, "A Trapped Ion Quantum Simulator for Two-Dimensional Spin Systems," November 2021.

Berry College, Rome, GA, "A Trapped Ion Quantum Simulator for Two-Dimensional Spin Systems," November 2017.

PRESENTATIONS

M. D'Onofrio, Y. Xie, A.J. Rasmusson, J. Cui, A. Kyprianidis, Evangeline Wolanski, and P. Richerme, "A Trapped Ion Quantum Simulator for Two-Dimensional Spin Systems," *MCAW*, Purdue, IN, November 2021.

M. D'Onofrio, Y. Xie, A.J. Rasmusson, E. Wolanski, J. Cui, and P. Richerme, "Characterization and Control of Radial 2D Crystals in a Linear Paul Trap," *DAMOP*, Virtual Meeting, June 2021.

M. D'Onofrio, Y. Xie, A.J. Rasmusson, J. Cui, P. Madetzke, E. Wolanski, and P. Richerme, "Characterization of Radial 2D Ion Crystals for Quantum Simulation," *QED-C*, e-Poster Session, August 2020.

Y. Xie, M. D'Onofrio, A.J. Rasmusson, N. Schlossberger, M. Lollie, A. Henderson, and P. Richerme, "A Trapped Ion Quantum Simulator for Two-Dimensional Spin Systems," *MCAW*, Evanston, IL, November 2019.

M. D'Onofrio, Y. Xie, A.J. Rasmusson, N Schlossberger, M. Lollie, A. Henderson, and P. Richerme, "A Trapped Ion Quantum Simulator for Two-Dimensional Spin Systems," *Gordon Research Conference and Seminar*, Newport, RI, June 2019.

M. D'Onofrio, Y. Xie, A.J. Rasmusson, N. Schlossberger, M. Lollie, A. Henderson, and P. Richerme, "A Trapped Ion Quantum Simulator for Two-Dimensional Spin Systems," *DAMOP*, Milwaukee, WI, May 2019.

M. D'Onofrio, M. Crum, S.A. Hilbert, "An Acoustic Analog for a Quantum Mechanical Level-Splitting Route to Band Formation" *2016 Symposium on Student Scholarship*, Rome, GA, April 2016.

M. Crum, M. D'Onofrio, S.A. Hilbert, "Acoustic Analog to Level-Splitting Route to Band Gaps" *2016 Winter Meeting of the American Association of Physics Teachers*, New Orleans, LA, January 2016.

RECOGNITION

College of Arts and Sciences Travel Award, Indiana University, $200, November 2019.

Provost's Travel Award for Women in Science, Indiana University, $900, June 2019.

Provost's Travel Award for Women in Science, Indiana University, $900, May 2019.

GAANN Fellowship, Indiana University, May 2016-August 2018.

Lawrence E. McAllister Physics Award, Berry College Department of Physics, April 2016.

Society of Physics Students Outstanding Presentation Award, 2016 Winter Meeting of the American Association of Physics Teachers, January 2016.

Berry Research Development Fund Travel Grant, $456.70, December 2015.

Barber, Gordon Scholarship, Berry College Department of Physics, August 2015-May 2016.

Delta Scholarship Fund Award for Excellence, August 2014-May 2015.

Berry Dean's Scholarship, August 2013- May 2016.

Georgia Zell Miller Scholarship, August 2013- May 2016.

SERVICE TO INSTITUTIONS

Physics Graduate Student Council Indiana University Physics Department
Aug 2017-Feb 2018/March 2018- May 2019 Bloomington, IN
Position: Founding Member/President

Society of Physics Students Berry College
Sep 2015-Jan 2016 Mount Berry, GA
Position: Co-Founder/Vice President

ProQuest LLC
789 East Eisenhower Parkway
P.O. Box 1346
Ann Arbor, MI 48106 - 1346 USA